Thèse présentée pour obtenir le grade de

DOCTEUR DE L'ÉCOLE POLYTECHNIQUE

Specialité : Physique

par

Ermias Tujuba ATOMSSA

Suppression et flot elliptique du J/ψ dans les collisions Au+Au à 200 GeV dans la région à mi-rapidité de l'expérience PHENIX

Soutenue le 2 décembre 2008 devant le jury composé de :

M. Federico Antinori	
M. Michel Gonin	*Président du jury*
M. Raphaël Granier de Cassagnac	*Directeur de thèse*
M. Jean-Yves Grossiord	*Rapporteur*
M. Christian Kuhn	*Rapporteur*
M. Michael J. Leitch	
M. Helmut Satz	

To my parents ...

Résumé

Le méson J/ψ est considéré comme une sonde privilégiée de la formation du Plasma de Quarks et de Gluons (PQG) lors des collisions d'ions lourds. L'écrantage de la force de couleur a été proposé comme mécanisme de suppression *anormale* du J/ψ dans un milieu déconfiné, au-delà de la suppression *normale* dans la matière nucléaire ordinaire. Les premières mesures systématiques de la suppression du J/ψ ont été effectuées par les expériences NA38, NA50 et NA60 basées au SPS du CERN. Dans les systèmes les plus lourds étudiés, les résultats ont montré une suppression additionnelle par rapport à ce qui est attendu de l'absorption par la matière nucléaire normale. L'interprétation en termes de fonte dans le PQG a pourtant été contestée car des modèles d'absorption par des *comovers* hadroniques ne faisant pas intervenir un état déconfiné ont été capable de reproduire le résultat.

L'accélérateur RHIC au Brookhaven National Laboratory (États Unis) a été construit dans la perspective d'effectuer des mesures similaires à une énergie dix fois plus importante. La densité d'énergie atteinte au RHIC devait permettre de créer un PQG plus chaud, rendant ainsi la signature de suppression encore plus significative. Le détecteur PHENIX est, des quatre expériences qui furent installées au démarrage de RHIC, celle qui a une conception optimale pour la mesure du J/ψ : dans les canaux de décroissance en dimuon à rapidité vers l'avant, et en dielectron à mi-rapidité. Depuis, la collaboration PHENIX a effectué, entre autres, des mesures du taux de production du J/ψ en collisions p+p, d+Au, Cu+Cu et Au+Au à des énergies de collision par paire de nucléons allant de 19 GeV à 200 GeV. Le travail présenté ici couvre l'analyse de données prises par les spectromètres à mi-rapidité de PHENIX en collisions Au+Au à 200 GeV. Le facteur de modification nucléaire est mesuré en fonction de la centralité, et ensuite comparé à des extrapolations de la suppression due à la matière nucléaire froide, fondées sur les mesures effectuées dans des collisions d+Au à la même énergie. Malgré le fait que la suppression observée dans les collisions les plus centrales atteint un facteur plus grand que trois, une majeure partie peut être attribuée aux effets nucléaires froids, essentiellement dû aux incertitudes associées aux extrapolations. La signifiance de la suppression au delà des extrapolations s'avère être marginale. D'autre part, la comparaison avec les résultats des mesures effectuées au SPS du CERN et vers l'avant dans PHENIX présent des aspects étonnants qui semblent contrarier la vision intuitive d'une suppression qui croît avec la densité d'énergie locale.

Ce dernier constat a conduit à la spéculation que la régénération, un mécanisme de production des J/ψ par association de quarks c et $\bar{c}$ non corrélés, pourrait jouer un rôle important dans les collisions d'ion lourds les plus centraux. Le flot elliptique du J/ψ en fonction de p_T, une autre mesure présentée dans ce travail, est un outil potentiel pour tester le scénario de la régénération. Le résultat n'est pas concluant à cause des incertitudes expérimentales importantes, et reste compatible avec des modèles fondés sur une régénération maximale aussi bien que des modèles qui n'incorporent pas la régénération. Malgré l'obstacle statistique, il s'agit d'une démonstration de la faisabilité d'une mesure du flot elliptique dans un environnement à haute multiplicité.

Mots clés : PQG, J/ψ, RHIC, PHENIX, suppression, regeneration, flot elliptique

Abstract

J/ψ are considered to be one of the key probes of the Quark Gluon Plasma (QGP) formation in heavy ion collisions. Color screening was proposed as a mechanism leading to anomalous suppression beyond normal absorption in nuclear matter if J/ψs were created in a deconfined medium, providing a direct evidence of deconfinement. The first experiments that performed a systematic measurement of the suppression of J/ψ in heavy ion colliding systems were the CERN SPS experiments (NA38, NA50, and NA60). Their results demonstrated that there is indeed an extra suppression with respect to what is expected from normal nuclear absorption in the heaviest of the colliding systems that were studied. However, the interpretation of these results in terms of melting in the QGP was challenged by hadronic *comover* absorption models that do not involve the formation of a deconfined state.

The RHIC accelerator at the Brookhaven National Laboratory (USA) was constructed with the perspective of performing similar measurements but at a $\sim 10\times$ higher energy. The higher energy density that is available at RHIC should create a hotter QGP, and render the suppression signature more significant. The PHENIX detector is one of the four experiments that were installed at RHIC, with a design that is optimal for the measurement of the J/ψ meson at forward rapidity in the dimuon decay channel, and at mid rapidity in the dielectron decay channel. Since day one operation in 2001, PHENIX has measured, among many other observables, J/ψ yields in p+p, d+Au, Cu+Cu and Au+Au collisions in a wide range of energies going from 19 GeV to 200 GeV per pair of nucleons. The work presented here covers the analysis of data taken by the mid rapidity spectrometers of PHENIX in Au+Au collisions at 200 GeV. The nuclear modification factor is measured as a function of centrality, and compared to extrapolations of cold nuclear matter suppression constrained in d+Au collisions at the same energy. Though the suppression seen in the most central collisions goes up to a factor of more than three, given the large errors in the extrapolations, most of it can possibly be accounted for by cold nuclear effects, and the significance of the extra anomalous suppression is small. More strikingly, comparisons to the CERN SPS results and to the suppression measurement at forward rapidity in PHENIX show features that seem to suggest the violation of the intuitive picture of increasing suppression with local energy density.

This has led to the speculation that regeneration, a J/ψ production mechanism by association of uncorrelated c and $\bar{c}$ quarks, might be at play in central heavy ion collisions. A second measurement presented in this thesis, the elliptic flow of J/ψ as a function of p_T, is a potential tool to test the regeneration scenario. The result is currently inconclusive since, owing to the large uncertainties, it is compatible both with models that are based on maximum recombination, and models that do not consider any regeneration. It remains however a good proof of principle of the feasibility of the measurement in the high multiplicity environment at this energy.

Keywords: QGP, J/ψ, RHIC, PHENIX, suppression, regeneration, elliptic flow

Acknowledgements

Following tradition, I would like to give here credit to all those who, directly or indirectly, have done something to make the hard days of completing this thesis bearable. Of course doing so is kind of hard, so I might have inadvertently omitted to mention some, and I would like to apologize in advance if you reader feel that your name should have figured here, but get more and more deceived as you go through the lines. For you such reader, I give the deepest of thanks, and hope that you will forgive me!

First thing is first, and I would like to thank deeply my parents without whose constant support all this would not have been possible. I dedicate this thesis to them. They have, against all odds, allowed me to have all I needed as a kid to pursue my dreams. I thank deeply mom, who after the painful loss of dad, did all the sacrifices to let us continue thrive in the best schools. Without that early devotion, I am sure I would not have been able to reach where I stand now. I would also like to thank all my brothers and sisters. Thanks Yared, for the wonderful chats on all and nothing; Daniel, for being there, even when things were not so easy for yourself; Hanna, for making each and every one of my stays in Addis such unforgettable experiences, I cherish them; Lydia, for the wonderful welcome you reserved me in Oslo; Betty and Rebekka, for your kindness and love. All of you, your strength and courage have been my source of inspiration in the hardest of times during these years away from you.

Thanks to all Addis folks who have kept being wonderful friends despite my absence. Johnny, for your incredible friendship, and constant, endless sense of humour that made you invaluable to spice up the parties. Tesfish, for the chats during the many many late evenings at the lab, without which I would have been terribly lonely. Anteneh for all the 'errita'; Anteneh and Babeth for keeping my French up during the vacations. Thank you Araya, Dawit and Yirgalem of AAU for the constant interest you have shown about my progress.

Merci à Irina et Dimitry, pour votre soutien pendant les jours menant à ma soutenance. Vous avez fait preuve d'une incroyable gentillesse en m'aidant à préparer le magnifique pot de thèse. Merci Maxime pour ton amitié, et les rappels réguliers de l'avancement de ta propre rédaction. Même si ça devenait pénible vers la fin, c'était un bon coup de pied aux fesses pour me rappeler qu'on avait le même échéancier, ... et que je devais d'accélérer. Sans compte de m'avoir logé quand je me faisais jeter de partout. Je te remercie et tous nos amis 'wesh mehdi', en particulier Joshua, Benjadinde, Antony et Nassim pour les voyages de découverte de la France profonde, en goûtant le sacristain en Normandie et en faisant du jogging sur les collines de Sainte Agnès en Côte d'Azur. De vous être présenté régulièrement à nos sessions footballistiques de dimanche soir, et pour les maintes soirées de billard–bowling–bière ! Je voudrais aussi remercier ici Nicole, Michèle et Philippe, pour votre hospitalité pendant certains weekends longs et les vacances, et de vous être occupé de mon initiation au ski de fond.

I would like to thank the management of the Laboratoire Leprince Ringuet, in particular Mr. Henri Videau, for welcoming me to do my thesis. Special thanks to Mr. Jean-Louis Badevant and Mr. André Rougé for their support that allowed me to obtain the necessary financial support. Thank you to all members of my examination comette, for having accepted to be part of it despite the short notice and the few date modifications, and for the valuable comments and corrections that you gave me, in particular my reporters, Dr. Jean-Yves Grossiord and Dr. Christian Kuhn and also Dr. Michael J. Leitch. I would also like to thank Pr. Dr. Helmut Satz and Dr. Federico Antinori.

A deep thanks goes to Raphaël, my adviser, for having been more than just an adviser, but also a good friend. Thank you for your patience and follow up. You were available, within the measure that your overbooked agenda allowed you, even sacrificing your weekends, to answer to my sometimes very last minute questions and calls for help, and that was really appreciated! Thanks for the guidance in discovering first New York, and then BNL, which, I agree, is the ideal order. Thanks to the other members of the group. Frédéric and Hugo for the wonderful physics discussions and many 'pauses clopes'. Olivier and Michel, thank you for having offered your help even for very practical and personal matters, you know what I am talking about... The human qualities of this group were indispensable for the successful completion of this thesis. I have learned a lot from all of you, not only about the quark gluon plasma, but also about ongoings in the lab, and at the head of the French state through the fun discussions after lunch, and the 'petit et grand tours'.

Je voudrais ici saisir l'occasion pour remercier les gens qui étaient proches de notre groupe pour une raison ou une autre; Franck et Simon, pour votre patience à supporter ma présence dans la salle d'électronique, pendant la tentative avortée de faire ma thèse sur le SVD; Alain pour ton soutien moral, et pour m'avoir souvent dépanné ces jours de dimanche, où je me rendis compte après être arrivé au labo, que, hélas, j'avais oublié de ramener mes clefs de bureau; Patrice pour tes blagues extrêmes qui égayaient les déjeuners, et tes rappels constants que je risquais le charter si je ne travaillais pas dur. Mon séjour en France et au labo dépendait d'une paperasserie horrible, qui, sans l'aide de Brigitte, Maité et Patrice, m'aurait rendu assez misérable. Un merci chaleureux à Audrey de l'EDX d'avoir toléré mes visites fréquentes, autour du mois de septembre de chaque année à demander son aide, toujours accordée avec une bonne dose d'humour et de gentillesse, pour s'occuper d'une certaine nécessité administrative infâme.

Then come all the young folks of our lab. First Catherine, who was going under the same 'galère', almost synchronously with me, and whose kind friendship will never be forgotten. Thank you for having shared all the hard and good times during these three+ years. Thanks for having allowed our wonderful football team to reach the semifinals, through your participation and ten goals (though you would not admit it)! Thanks Giulia, for the wonderful chats, you've been a good friend. Thanks Zaida, for your help and availability and support, for the many 'sorties ciné'. Thank you the 'ex-thésards' of our lab, for smoothing the ground for us the later 'thésards', it is not always easy being the first. Vi Nham, whose help and advice have often accompanied me and were valuable, especially at the beginning and towards the end of my thesis. Andry for the nice desserts that you brought from time to time and helped us escape the terrible ones at Magnan. Julien and Haig, for your participation to the LLR football team, Julien for the 'dépannages informatiques'. Thanks Marcel for the fun jokes in corridors, Julia for the wonderful company, good luck and 'bon courage pour la suite'. Going to other young people outside of our lab, thanks to the Hiroshima group for

their welcome in my improvised visit to Japan, especially Misaki, Kotaro and Kazu for their hospitality. A deep thanks goes to Keiko, for insuring that I would not get lost in Tokyo. Àstrid, for convincing and encouraging me to take part in the ASAP evenings whenever I was around at BNL. Thank you Sasha, for the help in the many 'déménagements', and Feng for the pseudo-philosophical conversations, that allowed me to learn, among other things, a lot about Chinese culture!

I write this last paragraph to thank all those people at BNL (and outside), who were always available for discussions, and without whose active reply to my questions and interrogations, my risky decision to work with the central arm could have turned into a disaster. Thank you Taku for having been my ultimate recourse when I was completely blocked with analysis; Cesar, for the nice discussions; I would also like to deeply thank senior members, Yasuyuki, Tony, Wei and Marzia, for their help and advise. Thank you Ágnes for reading *in extremis* parts of my thesis and suggesting valuable corrections.

So here I am, over with my acknowledgements. I really depended on all of you mentioned here and many others. I'm really pleased to have completed this thesis, and I owe you all one too many!

Contents

Introduction

In the standard model of fundamental particles and interactions, fractionally charged quarks and neutral gluons make up hadronic matter, which represents the majority of the mass of an atom, and thus that of the visible universe. The standard model sector that deals with the strong interaction between quarks and gluons is called *quantum chromodynamics* (QCD). It is a quantum field theory based on a special unitary symmetry (SU3) that leads to the conservation of a quantum number of quarks and gluons called *color* with three degrees of freedom. The running of the QCD coupling constant α_s, meaning its dependence on the energy scale μ at which the observation is made is shown in Fig. 1. This tendency is inverse to the dependence of the coupling constant of *quantum electrodynamics* (QED), the theory of the electromagnetic interactions, conferring to the strong interaction most of its peculiarities. At very high energy, corresponding to short distance scales, α_s is small. This property is referred to as *asymptotic freedom*. As the energy scale decreases, which is equivalent to increasing the distance scale, α_s gets stronger. This results in the *confinement* of quarks into colorless hadrons, and in the fundamental impossibility to observe isolated objects with net color (quarks and gluons).

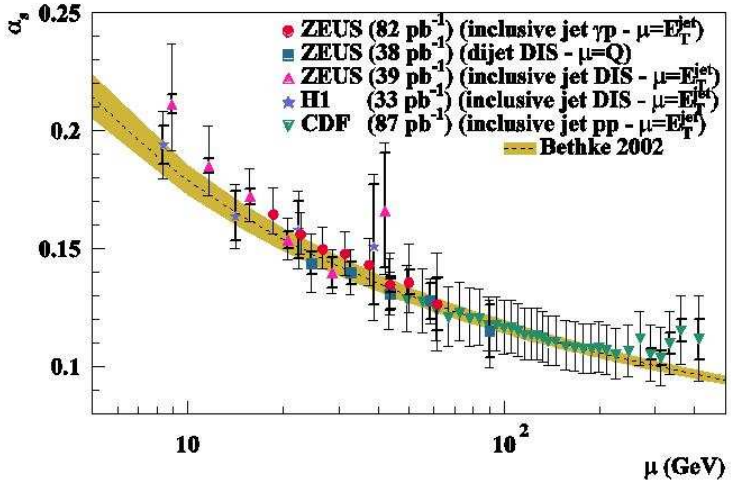

Figure 1: The running of the QCD coupling constant, vs. the energy scale μ in GeV.

One of the most astounding success of QCD theory is the very detailed quantitative confirmation of the running of α_s by deep inelastic scattering (DIS) experiments. The experimentally measured values of the α_s at different energy scales by DIS experiments is compared to theoretical prediction from QCD in Fig. 1.

The Quark Gluon Plasma (QGP) is a state of matter made up of *deconfined* quarks and gluons. Under specific circumstances, quarks and gluons can be made to evolve without belonging to any hadron in a volume which is large compared to the size of a nucleon. Their mean free path becomes much larger than the typical size of hadrons of around 1 fm, where they stay confined under normal conditions. This is *not* asymptotic freedom, where valence quarks and gluons within a nucleon are seen as being free from each other when probed at a very short distance (or high energy) scale. Quarks in a QGP can indeed evolve freely from one end of the volume to another, and finally hadronize with other quarks that, before QGP formation, were initially confined into independent hadrons.

There are two necessary conditions to create a QGP state: high temperature or pressure and high energy/matter density. These are conditions which are believed to have prevailed in the first instants of the Big Bang, immediately after the electroweak transition (∼10 ps after t_0) and lasting for a few microseconds. In this period, matter must have existed in a state of deconfined QGP. Only at later times, when the temperature of the universe started to cool down, did the thermal motion of the quarks become small enough (k_bT[1] smaller than the strong interaction potential) to permit the association of quarks into hadrons. For a discussion on the potential relics from these early times, see [1]. There are also astrophysical arguments that the interior of some neutron stars is dense and hot enough for the existence of a state of QGP. But the observational evidences are not strong enough and disputed. For a discussion of the latest candidate see [2].

The creation of a QGP in a laboratory has been a center of interest for a large high energy nuclear physics community for over the past 30 years. The idea about how to investigate the QGP experimentally through heavy ion collisions was initially proposed by T. D. Lee [3]. Since then, a number of accelerators have provided collisions between heavy ions, with ever increasing energy, from Bevatron-Bevalac at LBL (Lawrence Berkeley National Laboratory) to AGS (Alternating Gradient Synchrotron) at BNL (Brookhaven National Laboratory), SPS (Super Proton Synchrotron) at the CERN (European Organization of Nuclear Research) and RHIC (Relativistic Heavy Ion Collider) at BNL. The LHC (Large Hadron Collider) at the CERN is expected to provide even more energetic collisions between heavy ions, and the estimated energy per collision will approach macroscopic values (5.5 TeV×207=$\frac{1140\ \text{TeV}}{1.6\times10^{19}\text{eV/J}}$=$10^{-4}$J).

The work presented in this thesis will concentrate on data from PHENIX (acronym for Pioneering High Energy Nuclear Ion eXperiment), one of the four experiments operating at RHIC, in collisions between gold nuclei at an energy per nucleon pair of $\sqrt{s_{NN}}$ = 200 GeV. The focus here will be on one of the oldest recognized signatures of the QGP in heavy ion collisions, the anomalous suppression of J/ψ. In the following chapter, the basics of QGP physics in heavy ion collisions will be exposed, followed by a discussion of what has already been learned (both theoretically and experimentally) about the J/ψ signature. In chapter 2, the experimental apparatus of PHENIX relevant for this work will be explained in detail. In chapter 3, the data taking conditions will be summarized. After an explanation of all the steps taken to extract the J/ψ yield from this data in chapter 4, the interpretation and discussion of the results for two observables will be given in the last two chapters: "J/ψ suppression" and "J/ψ elliptic flow".

[1] k_bT is the typical kinetic energy possessed by constituents of a system due to thermal motion at a temperature $\sim T$. The Boltzmann constant k_b=8.6×10^{-5} eV/K.

Chapter I

The Quark Gluon Plasma

This chapter is intended as a general introduction to the physics of the Quark Gluon Plasma (QGP) and in particular the use of the J/ψ meson as a signature of its creation in relativistic heavy ion collisions. It starts with a brief overview of the lattice QCD picture of the QGP state in Sec. I.1. The remaining part of this introductory chapter will be dedicated to the experimental signals and phenomenological understanding of the system that is created in heavy ion collisions. In Sec. I.2, a brief description of the chronology of a typical heavy ion collision in the framework of hydrodynamics inspired models will be given, to be followed by studies that exploit the hadronic composition of the bulk of the produced particles (cf. Sec. I.2.1). Results on the measurement of typical hard probes, particles that are created early in the collision in inelastic nucleon–nucleon collisions, are shown (cf. Sec. I.2.2) as a demonstration of how hard probes can shed light on the nature of the medium produced in heavy ion collisions. This will serve as a basis over which the particular case of the use of the J/ψ meson as a probe will be developed in Sec. I.3. In this last section, after a brief historic introduction, all those aspects of J/ψ production and absorption that are relevant for the measurement performed in this thesis will be presented.

I.1 Lessons from lattice QCD

An essential part of the theoretical work in QCD concerns the asymptotically weak coupling limit of the strong interaction. The main reason for this is that the equations of QCD can be solved perturbatively just as in QED in this regime where α_s takes small enough values. This is what is referred to as perturbative QCD (pQCD). Unfortunately an essential part of QGP physics accessible in heavy ion collisions is non perturbative, consequently intractable by the analytical techniques that have led to the well established understanding of pQCD. The only[1] possible way to study the QGP theoretically from first principles is offered by lattice QCD (lQCD). lQCD is the numerical implementation of QCD on a discrete space-time lattice. lQCD has been used in the past to predict important properties of the QGP. The two main themes that have been explored widely by lQCD and relevant for the experimental investigation of the QGP are the equation of state of deconfined medium and the heavy quark interaction potentials in QGP. The current knowledge of the equation of state from lQCD

[1]Recently there has been some success in describing the medium created in heavy ion collisions in the framework of the AdS/CFT correspondence, involving concepts from string theory. See [4] for the original proposition and [5] for recent developments.

studies will be addressed here. The question of heavy quark potentials will be deferred to Sec. I.3 on J/ψ suppression.

The properties of a thermalized QGP medium can be characterized by thermodynamic quantities such as energy density (ε), entropy density (s), fermion chemical potentials (μ_f[2]), pressure (p) and temperature (T). An equation of state describes the relation between these thermodynamic quantities. In addition to understanding the phase transition from normal hadronic matter into QGP, an equation of state is an essential ingredient to calculations of the evolution of the bulk of particles in the medium.

In the lattice formulation of QCD, the thermodynamic quantities can be inferred from the grand canonical (GC) partition function, given as an integral over the fundamental quark (ψ,$\bar{\psi}$) and gluon (A_ν) fields of the exponential of the Euclidean action [6]

$$Z(V,T,\mu_f) = \int \mathcal{D}A_\nu \mathcal{D}\bar{\psi}\mathcal{D}\psi e^{-S_E(V,T,\mu_f)} \tag{I.1}$$

where V is the volume, T the temperature of the system, and μ_f the chemical potential for the quark flavour of mass m_f among the $f = 1, ..., n_f$ being considered. The lQCD calculations performed by different groups differ in their choice of the number and masses of fermions that are included. The Euclidean action $S_E \equiv S_G + S_F$ is composed of a gluonic S_G and fermionic S_F parts, equal to the space-time integral of the gauge field interaction part (trace of the field strength tensor $F_{\mu\nu} = \partial_\mu A_\nu - \partial_\nu A_\mu - ig[A_\mu, A_\nu]$) and gauge field - fermion interaction parts of the QCD Lagrangian respectively

$$\begin{aligned} S_E(V,T,\mu_f) &= S_G(V,T,\mu_f) + S_F(V,T,\mu_f) \\ S_G(V,T) &= \int_0^{1/T} dx_4 \int_0^v d\mathbf{x}\ \frac{1}{2} F_{\mu\nu}F^{\mu\nu} \\ S_F(V,T,\mu_f) &= \int_0^{1/T} dx_4 \int_0^v d\mathbf{x} \sum_f^{n_f} \bar{\psi}_f(\gamma_\nu[\partial_\nu - igA_\nu] + \mu_f\gamma_0 + m_f)\psi_f \end{aligned} \tag{I.2}$$

The space integral runs over the volume of the system, and the time integral runs from 0 to the inverse of the temperature. The partition function is implemented on the lattice by some choice of lattice size ($N_\sigma^3 \times N_\tau$) and spacing a, from which the volume and temperature are derived as

$$V = (N_\sigma a)^3 \quad , \quad T^{-1} = N_\tau a. \tag{I.3}$$

Thermodynamic quantities like the pressure p and energy density ε can then be calculated using GC ensemble relations

$$\frac{p}{T^4} = \frac{1}{VT^3} lnZ(V,T,\mu_f) \tag{I.4}$$

$$\frac{\varepsilon - 3p}{T^4} = T\frac{d}{dT}\left(\frac{p}{T^4}\right)\Big|_{fixed\ \mu/T} \tag{I.5}$$

[2]The fermionic chemical potential is the energy required to add one more fermion of a given set of quantum numbers into the system.

The dependence $p(T)$, or equivalently $\varepsilon(T)$, is the equation of state that completely describes the thermodynamic properties of the QGP. Fig. I.1 shows the temperature dependence of the entropy density (energy density divided by the fourth power of T) [6], where a sharp increase of ε/T^4 is observed at a critical temperature which is calculated to be of the order of T_0=170 MeV[3]. The entropy density is proportional to the number of degrees of freedom (n_{dof}). Before the transition, the pion gas has $n_{dof} = 3$ (or three states: $\pi^{\pm}, \pi^0$), whereas after the transition, the number of degrees of freedom rises to the number of quark and gluon helicity states[4]

$$n_{dof} = 8_c \times 2_s + 3_c \times \ N_f \times 2_s \times 2_{q\bar{q}} \approx \ 40, \tag{I.6}$$

where the number of flavours N_f is taken to be 2. The rapid rise in entropy around T_0 reflects this explosion of the number of degrees of freedom that accompanies the phase transition from normal hadronic matter to QGP. In the very high temperature limit, the entropy density approaches the Boltzmann limit of ideal (non interacting) gas of quarks and gluons (depicted by the arrows on the right side).

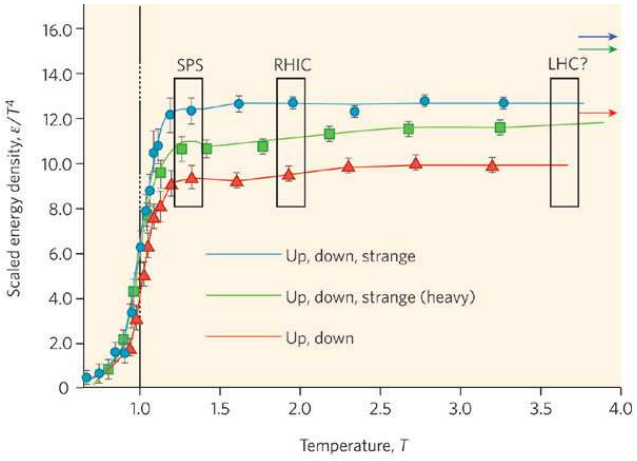

Figure I.1: Evolution of the entropy density as a function of the temperature, in units of T_0.

The nature of this phase transition can be studied by the derivatives of special lQCD observables (called the chiral condensate and chiral susceptibility). A singularity in the first derivative of these observables as a function of temperature implies first order phase transition, whereas a singularity in the second derivatives implies a second order phase transition at the temperature where the singularity occurs. If there is no singularity, then a local maximum in these observables implies a rapid cross over at the position of the local maximum. These observables can be used to map a phase diagram in the temperature vs. baryonic chemical potential space. The current knowledge of this phase diagram is given by the schematic

[3]For convenience, the eV unit is adopted for measuring temperatures. The temperature stated in this unit refers to the average thermal kinetic energy $k_B T$ of the constituents of a system equilibrated at an absolute temperature of T. A temperature of 100 MeV corresponds to $\frac{1^8 \text{ eV}}{8.16\times10^{-5} \text{ eV/K}} = 1.16\times10^{12}$K.

[4]The various terms and factors, from left to right, stand for: first term for the eight color states and two spin states of the gluons, second term for the three color states, the number of flavours considered (2 in this case, up and down), two spin states of the quarks and a final factor of two to account for the presence of antiquarks.

diagram in Fig. I.2. The vertical axis is temperature in MeV. On the horizontal axis is the net baryon density in a scale in which the value 1 denotes the net baryonic density of normal nuclear matter ($\sim$0.17 GeV/fm^3).

This phase diagram shows a transition from normal hadronic matter to a deconfined state of QGP going to higher temperature or going to high net baryon density. It is believed to have a characteristic critical point, where the order of the phase transition changes. Current lQCD calculations with dynamic (massive) quarks [7, 8] at zero baryonic chemical potential μ_b[5] using different number and combination of light and heavy quarks agree in that the transition into QGP takes place as a rapid cross over rather than a first order phase transition at a temperature of about 170 MeV with a systematical uncertainty of $\sim$ 10 MeV. The equivalent critical density[6] is 0.7$\pm$0.2 GeV/fm^3, around five times the nuclear density.

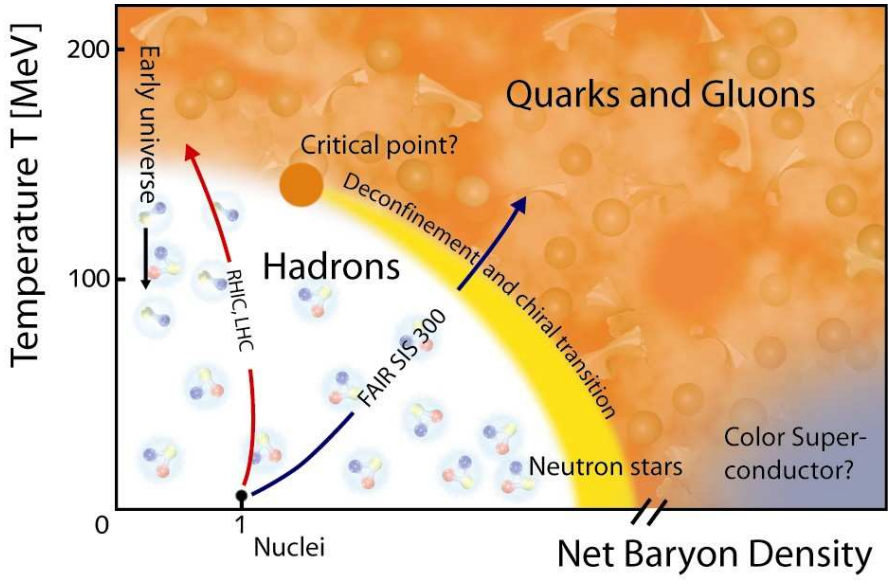

Figure I.2: Artist view of the baryonic potential vs temperature phase diagram of QCD.

The calculations at non zero baryonic density are less reliable (with larger systematical uncertainty). Results have recently started to be available [9], and they agree in that the transition temperature drops only very slightly (1-2%) in going up to a third of the way to the net baryonic density of nuclei. It is expected that at some net baryonic density, the transition stops to be a rapid cross over and becomes a first order phase transition. This critical end point is depicted in Fig. I.2 as a large orange point.

[5]Formally, the baryonic chemical potential is the energy required to add one more baryon into (or remove one anti-baryon from) the system. As the net baryon density increases in a thermal system, it becomes more and more energetically costly to add another one, so the net baryon density is monotonically increasing with μ_b and thus sometimes used as an approximation to it.

[6]Note that this is the total density not baryonic density.

I.2 Lessons from experiment

So far, the only experimental way accessible to study the QGP is offered by high energy heavy ion collisions. Enough energy can be liberated during these collisions through the hard scattering between nucleons in the target and projectile nuclei in a short enough time to stimulate the phase transition of the available matter into a deconfined state of QGP. There is a major inconvenience, though not inextricable, in this approach. Namely, the lifetime of the medium created is very short. Indeed in a time of the order of 10^{-23} to 10^{-22} s (3 to 30 fm/c) it would have cooled back and finished its reverse phase transition to hadronic matter. The only possible experimental signatures of what took place during this transitory existence of the QGP are encoded in (1) The momenta distributions of the products from initial nucleon-nucleon collision that traverse the medium in their way out and (2) the nature of hadrons that are formed in the bulk of the medium from hadronization of the deconfined quarks.

I.2.1 Describing the medium

The schematics in Fig. I.3 is an artist view of the time evolution of a heavy ion collision. At ultrarelativistic energies, the nuclei are flattened due to Lorentz contraction, as represented by the left most diagram. During nuclear interpenetration, initial nucleon-nucleon scatterings occur. These are the hardest scatterings that happen throughout the event history, since in later stages, partons get softer and softer and the frequency of high momentum transfer reactions decreases. This takes place for interval of time determined by the relative speed and thickness of the nuclei. At top RHIC energy ($\sqrt{s_{NN}}$=200 GeV) and for gold nuclei with radius R $\approx$ 7 fm, the crossing time is of the order of $\tau_{cross} = R\gamma/2 \approx 0.13$ fm/c [10]. After crossing, the initial partons and secondaries are produced on a time scale of the order of $\tau_{form} \approx 0.7$ fm/c [10], called formation time. The transverse energy of formed particles per unit volume is an indication of the energy density achieved. If it is larger than the transition energy density predicted by lQCD (of the order of 1 GeV/fm^3), then a QGP should *in principle* be formed.

In case of plasma formation, the system evolves as a hot and deconfined medium for a short period of time, for the duration of which it is now understood to achieve local thermal equilibrium due to the extremely high reaction intensity on a time scale of the order of $\tau_{therm} \approx$ 0.6-1 fm/c [10], called thermalization time. This system gradually cools down to hadronization, expanding hydrodynamically at the same time. The complete transformation back to a hadronic gas is estimated to be complete at a time scale of $\tau_{hadr} \approx$ 4-6 fm/c [10], called hadronization time. We can schematically categorize the ensemble of produced particles into the *soft* (also called *bulk*) and the *hard* components. Particles in the first category are formed inside the medium, and populate essentially the low end of the p_T spectrum ($\lesssim$2 GeV/c). At RHIC, they constitute a majority the total emitted particle multiplicity. Particles created in the initial hard scatterings constitute the *hard* component and populate the higher end of the p_T spectrum.

Before going into discussions about the system created in heavy ion collisions as 'matter' and not as a mere collection of particles, it is in order to recall the importance of local thermalization. The main condition for local thermalization of a system is that the mean free path of its constituents becomes much smaller than the system size. In other words, the

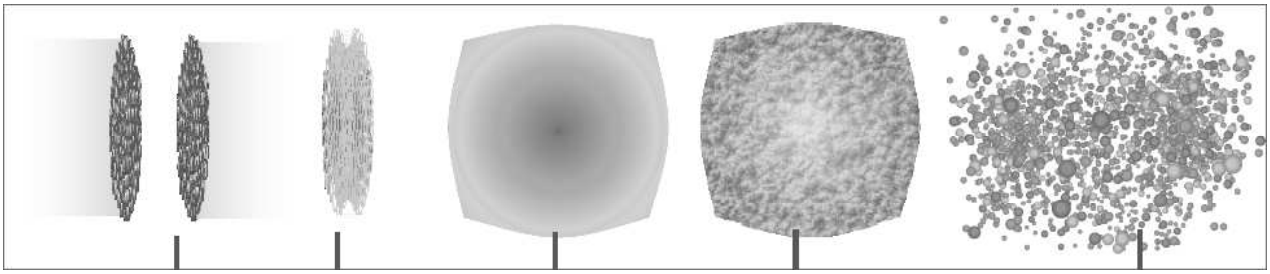

Figure I.3: Artist view of the evolution history of heavy ion collisions.

frequency of the interactions should be high enough so that all constituents interact at least a few times during the lifetime of the system. In such a system, external perturbations of the macroscopic properties (volume or pressure) are quickly diffused by auto-adjustments through redistribution of the microscopic variables (momenta of constituents) on a short time scale compared to the system lifetime. Only under these circumstances can we treat the created matter on hydrodynamical grounds.

Heavy ion collisions leave behind them a charged particle multiplicity of the order of a few thousands at RHIC[7] (and probably even more at the Large Hadron Collider), and possibly in a deconfined state, where colored degrees of freedom are visible and strongly interacting. Systems with a number of constituents not far from this order of magnitude have been known to achieve equilibrium. For instance, experiments with a few hundred thousand trapped cold fermionic atoms with tunable interaction strength have been shown to behave hydrodynamically [12] if interaction rates are set to be high enough, and experiments with even smaller number of particles are underway. This demonstrates that the important factor is not the number of particles but the interaction rate. Similarly it is not impossible that local thermalization is achieved in heavy ion collisions, and as it will be shown later in this section, experimental evidences support that it is indeed the case, and on a very short time scale.

I.2.1.1 The Glauber model

The Glauber model [13] (named after Prof. Roy Glauber, for his pioneering contribution to its elaboration) is a semi classical geometrical description of the collision process between two nuclei of atomic masses A and B. It is used to calculate essential characteristics of nuclear collisions, such as the inelastic cross section σ_{inel}^{AB}, the number of participating nucleons N_{part}, the number of spectator nucleons $N_{spect} = A + B - N_{part}$, the number of binary nucleon-nucleon collisions N_{coll} and the eccentricity (ε)[8] in terms of the impact parameter b. It is easily adaptable to a framework where the averages of these quantities can be calculated for an experimental selection of events.

There are two major 'experimental' inputs to the Glauber model, that can not be predicted within the model. These are:

- **The nuclear charge density function,** $\rho(r)$: This is usually parametrized as a radi-

[7] At midrapidity, the number of charged particles reaches $dN_{ch}/d\eta|_{\eta=0} = 670$ in the most violent Au+Au collisions and they sum up to about 6000 particles (of any charge) over the full rapidity range [11].

[8] Eccentricity is a parameter that quantifies how much the overlapping region deviates from a perfect circle, and approaches the shape of an oval. It is calculated as $\varepsilon = \frac{<Y^2-X^2>}{<Y^2+X^2>}$, where X and Y are the positions in the transverse plane of the participating nuclei. For circles, ε=0, and it increases for more oval shapes.

ally symmetric Woods-Saxon distribution

$$\rho(r) = \rho_0 \times \frac{1 + w(r/R)^2}{1 + \exp(\frac{r-R}{a})} \tag{I.7}$$

where ρ_0 is the density at the center of the nucleus, R is the typical radius and a is the "skin-depth" (also known as diffuseness) of the nucleus. w characterizes the departure from perfect sphericity. For gold nuclei, namely the beam particles used for this thesis, (R,a,w)=(6.38, 0.535, 0) in fermis.

For deuterons, the distance r_{pn} between the proton and the neutron is drawn from the distribution $p(r_{pn}) = 4\pi\ r_{pn}^2\phi^2(r_{pn})$, where $\phi(r_{pn})$ is the Hulth'en function:

$$\phi(r_{pn}) = \frac{1}{\sqrt{2\pi}} \frac{\sqrt{ab(a+b)}}{b-a} \times \frac{e^{-ar_{pn}} - e^{-br_{pn}}}{r_{pn}} \tag{I.8}$$

used with a=0.228 fm^{-1} and b=1.18 fm^{-1}.

- **The inelastic nucleon-nucleon cross section,** σ_{inel}^{NN}: Due to the possibility that the elementary N-N collisions in nuclear interactions can involve soft (low momentum transfer) processes, σ_{inel}^{NN} can not be calculated from pQCD, and must be inferred from experimental measurements. The value of σ_{inel}^{NN}=42 mb, relevant at top RHIC energy ($\sqrt{s_{NN}}$=200 GeV) is used for Glauber calculation at RHIC. This cross section is as low as 32 mb for the low energy SPS runs ($\sqrt{s_{NN}}$=19.6 GeV).

Further assumptions should be done to actually implement the model. Two approaches with slightly different assumptions have been developed.

- **The Optical-limit approach.** Here it is assumed that (1) Nucleons carry sufficiently high momentum so that they are essentially undeflected from their longitudinal path as nuclei pass through each other (eikonal approximation). (2) The nucleons move independently in the nucleus, ie. nucleons within a nucleus do not interact with each other. (3) The size of the nucleus is large compared to the effective cross section of nucleons. The first assumption is valid for collision energies larger than typical electromagnetic interaction potential between nuclei. This is valid for SPS and RHIC energies. If not valid it should be corrected by considering non eikonal paths [14]. The third assumption essentially allows the use of continuous nuclear density such as shown in Eq. I.7 and Eq. I.8.

  Based on this approximation it is possible to derive analytical solutions for the differential inelastic cross section ($\frac{d^2\sigma_{inel}^{AB}}{db^2}$), $N_{coll}(\mathbf{b})$ and $N_{part}(\mathbf{b})$ in terms of the nuclear thickness function $T_{AB}(\mathbf{b})$[9] and inelastic nucleon-nucleon cross section σ_{inel}^{NN}.

- **Monte Carlo approach.** In this approach, only assumptions (1) and (2) from the optical-limit approach is kept. In addition it is assumed that the nucleon-nucleon collision cross section does not change irrespective of how many times the given participants have already undergone inelastic collisions. Practically, the simulation is performed by

[9] $T_{AB}(\mathbf{b}) = \int T_A(\mathbf{s})T_B(\mathbf{s}-\mathbf{b})d\mathbf{s}$ is the convolution of nuclear charge density functions of nucleus A and B in the transverse plane (integrated over z), $T_{A/B}(\mathbf{r}) = \int_z \rho_{A/B}(\mathbf{r}, z)dz$.

the following steps. (a) The positions of each of the nucleons in the colliding nuclei are drawn from a random probability distribution function set to be the nuclear charge density (Eq. I.7 or Eq. I.8 for example). The assumption of continuous nucleon density used in the earlier approach is thus not necessary here. (b) A random impact parameter is chosen from the distribution $d\sigma/db = 2\pi b$. (c) The nucleus-nucleus collision is treated as a sequence of independent binary nucleon-nucleon collisions. A nucleon from nucleus A undergoes an inelastic collision with a nucleon in nucleus B if and only if their distance in the transverse plane to the beam axis satisfies $d \leq \sqrt{\sigma_{NN}/\pi}$[10]. This gives the operational definition to count the number of participating nucleons N_{part} and the number of binary collisions N_{coll}. A given throw results in an inelastic nucleus-nucleus interaction if there is at least one inelastic nucleon-nucleon. (d) Finally, quantities such as $\frac{d^2\sigma^{AB}_{inel}}{db^2}$ and the averages $< \varepsilon >$, $< N_{coll}(b) >$ and $< N_{part}(b) >$ are calculated by simulating many nucleus-nucleus collisions.

These two approaches give essentially the same results as long as σ^{NN}_{inel} is not too large. The Monte Carlo approach, adapted by PHENIX and used for the data presented in this thesis, is very suitable for relating the mean values of the geometrical variables to centrality selections in real data events. The mapping is done by (a) dividing the real data event distribution with respect to some measured quantity which is monotonic to the impact parameter (typically charged particle multiplicity, dN_{evt}/dN_{ch}) into equal parts, defining this way the experimental *centrality classes*, (b) dividing the impact parameter distribution (dN_{evt}/db) simulated events into the same number of equal parts as real data, (c) calculating the averages $< \varepsilon >$, $< N_{coll}(b) >$ and $< N_{part}(b) >$ for each slice of simulated *impact parameter selection* and finally, (d) calculating for each experimental centrality classes the geometrical parameters averaged over the corresponding impact parameter selection in simulation. This procedure uses the underlying assumption that the multiplicity of produced particles is monotonically related to the impact parameter b. This is generally true, and even more so when the charged particle multiplicity is high, implying that the event by event fluctuations are small.

I.2.1.2 The Bjorken picture

The first quantitative picture of the space-time evolution of the system created in heavy ion collisions was formulated by J. D. Bjorken [15]. The motivation was to understand the mid rapidity region, and make quantitative predictions for the produced particle multiplicity and the energy density that is reached in this region of phase space. The basic assumption of the picture is that in the laboratory reference frame, the incoming nuclei are highly Lorentz contracted. This implies that in a short time scale after the complete interpenetration of the incoming nuclei, the system left behind, a slice of which is shown by the hashed region in Fig. I.4 is composed uniquely of the quanta produced in the inelastic collisions between the participating nucleons, and not of the baryonic content (spectators) of the colliding nuclei. In other words, particles detected at mid rapidity are essentially secondaries radiated from the hot system left behind by the colliding nuclei.

The Bjorken picture defends that this system should behave as a fluid close to the collision axis (r=0 in a cylindrical coordinates), expanding *longitudinally* with a local speed of z/t,

[10] This is referred to as the black disk overlap. Alternative overlap functions such as Gaussian distribution can also be used.

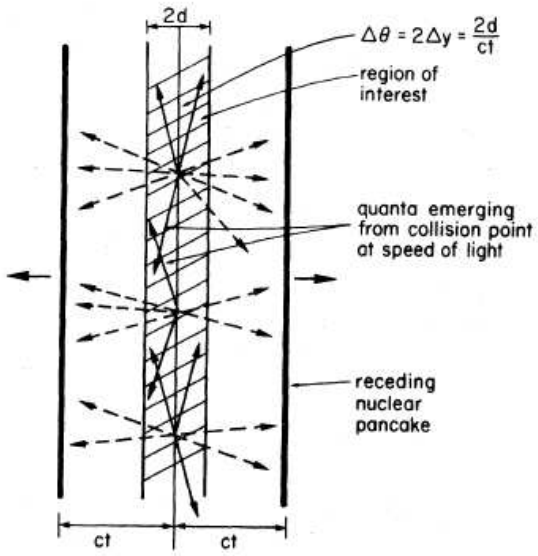

Figure I.4: Bjorken's view of a nucleus-nucleus collision. The baryon free central rapidity region that's left between the receding pancakes is depicted as a hashed region of thickness 2d.

where z is the distance from the midpoint and t is the time elapsed since nuclear interpenetration of infinitesimal duration by assumption. At large transverse distance of the order of the nuclear radius, an inward moving rarefaction front forms, where matter beyond this front no longer follows the longitudinal hydrodynamic expansion, but radiates outwards, cooling back rapidly to normal hadronic matter.

To estimate the energy density, Bjorken puts forth the following argument. At time t after nuclear interpenetration (Fig. I.4), all the quanta contained in the slab of dimension 2d (hashed region) end up forming secondaries within a rapidity window of size $\Delta y = 2d/t$ [11]. The total transverse energy $\frac{dE_T}{dy}\Delta y$ carried by these secondaries hence constitutes a lower limit of the energy contained within the slab at time t. The energy density can therefore be estimated as

$$\begin{aligned} \varepsilon &= E/V \\ &= \frac{1}{2d \times A}\frac{dE_T}{dy}\Delta y \\ &= \frac{1}{At} \times \frac{dE_T}{dy} \end{aligned} \tag{I.9}$$

where A is the transverse area of the overlap region. This estimate is still widely used to compare the energy densities achieved at accelerators. The value of t that should be

[11] The longitudinal velocity of the secondaries formed within the slab is necessarily less than the longitudinal velocity of the surfaces $\beta_{surf,||} = d/t$. In addition, at mid rapidity, longitudinal velocity and rapidity ranges are interchangeable ($\Delta y = \Delta\beta_{||}$). Therefore, the secondaries are contained within a rapidity window of $\Delta y = 2d/t$.

substituted in Eq. I.9 is not a precisely defined value. Bjorken used 1 fm/c in his estimation, but this value may not make any sense at SPS ($\sqrt{s_{NN}}$ =17 GeV) where the ion crossing time is $R\gamma/2 \approx 1.5$ fm/c, and even less so at AGS ($\sqrt{s_{NN}}$ =5 GeV) where $R\gamma/2 \approx 5.4$ fm/c. It is still instructive to compare the energy density estimate using Eq. I.9 at the different accelerators and by assuming t=1 fm/c with the energy density of $\sim$ 1GeV/fm^3 required for a phase transition. Using the measured dE_T/dy values one finds an energy density of $\sim$ 1.5 GeV/fm^3 at AGS, $\sim$ 2.9 GeV/fm^3 at SPS and $\sim$ 5.4 GeV/fm^3 at top RHIC energy ($\sqrt{s_{NN}}$ = 200 GeV). All these energy densities estimated by the Bjorken formula are larger than the required energy density for the formation of a plasma.

I.2.1.3 Ideal hydrodynamics

Pushing Bjorken's idea a little further, there has been considerable success in describing the expanding QGP stage of heavy ion collisions in terms of ideal relativistic fluid hydrodynamics [16]. Such a treatment relies on the underlying assumption that the medium created in heavy ion collisions thermalizes in a very short time after ion crossing, because at least local thermal equilibrium must be achieved before treating the medium hydrodynamically and describing it using thermodynamical quantities. Although the mechanisms allowing for fast thermalization are rare and very disputed, the experimental evidence from the momentum distributions of the *bulk* of emitted particles that this indeed happens is overwhelming. Before showing these evidences, a brief discussion of the ingredients for hydrodynamics are given below.

- The master equation of relativistic hydrodynamics is the conservation of the energy momentum tensor :

$$T^{\mu\nu}(x) = (\varepsilon(x) + p(x))u^{\mu}(x)u^{\nu}(x) - p(x)g^{\mu\nu} \tag{I.10}$$

  where $\varepsilon(x)$, $p(x)$ and $u^{\mu}(x)$ are the energy density, pressure and four velocity fields as a function of the space-time vector x, and $g^{\mu\nu}$ is the metric tensor. The local conservation of this tensor

$$\partial_{\mu}T^{\mu\nu} = 0, \qquad (\nu = 0, 1, 2, 3) \tag{I.11}$$

  implied by the assumption of local thermal equilibrium, provides the basis for the calculations.

- A nuclear Equation of State (EoS) is essentially the relation between the spatial functions of thermodynamical quantities like pressure and energy density. It can either be extracted from lQCD or modeled. In [16], as an example, the EoS of the system is treated in two different limits. In the low temperature regime, the system is treated as a non interacting hadron gas with $p = 0.15\,\varepsilon$. As the temperature increases, the system is treated as a non interacting gas of massless u, d and s quarks with higher entropy than a hadron gas, following $p = \frac{\varepsilon}{3} - \frac{B}{3}$, where $B \approx (230\text{ MeV})^4$ is an external bag pressure adjusted to insure continuity at the transition temperature.

- Boundary conditions are used to constrain the beginning and ending time of the hydrodynamic evolution. The medium can not be described by ideal hydrodynamics until a stage is reached where the medium attains local thermalization. The initial time to

turn on the hydrodynamic evolution and the initial energy and pressure distributions are estimated using a model or from fits of the predictions to data.

Equivalently, hydrodynamical calculations can not describe the system once it has become so sparse that the collision rate is low or the mean free path of constituents is large. Hydrodynamical equations have to be turned off 'by hand' towards the end of the evolution at a time determined by the condition that the mean free path of constituents become of the same order of magnitude as the overall size of the system. This is referred to as *freeze-out*.

At this point, the four momentum of each volume element is passed to the particles that are at that location, and these later are allowed to propagate and decay according to their nature (*free streaming*).

The high p_T end of the spectrum of particles also elude hydrodynamics, because these particles interact seldom on their way out, and thus do not suffer sufficient number of scatterings to thermalize with the system. In other terms, the number of collisions required to significantly change the momentum increases with the magnitude of the momentum, making it unlikely that high p_T particles receive enough kicks to thermalize with the medium.

I.2.1.4 Elliptic flow

Hydrodynamical model calculations have been strikingly successful in describing spectra and collective properties of soft particles (p_T smaller than ≈ 2 GeV/c), which is very compatible to their domain of application (high p_T particles being too fast to thermalize locally). The main evidence comes from the azimuthal anisotropy of produced particles with respect to the reaction plane in non central collision. This class of collisions are distinguished from the fully central collisions in that the collision region does not have a circular shape (cf. Fig. I.5). The consequences are of huge importance. In fact, the spatial anisotropy of the created medium leads to a pressure gradient that will be much stronger in the *in plane* direction (parallel to the impact parameter vector cf. Fig. I.5), if and only if thermal equilibrium is achieved fast enough before the spatial asymmetry is lost through expansion.

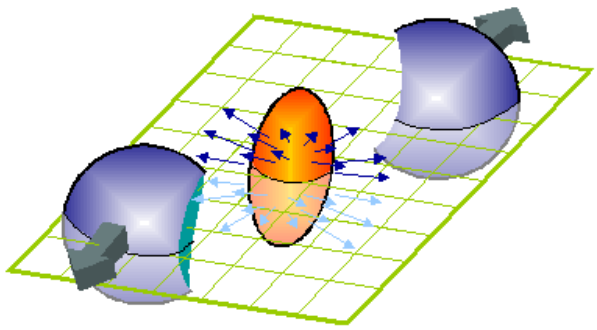

Figure I.5: Birds eye view of a heavy ion collision.

Although the initial spatial anisotropy is impossible to observe directly, the pressure gradient that it creates is transformed into a momentum anisotropy through the interactions among

its constituents. This effect is readily measurable because the azimuthal angle ϕ of momenta of particles produced in such conditions should be strongly correlated to the azimuthal angle Φ of the *in plane* direction, also called the reaction plane (RP). This correlation can be quantified by the second Fourier coefficient (v_2) of the azimuthal angle distribution emitted particle momenta, called *elliptic flow*. For identified particles of type i, the distribution of the azimuthal angle difference $\phi - \Phi$ between the momenta and the reaction plane direction can be expanded as:

$$\frac{dN_i}{d(\phi-\Phi)}(b) = A\left(1 + 2v_2^i(b)\cos\left(2(\phi-\Phi)\right) + 2v_4^i(b)\cos\left(4(\phi-\Phi)\right) + \cdots\right) \tag{I.12}$$

The sin terms disappear in this expansion because of the reflection symmetry with respect to the reaction plane. Elliptic flow is a self quenching process, in the sense that strong flow results in the reorganization of the spatial distribution in a way that leads to the loss of the spatial anisotropy, and hence the pressure gradient difference in the *in* and *out* of plane directions. So if elliptic flow does not develop early, then there is little chance that it does later. As a result, the magnitude of v_2 reflects the earliness of the onset of thermalization, as well as the frequency of the interaction of the observed particle with the *bulk*.

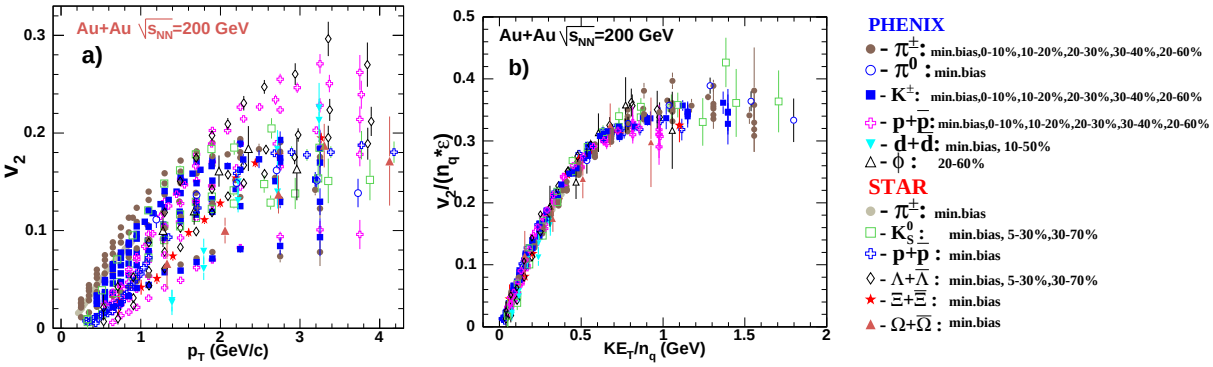

Figure I.6: a) Identified hadron v_2 vs. p_T. b) Identified hadron v_2 scaled by the number of quarks (n_q) and eccentricity (ε) vs. the number of quark scaled transverse kinetic energy (KE_T/n_q).

The measured elliptic flow of identified particles shown in Fig. I.6a exhibits a remarkably strength (going as high as $\sim 30\%$, the maximum allowable value being 50%). Such a strong magnitude of flow is excluded by calculations [16] unless the onset of hydrodynamics (equivalent to the achievement of local thermal equilibrium) is very early, of the order of $\lesssim 1$ fm/c. Besides the amplitude, another strong piece of confirmation of thermal equilibrium and hydrodynamics comes from the mass ordering of elliptic flow. Detailed solutions of Eq. I.11 with initial conditions of an elliptically shaped fireball [17] predict that the elliptic flow should scale with the transverse kinetic energy $KE_T = m_T - m$, where m_T is the the transverse mass, $\sqrt{m^2 + p_x^2 + p_y^2}$. According to this calculation, all other dependencies (on p_T or η) are apparent and can be mapped to KE_T. The data follow this scaling strikingly well as can be seen in Fig. I.6b, where $v_2/\varepsilon n_q$[12] of different species of hadrons measured with different

[12]Here n_q is the number of valence quarks that the hadron is made up of, and ε is the *eccentricity* of the

systematics is plotted against KE_T/n_q [18]. The fact that n_q normalization is required to bring all flow measurements to the universal curve only makes sense if the degrees of freedom in the expanding medium are partonic. This is an important experimental proof of deconfinement.

I.2.1.5 Hadron abundances

Another important piece of evidence that supports thermalization in heavy ion collisions comes from hadrochemistry, or the quantitative study of the hadronic composition of the *bulk*. The basic idea behind hadrochemistry is that if equilibrium is achieved in heavy ion collisions, then two unique variables, temperature T and baryonic chemical potential μ_b, should dictate the relative abundance of hadrons emitted in the framework of the Grand Canonical (GC) ensemble, in order to insure baryonic conservation. If a complete statistical treatment of the medium as a GC ensemble that considers all dynamical effects including decays is implemented, then the predicted hadron yield ratios can be adjusted to the measured values and the T and μ_b that prevailed at hadronization can be inferred. Several authors among which [19, 20] succeed in doing so with a surprising precision over a wide range of hadrons. Their fit over the yield ratios measured at RHIC in $\sqrt{s} = 200\ GeV$ Au+Au collisions is shown in Fig. I.7. Similar procedure was used to extract the T and μ_b from a number of other energies and collision systems. The results found are summarized in Fig. I.8.

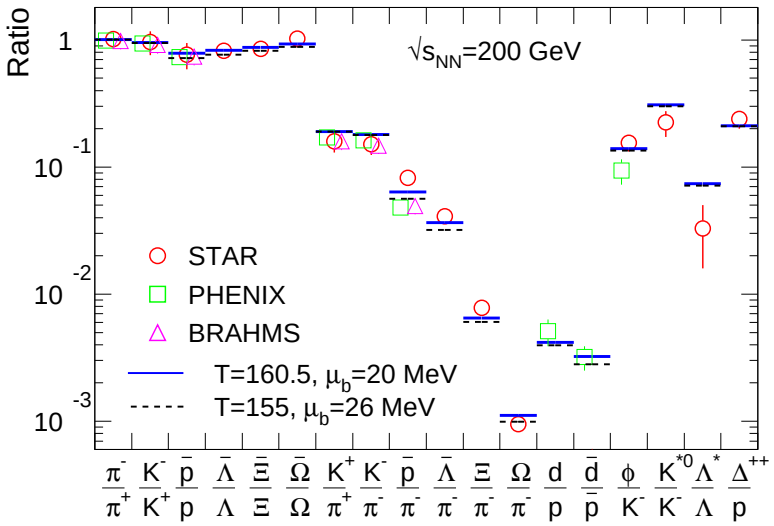

Figure I.7: Hadron yield ratios and predictions from a statistical model at top RHIC energy $\sqrt{s} = 200$ GeV.

As the collision energy increases, the temperature at which hadronization takes place increases until it reaches and hits a plateau. This saturation can be interpreted as a signal

collision (cf. Sec. I.2.1.1). The initial spatial anisotropy is larger for more eccentric collisions, leading to more elliptic flow. Normalizing by the eccentricity variable allows one to compare results from different centrality selections.

of the phase boundary, as hadrons can not be formed beyond the critical temperature T_c of plasma formation. Indeed this is an indirect measure of the critical temperature, and the plateau value of $T_c = 161 \pm 4$ MeV is in reasonable agreement with lQCD predictions ($T_c \simeq 170$ MeV.) Of course, if thermalization is not achieved, there is no reason to expect that the GC hadron abundance ratio distributions should fit to the observed values. The fact it does is a strong indication that thermalization indeed takes place.

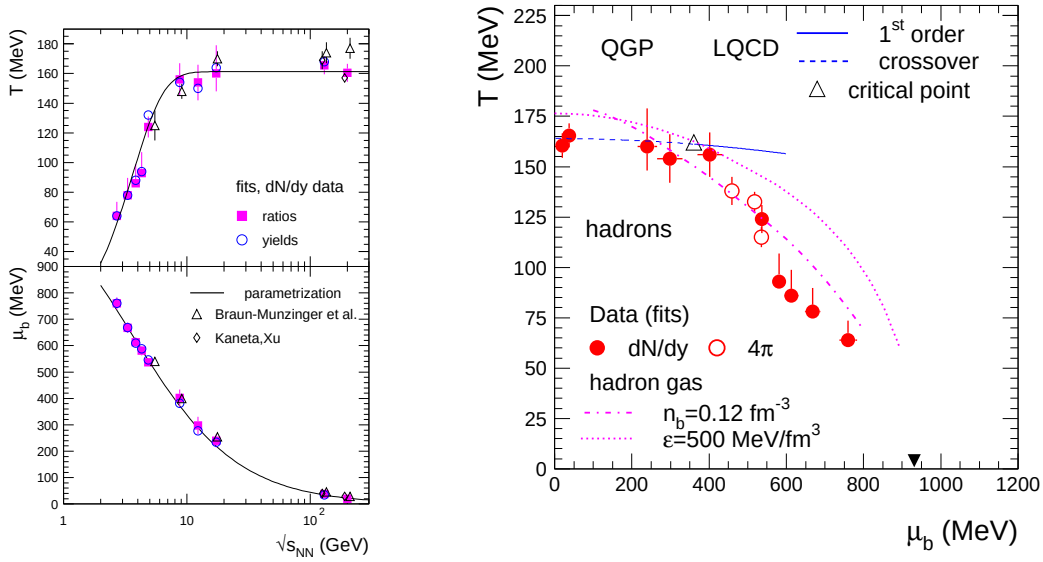

Figure I.8: Left: The T (top panel) and μ_b fit results from statistical hadronization models at different experiments as a function of CMS collision energy. Right: Scatter plot on the T vs. μ_b space.

I.2.2 Probing the medium

The QGP created in relativistic heavy ion collisions exists for such a short time that it is impossible to study its properties directly. As was demonstrated in the previous section, it can however be studied through the spectra of emitted particles and their correlations, because to a large extent, these are determined by the medium in which they are produced, and by the interaction mechanisms that are dominant. There is a class of particles, called hard probes, that we can use to learn about the system. Hard probes are particles created in the initial hard scatterings between nucleons of projectile and target nuclei. Ultimately, they propagate through the created medium, and at detection carry the fingerprint of their interaction with the medium.

Hard probes are essentially all produced in initial nucleon-nucleon scatterings because the $\sqrt{s}$ energy available in later collisions inside the medium decreases very fast. So it is practically impossible to have high momentum transfer collisions inside the medium. This implies a major characteristics of hard probes. Namely, in the absence of other competing mechanisms, the rate of these processes (and thus the yield of hard probes) should be proportional to the

number of binary collisions between nucleons (N_{coll}) of the initial target and projectile nuclei. By comparing their spectra when they propagate through a QGP medium (i.e., in heavy ion collisions), to their spectra while they are produced and detected without interaction (i.e, in proton-proton collisions) we can learn about their interaction with the medium through which they have propagated and by consequence about the medium itself.

A more than often used quantity that characterizes in the simplest manner this interaction of a hard probe with the medium is provided by the nuclear modification factor or R_{AA} (sometimes called more simply the suppression ratio) defined by:

$$R_{AA} = \frac{1}{< N_{coll} >} \times \frac{Y_{A+A}}{Y_{p+p}}. \tag{I.13}$$

In this equation, Y_{A+A} represents the total yield in a collision between nuclei of atomic mass A, whereas Y_{p+p} is the same quantity in proton-proton collisions. Y_{p+p} is sometimes regarded as a calibration of the hard probe, as the proton-proton yield can often be confirmed independently by comparing to pQCD calculations. The last element in Eq. I.13 is the quantity $<N_{coll}>$ which is the experimentalist's estimation of the average number of binary collisions that take place in the event selection. An R_{AA} value of greater than one would indicate predominance of other production mechanisms than initial hard scatterings, and a value lower than one would mean that the destruction mechanisms of the probe are dominant. In other words, an R_{AA} value equal to unity implies that the system acts as a simple superposition of incoherent N_{coll} collisions with respect to this probe. The p_T, rapidity and centrality dependencies of R_{AA} have been used extensively to confront model calculations to data for a variety of hard probes including heavy flavours, photons and high p_T identified hadrons, carrying information about underlying jets.

It happens sometimes that a hard probe is affected by the spectator nucleons in the projectile/target. Such an effect is quite conceivable, because hard probes are created starting from the earliest moments of the collision, even before the nuclei have passed through each other completely. In such circumstances, control experiments should be done by measuring the same observable of the hard probe in p+A or d+A type collisions, and eventually subtract out the cold nuclear matter effect from what is measured in A+A type collisions. This is particularly true for quarkonium detection, as will be explained in Sec. I.3. Before going there, a few measurements which have led to important discoveries will be discussed and used as illustrations of the power of hard probes.

I.2.2.1 Photons

Direct photon production in hard processes is a particularly useful hard probe. Photons do not interact with the medium created in heavy ion collisions. As such, the production of hard photons should follow N_{coll} scaling. However, the identification of photons from hard processes is not straight forward, except at high p_T where they dominate the inclusive yield. The direct photon p_T spectrum measurement by PHENIX [21, 22] at $\sqrt{s_{NN}} = 200$ GeV using an electromagnetic calorimeter is shown by full symbols on Fig. I.9. Due to high background, this measurement is only possible for $p_T > 4$ GeV/c. The lowest set of points is the yield measured in p+p collisions [21]. The three upper sets of points are Au+Au collision measurements with centrality selection of 20-40%, 0-20% and minimum bias respectively [22][13]. The full lines are

[13]The scale factors 10, 10^2 and 10^4 are there just for readability of the plot.

the various pQCD theory prediction confirmations of the p+p measurement. The p+p data are also fitted with a modified power law function ($B(1+p_T^2/b)^{-n}$) the result of which is shown by the dotted line. In the Au+Au case, the dotted lines are the p+p power law fit scaled by the number of collisions (N_{coll}) for the selected centrality. Above p_T of 3 to 4 GeV/c, the N_{coll} scaled p+p predictions are in very good agreement with the Au+Au measurements, indicating that the hard photon yield scales with the number of binary collisions and experimentally confirming that photons are not affected by the medium. Another way to visualize the N_{coll} scaling of hard photons is by plotting the p_T dependence of the R_{AA}, which is shown in Fig. I.10 on the right for central event selection, where, as expected, the R_{AA} for photons (purple squares) is remarkably compatible with one over a wide p_T range[14].

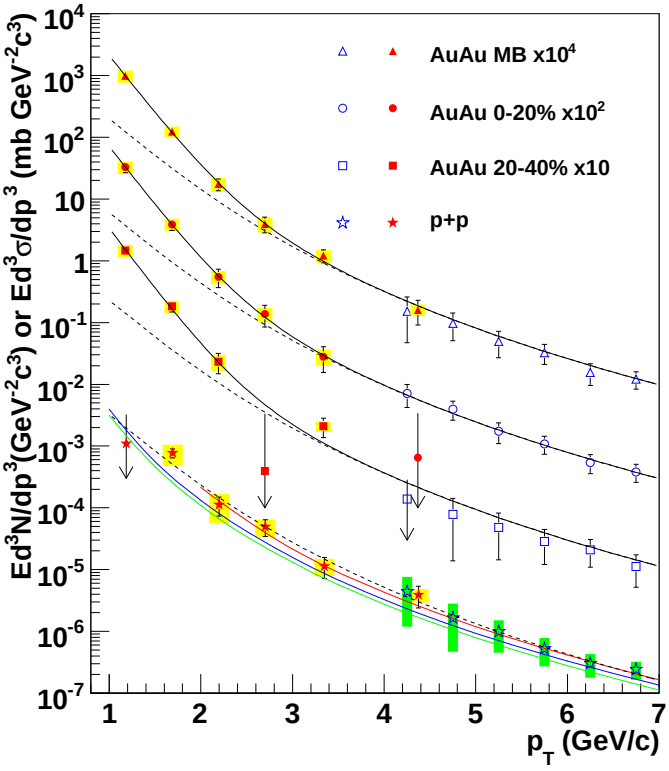

Figure I.9: The photon p_T spectrum by PHENIX in p+p and Au+Au collisions. The high p_T end ($>$ 4 GeV/c, open markers) end is the hard component measured directly by the electromagnetic calorimeter. At low p_T (closed makers) the virtual photons measured as excess in the low p_T low invariant yield region of the dielectron mass spectrum.

For p_T lower than 3 to 4 GeV/c, it is possible to estimate the virtual photon yield through conversion into electron-positron pair. The net virtual photon yield can be counted from the excess in the dielectron spectrum above the yield expected from hadron decays. The on-shell photon yield can then be extracted from the measured virtual photon yield using exact QED relations. The photon spectrum extracted by this method [23] is shown in Fig. I.9 (closed markers) for $p_T < 4$ GeV/c. In this range, while the p+p measurement is in the continuity of

[14]Below $p_T = 4$ GeV/c, the direct photon measurement allows only to put upper limits.

the modified power law fit at higher p_T, there is a statistically significant excess in the Au+Au spectrum with respect to the expectation from N_{coll} scaling of p+p fit result. This excess is therefore not due to hard processes, and one of the possible explanations is thermal photon production in the plasma. To account for the excess, the Au+Au points are fitted by a sum of the N_{coll} scaled p+p modified power law fit result plus an exponential term ($\exp(-p_T/T)$), the result of which is plotted as full black lines. If the excess is due to thermal photons, the initial temperature of the radiating dense medium T_{init} is related to the inverse slope T in the exponential term through the thermodynamical expansion of the medium. The results of the fit for T[MeV] in the different centrality selections are $T = 221 \pm 23(stat) \pm 18(syst)$ for 0-20%, $T = 214 \pm 20(stat) \pm 15(syst)$ for 20-40% and $T = 224 \pm 16(stat) \pm 19(syst)$ for minimum bias. Hydrodynamics based thermal models [24, 25] predict that $T_{init} \sim (1.5 - 3) \times T$ and reproduce the minimum bias p_T spectrum with values of T_{init} ranging from 300 to 600 MeV with different values for the onset time of hydrodynamics. This range is well above the transition temperature of ∼170 MeV predicted by lQCD.

Jets

Jets represent one of the very well calibrated hard probes, as their production in e+e, e+p and p+p has been studied in great detail, due to their accessibility in pQCD calculations. But their measurement in heavy ion environment is a huge challenge. The secondaries from intermediate p_T jets (the only ones accessible at RHIC), are completely overwhelmed by the ambient particle multiplicity from the *bulk* soft particles, and hardly show up as localized excesses in calorimeters. Consequently, full jet reconstruction has so far been practically impossible in heavy ion collisions[15]. At the LHC, the increased collision energy where cross section of high p_T jets is larger as well as the more resolved calorimetry available will hopefully alleviate this limitation. In the meantime, other powerful analysis techniques have been developed to study the medium effect on jets.

Fig. I.10 left shows the two particle azimuthal angle correlation $\Delta\phi$ between a *trigger* particle in a high p_T window, and *associated* particles in a lower p_T window [27]. In vacuum situation, if the *trigger* particle comes from a jet, then other particles in the same jet form a near side peak at $\Delta\phi$ close to zero, whereas the *associated* away side jet shows up as a peak at $\Delta\phi$ close to π. Angular correlation can this way be used to get a tomography of jets, although the jets are not reconstructed *per se*. This technique was exploited to study the jet interaction with the medium formed in heavy ion collisions. Comparing the azimuthal correlations in three different colliding systems: proton-proton(p+p), deuteron-gold (d+Au) and gold-gold (Au+Au) collisions, the observation is that the away side peak survives in p+p and d+Au collisions, as well as in peripheral Au+Au collisions whereas it is highly suppressed in central Au+Au collisions. In p+p or d+Au collisions, when two partons undergo a hard scattering, they are deviated back to back azimuthally and propagate unhindered to create jets. On the other hand, in Au+Au collisions, one of the two scattered partons travels more distance in the created medium before fragmenting into a jet. In doing so, it looses energy through multiple interactions with the deconfined medium before it can fragment into a jet. This leads to the suppression of the away side peak that is observed in the Au+Au correlation spectrum. The magnitude of suppression can not be explained by the presence of ordinary nuclear matter on the path of a highly energetic parton, and has allowed a conclusion that

[15] Recent claims have been given that it was achieved by the STAR experiment at RHIC [26].

the medium created in Au+Au collisions is a very opaque medium.

I.2.2.2 Suppression of high p_T particles

Additional evidence for the opacity of the medium to hard scattered partons comes from the study of high p_T spectrum of identified hadrons and photons in p+p reference, d+Au control and Au+Au collisions. Fig. I.10 on the right shows the p_T dependence of R_{AA} for photons [22], and π^0s [28] up to 13 GeV/c and for ηs [29] up to 10 GeV/c as measured by the PHENIX experiment at RHIC. As a reminder, this measurement is the ratio of the p_T spectrum of the identified hadrons/photons in Au+Au collisions to their spectrum in p+p collisions, scaled by the average number of binary nucleon-nucleon collisions in the Au+Au event selection as introduced in Eq. I.13. The most striking observation is that hadrons (which are made up of strongly interacting constituents) are suppressed by a factor of 5 at high p_T, whereas photons, which are blind to strong interactions in the medium go out unmodified up to the highest measured p_T[16]. Such a strong suppression of high p_T hadrons is unlikely in ordinary nuclear matter.

The softening of the p_T spectrum of charged hadrons is again due to the energy loss to which the underlying partons are subjected to before hadronization. The yellow line shown on the plot is a prediction of R_{AA} from a model based on collisional energy loss mechanism in a deconfined medium with a typical gluon density per unit of rapidity[17] dN^g/dy of ~ 1100. Here again, the suppression effect is absent in d+Au collisions.

I.2.2.3 Open heavy flavour

Heavy flavour production is yet another hard probe. The measurement of heavy flavour is not so straightforward in heavy ion environment. The reason is that the high multiplicity environment renders difficult the two traditional techniques used to measure open heavy flavour either through direct identification, namely invariant mass reconstruction of hadronic decays (e.g. $D^0 \rightarrow K^+\pi^-$) or displaced vertex measurements of the leptons from semileptonic decay of heavy flavoured mesons.

A workaround has been developed. It involves estimating the heavy flavour contribution via semi-leptonic decays to the inclusive lepton (electron or muon) yield, as the excess with respect to the spectrum expected from all other known sources of leptons. For electrons, the background includes (1) Conversions of photons from light hadronic decay origin and direct radiation, (2) Dalitz decay of light vector mesons, and (3) Electroweak decay of kaons ($K^{\pm} \rightarrow \pi^0 e^{\pm}\nu(\bar{\nu})$ also known as K_{e3}). Sources (1) and (2) are called *photonic* due to the nature of their origin, that involves a photon at some point. Background source (3) as well as

[16] The following precautions have to be made while making this statement. Recent preliminary data that goes up to 20 GeV/c in p_T for photons and π^0s have been made available. While the π^0 R_{AA} remains down at the level of 0.2, the photon R_{AA} starts to deviate from 1 at p_T around ~ 18 GeV/c. According to [30], this could come from three causes a) Isospin charge asymmetry, Au+Au is a superposition of collisions between neutrons and protons, whereas the normalization is based on p+p, b) Direct photon yield contributions from processes like g+q$\rightarrow$ γq imply that any energy loss by the quark is carried on to the final state, c) Modification of gluon PDFs in nuclei with respect to free nucleons (cf. Sec. I.3.2), also called EMC effect at large x values [31]. At high p_T, corresponding to a large parton momentum fraction (x) values, a depletion of partons occurs, resulting in a lower yield.

[17] A more systematic fit [32] to the data, taking correctly into account all the experimental errors has been tried with a result of $dN^g/dy = 1400\ ^{+200}_{-375}$, but with a larger error.

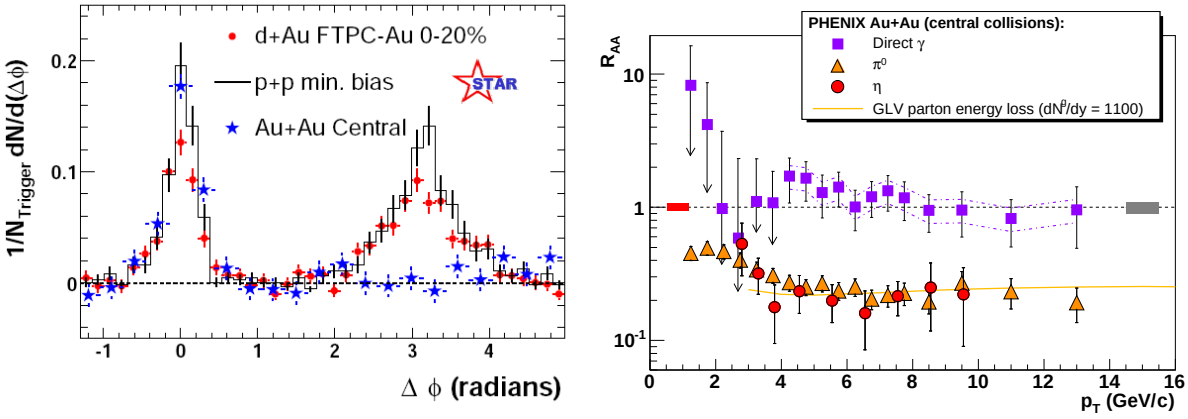

Figure I.10: Jet quenching in heavy ion collisions. Left: The azimuthal angle correlation of intermediate p_T particles to a high p_T leading trigger particle. Right: The R_{AA} vs. p_T for π^0s, ηs and direct photons (γs).

the signal from heavy flavour decay are both electroweak decays, and are collectively called *non-photonic sources*. The background is dominant over the source at low p_T (S/B < 0.2 for $p_T < 0.5$ GeV/c but this tendency is reversed with increasing p_T (S/B > 1 for $p_T > 2$ GeV/c. The photonic background dominates the non photonic background over the whole p_T range[18].

There are two background subtraction methods employed, each with a dynamical range where it is more precise. In the first technique, called *cocktail subtraction*, a cocktail of the background sources, dominated by pion Dalitz decay and the pion$\rightarrow 2\gamma$ decay followed by photon conversion, is carefully simulated, using measured cross sections for pions, and extrapolating using an m_T scaling for other hadrons[19]. The pion yield is measured to a good precision, and therefore a modified Hagedorn parametrization $E\frac{d^3\sigma}{d^3p} = \frac{c}{(\exp(-ap_T - bp_T^2) + p_T/p_0)^n}$, fitted to the measurement, is used as input distribution for the simulation. For other mesons, where the precision of the measurement is not very high, the p_T spectrum is extracted from that of pions by replacing the pion p_T by $\sqrt{p_T^2 + m_{meson}^2 - m_{\pi^0}}$. With this physically motivated parametrization, the high p_T end of the spectra is more or less similar for all light hadrons. Therefore the global normalization between the different hadrons yields is calculated in the $p_T > 5$ GeV/c range from data. The direct photon yield is similarly parametrized from measurements. The K_{e3} contribution can not be estimated by this method, and has to be extracted from an independent simulation. The background cocktail constructed this way is known with a systematical uncertainty of better than 15% over the whole p_T range. It is subtracted from the inclusive electron yield to get the net contribution from the heavy flavour signal. This technique has a very good statistical precision at high p_T (>1.6 GeV/c), because the signal to background ratio is high in this range.

At low p_T, the relatively high contribution of background sources magnifies the systematical uncertainty from the cocktail calculation. A direct measurement of the photonic background is thus required in this domain. The second background subtraction technique called *converter subtraction method* is employed here, and offers an estimation of the heavy flavour

[18] At high p_T, a possible non negligible contribution from Drell-Yan and decays of quarkonia is under investigation.

[19] The second most dominant hadron is the η.

contribution with better precision to the lowest p_T ($\sim$ 0.3 GeV/c). The idea is to introduce a converter material of known radiation length within the detector acceptance and to measure by how much the total electron yield increases. This increase can only be due to conversion electrons from photonic background sources. One can then triangulate to calculate the contribution from the totality of the photonic background sources in the presence of the detector apparatus without the converter, the radiation length of which is precisely known. This estimation of photonic background sources is subtracted from the inclusive electron yield measured with no converter material in the acceptance to obtain the yield from all non photonic sources. Once the photonic background has been subtracted, simulation has to be done to subtract background contribution from the K_{e3} decay. At this point, the remaining electron yield comes from heavy flavour decay only. This method is statistically limited at high p_T, because the additional converter material is only inserted for a short period of data taking time.

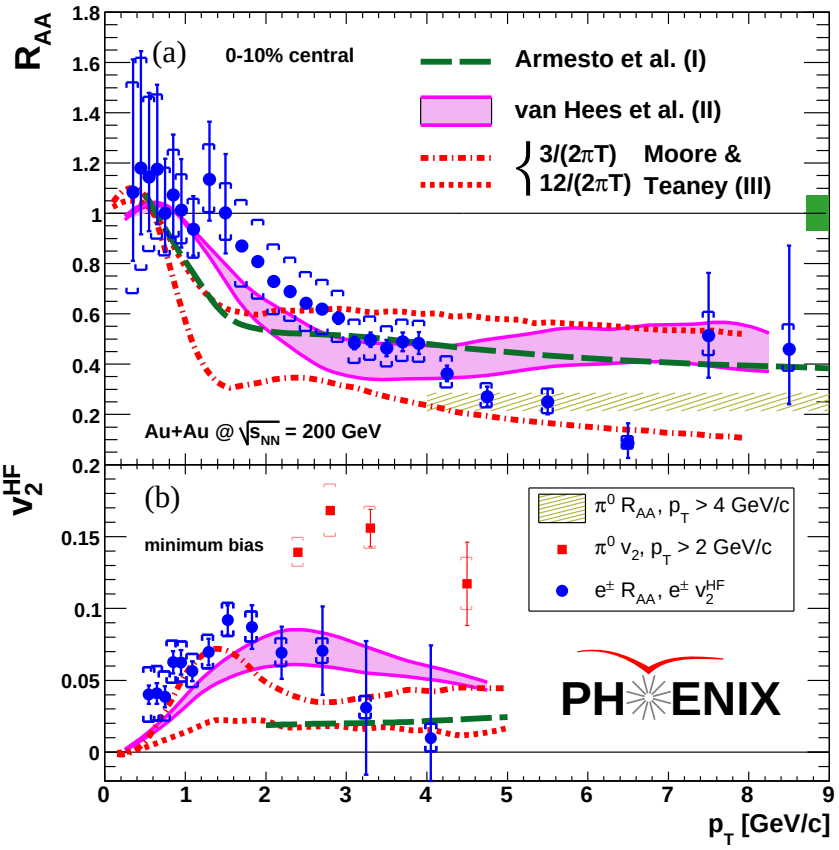

Figure I.11: The suppression (Top panel) and elliptic flow (Bottom panel) of non-photonic electrons as measured by PHENIX [33], together with model predictions and measurements for pions.

Both these subtraction techniques are used by PHENIX to extract the result in Fig. I.11 which shows the measurement of the nuclear modification factor R_{AA} for 0-10% most central event selection and the elliptic flow (v_2) of non photonic electrons for minimum bias event selection, together with the R_{AA} and v_2 measurement for pions. It is important to note that none of the above mentioned methods are capable of disentangling the B meson decay contribution from the D meson decay contribution. Curves from various theoretical calculations

of the same quantities are plotted together. Since the parent D/B meson is boosted in the lab reference frame, there is an angular correlation between the parent meson and the decay electron. Consequently the v_2 of non photonic electrons should be a very good indicator of the flow of the parent meson, especially at high p_T. The momentum of electrons is also related to that of the parent meson in the lab frame. On either of the two measurements, R_{AA} and v_2, no correction is applied on the data points to account for this, they are simply R_{AA} and v_2 for non photonic electrons. But the theoretical predictions, also shown on the plot, take into account the correct dynamics of the semileptonic decay, so the comparison between data and theory is valid. The degree of suppression at high p_T (> 4 GeV/c) is very close to that of pions (yellow hashed band). The high magnitude of flow indicates that the heavy flavour thermalization takes place in a time scale that is of the same order of magnitude as the short time scale of the flow development.

Two classes of model calculation are also shown in the plots of Fig. I.11. A calculation based on the path length dependence of the energy loss of heavy quarks [34] (green broken line) reproduces the R_{AA}, by assuming a very large gluon density and quite strongly coupled medium, but underestimates the v_2 at intermediate p_T. Another set of calculations, based on a modelization of the movement of heavy c and b quarks in the medium by a Langevin diffusion equation with drag coefficient D_{HQ} and medium viscosity η are shown in the same figure by the broken red lines [35] and pink band [36]. These calculations reproduce fairly well both the R_{AA} and v_2, under the condition that a very high diffusion constant is used. The high diffusion coefficient implies a viscosity to entropy ratio $\eta/s \approx (4/3 \text{ to } 2)\times 1/4\pi$, quite close to a lower bound of $1/4\pi$ conjectured by AdS/CFT correspondence [37]. The viscosity to entropy ratio estimated this way is also in line with the very low viscosity extracted from the data using the totally independent analysis of identified hadron v_2 on ideal hydrodynamics grounds [38]. The low viscosity due to the strongly interacting nature of the 'fluid' created in heavy ion collisions is nowadays one of the most firmly established results in the field.

I.2.3 Summary

All the above stated signatures seem to point to a system of strongly coupled low viscosity fluid to be formed in high energy heavy ion collisions. This picture that emerged little by little in the past few years is in contrast with the weakly interacting ideal gas of deconfined quarks and gluons that was expected. It may be that the energy density achieved at RHIC is not high enough to create that kind of excitation. The fluid created at RHIC is in itself a very rich laboratory for the study of complex QCD systems. As for deconfinement, the hard probes discussed in the above sections are not directly linked to it, although they indirectly strongly support the conclusion that a deconfined medium is created. It is from this point of view that J/ψ (and other quarkonia) suppression is still considered to be an important probe, since it directly tests deconfinement. The next section will deal with this question.

I.3 The J/ψ probe

In the previous section, it was illustrated how hard probes can be used to study the medium, mostly through the modification of the probe spectra in heavy ion collisions as compared to that in proton-ion or proton-proton collisions where no QGP formation is expected. Quarkonia (sing. quarkonium) – bound states of a heavy quark (c or b) and its anti-quark – are other important hard probes of the medium. The work presented in this thesis focuses on the J/ψ quarkonium state, so this section will be dedicated to explaining the details of the theoretical and experimental knowledge so far acquired about the J/ψ, and more generally about quarkonium interaction with the medium created in heavy ion collisions.

I.3.1 Basics of J/ψ suppression

As all hard probes, J/ψs are created in initial binary collisions. Due to a long lifetime ($\sim$ 2000 fm/c) J/ψs do not decay until long after passing through the medium. In addition,q thermal production of c quarks is disfavoured, because of the large c quark mass. This implies that the breakup and eventual recombination in the medium can be calculated without making any assumptions about the thermodynamic abundance of c and $\bar{c}$ quarks as long as one knows their conserved number initially available. The production rate in a bare nucleon-nucleon collision can be checked against pQCD calculations, again due to the high mass of the c quark and thus relatively large energy scale of the interactions in which it can be created. A final, but experimentally significant advantage of the J/ψ is its significant branching ratio into dileptonic decay channels – (5.93$\pm$0.06)% for J/$\psi \rightarrow \mu^+\mu^-$ and (5.94$\pm$0.06)% J/$\psi \rightarrow e^+e^-$ [39] – which facilitates its detection through dilepton invariant mass spectra.

I.3.1.1 The historical paper

J/ψ suppression is one of the oldest recognised direct signature of deconfinement in the QGP. Color screening in the high gluon density medium was proposed by K. Matsui and H. Satz [40] as a mechanism leading to the destruction of J/ψ. In their paper they argue that if QGP is created in heavy ion collisions, the screening radius r_D becomes smaller than the hadronic size $r_{J/\psi}$ of the J/ψ at some temperature T not far from the critical transition temperature T_c, assumed in the paper to be $T_c \approx 200$ MeV. This leads to the melting of the J/ψ, with the constituent c and $\bar{c}$ quarks then evolving independently to hadronize into D mesons.

To demonstrate this effect, the authors rely on the then existing lQCD calculations of the correlation length $\xi(T)$ that intervenes in the correlation function $\Gamma(r,T)$ between the two heavy quarks separated by a distance r

$$\Gamma(r,T) \sim \exp[-r/\xi(T)] \tag{I.14}$$

as an upper bound of r_D. The lQCD calculations were done for static quark-antiquark system (zero spatial momentum of the J/ψ with respect to the plasma rest frame) in the absence of dynamical quarks (purely gluonic thermal environment). The lattice calculation the authors relied on for estimation of numerical values gave a temperature dependence of $\xi(T)$ that is steeply decreasing from a value of $\sim$ 1 fm at $T \approx 210$ MeV, and going down to $\sim$ 0.3 fm at $T \approx 240$ MeV $= 1.2\ T_c$ and that slows down onwards to take a value of $\sim$ 0.2 fm at $T \approx 300$ MeV $= 1.5\ T_c$. The authors argue that the presence of color charge carrying dynamic

quarks can only make the screening more effective and decrease $\xi(T)$, and consequently r_D at any given temperature.

The typical value of r_D estimated this way lies in the range 0.2 to 0.3 fm at $T/T_C \approx 1.5$. The hadronic radius of the J/ψ is explored assuming the Cornell potential

$$V(r) = -\frac{\alpha_{eff}}{r} + \sigma r \tag{I.15}$$

composed of a first effective Coulombic term, and a second confining term that depends on the medium temperature. Minimizing the energy of a bound $c\bar{c}$ state

$$E(r) = 2m + 1/2mr^2 + V(r), \tag{I.16}$$

inserting typical numerical values for $\alpha_{eff} \approx 0.5$ and $\sigma \approx 0.16$ (GeV)^2 at zero temperature, and setting $m = 1.56$ GeV/c^2, the authors find back the charmonia spectrum with $E_{min} = 3.1$ GeV and $r_{J/\psi}$ of the order of 0.2 fm. At high temperature, of the order of T_c, the string tension is zero, and the $r_{J/\psi}$ is determined uniquely by the color screened Coulombic potential

$$V(r) = -\frac{\alpha_{eff}}{r} exp(-r/r_D) \tag{I.17}$$

which can still lead to a bound state. The minimization of the energy in Eq. I.16 with the potential in Eq. I.17 gives the range of values $0.5 < r_{J/\psi} < 1.3$ for the J/ψ hadronic radius, for numerical values of α_{eff} from lQCD ranging from ~ 0.5 (at $T = 0$) to ~ 0.2 (at $T = 1.5\ T_c$). The authors deduce from these numerical estimations and the $\xi(T)$ dependence from lQCD that a plasma temperature as low as $T = 1.2\ T_c$ prevents the formation of J/ψ.

The authors then study the fulfilment of the necessary conditions so that the suppression of the J/ψ due to color screening be an unambiguous signature of deconfinement, and answer the following concerns:

- Is the J/ψ formed before the plasma thermalizes? For this question, they rely on the available typical thermalization time of 1 fm/c, and exclude this possibility, saying that even though the formation of the $c\bar{c}$ pair takes place on a much shorter time scale than 1 fm/c, the actual bound state is created on a time scale close to that of ordinary hadrons of the order of 1 fm/c. In addition, they point out that in any case, even if J/ψs are created very early, they will necessarily evolve inside the medium within a volume comparable to the nuclear size. They conclude that early formation time will not prevent the J/ψ from evolving within the medium and being suppressed in the case of formation of a deconfining plasma.

- Are there other mechanisms that will suppress the J/ψ yield? The authors argue that nuclear absorption of J/ψ should be the main contributor, but estimate that the cross sections involved ($\sim$3 mb) is not significant compared to the suppression by the plasma. Later, the question of the contribution of nuclear absorption in heavy ion collisions happens to be a not so straightforward one. Practical experience has shown that nuclear absorption can have considerable effects, and constraining it in systems where no QGP is expected (such as nucleon-nucleus collisions) is mandatory to isolate the plasma effects (see Sec. I.3.3).

- Is there a dynamical range where thermal dilepton yield is too large to see the J/ψ signal? The authors extrapolate measured cross sections of thermal dileptons in hadronic collisions to heavy ion collisions at SPS and RHIC energies and conclude that this should not be the case. This conclusion is supported by data at heavy ion colliders to date.

- Will the suppressed J/ψs be compensated for during the hadronization transition? The authors argue that the presence of the plasma should prevent this from happening, especially in central collisions of large nuclei. They note however that for smaller nuclei and peripheral collisions, the J/ψ suppression from the plasma should be somewhat attenuated, because nothing prevents the formation of J/ψ at the periphery of the overlap region. The answer to this question is nowadays a very debated issue. Some measurements, including the result reported in this thesis, suggest the possibility that the contribution from recombination of charm quarks produced in separate hard processes could be significant. This recombination mechanism is not proven yet, but will certainly be the subject of experimental test using different approaches, one of which, the J/ψ elliptic flow measurement, is also part of the work presented here.

I.3.1.2 Lattice QCD results

Since the publication of this paper, there has been considerable progress in the understanding of how the J/ψ interacts with the medium, mostly propelled by the increased sophistication of lQCD simulations. The temperature (T) dependence of the spatial quark–antiquark current correlators ($G_H(\tau, T)$) in Euclidean time (τ) encode the quarkonium-medium interaction information and can be computed on the lattice. The correlators are defined as

$$G_H(\tau, T) =< j_H(\tau) j_H^{\dagger}(0) > \tag{I.18}$$

where $j_h = \bar{q}\Gamma_H q$ is the mesonic current in a given quarkonium state (channel). The four possible vertex operators Γ_H correspond to the various channels ($1 \rightarrow \chi_{c0}, \chi_{b0}$, $\gamma_5 \rightarrow \eta_c, \eta_b$, $\gamma_\mu \rightarrow J/\psi, \Upsilon$, $\gamma_4\gamma_5 \rightarrow \chi_{c1}, \chi_{b1}$).

One possible way to infer the melting temperature from the lattice computed correlators is to use the resonance mass (M) and temperature (T) dependent spectral functions ($\sigma_H(M, T)$), which, for each resonance quarkonium channel H, are related to the corresponding correlator through an integral equation

$$G_H(\tau, T) = \int_0^{\infty} dM \sigma_H(M, T) K(\tau, M, T). \tag{I.19}$$

where $K(\tau, M, T) = cosh[M(\tau - 1/2T)]/sinh(M/2T)$ is a physically motivated convolution kernel. An exact derivation of this relation can be found in reference [41]. The presence of a peak in the spectral function at a given temperature indicates the survival of the resonance, whereas, the peak progressively broadens when the temperature starts to approach the melting temperature of the resonance.

The only currently available method for inverting this integral equation is called the Maximum Entropy Method (MEM) [42] and proceeds through minimization of a conveniently defined likelihood function, and selecting a spectral function that best fits the integral in Eq. I.19 to the lattice data correlators $G_H(\tau_i, T)$ and their errors calculated at a discrete set of temporal points.

This use of spectral functions to infer melting temperatures is not very robust. On the one hand, threshold enhancements can blur the T dependence of the integral under the the spectral curve. On the other hand, the use of MEM, especially at high temperature[20], does not allow a very fine scan of the temperature dependence, because of the complexity of the numerics.

I.3.1.3 Potential models

An option to study the quark-medium interactions is to resolve a non relativistic Schrödinger equation by relying on some physically motivated potential that has a temperature dependence. The basis for using potential models at high temperature lies in their spectacular success to describe quarkonium spectra at zero temperature. The basic idea behind potential models is to represent the heavy quark pair in a static picture, and encode the quarkonium-medium interaction in the temperature dependence of the potential. At zero temperature, the potential can be derived from QCD [43]. However the derivation of finite temperature potentials directly from QCD is complicated. In the lack of QCD derived finite temperature potentials, some assumptions have to be made about the variation of the potential as a function of temperature.

A widely adopted strategy is to use lQCD calculated potentials. The *free energy*, $F(T)$, and *internal energy*, $U(T)$, of a bound $Q\bar{Q}$ state can be calculated within the framework of lQCD. Fig. I.12 shows an example of a calculation of these energies [44]. Calculations using the free energy extracted from lattice give low dissociation temperature ($\sim$ 1.1 T_c for J/ψ and even lower for other charmonium states [45], and have led to the conclusion that the free energy is only a lower limit to the true potential. This in turn has motivated the exploration of the internal energy instead as an effective representation of the heavy quark interaction potential. The more attractive internal energy yields values of 1.5 to 2 T_c [46] for J/ψ melting temperature. The overshoot of the internal energy for $T > T_0$ above the zero temperature potential (cf. Fig. I.12, right) is one of the arguments against the use of the internal energy in potential models. The correct potential to use is somewhere between the free and internal energies. Linear combinations of the internal and free energies, with temperature dependent coefficients obtained from the QCD equation of state, have been used by some groups [47] with melting temperatures in between those found in internal energy and free energy based potential model calculations.

In addition to the difficulties associated with obtaining an appropriate potential, the use of potential models presents additional challenges. It is not clear to date how to map the melting temperatures of the quarkonium states. Though the Schrödinger equation is a good approximation for tightly bound states like the Υ family, thermal broadening can be significant in the less bound states [48, 46]. This effect can render ambiguous the mapping of the melting temperature through the interplay between the size of the state and the screening radius. The correct accounting of thermal broadening effects might be the next logical step in potential model studies.

The cited references above are far from being exhaustive. There is a great diversity of

[20] At high temperature, the number of temporal points at which $G_H(\tau, T)$ can be calculated is small, because for a given lattice spacing a, T and the number of points in the temporal direction, N_τ are related by $T = (N_\tau a)^{-1}$ (cf. Eq. I.3). The statistics based MEM method thus is less reliable because of less input points from lattice simulation.

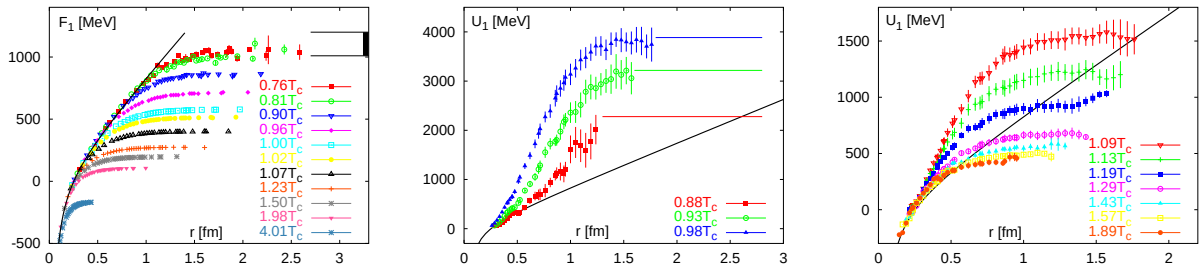

Figure I.12: The heavy quark pair free energy (left) and internal energy (for $T < T_0$ middle and for $T > T_0$ right). On the left plot, the line is the zero temperature Cornell potential. Figures reproduced from [44].

calculations, and given the disparity in the results on melting temperatures, and the above mentioned difficulties in the mapping of the melting temperatures, the only information relatively certain for the time being, and an important one for phenomenological purposes, is the ordering of the melting temperatures of the different quarkonium states, that can be schematically expressed as

$$T_c(\Upsilon) \;>\; T_c(J/\psi) \;>\; T(\chi_b) \;\sim T(\chi_b') \;>\; T(\psi') \;\sim T(\chi_c) \;\sim T(\chi_b') \;\sim T_c(\Upsilon'') \quad \text{(I.20)}$$

In subsequent stages of the collision involving heavy ions, there are a number of competing mechanisms that can enhance or suppress the J/ψ yield. The two major contributors to the suppression are absorption by nuclear fragments from incident nuclei, and an eventual melting in the QGP. It is not impossible that a pair of uncorrelated c and $\bar{c}$ quarks that are close enough in phase space recombine to form a bound charmonium state and *enhance* the J/ψ yield. In addition, the modification of nuclear PDFs in nuclei as compared to that of free nucleons affects the J/ψ production rate. All these competing mechanisms can modify the resulting J/ψ R_{AA} values. It is thus essential to measure if possible, or at least model and understand their variation as function of rapidity, p_T and centrality of collisions. In the next few sections the current knowledge on each one of the above mechanisms will be exposed.

I.3.2 Production of J/ψ and initial state effects

The main production mechanism of J/ψ (and other quarkonia) at high energy hadronic collisions is through the fusion of gluons. Understanding the J/ψ production mechanism is a prerequisite for its utilisation as a hard probe of the medium formed in heavy ion collisions in two respects. On the one hand, the R_{AA} ratio is formed by normalizing the A+A yield by the p+p yield. It is therefore reassuring though not mandatory, if experimental cross sections measured are confirmed by theoretical calculations. On the other hand, some of the processes that affect the interaction of the J/ψ with the medium in the more complex p+A and A+A type collisions can depend on the production mechanism [49]. Though this effect may not be visible with the currently available precision, it is worth having as complete a picture as possible for future measurements. There has been a lot of attempts to reproduce quarkonium cross section data in p+p collisions by theoretical calculation predictions, with more or less success depending on the underlying assumptions. The quarkonium production

cross section calculations can be classified into three categories depending on what kind of initial state is assumed for the pre-hadron $Q\bar{Q}$ pair that later forms a J/ψ. These models are briefly described below:

- Color singlet models (CSM)
  These models are based on the assumption of the *factorisation* of the production of the *on shell* $Q\bar{Q}$ pair from its subsequent binding to form the quarkonium. The production is assumed to be a perturbative hard process and calculated in the pQCD framework by summing amplitudes from all contributing Feynman diagrams (at leading order for most of the existing calculations). For the binding to take place, the *static* approximation is used, where the velocity of each of the heavy quarks in the $Q\bar{Q}$ pair is at rest in the formed quarkonium frame. The $Q\bar{Q}$ pair is also assumed not to change color or spin state in the binding process, which implies that only color singlet (color neutral) pairs can hadronize into a quarkonium, which itself is colorless. The initial predictions (cf. [50] for a comprehensive list) underestimated the cross section measured at Tevatron [51] and at RHIC [52] by up to a factor of ≈ 100. A recent calculation [53] in the color singlet approach that drops the requirements of *on shell* and *static* $Q\bar{Q}$ in the perturbative part of the calculation manages to reproduce both the p_T dependence of the cross section at Tevatron and RHIC, as well as the high p_T longitudinal polarization of direct J/ψ and ψ' at Tevatron [54].

- Color octet models (COM)
  The color octet models also assume factorization between the hard $Q\bar{Q}$ production and its hadronization, described here in the framework of Non-Relativistic QCD (NRQCD) [55], and without assuming the *static* approximation. This formalism allows the evolution of a pair in a color octet state to form into a colorless quarkonium state with the emission of one gluon. Actual calculations are done through a semi empirical extraction of the octet contribution of the non perturbative matrix elements that describe the hadronization. A calculation [56] of total cross section reproduces very well the data from Tevatron [51] and RHIC (cf. Fig. I.13 for the rapidity dependence). However, the color octet mechanism invariably results in a transversely polarized quarkonia, which is strongly contradicted by measurements at Tevatron [54].

- Color evaporation model (CEM)
  In this model [57], the $Q\bar{Q}$ pair is not assumed to be in the color singlet state after the hard process in which it is created. Rather, the color and polarization states of the pair are assumed to be completely randomized through multiple soft processes before hadronization, and only those pairs that end up in a color singlet state at the onset of hadronization form quarkonia. The quarkonium cross section is then calculated through

$$\sigma_{onium} = \frac{1}{9}\int_{2m_Q}^{2(m_q+m_Q)} dm \frac{d\sigma_{Q\bar{Q}}}{dm} \tag{I.21}$$

  where $\frac{d\sigma_{Q\bar{Q}}}{dm}$ is the differential cross section of $Q\bar{Q}$ pair production as a function of mass of the pair, and the integration limit goes from $2m_Q$, the mass of the lightest quarkonium state to $2(m_q + m_Q)$, the mass of the lightest open heavy flavour pair (open charm for charmonia and open bottom for bottomonia) states. The factor 1/9 is the probability

that the initial $Q\bar{Q}$ ends up in a color singlet state before the onset of hadronization. The fractional cross section of a particular onium state, for example the J/ψ is calculated as

$$\sigma_{J/\psi} = \rho_{J/\psi} \times \sigma_{onium} \tag{I.22}$$

where the coefficients ρ for the different quarkonia are fixed from a phenomenological fit to data. By construction, this model can not predict the polarization state of the quarkonia in the final state, which reduces the number of possibilities to experimentally test the CEM models.

To summarize, although there are a number of models available, the J/ψ production mechanism has not so far been elucidated completely. More precise measurements are expected to bring additional constraints (through for example detailed p_T and rapidity dependencies of the cross section) and polarisation at different collision energies for theoretical models to be tested against.

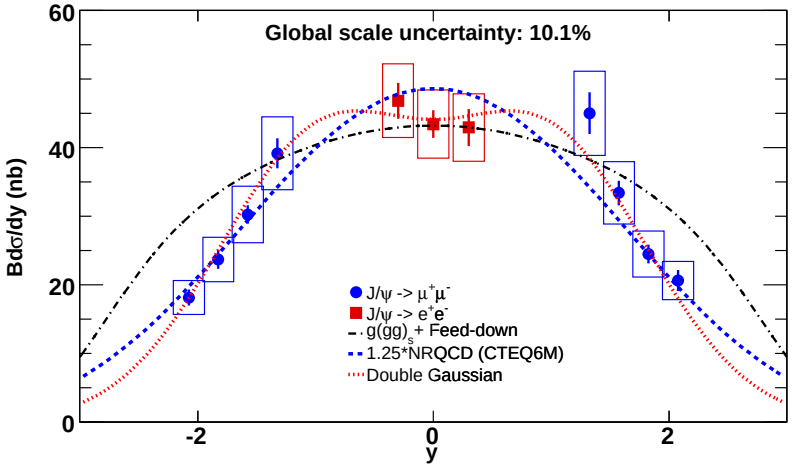

Figure I.13: The rapidity distribution of J/ψ cross section in p+p collisions at $\sqrt{s_{NN}}$=200 GeV, measured by the PHENIX experiment. This figure is reproduced from [52].

Feed down

Part of the ground state charmonia yield comes from feed down of excited $c\bar{c}$ resonance states of ψ' and χ_c. In addition, there is some contribution from the decay of B mesons, especially at high p_T, although this contribution is believed to be small at RHIC energies. Contributions from excited states can be characterized by the feed down ratio, which is the fraction of the detected J/ψ yield that comes from the decay of a particular excited state. The experimental and theoretical constraints on the feed down ratios quantity is far from being established. This is illustrated by Fig. I.14, that shows the ratios R(ψ')[21] and R(χ_c) as a function of

[21] What is shown in the Fig. I.14 is actually the ratio $N(\psi' \rightarrow e^+e^-)/N(J/\psi \rightarrow e^+e^-)$ in p+p collisions. The actual feed down ratio R(ψ') to J/ψ is calculated from this yield ratio by using the branching ratios $B(\psi' \rightarrow e^+e^-) = (7.35\pm0.18)\times10^3$, $B(J/\psi \rightarrow e^+e^-) = (5.94\pm0.06)\%$ and $B(\psi' \rightarrow J/\psi) = (56.1\pm0.9)\%$ [39], using the formula: $\mathrm{R}(\psi') = \frac{B(J/\psi \rightarrow e^+e^-)B(\psi' \rightarrow J/\psi)N(\psi' \rightarrow e^+e^-)}{B(\psi' \rightarrow e^+e^-)N(J/\psi \rightarrow e^+e^-)}$.

collision energy. The general tendency seems to suggest that there is little dependence on the energy, although the experimental errors are large and do not exclude feed down ratios dependent on the collision energy. There have been attempts to extract universal values (cf. for example [58] where R(ψ') and R(χ_c) are estimated to be (8.1±0.3)% and (25±5)% respectively from a global analysis of available charmonium hadro production data.).

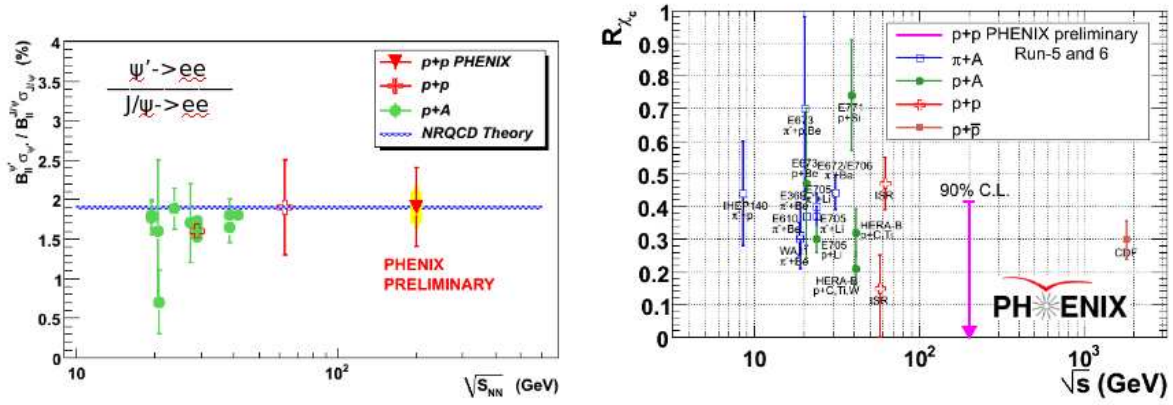

Figure I.14: The experimental constraint on the feed down fraction from ψ' (left side) and χ_c (right side) resonances as a function of collision energy [59]. At top RHIC energy, the relevant energy scale for the R_{AA} measurement presented here, the constraint on the ψ' feed down ratio is 8.0±2.5%, and only an upper bound of <42% at 90% confidence level is available for the χ_c feed down ratio.

The disappearance of quarkonium states at different temperatures has been hailed as compelling opportunity to pin point (with an accuracy limited to the graduation offered by the melting temperatures of the states) what peak temperature was achieved in a given energy and a given system. This is indeed potentially interesting, but practically difficult because it is experimentally challenging to measure the resonances directly, especially the excited state χ_c and χ_b since they decays almost completely into a J/ψ(1S) and Υ(1S) ground states plus a very soft photon of energy not exceeding a few hundreds of MeV, hidden in a large direct and conversion photon background. The challenge is exacerbated in heavy ion systems, though measurements in cleaner p+p and p+A collisions exist.

Even though direct reconstruction of the excited states has not yet been done in A+A systems, it is still possible to indirectly see the suppression of the excited states as a stepwise disappearance of the total J/ψ yield, resulting from the *sequential melting* of its contributors. However the use of such an approach requires a very high level of accuracy in the systematical measurement of the J/ψ R_{AA} at different energies, as well as a clear understanding of the feed down ratios, not to mention cold nuclear matter effects. Both these requirements are not fulfilled currently. In addition, one should be reminded that the formation time of the quarkonium states also influences the amount of time they evolve in the medium, and consequently make the amount of modification that they are subjected to depend on kinematics. This renders more complicated the interpretation of any signature of sequential melting in the J/ψ R_{AA} as coming from the suppression of its contributors.

Shadowing

In heavy ion collisions at RHIC energies, as mentioned before, J/ψs are dominantly produced through gluon fusion. The J/ψ yield is therefore sensitive to the parton distribution function (PDF) of gluons. Measurements of heavy flavour in lepton – ion deep inelastic scattering experiments have shown that the PDFs in nucleons bound to nuclei must be modified with respect to what they are in free nucleons to explain observed spectra [60, 61]. The low x part of this modification is referred to as *shadowing*. Quantitative calculations of the ratio for a nucleus of atomic mass A ($R_A(x,Q^2) = \mathrm{F}_A(x,Q^2)$ / $\mathrm{AF}_p(x,Q^2)$, where $\mathrm{F}(x,Q^2)$ is the parton distribution function) are based on global fits to data at different collision energies, p_T and rapidity domains and assumptions that are used to extrapolate to unexplored regions of the (x,Q^2) space.

The most widely used parametrizations in the literature [62, 63, 64, 31, 65] are summarized in Fig. I.15. The gluon shadowing ratio, the relevant one for quarkonium studies, has up to a factor of 20 discrepancy at low x between some calculations. This huge uncertainty is an important handicap. The situation at intermediate x, which is probed by mid rapidity J/ψs at RHIC energies, is marginally better. If there is no additional clarification of this issue, it will potentially become a major problem at LHC where the relevant x regions ($\lesssim 10^{-3}$) are poorly constrained. The major bottleneck for more stringent constraints comes from the lack of data on which the global fits strongly depend (see for example [65]).

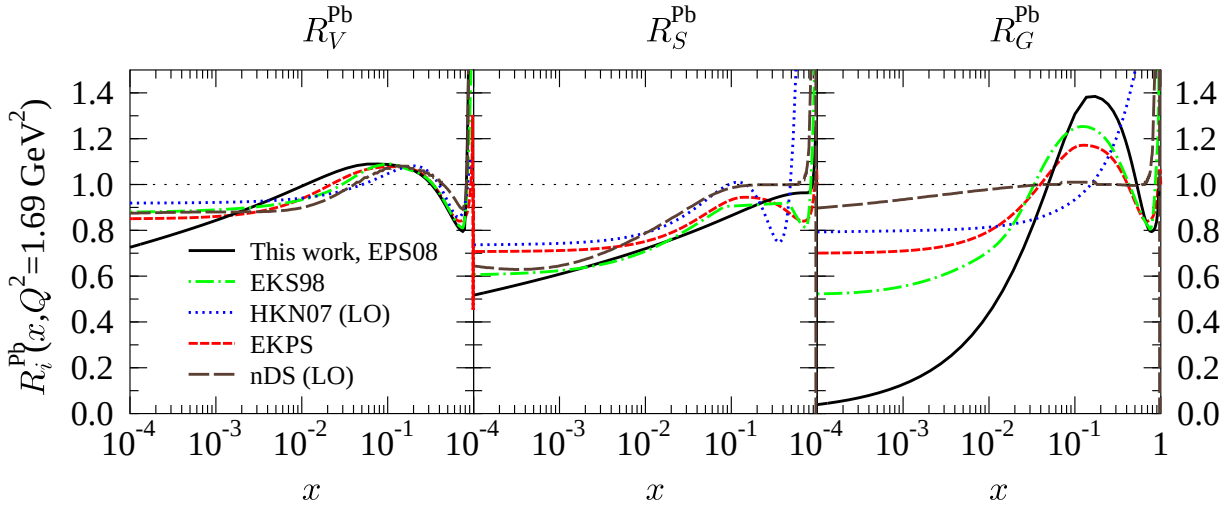

Figure I.15: Shadowing ratios R_A for valence quark (left panel), sea quark (middle panel) and gluons (right panel) calculated for Pb+Pb collisions by various groups.

Cronin effect

The partons that undergo hard scatterings sometimes suffer from multiple elastic scatterings on partons coming in the other direction before their final interactions. This leads to a Brownian motion in the transverse plane and broadens the p_T spectrum. The so called Cronin effect is the broadening of the p_T spectrum of produced particles. This effect can be seen as a

rapid increase of the cross section of the observed probe as a function of p_T. It was observed at various energies in particular at Fermilab [66] in proton – ion collisions and SPS [67] in Pb+Pb collisions.

I.3.3 Nuclear absorption

J/ψs produced in the initial hard scattering between nucleons in projectile and target nuclei are subject to break up through interaction with the spectator nucleons which do not undergo an inelastic scattering. In the literature, this is often referred to as cold nuclear matter (CNM) absorption or break-up[22].

The nuclear modification factor measured in nucleus-nucleus collisions reflects the cumulative effect of melting in the QGP and CNM break-up in addition to the other suppression or enhancement mechanisms explained above. It is therefore essential to subtract out the CNM break-up contribution from the measured R_{AA} in heavy ion collisions before interpreting results in terms of QGP effects. One way to estimate it is by measuring J/ψ in situations where no QGP formation is expected, but the produced J/ψs are swept through by the same amount of cold nuclear matter at the same energy at which the heavy ion measurement is made. Collisions between protons or very light nuclei such as deuteron and heavy ions can be used to do this experiment. Although this is the ideal method, such data is not always available in a sufficient amount, and theoretical models can be useful. Below efforts to pin down the CNM effects by various experiments is given in the light of which theoretical coverage of the subject are reviewed.

I.3.3.1 Results from CERN-SPS experiments

A series of experiments at the CERN Super Proton Synchrotron (SPS) by the names NA38, NA50 and NA60 have measured J/ψ cross sections through the dimuon decay channel in various ion-ion collisions including p-ion. These experiments were located in the North Area (from which their name derives) experimental hall, and shared the same apparatus: a muon spectrometer based on multiwire proportional chambers, although NA60 was upgraded with a silicon vertex tracker. They operated in fixed target configuration where the projectile nuclei were accelerated to energies of 158 AGeV, 200 AGeV, 400 AGeV and 450 AGeV.

The NA50 collaboration has verified [68, 69] that the Drell-Yan yield in a similar mass window as the J/ψ and ψ' is exempt from initial state effects such as shadowing and scales with N_{coll}. As such, it can be used as a reference against which the J/ψ yields can be compared. The Drell-Yan yield in the mass window from 2.9 GeV/c^2 to 4.5 GeV/c^2 is thus used as an unnormalized expected yield of J/ψ. This ratio will be summarized for a large variety of collision systems in Fig. I.19 as a function of the average path length L of the J/ψ on its way out. All the light ion system data falls on a universal curve that can be fitted with an exponential $exp(-\sigma_{breakup}\rho_0 L)$, where $\sigma_{breakup}$ is the inelastic breakup cross section of J/ψ on cold nuclear matter, and ρ_0 is the nuclear density.

To extract the break up cross section in a least biased way, the ratio of the measured cross section in p+A collisions to the atomic mass of the nucleus σ/A is plotted as a function of

[22] Although there is only semantic difference between the two terms, hereafter, a choice will be made and the term break-up will be employed to refer to the absorption suffered not only by the formed J/ψ, but also the pre-hadronic $Q\bar{Q}$ state.

average length L. For purely cold nuclear absorption, the dependence of σ/A on L should be linear, with the slope providing the CNM break up cross section [69]. The cross section to atomic mass ratios measured by NA50 in different p+A collisions with berylium, aluminum, copper, silver, tungsten and lead targets is shown in Fig. I.16 on the left by full circles for J/ψ and by open squares for ψ'. The breakup cross sections extracted are $\sigma_{breakup} = 4.2 \pm 0.5$ mb for the J/ψ and $\sigma_{breakup} = 7.7 \pm 0.9$ mb for the ψ' [69]. This result is in accordance with the expectation from the relatively large radius of the ψ' as compared to the J/ψ.

I.3.3.2 Results from FERMILAB experiments

The E866 experiment is a drift chamber plus hodoscope detector within a field created by two magnets. It operated at Fermilab with a beam of protons at 800 AGeV on fixed targets of berylium iron and tungsten. The experiment has a very wide acceptance in p_T and x_F[23] for J/ψ and ψ' which allowed the collaboration to perform a comparative study of the cold nuclear matter suppression patterns of these two mesons. The E866 experiment's approach to CNM effects is a bit different to the one of SPS, since they are parametrized through α defined by

$$Y_{pA}(x_F, p_T) = Y_{pp} \times A^{\alpha} \tag{I.23}$$

where Y represents the J/ψ yield. α is measured as a function of x_F, x_2 and p_T. A value of α equal to unity implies no CNM effect, whereas a lesser value indicates the predominance of absorptive effects. Assuming that there is no shadowing, one can relate the value of alpha to the break-up cross section through an analytic expression.

The value of α of J/ψ and ψ' (done by the E866 experiment) as a function of x_F, as well as the integrated value for D mesons (done in another experiment at Fermilab, E789, a predecessor of the E866), is shown in Fig. I.16 on the right [66]. This result gives a confirmation of the SPS observation with respect to the comparison of the CNM suppression effect on J/ψ and ψ' at least for low x_F values, namely the ψ' are more suppressed than the J/ψ due to CNM absorption. In addition, the D meson α is compatible with one, providing a robust control on the overall normalization.

I.3.3.3 Results from PHENIX

The RHIC CNM reference for J/ψ, which is of primary importance for the work presented here, was measured in deuteron on gold (d+Au) collisions. The J/ψ suppression ratio in d+Au, R_{dA} is plotted on the left side of Fig. I.17 as a function of rapidity and N_{coll} (centrality). N_{coll} is estimated from the charged multiplicity at forward rapidity ($3 < \eta < 3.9$) in the gold going direction by using a Glauber approach. $R_{dAu}(y)$ shows a modulation that is reminiscent of the shadowing dependencies. This modulation is indeed interpreted as being a result of the different regions of the momentum fraction x in the gold nucleus[24] probed by the rapidity

[23] x_F is the difference between the momentum fractions of the gluons participating in the fusion process that creates the J/ψ. If x_p is the momentum fraction in the proton and x_A the one in the ion, then $x_F = x_p - x_A$.

[24] The rapidity and transverse mass $m_T = \sqrt{m^2 + p_T^2}$ of the J/ψ produced are related to x and the center of mass collision energy $\sqrt{s}$ through $x = \frac{m_T}{\sqrt{s}} e^y$, neglecting any other products in the final state, in particular the soft gluon emitted to color neutralize the $c\bar{c}$ pair.

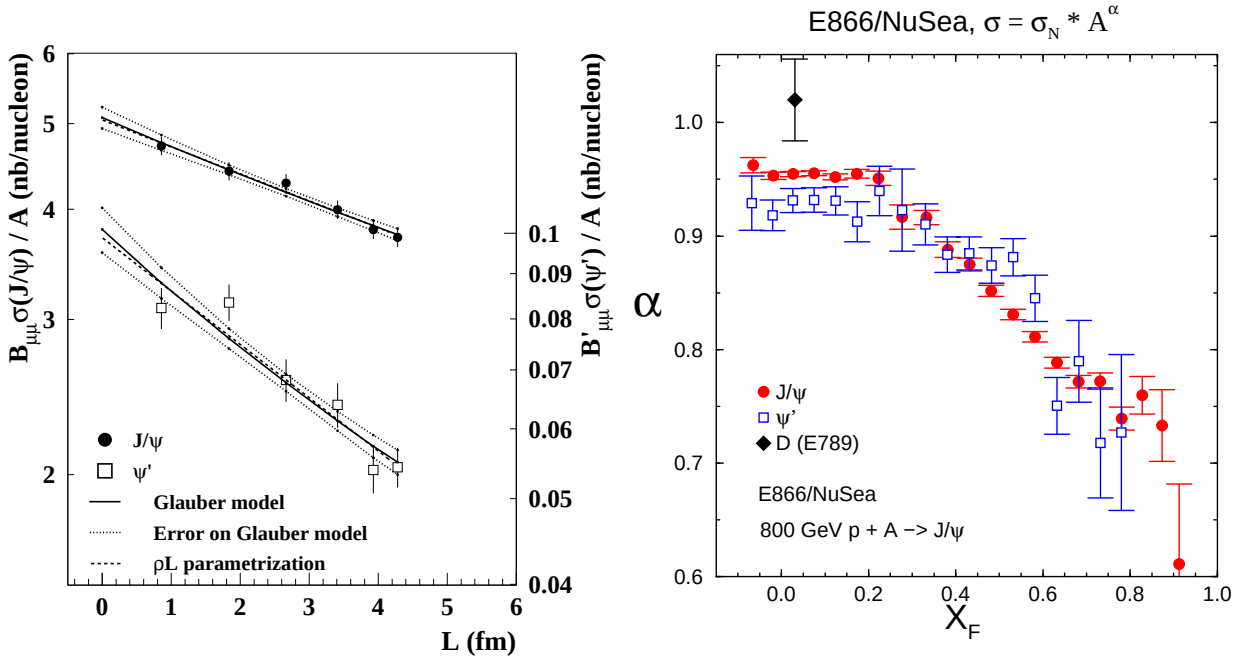

Figure I.16: Left: The evolution of σ/A as a function of average length L for different atomic targets from NA50 [69] for J/ψ (full circles) and ψ' (empty squares). Right: α as a function of x_F from E866 [66] for J/ψ (full red circles) ψ' (empty blue squares) and D mesons (full black diamond).

acceptance windows of PHENIX, and consequently due to the shadowing modification in that region.

I.3.3.4 Model extrapolations

Once J/ψ production has been measured in a cold nuclear matter control experiment (d+A or p+A) where no QGP is formed, the next step is to deduce to what level of suppression this would extrapolate to in A+A collisions. In other words, get an estimation of how much the suppression would be if one could 'turn off' the suppression by QGP. In the SPS case, this was done intuitively by a mere continuation of the exponential function that fitted best to the p+A 'measured over expected' J/ψ yield vs. path length L. At RHIC, the extrapolation has to be done as a function of centrality. Two approaches have been employed so far.

Full models

The cold nuclear matter suppression was modeled in an extension of the CEM formula for J/ψ cross-sections which can schematically be expressed as [70] an integral over the mass of the final state of a symmetrized product of nuclear PDF $F(x, Q^2, \overrightarrow{r}, z)$, elementary nucleon-nucleon cross-section σ and an impact parameter $\overrightarrow{b}$ dependant product of survival probability $S(\overrightarrow{r}, z) \times S(\overrightarrow{b} - \overrightarrow{r}, z)$:

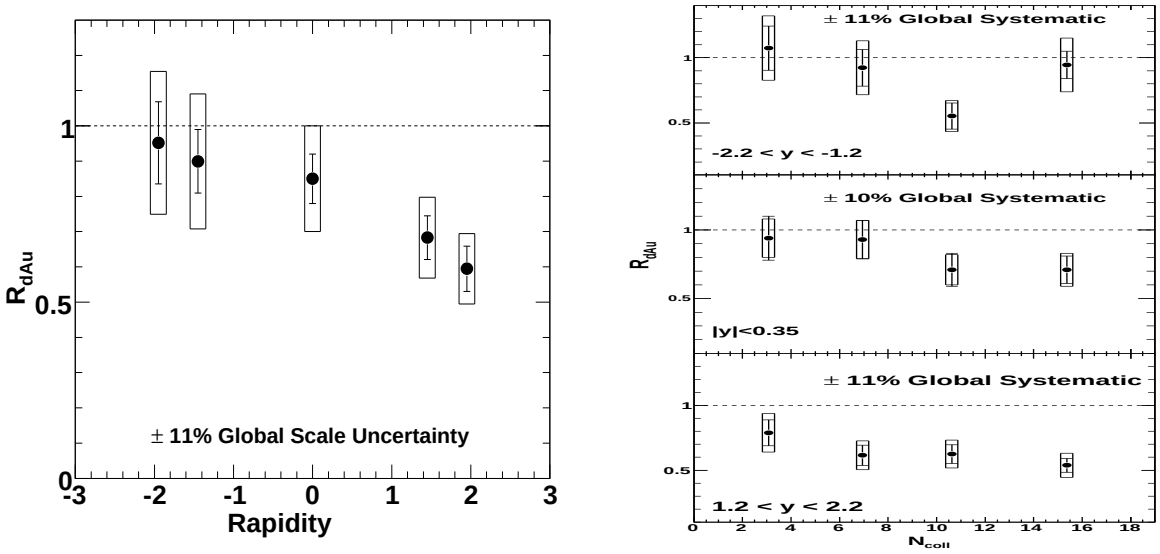

Figure I.17: R_{dA} in d+Au collisions at top RHIC energy, as a function of rapidity y (left) and as a function of rapidity and centrality (right). The error bars are statistical and point to point uncorrelated systematical errors and boxes are correlated systematical errors that are not global. Global correlated systematical error is 11%. The exact meaning of these two types of errors will be explained in chapter 4.

$$\frac{d\sigma}{dyd^2bdzd2rdz'} = 2F_{J/\psi}\sum_{i,j}\int_{2mc}^{2m_D} MdM \quad F_i^A(x_1,Q^2,\overrightarrow{r},z)F_i^A(x_2,Q^2,\overrightarrow{b}-\overrightarrow{r},z')\frac{\sigma_{ij}}{M^2}\times$$
$$S_A^{abs}(\overrightarrow{r},z)S_B^{abs}(\overrightarrow{b}-\overrightarrow{r},z) \qquad \text{(I.24)}$$

where $F_{J/\psi}$ is the universally fixed fraction of $c\bar{c}$ pairs that hadronize to J/ψ, and $x_{1,2}$ is approximated to first order as $\frac{M_{J/\psi}}{\sqrt{s_{NN}}}\times exp(\pm y)$, neglecting the p_T of the J/ψ and assuming no soft gluon emission. The nuclear PDFs $F_i^A(x_1,Q^2,\overrightarrow{r},z)$ are generalized from the nucleon PDF $f_i^N(x,Q^2)$ through multiplication by an appropriate nuclear density $\rho_A(s)$ and a shadowing ratio (EKS98 or NDSG), the argument s of the nuclear density being the amplitude of the radial+longitudinal position vector $(\overrightarrow{r},z)$. The survival probability of the J/ψ from nuclear absorption is embodied by the function $S_A^{abs}(\overrightarrow{r},z)=exp(\int_{-z}^{\inf}dz'\rho_A(\overrightarrow{r},z')\sigma_{abs}(z'-z))$, where z is the production point and z' is the absorption point. The path length dependence of the absorption $\sigma_{abs}(z'-z)$ is simulated by allowing for J/ψ in both color octet and color singlet models, and taking into account the local nuclear density. The prediction of R_{AA} using the cross-section calculated from this approach is shown on the left of Fig. I.18. The principal objection to this method is that it depends strongly on CEM model and the shadowing scheme which as already pointed out are quite poorly known.

Data driven method

To circumvent the model dependence in the shadowing scheme, another more data driven method, suggested in [71], was implemented using RHIC R_{dA} data from d+Au collisions as a

function of rapidity and centrality (cf. Fig. I.17, right). The first assumption in this method is that the suppression depends only on the local impact parameter of the J/ψ creation point. With this in mind, the suppression ratio contribution at a given rapidity of a particular collision between nucleon 1 of the projectile nucleus and nucleon 2 of the target nucleus can be estimated from the physically motivated formula:

$$R_{AA}^{CNM}(y) = R_{dA}(-y, b_1) \times R_{dA}(y, b_2) \tag{I.25}$$

where b_1 is the impact parameter of nucleon 1 with respect to the target nucleus center, and b_2 is the impact parameter of nucleon 2 with respect to the projectile nucleus center, and the function R_{dA} is inferred from data. This formula would propagate correctly the effects on the survival probability contribution from both the shadowing and CNM breakup, the two main nuclear effects at RHIC. As the R_{dA} contribution of shadowing is proportional to the PDF distribution, and the absorption contribution goes like $exp(-\rho\sigma L)$, the formula in Eq. I.25 reflects only the factorization $R_{AA} \propto \mathrm{PDF}_1 \times \mathrm{PDF}_2 \times exp(-\rho\sigma(L_1 + L_2))$.

To integrate the above described calculation of the nuclear modification ratio for the p+A and A+p cases to the full ion – ion collision, a simulation of an A+A collision is performed in the Glauber[25] framework at a desired impact parameter b. This provides the local impact parameters b_1^i and b_2^i of each elementary nucleon-nucleon collision i, which will allow to express the R_{AA}^{CNM} of the simulated A+A collision as an average of the corresponding $R_{dA}(y, b_i)$ over the N_{coll} binary elementary collisions using Eq. I.25:

$$R_{AA}^{CNM}(y, N_{coll}) = \frac{1}{N_{coll}} \sum_{i=1}^{N_{coll}} R_{dA}(-y, b_1^i) \times R_{dA}(y, b_2^i) \tag{I.26}$$

where $R_{dA}(y, b_i)$ is extracted from a phenomenological fit to the measured R_{dA}. The resulting prediction is shown on the right side of Fig. I.18 for J/ψ produced at mid rapidity in Au+Au collisions at $\sqrt{s_{NN}} = 200\ GeV$. The yellow error band is calculated by propagating the errors on the R_{dA} measurement. With the currently available measurement (cf. Fig. I.17, right), this method gives an impractically large error band, but it has the incontestable merit of being minimally dependant on models. Besides, larger d+Au data sample (already available, but not fully analyzed yet) should help to alleviate this.

I.3.4 Anomalous suppression

Once all the above effects have been estimated and subtracted, any leftover J/ψ suppression in A+A collisions is called *anomalous* suppression. A statistically significant anomalous suppression is the long sought for direct evidence of deconfinement. The CERN SPS experiments NA38, NA50 and NA60 were the first to perform J/ψ suppression measurements in heavy ion systems. The projectile heavy ions were accelerated to the same energy as the protons (158 AGeV through 450 AGeV) on heavy ion fixed targets[26]. The "measured/expected"[27] ratio over a wide range of systems is summarized with the same measurement from light-heavy

[25] Reminder: Glauber model uses Woods-Saxon nuclear distribution for the nucleon density.

[26] The J/ψ measurements were done in collisions involving the following ions: Sulfur-Uranium, Oxygen-Copper, Oxygen-Uranium, Lead-Lead and Indium-Indium.

[27] The "expected" yield is represented by the Drell-Yan yield in a mass window close to the J/ψ mass window as explained in section I.3.3.

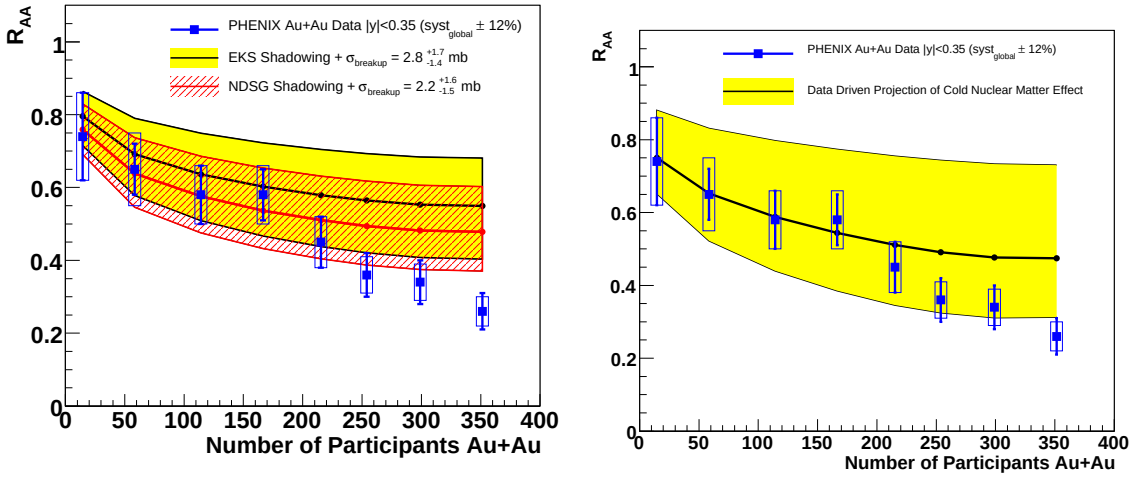

Figure I.18: R_{AA}^{CNM} extrapolations at mid rapidity ($|y|$ <0.35) for top RHIC energy. Left: Using full modelization [70], and assuming EKS98 (yellow band) and NDSG (red hashed band) shadowing schemes. Right: Using a data driven method [71]. The data points are the R_{AA} measurements in Au+Au collisions at the same energy and (mid) rapidity. The error bars are statistical and point to point uncorrelated systematical errors. The error boxes are the correlated systematical errors. The global systematical error is 12%. Figures reproduced from [72].

systems in Fig. I.19. The path length dependent exponential damping observed in smaller systems is broken for central heavy-heavy ion systems, whereas the continuity with light-heavy systems is preserved by the peripheral heavy-heavy systems. It is now accepted that the extra absorption is due to QGP formation, although some models [73, 74] have reproduced the trend without assuming plasma formation.

The next natural step in the investigation of the anomalous suppression was to increase the collision energy. One of the main design objectives of the PHENIX experiment at RHIC is to accomplish this. The RHIC collider can deliver collisions between heavy ions in collider configuration (both colliding ions are accelerated). The top center of mass collision energy per nucleon pair attained is $\sqrt{s_{NN}} = 200$ GeV, an order of magnitude higher than the SPS top energy. The first J/ψ R_{AA} measurement [75] in Au+Au collisions at $\sqrt{s_{NN}} = 200$ GeV at forward rapidity ($1.2 < |y| < 2.2$) and mid rapidity ($|y| < 0.35$) as a function of centrality (N_{part}), shown in Fig. I.20 raised two puzzles.

On the one hand, the suppression in Pb+Pb collisions at SPS expressed in terms of R_{AA} showed a very similar trend as the R_{AA} of the mid rapidity data at RHIC. Despite the difference in rapidity range between the SPS measurement ($0 < |y| < 1$) and the central rapidity PHENIX measurement, it is startling to see the same level of suppression with collision energies as different as at SPS and RHIC. The direct comparison between the RHIC and SPS measurements can be criticised by the fact that in the R_{AA} measurements, the cold nuclear matter effect contribution has not been subtracted out. Indeed such an exercise at RHIC has been done as shown in Fig. I.18, but so far is hampered by the poor statistics d+Au measurement that is available. Despite these points, naively one would expect to get a stronger suppression at RHIC, since higher collision energy implies higher energy density and therefore a hotter medium.

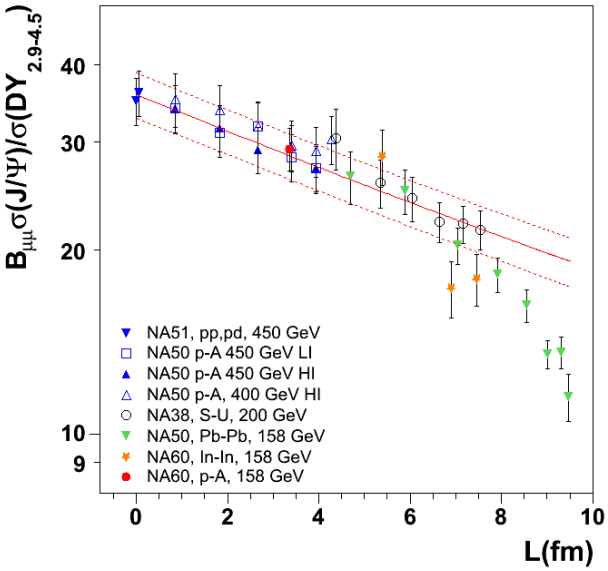

Figure I.19: Summary of CERN SPS experiment results on J/ψ suppression. The different points are explained in the text.

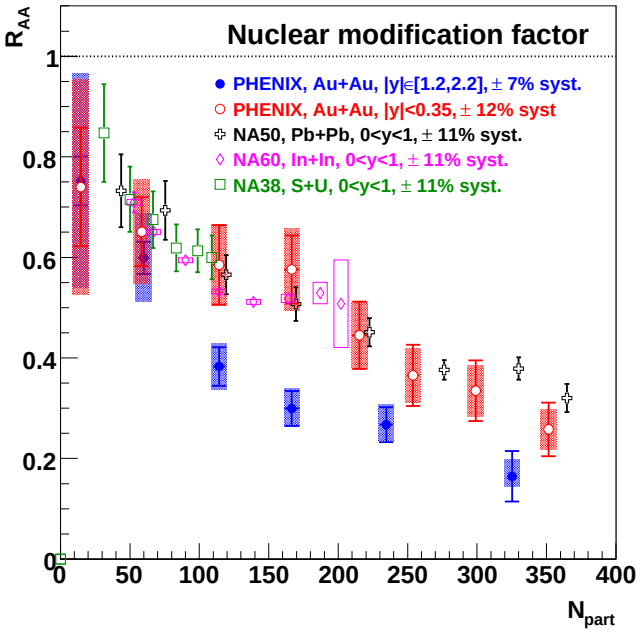

Figure I.20: PHENIX J/ψ R_{AA} measurement as a function of centrality (N_{part}) in Au+Au collisions at $\sqrt{s_{NN}}$=200 GeV at mid (red open circles) and forward (blue closed circles) rapidities together with the same measurement at CERN SPS in In+In collisions at 158 AGeV (pink open diamonds), Pb+Pb collisions at 158 AGeV (black markers) and S+U collisions at 200 AGeV (green open squares).

On the other hand, the energy density of the medium should in principle be stronger at mid rapidity as compared to forward rapidity, since a larger fraction of the particles produced in the heavy ion collision are radiated in this region. Arguing again on the basis of a suppression that increases with the local density in the phase space region where the J/ψ is created, one would expect more suppression in the mid rapidity region than in the forward rapidity region. Note however that in a recent claim [76], it was proposed that the difference between the mid and forward rapidity J/ψ R_{AA} can be explained by effects that do not necessarily involve the formation of a deconfined medium.

The two widely advocated scenarios to explain this trend are sequential melting plus CNM effects and regeneration. In the sequential melting plus CNM effects scenario, the suppression seen both at RHIC and at SPS would come from the melting of the feed down components of the measured J/ψ. In both the RHIC and SPS measurements, no subtraction of the feed down components is performed. The measured suppression therefore reflects the combined suppression of all the ground J/ψ state and the excited states that contribute significantly to the total J/ψ yield. As it was pointed out in Sec. I.3.1.2, the excited states melt at a temperature lower than that of the J/ψ. If the temperatures attained both at RHIC and at SPS are below the dissociation temperature of the J/ψ and above those of the χ_c and ψ', then that would explain the similarity of the total suppression observed both at RHIC and at SPS. However sequential melting alone does not explain the rapidity dependence of R_{AA} and the observed difference will need to come from CNM effects, unlike those shown earlier, that tend to result in stronger suppression at forward rapidity. The most obvious way to test the sequential melting scenario is to measure directly the suppression of the excited states and subtract out their contribution from the measured J/ψ R_{AA}. But as pointed out in Sec. I.3.2, this is practically impossible with the currently available statistics.

The second scenario is regeneration. Regeneration is a mechanism by which a c and a $\bar{c}$ quark pair created in uncorrelated hard processes combine to form a J/ψ. The probability of combination of uncorrelated charm quarks increases with the square of the number of $c\bar{c}$ pairs that are free in the medium. In other words, if there is a regeneration component to the observed J/ψ yields in heavy ion collisions, then the fraction of regenerated J/ψ should increase quadratically with the number of $c\bar{c}$ pairs. This would instantly explain the rapidity trend of the R_{AA} of J/ψ, as more $c\bar{c}$ are created at mid rapidity than at forward rapidity. In addition, measurements have shown that the $c\bar{c}$ production rate at RHIC is very high. At least 10 $c\bar{c}$ pairs are created per central Au+Au collision [77]. The implication would be that if regeneration indeed takes place, then it would compensate a large destruction of J/ψ. Even if the higher energy density at RHIC suppresses J/ψs more than at SPS, the net effect on the observed R_{AA} would be to bring it closer to the SPS R_{AA}. The apparent agreement of the two R_{AA}s (RHIC and SPS) would then be due to pure coincidence. The value of R_{AA} resulting from regeneration can be calculated within various models, many of which succeed to reproduce the suppression ratio observed both at mid and forward rapidities. A comparison will be done in chapter 5, where the R_{AA} measurement from a new data set will be shown.

An optional way to test regeneration is inspired by the observation of a strong flow of electrons from open heavy flavour semileptonic decay [33]. The flow of the heavy quarks underlying the charmed mesons that is behind the flow of open charm should in principle be reflected in the regenerated component of the J/ψ yield. The other measurement presented in this thesis, the elliptic flow v_2 of J/ψ is a first step towards testing the regeneration mechanism.

Chapter II

Experimental Setup

II.1 The RHIC accelerator

The Relativistic Heavy Ion Collider (RHIC) is a versatile particle accelerator at the Brookhaven National Laboratory on Long Island, in the state of New York. Through the pair of superconducting rings that cross at six interaction regions, different species of atomic nuclei as well as polarized protons are accelerated at various energies. This has allowed its experiments (BRAHMS, PHENIX, PHOBOS and STAR) positioned at four of the six interaction regions to collect data in various collision configurations most of them mentioned in the list below.

- p+p interactions at 64 GeV, 200 GeV
- Au+Au interactions at 9.2 GeV, 19 GeV, 62 GeV, 130 GeV and 200 GeV
- Cu+Cu interactions at 19 GeV, and 200 GeV
- d+Au interactions at and 200 GeV

The work reported in this thesis is based on the high luminosity Au+Au run of the 2007 data taking seasons where an integrated luminosity of 810 μb^{-1} was collected. More details about the data taking conditions of this run as well as of the run of the 2004 data taking season, which is also of some relevance for later discussions, will be given in chapter 3.

II.2 The PHENIX experiment

PHENIX is one of the four experiments that operate at RHIC. It is designed to have good electron and hadron identification as well as muon detection capabilities, in a wide range of environments going from p+p collisions to central Au+Au collisions where the total charged particle multiplicity goes up to a few thousands. Among many other physics goals, PHENIX is optimized for the detection of lepton pairs, allowing the reconstruction of the dileptonic decay of light vector mesons (ϕ,ρ and ω) and quarkonia. In this chapter, the PHENIX detector subsystems that are relevant for the $J/\psi \rightarrow e^+e^-$ analysis will be discussed in detail II.3.3. The PHENIX detector can be split into three major parts shown in Fig. II.1: The forward rapidity spectrometers, the mid rapidity spectrometers and the global detectors.

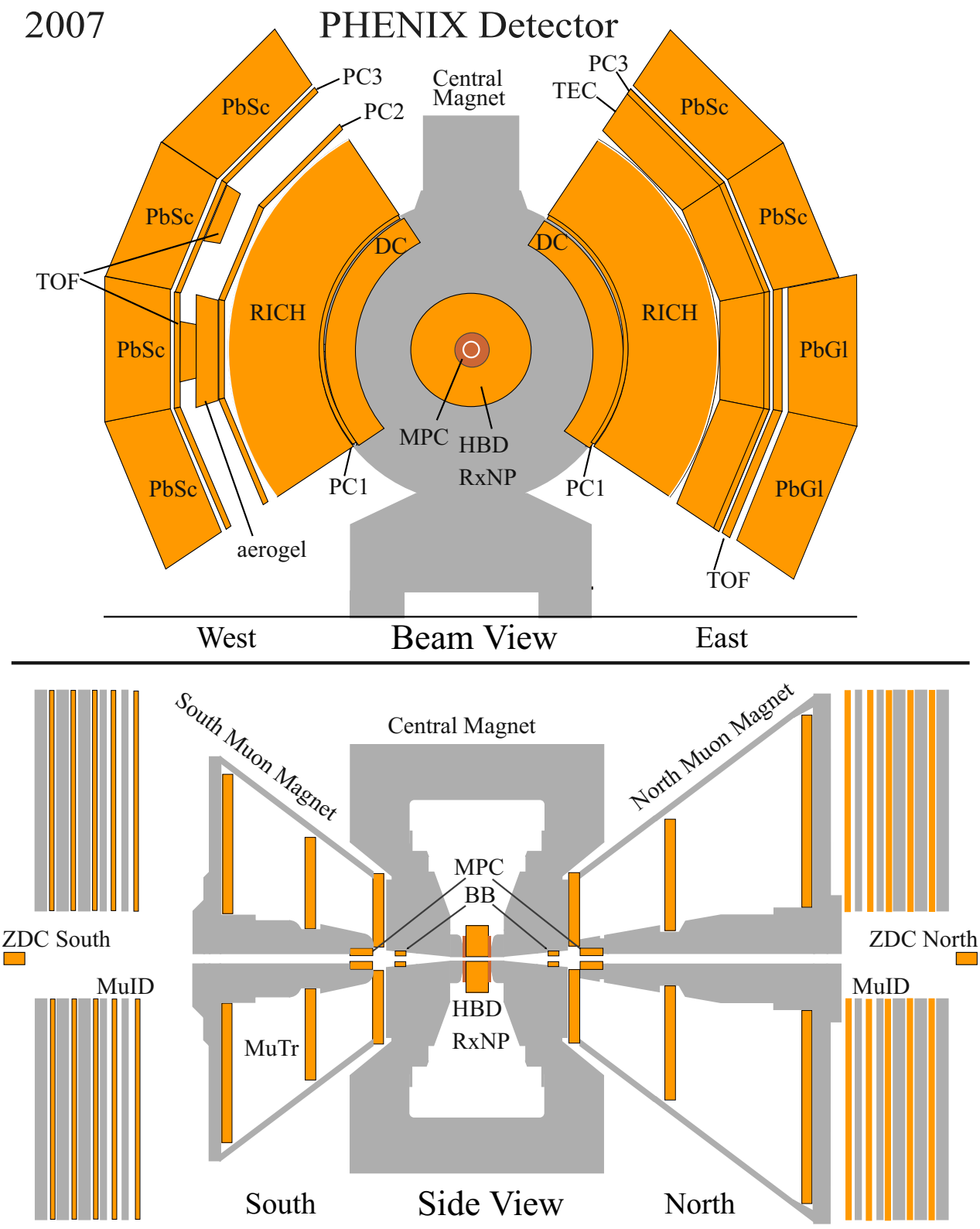

Figure II.1: PHENIX central (top) and forward (bottom) arm spectrometers.

The two forward rapidity spectrometers ($1.2 < |y| < 2.2$), depicted on the bottom half of Fig. II.1, are used for the detection of muons. Each spectrometer is made up of a tracker (MuTR) consisting of successive planes of cathode strip chambers. The magnetic field has a radial symmetry that deviates charged particles in the azimuthal direction, while conserving their polar inclination. Momenta of charged tracks are reconstructed by measuring the amount of deviation in the azimuthal direction.

The major source of background in the trackers is from hadrons, mainly pions and kaons. To improve the signal to background ratio, the trackers are preceded by a thick frontal absorber made of steel, that stops a large fraction of the low momentum hadrons, and lets go through muons with an average energy loss of ~ 2 GeV. This fixes the minimum momenta of reconstructable muons to a similar order of magnitude ($p \gtrsim 2$ GeV/c). Even though the frontal absorber stops low momentum hadrons, it is still necessary to reject the higher momentum hadrons that survive and make it to the trackers. These hadrons are called punchthrough hadrons.

The rejection of punchthrough hadrons is accomplished by using information from the muon identifier (MuID). The muon identifier is a series of planes made up of tubes enclosing single wire proportional chambers. The interspacing between these active detector planes is occupied by further steel absorber planes. The magnetic field in the tracker region is excluded from getting into the MuID region by return yokes, that also serve to further absorb punchthrough hadrons. There are five identification planes, and the probability that a charged hadron reaches a plane decreases the further out the plane is from the interaction region. Although this holds true for muons as well, muons have a much higher probability than hadrons of making it to deeper MuID planes.

The association of straight line tracks reconstructed from hits in the MuID planes with the curved tracks reconstructed in the MuTR provides a method to identify tracks in the MuTR as belonging to muons or punchthrough hadrons. The deeper a track goes into the identification planes, the more likely it is to be a muon. The exact criterion of muon identification (number of identification planes that the track is required to attain) is optimized during analysis, through a compromise between the cut rejection power and its efficiency. As this part of the PHENIX detector is not relevant to the $J/\psi \to e^+e^-$ analysis, it will not be discussed further.

At mid rapidity a pair of spectrometers called *the central arm spectrometers*, and shown on the top half of Fig. II.1, are used for the detection, identification and momentum reconstruction of electrons, photons and charged hadrons. The pseudo rapidity coverage of the central arm spectrometers is $|\eta| < 0.35$ while their azimuthal coverage is split into $2 \times 90°$. Due to their geographical orientation, the two half spectrometers are referred to as *east* and *west* arms. The reference frame axes are defined as follows. The z axis is parallel to the beam axis. The y axis is in the upward direction. The x axis is given by the right hand rule, and points in the direction of the west arm. The detectors of the central arm spectrometers are described in Sec. II.4.

II.3 Global detectors and event geometry determination

Before the discussion of the subsystems in the central arm of the PHENIX detector, the global detectors which are used for the reconstruction of event by event collision geometry will be detailed in this section.

II.3.1 Beam Beam Counter

The PHENIX beam beam counter (BBC) [78, 79] is the primary start timing detector of the whole experiment. Its main purpose is to detect inelastic collisions, to provide precise timing information and to determine the interaction position for each collision. The RHIC collider provides bunches with a longitudinal dimension of RMS about 25 cm, and bunch crossing time of about 2 ns. These precisions are far from sufficient for the tracking algorithms that rely on a well known vertex position, as well as for use as start timer for time of flight detectors whose resolution can be as good as 100 ps.

The BBC provides the basic trigger of inelastic collisions for the whole experiment by detecting charged secondary particles from collisions at very forward rapidity (pseudorapidity range from 3.0 to 3.9) over full azimuth at a distance of about 1.44 m on each side of the center of the detector (north and south, corresponding to the right and left sides respectively of the bottom half of Fig. II.1). The BBC module on each side measures the arrival time of leading particles which travel almost at the speed of light. The average and the difference of the arrival times in the two modules provide respectively the start time for the collision and its vertex position longitudinally along the beam axis. There were three major technical challenges for the construction of this detector.

1. The huge difference in the charged particle multiplicity between p+p and Au+Au collisions. Only a few charged particles are expected in the BBC acceptance for the p+p case while this number can go up to about 1000 for Au+Au collisions [80]. The BBC had to be designed for such a wide dynamic range of particle multiplicity.

2. The physical location of the detector exposing it to substantial radiation doses ($\sim 10^{10}$ γ/cm^2 and 10^{11} neutrons/cm^2 per RHIC year). The detector needs to be radiation hard at this level.

3. The detector is installed just in front of the central arm magnets, which generate a field of about 0.3 T, essentially parallel to the beam axis. The photomultipliers therefore needed to be operational in a high intensity magnetic field.

Faced with these challenges, each BBC (North and South) module was built as an array of 64 identical elements consisting of four components (cf. Fig. II.2 (a)): a Čerenkov radiation material, a photomultiplier tube (PMT), a high voltage module and mechanical accessories to pack the ensemble and mount on a frame. To avoid using any glue or grease to join parts together, the Čerenkov radiator was designed simply as a thick window of the PMT. It is constructed from fused quartz with a hexagonal geometry inscribing a circle of radius 1" and thickness of 3 cm. The PMT is a fitting 1", 15 layer fine mesh dynode from Hamamatsu (R3432), operational in strong magnetic field. The array of 64 is mounted on a circular frame

of 30 cm outer diameter and 10 cm inner diameter around beam pipe. It measures 25 cm long (cf. Fig. II.2).

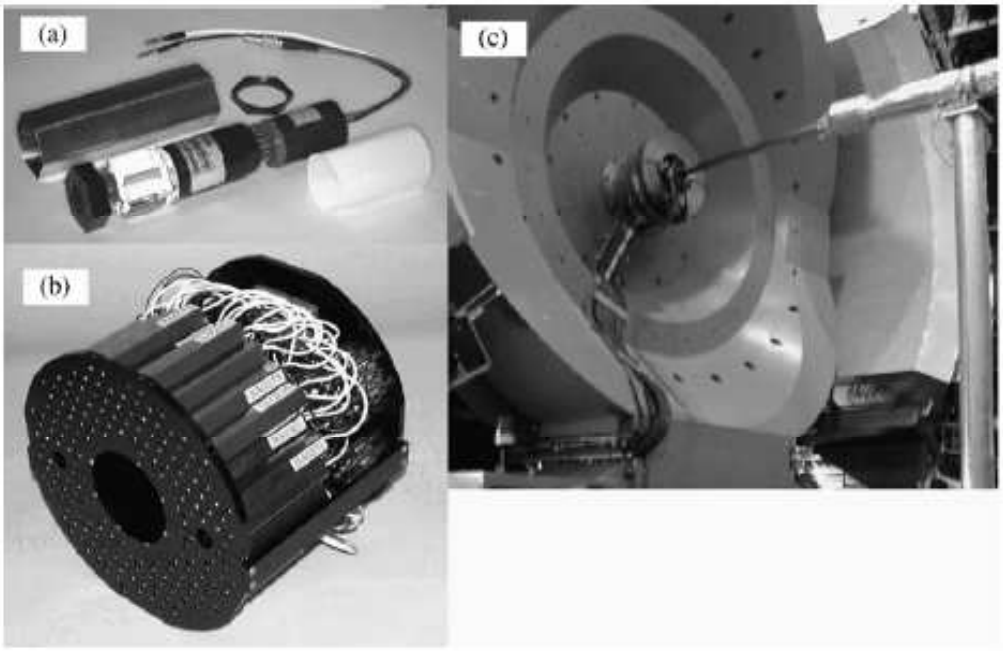

Figure II.2: BBC detector, A) A single PM element, B) An assembled module, C) Installed module.

The intrinsic time resolution of individual PMT elements is of the order of 100 ps, and improves to ≈ 50 ps after slewing corrections [1]. The global time of a module is computed from the average TDC counts of each PMT element that it is composed of. This results in a global time resolution per module of about 40 ps, well under the timing resolution requirement by the time of flight detectors (100 ps).

II.3.2 Zero Degree Calorimeters

All four experiments at the RHIC collider facility are equipped with identical Zero Degree Calorimeters (ZDC) [81] at very forward rapidity in both beam directions for common luminosity determination and beam monitoring. The energy at zero degree (carried by neutral particles undeflected by the beam line intersecting region dipoles) is known to be related to the impact parameter in the nuclear collision [82], a property that is exploited to experimentally categorize events into centrality classes. The ZDCs are hadronic calorimeters that measure the energy carried by spectator neutrons and evaporation neutrons from unstable fragments.

The ZDCs are placed in the space immediately after the splitting of the two beam pipes (cf. Fig. II.3 A), about 17.5 m away from the beam intersection point. Such a location limits the total width of the calorimeters to 10 cm. The main concern in the design was to minimize shower leakage with such a tight aperture, which otherwise would adversely affect the energy

[1] TDC and ADC values are usually correlated. This dependence of TDC readings on ADC readings should be parametrized out before using TDC readings for time measurement, and is what is referred to as slewing correction.

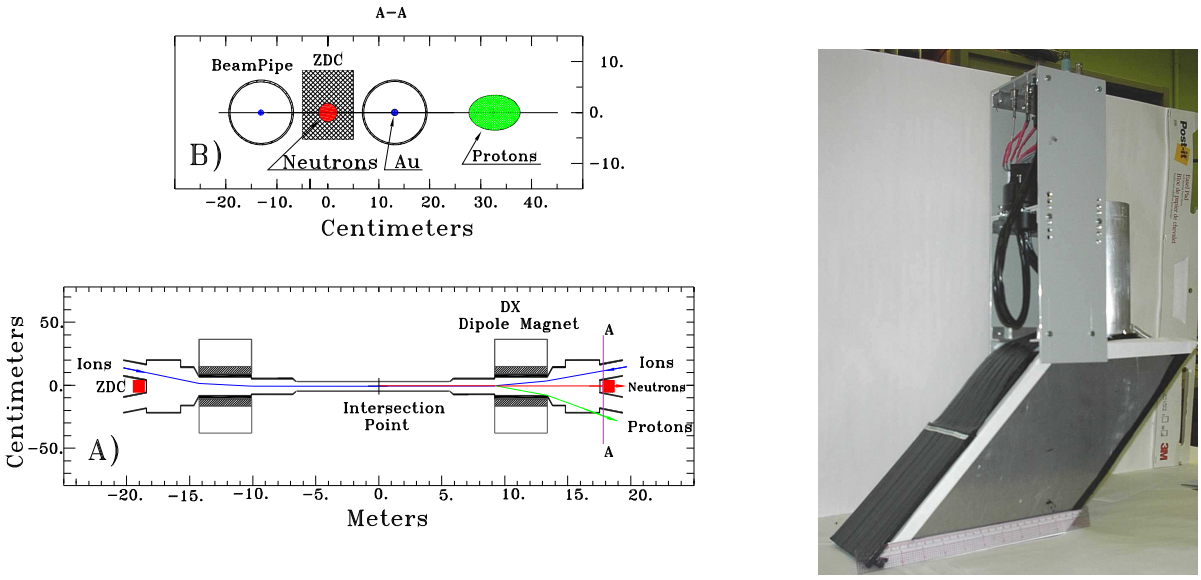

Figure II.3: The ZDC detector. Top left: A cross-section perpendicular to beam axis, showing where projectiles of different nature arrive at the ZDC position (17 m from the center of PHENIX). Bottom left: A cross section along the axis, showing the position of the ZDC (red boxes at 18m). Right: View of the ZDC detector prior to installation.

resolution. The design goal was to have a cleanly resolved single neutron peak in peripheral collisions. This imposes $\frac{\sigma_E}{E} \leq 20\%$ at $E_n = 100$ GeV, because the natural spread of neutrons emitted by evaporation is around 10%.

The ZDC design consists of a stack of three 5 mm ($2\lambda_I$) thick tungsten absorber plates each followed by commercial grade PMMA[2] optical fibers to sample Čerenkov light emitted by high speed charged shower secondaries. Twenty optical fibers of 0.5 mm diameter are bundled together and glued to form a single ribbon-like structure sandwiched between the tungsten plates. The ensemble is installed at an inclination of 45° with respect to the beam direction (cf. Fig. II.3, right). This orientation was chosen to optimize the detection of the Čerenkov light emission from rapid (β close to one) secondaries, which forms a cone of 45° opening angle. The lower energy shower component has less aligned emission angle and is therefore suppressed. The light is collected by a 12 stage general purpose PMT from Hamamatsu (R329-2). The three fiber ribbons from one module are grouped together to fit the circular aperture of a single PMT with a radius of 39 mm. Seven fibers are pulled out from the PMT aperture and connected to an external LED flasher for PMT gain monitoring.

The ensemble was tested before installation using 100 GeV and 160 GeV proton beams with 1% energy spread. The energy resolution of $\frac{\sigma}{\sqrt{E}} = \frac{85.(\%)}{\sqrt{E(GeV)}} \oplus 9.1(\%)$ stable to within 1 cm from the edge of the calorimeter met the design goals at a satisfactorily large area around the zero degree beam spot.

[2]Poly Methyl MethAcrylate, $(CH_2 = C(CH_3)CO_2CH_3)_n$ or Acrylic is a kind of transparent plastic.

II.3.3 Event centrality determination

As discussed in Sec. I.2.1.1, the number of binary collisions and number of participants calculated for impact parameter based fractions of the total cross section under the Glauber model framework need to be linked to the experimentally determined centrality classes. For this purpose, one needs to identify experimentally measurable variables that have a monotonic dependence on the impact parameter, and categorize events according to these variables into equally populated portions. The BBC charged multiplicity measurement (Q_{BBC}), possibly coupled to the ZDC neutral particle energy measurement (E_{ZDC}), can play the role of such a variable. The BBC response is a monotonically decreasing function of the impact parameter, so it qualifies alone as a centrality classification variable. The ZDC response on the other hand is not monotonic with the impact parameter over the whole impact parameter range, and can only be used in conjunction with Q_{BBC} as centrality classification variable. There are two regions where E_{ZDC} is monotonic, depending on whether or not coalescence of spectator neutrons with protons to form light nuclei (deuteron and tritium mainly) is significant.

- From peripheral to mid central collisions: E_{ZDC} increases with decreasing impact parameter (increasing centrality). The reason here is that as the size of the nuclear overlap region gets larger, the number of spectator nucleons increases. But the density of spectator nucleons is not large enough for coalescence process to become important. Therefore the increase in spectator neutrons is directly reflected as an increase in E_{ZDC}. For extremely peripheral collisions, E_{ZDC}=0. In this domain, E_{ZDC} is positively correlated to Q_{BBC}.

- From mid central to central collisions: E_{ZDC} decreases with decreasing impact parameter (increasing centrality). The reason is that in this domain, the number of spectator protons and neutrons increases to a point where coalescence starts to becomes a dominant player. Even though more spectator neutrons are expected in more central collisions simply because the overlap region is larger, they can not be detected, since the composite nuclei they form are charged and therefore swept away from the ZDC acceptance, resulting in a decrease in E_{ZDC} as centrality increases. E_{ZDC} becomes anti-correlated to Q_{BBC}.

The dynamics of coalescence in central collisions is not very well understood. It can however be clearly demonstrated by the E_{ZDC} to Q_{BBC} scatter plot, shown in Fig. II.4 in arbitrary units. The positive correlation between Q_{BBC} to E_{ZDC} is visible in the range $0 < Q_{BBC} \lesssim 0.2$ and the anti-correlation in the range $0.3 \gtrsim Q_{BBC}$.

The slicing of the event population to determine centrality classes can be done in various ways. The simplest method is to rely on Q_{BBC} alone. Traditionally, the events are classified into percentiles. The events that fall into centrality percentile i are events with a measured Q_{BBC} that is contained between Q_{min} and Q_{max} whose values are fixed in such a way that[3]

$$\frac{\int_{\infty}^{Q_{min}} \frac{dN_{evt}}{dQ_{BBC}} dQ_{BBC}}{\int_{\infty}^{0} \frac{dN_{evt}}{dQ_{BBC}} dQ_{BBC}} = \frac{i}{100} \quad and \quad \frac{\int_{\infty}^{Q_{max}} \frac{dN_{evt}}{dQ_{BBC}} dQ_{BBC}}{\int_{\infty}^{0} \frac{dN_{evt}}{dQ_{BBC}} dQ_{BBC}} = \frac{i+1}{100}, \tag{II.1}$$

[3]The PHENIX BBC trigger efficiency covers only 92% of the total inelastic cross section, thus the division is in reality made into 92 equal parts instead of 100 equal parts.

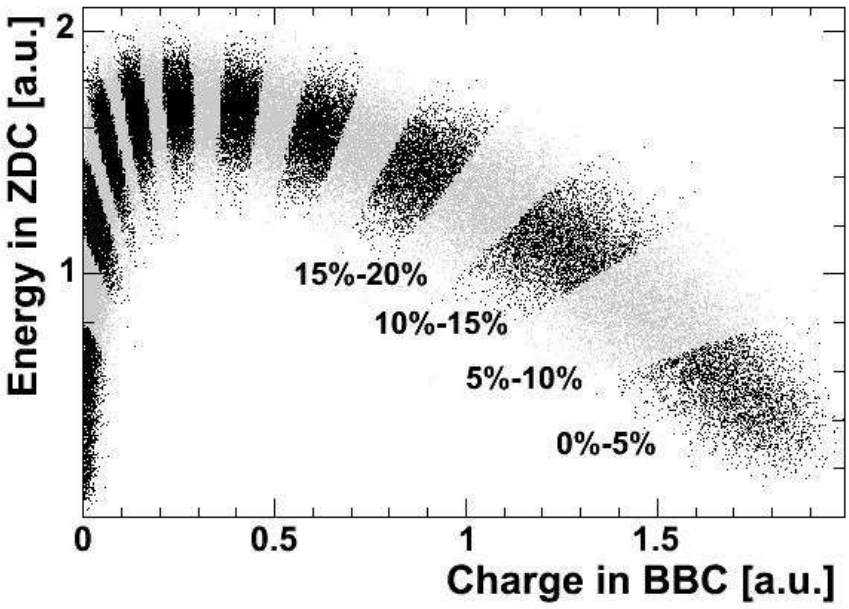

Figure II.4: Centrality classes in the E_{ZDC} vs. Q_{BBC} scatter plot. Alternating grey and black points are used to show the centrality classification into 20 groups. The most central events lie to the right of the plot, while the most peripheral ones lie to the left.

where ∞ is used in place of Q_{BBC}^{MAX} for readability. This procedure is equivalent to slicing the distribution shown in Fig. II.4 with 101 vertical bars in such a way that left (right) most bar lies at $Q_{BBC} = 0$ (Q_{BBC}^{MAX}) and equal number of events are contained between any two adjacent vertical bars[4]. Alternatively one can involve E_{ZDC} in defining the centrality classes. The classification is done in a similar way as in the case of the Q_{BBC} based classification (Eq. II.1), except that here, the variable Q_{BBC} is replaced by an angle α defined on the Q_{BBC} vs E_{ZDC} plane with the center ($Q_{BBC}^{CENTER}, E_{ZDC}^{CENTER}$) fixed to some convenient place (usually the center of gravity of the data points is used). This method, named *centrality by clock*, corresponds to the slicing depicted in Fig. II.4 by alternating gray and black areas. The most central 5% class lies at the right most, and the centrality decreases going counter clockwise. From a technical point of view, both centrality by clock method and Q_{BBC} based method are equivalent, except that the centrality by clock method uses more experimental information than the vertical slicing.

II.3.4 Reaction Plane Detector

For the measurement of the azimuthal distribution of rare probes such as J/ψ with respect to the reaction plane, a reaction plane estimation with a very good resolution is crucial, in order to compensate for the large statistical error associated with the measurement of such probes. The main objective of the reaction plane detector (RxNP) is to provide the event by event reaction plane with a resolution sufficient for measuring the elliptic flow of rare probes.

[4]The PHENIX BBC trigger has an efficiency of 92% for inelastic ion–ion collisions. As such the subdivision is done into 92 equal centrality percentiles. The remaining centrality percentiles from 93% to 100% do not contain any events.

The RxNP [83] is a pair of ring shaped scintillator detectors with a segmentation of 12 in azimuth and 2 in the radial direction, placed on either sides of the interaction region, just behind the forward muon arm spectrometers. The basic unit (cf. Fig. II.5 A) is a trapezoid shaped scintillator slab perforated vertically by multiple light collecting optical fibers (approximately a fiber per cm). The collected scintillation light output is read by one photomultiplier (Hamamatsu fine mesh dynode photomultiplier) per slab. A fully assembled sector of the RxNP is shown in Fig. II.5 B. The inner ring of the RxNP extends from 5 to 18 cm whereas the outer ring extends from 18 to 33 cm. This geometry maps into a pseudorapidity coverage of $1.0 < \eta < 1.5$ and $1.5 < \eta < 2.8$ respectively. The position along the beam axis z is 38 cm $< |z| <$ 40 cm. The whole assembly is preceded by 2 cm thick lead absorber, which improves the resolution by creating charged secondaries (mainly electrons through conversion). The RxNPs are installed in front of the central arm magnets in the north and south arms, as shown in Fig. II.5 C, encircling the beam pipe.

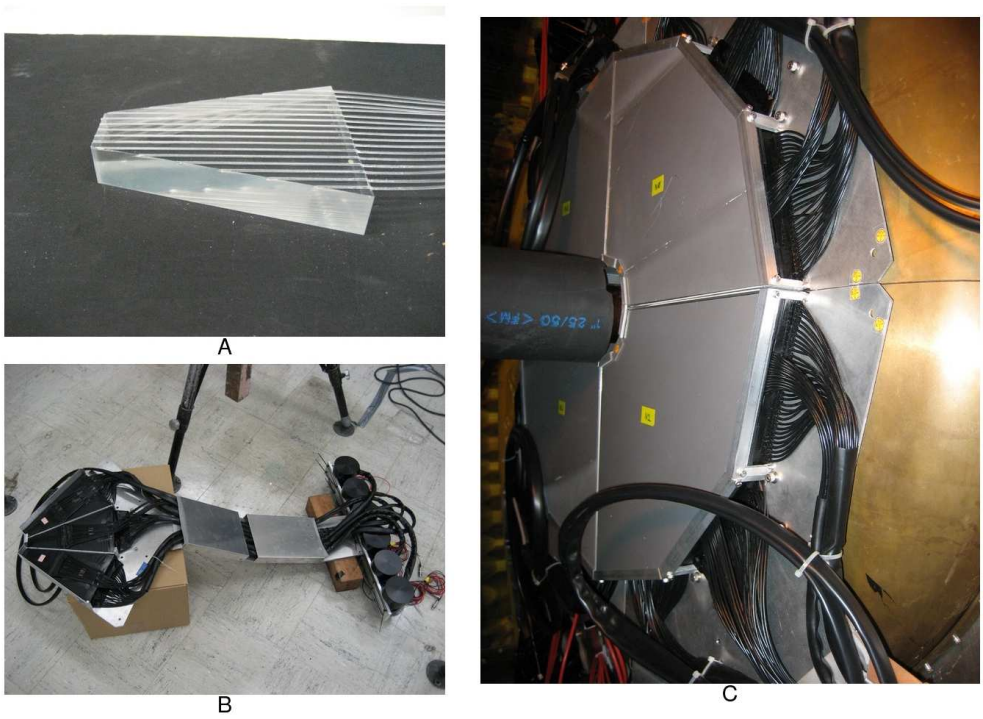

Figure II.5: RxNP detector (A) An uncovered scintillator slab - outer ring, with visible penetrating fibers (B) A fully assembled sector (three slabs) with photomultipliers (C) RxNP south fully mounted.

The reaction plane angle Φ_{RP} with coordinates (X,Y) in the plane normal to beam axis is estimated from the ADC readouts w_i of the photomultiplier attached to sector i through

$$(X, Y) = (\sum_i w_i \times \cos(n \times \phi_i), \sum_i w_i \times \sin(n \times \phi_i)) \quad \text{(II.2)}$$

where ϕ_i is the azimuthal position of the sector and n is the harmonic (for elliptic flow $n = 2$). The sum can run over all sectors or any group of sectors that form a closed loop in azimuth.

The measured azimuthal anisotropy (v_2^{mes}) of any particle is lower than its true azimuthal anisotropy (v_2^{tr}) because the measured reaction plane is smeared with respect to the true reaction plane. The values of v_2^{tr} and v_2^{mes} are related through the reaction plane resolution σ_{RP} by

$$v_2^{tr} = v_2^{mes}/\sigma_{RP}. \tag{II.3}$$

The reaction plane resolution can be estimated experimentally through the event average

$$\sigma_{rp} =< \cos(2 \times (\Phi_{RP,1} - \Phi_{RP,2}) >_{evts} \tag{II.4}$$

where $\Phi_{RP,1}$ and $\Phi_{RP,2}$ are reaction planes measured event by event using two statistically independent sets of tracks in each event, also called *sub-events*. This can be accomplished for example by fixing the sub-events to be tracks in different pseudorapidity ranges. Typically, this is done by comparing the north and south Φ_{RP} measurements $\Phi_{RP,N}$ and $\Phi_{RP,S}$.

The derivation of relations in Eq. II.3 and Eq. II.4 will be deferred to chapter 6. For now, it suffices to state that the better the resolution on the measurement of Φ_{RP}, the higher the value of σ_{RP} will be. The reason is that the typical difference of the measurements in the sub-events 1 and 2 diminishes as the resolution gets better, since both $\Phi_{RP,1}$ and $\Phi_{RP,2}$ tend to get closer to the true angle of the reaction plane. This pushes the value of the cosine closer to one. For infinite resolution, σ_{RP}=1, and σ_{RP} gets closer to zero as the resolution gets worse.

A worse resolution implies lower significance of the 'signal' that is being looked for in v_2 measurements, namely the amplitude of the modulation of the differential production rate of the particles with respect to the reaction plane ($\phi_p - \Phi_{RP}$, where ϕ_p is the azimuthal angle of the particle's momentum)

$$M(\phi_p - \Phi_{RP}) = \frac{dN}{d(\phi_p - \Phi_{RP})}(\phi_p - \Phi_{RP}). \tag{II.5}$$

Clearly, if the measurement of Φ_{RP} has a very poor resolution, the significance of true modulation of $M(\phi_p - \Phi_{RP})$ will be washed out in the measurement. In contrast, the significance of the modulation is kept intact if one can measure Φ_{RP} with infinite resolution. This loss of the significance of the modulation signal due to finite Φ_{RP} resolution will result in poorer statistical error in the extraction of the v_2.

The value of σ_{RP} is therefore an indicator of the statistical error to expect in the measurement of v_2. It is shown in Fig. II.6 for the BBC[5] and RxNP as a function of centrality. The resolution is best for mid central collisions, where the shape of the interaction region is most asymmetric. For more peripheral centralities, although the asymmetry of the initial interaction region remains high, the resolution starts to decrease because of the decrease in the charged particle multiplicity.

II.4 Central Arm Spectrometers

In this section, the Principal elements of the central arm spectrometer will be discussed.

[5]The measurement of Φ_{RP} by the BBC is possible, by using Eq. II.2, where the index i, instead of running over all sectors forming a closed loop, runs over any group of BBC PMTs that are uniformly distributed in azimuth.

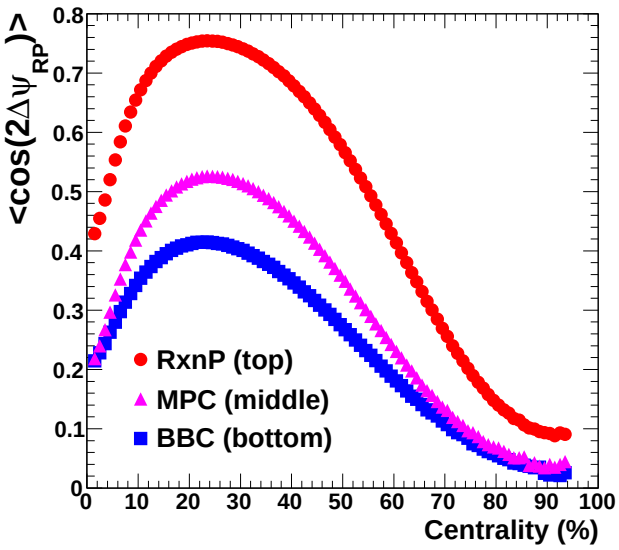

Figure II.6: RxNP reaction plane resolution compared to BBC reaction plane resolutions, as a function of centrality classes. The MPC (cf. Sec. II.4.7) can also be used to determine the angle of the reaction plane, with a resolution in between that of the BBC and the RxNP.

II.4.1 Magnetic field

Momentum reconstruction of charged particles requires a magnetic field. In the PHENIX central arm spectrometer volume, the magnetic field is generated by four water cooled copper coils contained inside warm carbon free steel frames [84]. These coils are wound around the beam axis as shown in the cut way view of Fig. II.7. The design was constrained by the following considerations.

- No material in the central arm spectrometer aperture. This precludes the use of a solenoid type coil that can generate an exclusively longitudinal field. On the other hand, it provides thick material (4.9 X_0) in the muon arm acceptance for hadron stopping.
- Uniformity at the level of 2 per mil in field integral mapping.
- Control over the radial field configuration, especially the possibility to have near zero field for small radius ($R \lesssim 50\ cm$), by polarizing the coils in opposite directions.
- Minimal field integral outside the tracking region ($\gtrsim 2\ m$), to avoid interference with outer detectors.
- Easily movable for maintenance and access.

The requirement on the possibility of having minimal field at small radius is satisfied by the ability to reverse the polarity of the two magnet coils. Fig. II.8 shows the longitudinal component of the magnetic field as a function of radial distance for three configurations : + where only outer coil is switched on (Outer, diamond markers in Fig. II.8), ++ (when both coils are switched on and have the same polarity (Outer+Inner, square markers in Fig. II.8), and +− where the coils are polarized in different directions (Outer-Inner, triangular markers

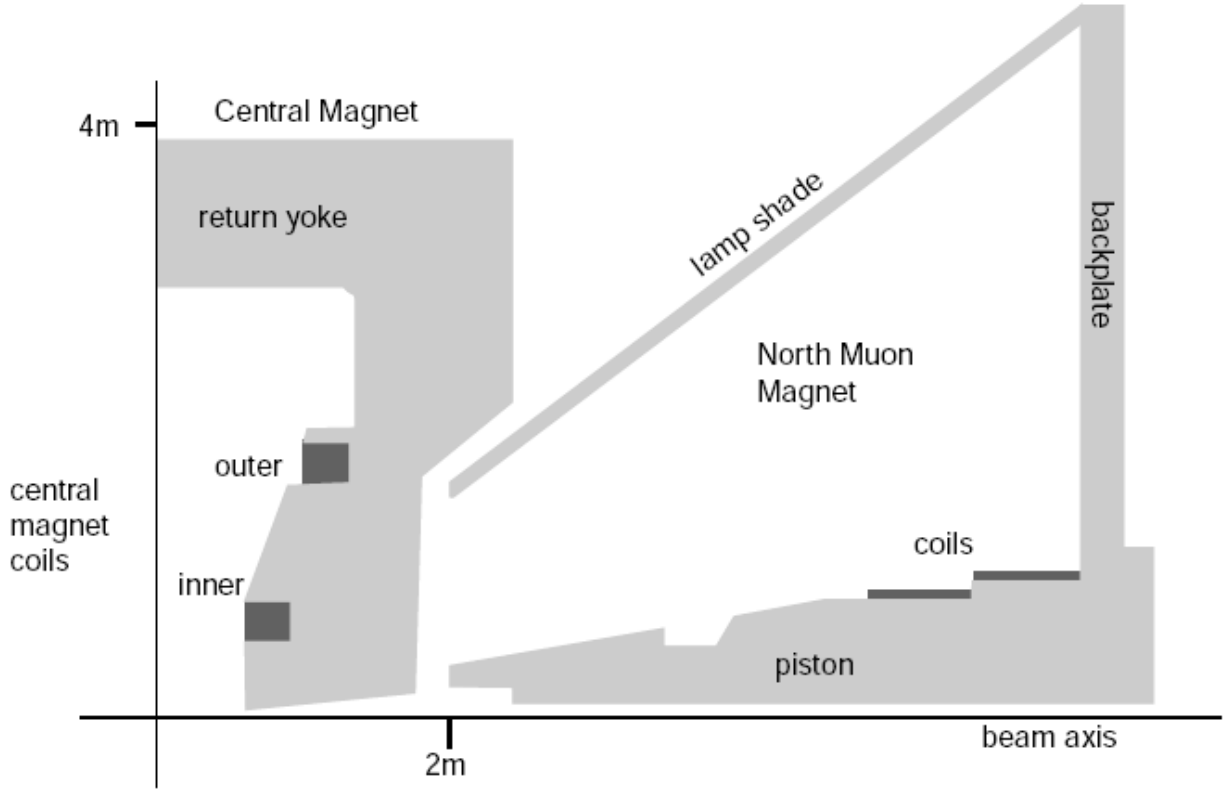

Figure II.7: Cut way quarter view of the PHENIX magnet system.

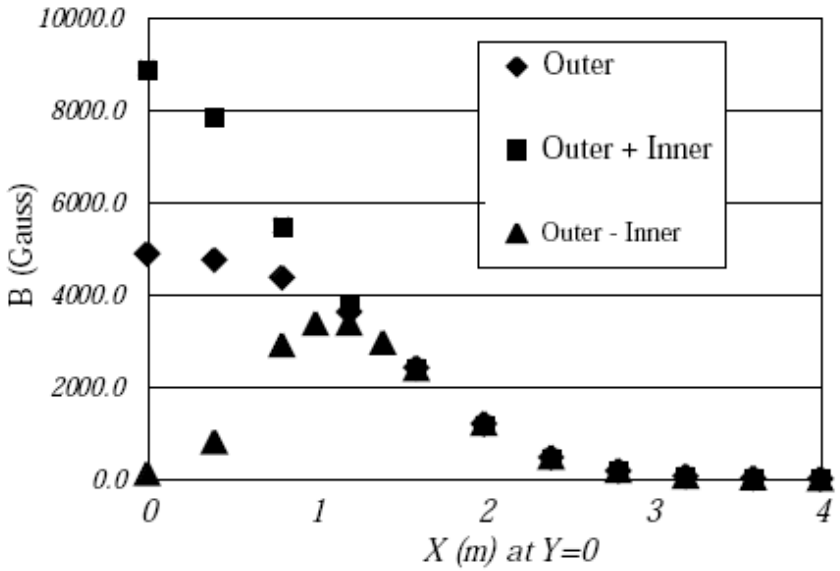

Figure II.8: The longitudinal component of the magnetic field as a function of radial distance for three configurations of the polarization in the inner and outer coils.

in Fig. II.8). The last configuration satisfies the need to have a small field amplitude near the interaction region. The field intensity in this configuration is lower than 1500 G as far out as $R = 50$ cm. It was used for the 2007 running period where a new hadron rejection detector called the Hadron Blind Detector (cf. Sec. II.4.6) was installed for the first time. This detector requires almost zero field to achieve good performance.

The field map calculation is done using a surface mapping technique. Hall probes are used to measure a single field component over a closed surface containing the useful volume that needs to be mapped. The field values inside the volume are calculated from a Green's theorem that relates the surface potentials to the field inside the volume.

II.4.2 Drift Chamber

Two multi-wire focusing drift chambers (DC) [85, 86] serve as the main tracking devices of the PHENIX central arm spectrometers, by providing hit positions as inputs for global tracking. The DCs are located at a radial distance of 2 m from the beam axis, one in each arm, and covering 90° in azimuth – $34° < |\phi| < 124°$ (recall Fig. II.1, p. 40). The total thickness in the radial direction of the DCs is about 50 cm, with a length of 1.8 m in the beam axis direction. A picture of a fully assembled DC is shown in Fig. II.10, together with the pad chamber (cf. Sec. II.4.3). This maps into a pseudo-rapidity acceptance of $|\eta| < 0.35$. Each drift chamber is split at $z = 0$ along the beam axis into two sections, called north and south sides, with independent readout electronics for each side. The mount frame in the shape of a truncated barrel is made of titanium, and covered with a Mylar (a type of polyester film) window to define the gas volume filled with a mixture of argon and ethane. The titanium frame is fitted with plates (called keystones) for wire attachment on the extreme ends. The left side of Fig. II.9 shows the geometry of a keystone. One DC edge holds 20 keystones, each covering an azimuthal angle of 4.5°.

On each keystone, a set of four parallel *anode* (or *sense*) wire nets and four matching *cathode* wire nets are soldered at a separation of ~ 2 cm. Another set of wires, called the *back*, *gate*, and *field*, are soldered very close to the anode wires. The space delimited by two cathode wire nets on either side of an anode wire net is called the *drift cell*. The arrangement of wires inside a drift cell is shown on the right side of Fig. II.9. Each anode wire is surrounded by a gate wire on one side and a back wire on the other, whereas a field wire is placed in between each anode wire. The wires nets are grouped into six radially stacked layers (cf. Fig. II.9 left). Two of the layers (X1 and X2, each with 12 anodes) run parallel to the beam axis, and provide high precision hit position measurement in the r-ϕ space, crucial for transverse momentum measurement. The U1,2 and V1,2 wire layers, each with 4 anodes, are mounted at a 6° stereo angle with respect to the beam axis, achieved by soldering them on keystone that are displaced by one unit from one side to the other of the titanium frame.

The high voltages of the different types of wire within a drift cell are chosen to create a well defined and localized charge collection 'alley' for each anode wire. When a charged particle passes through the drift cell, it leaves an ionization trail. The electrons dislodged from the ions drift towards the anode wire if they are created on the 'gate' side of the anode wire, whereas they are stopped from arriving at the anode wire if created on the 'back' side. The charge collection side (the 'gate' side) of the anode wires alternates from left to right as one goes outwards from the inner most anode wire (cf. Fig. II.9, right). This configuration allows to avoid left/right ambiguity, which would result if charges ware allowed to arrive on

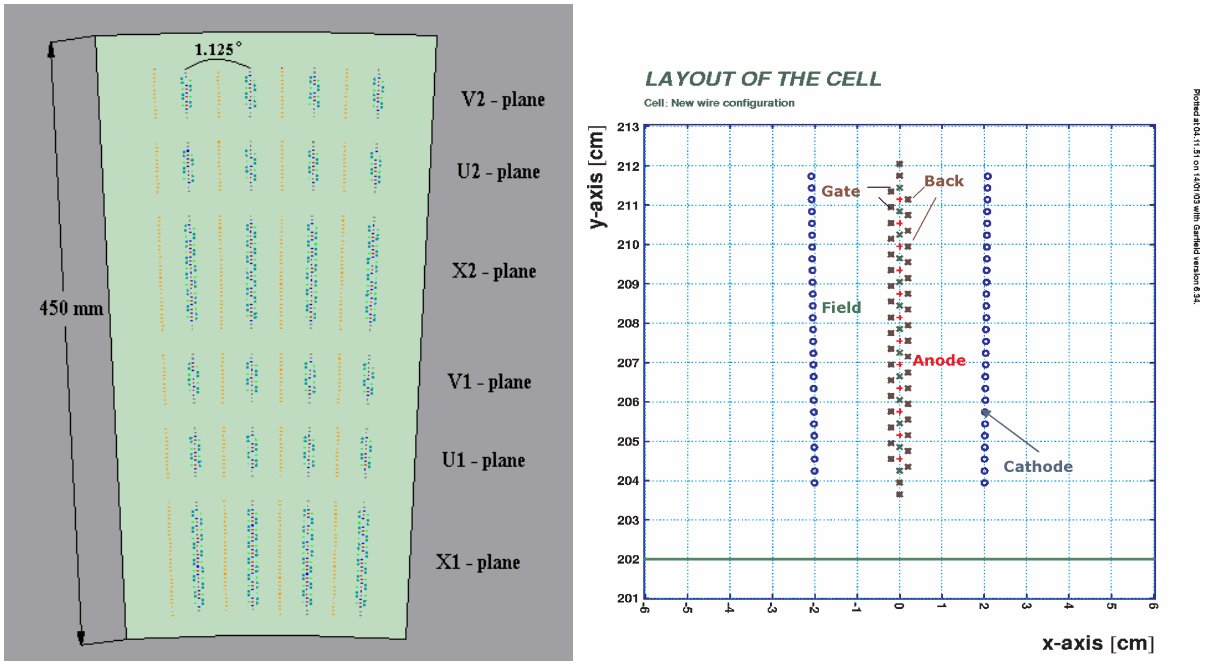

Figure II.9: A drift chamber keystone. Left: Placement of the X,U and V planes in a cell. Right: Wire arrangement inside a drift cell.

the anode wires from both sides[6].

Signal preamplification is achieved by creating a very strong electric field ($\approx$ 10 kV/m) between the gate and anode wires (with additional contribution from the field wires). The strong field stimulates the creation of electron avalanche when the primary electrons arrives at the gate level. The amplified electron signal is read out by an Analog Shaper Discriminator (ASD) that can digitize the time of arrival of the leading and trailing edges with a sampling of 0.8 ns. The time difference between the two edges is used to reject noise hits with too narrow pulses. The leading edge time t of the hit is used to calculate the distance of the ionization trail from the anode wire through $x(t) = V_{dr} \times (t - t_0)$. Here V_{dr} is the average drift velocity, and t_0 is the time at which the track produced its ionization trail. The resolution on the distance x for the X wire planes is $\sim$ 1.5 mm. This translates to a z position resolution from the U and V wires of 2 mm.

The values of V_{dr} and t_0 are determined from the time distribution of all recorded hits in each drift chamber arm. This distribution is shown in Fig. II.10 on the right, in units of the ASD bins (0.8 ns). It is characterized by a leading edge, composed of hits by tracks that pass very close to the anode wires and a trailing edge from hits by tracks that pass the farthest possible from the anode wires, meaning, close to the cathode wires[7]. The value of t_0 is estimated by the characteristics time of the leading edge, where as the difference between

[6]In the rare cases where a track passes right in the middle of gate and back wires, this mechanism of left/right disambiguation does not work, and a signal is produced on all anode wires regardless of the orientation of their gate/back wires. In such cases, the tracking algorithm ends up with a false track which is a mirror image of the true track that actually generated the hits. This is one of the mechanisms by which a 'ghost' track can be created.

[7]The excess at the leading edge is due to the double counting of tracks that pass between the anode and the gate wires, where left/right disambiguation mechanism does not work.

the characteristics times of the leading and trailing edges is used to calculate the average drift velocity through $V_d = \frac{<dist>}{t_0 - t_1}$, where $< dist >$ is the distance between the anode and cathode wires. The leading and trailing edges' characteristic times are estimated by the time at half height of the error function fit ($(1 + exp(\frac{t-t_0}{\Delta T})^{-1})$ to the edges.

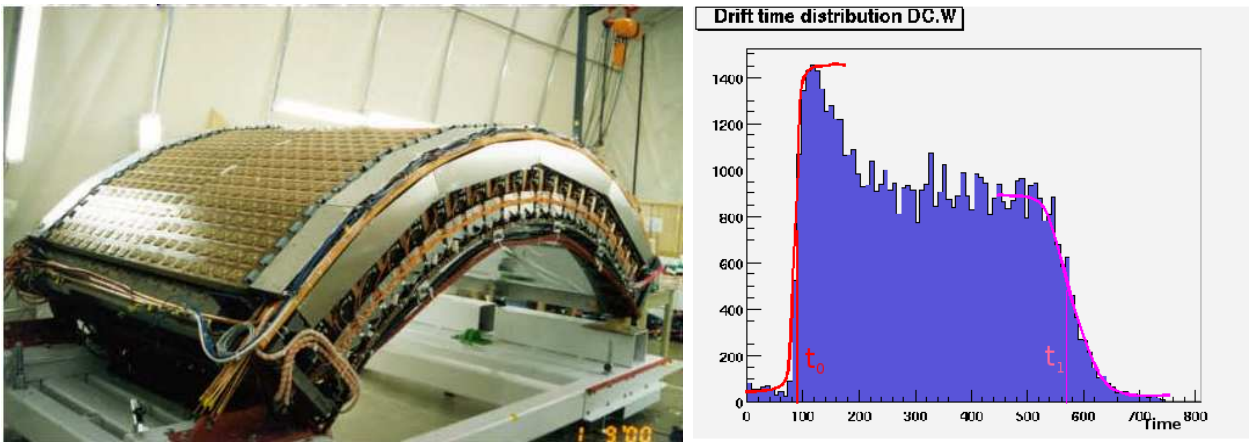

Figure II.10: Left: The DC and PC detectors. The PC, visible on the upper surface in this picture, uses the DC titanium frame as mechanical support. Right: ADC distributions of recorded hits in the DC.

II.4.3 Pad Chamber

The pad chambers (PC) [86] are multi-wire proportional chambers with cathode pad read out segmented into a pixel array. There are three PC layers. The inner most layer (PC1) lies at 2.5 m immediately after the DC, using the later as physical support (cf. Fig. II.10). The z direction hit position measurement by the PC1 at the DC exit provides information to fix the last missing component of the three dimensional momentum vector (p_z). PC2 and PC3 lie immediately before the RICH (cf. Sec. II.4.4) and EMCal (cf. Sec. II.4.5) at radii of 4 m and 5 m respectively.

The PC system assists in track hit association to the EMCal and RICH by fixing space points in 3D. Since the three PC layers reside outside of the magnetic field, the space points that they provide for each track follow a straight line. The PCs also provide charged particle veto for photon identification in the EMCal and serve in the fast track reconstruction algorithms for high level triggers.

The PCs are made up of a layer of anode and field wires sandwiched between two boards enclosing the avalanche multiplication gas region (Fig. II.11). The boards must be hard, and mechanically self supporting surfaces. To this end they were fabricated from honeycomb sandwiched between FR-4[8] layers. The surfaces of the boards are clad with a copper layer whenever they are part of the PC electrical system. The cathode pixel structure is etched on the anode facing side of the outer board. The other side of this board is used to attach read out cards. As such it must provide a good ground, and therefore, this surface is also completely covered with a copper layer. The honeycomb on the outer board is perforated to let through kapton cables from each pixel to the read out cards. The inner board is covered

[8]Fire Resistant 4, same material used for most Printed Circuit Boards.

with copper only on the anode facing side where it serves as a cathode plane. The opposite surface of the inner plane is free as it does not have any electrical function.

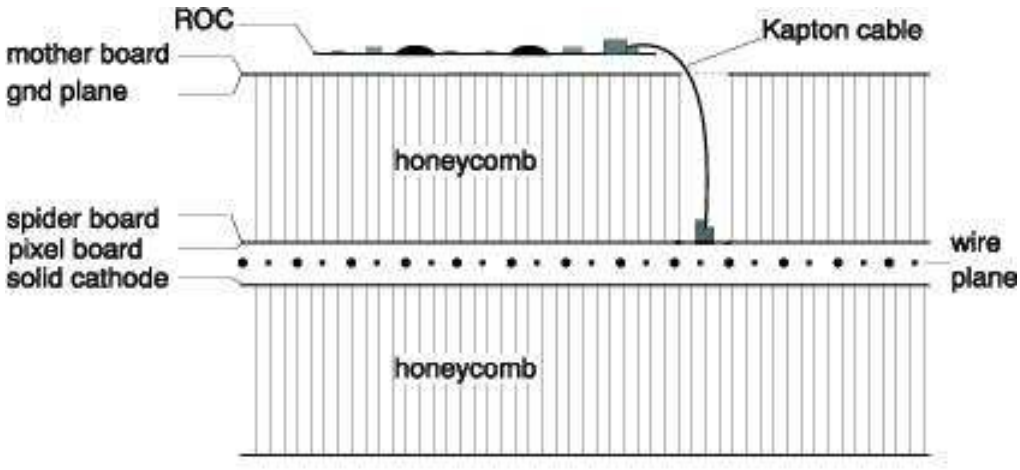

Figure II.11: Pad chamber wafer (not to scale).

The cathode pixel structure on the upper board is shown in Fig. II.12. On the left side of the figure, a *pad* that is connected to one readout channel is shown. A pad is made up of nine interconnected rectangular areas called *pixels*. Three layers of pads are superimposed in the interleaved fashion shown on the right side of Fig. II.12 in such a way as to cover the whole area. A set of three pixels coming from contiguous pads form what's called a *cell* (shown as a dark area in the middle of Fig. II.12).

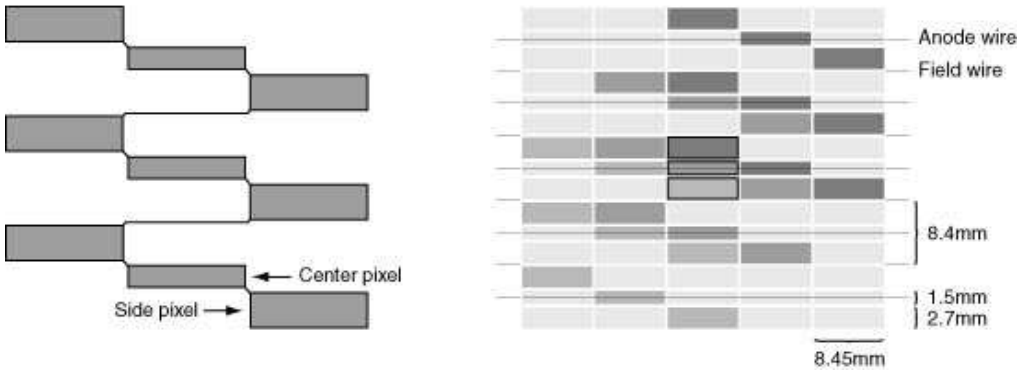

Figure II.12: Pad chamber pad-pixel-cell structure.

When a charged particle passes through the gaseous medium, the electrons from the avalanche it creates are collected by the anode wires whereas the positive ions are collected by the pads to form the signal. Given the cell structure, a single avalanche triggers signal on three pads. The cell position at which the track passed is then localized by the coincidence on the three pads that have fired.

This rather complex choice of pixelization reduces by a factor of three the number of read out channels required as compared to a conventional square shaped pixel structure for the same resolution. The reason is that nine square shaped pixels of the size of a cell are needed

in the conventional pixelization scheme to cover the same area as that covered by three pads in the pixelization scheme used by the PCs. At reconstruction, one only needs to convert pad clusters into a cell list, and once this conversion is done, the rest of the pattern recognition is exactly the same as if conventional pixelization was used.

II.4.4 Ring Imaging Čerenkov

The primary electron/hadron identification is provided within PHENIX by the Ring Imaging Čerenkov (RICH) detector [87]. The principal design goals during the construction of the RICH were to maximize the dynamical range of electron/pion identification and minimize material in the acceptance. A cut-through view of the resulting design is shown in the horizontal cross section schematics of Fig. II.13.

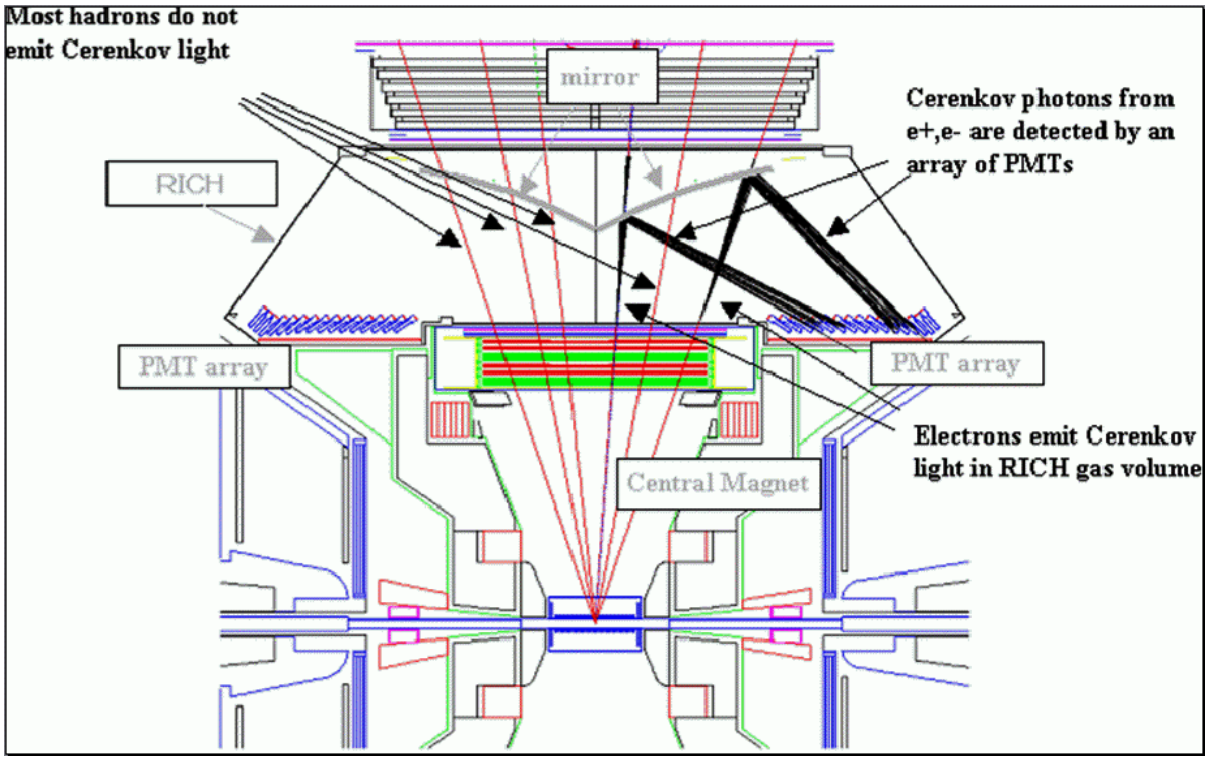

Figure II.13: Schematic cut-through view of the RICH detector.

The RICH entrance windows (just after the drift chambers, depicted as alternating red and green lines in the middle of Fig. II.13) have a surface area of 8 m^2 and are positioned at a radial distance of 4 m from the interaction region. They cover a pseudorapidity range of $|\eta| < 0.35$. The space between the entrance window and exit window contains only the radiating gas and a pair of intersecting spherically shaped mirrors (focal radius of 401 cm) and its supports (grey curves inside the trapezoidal volume of the RICH). The mirrors reflect Čerenkov light produced by tracks going faster than the speed of light in the radiating gas back to the photomultipliers (Hamamatsu H3171) placed on each side of the entrance window. The 1280 photomultipliers are fitted by 2" Winston cones (that serve for concentrating incoming light thereby improving light collection efficiency), and shielded from magnetic fields to be operational up to 100 G. The whole support structure and substrate of the mirrors is made

of ultralight Rohacell foam core and thin carbon fiber epoxy coating, with the objective of making the interaction length inside the acceptance as small as possible. The mirror surface is made from bare aluminium, whose reflectivity is not affected much through oxidation at wavelengths above 200 nm. The whole ensemble results in a radiation length of only 2%.

The mechanism of identification in this detector exploits the threshold effect in the creation of Čerenkov radiation in a medium with index of refraction $n > 1$. When a relativistic particle with speed $\beta > n^{-1}$ crosses such a medium Čerenkov light is emitted with an emission angle of $\theta = acos((\beta n)^{-1})$ and yield proportional to the light propagation length L and $sin^2\theta$.

Thus a charged particle with a speed β less than n^{-1} will not emit any Čerenkov radiation which translates to a critical momentum (emission threshold) given by:

$$p_c = m\gamma\beta = m \times n^{-1} \times \frac{1}{\sqrt{1-n^{-2}}} = \frac{m}{\sqrt{n^2-1}} \tag{II.6}$$

where m is the mass of the particle. A radiator of refractive index n can thus be used to separate electrons from charged pions by the detection of Čerenkov light, since only electrons emit in the range $p_{c,e} < p < p_{c,\pi}$.

In PHENIX, the 40 m^3 internal gas volume is filled with carbon dioxide (CO_2). The refractive index of CO_2 results in a momentum threshold value for Čerenkov emission of $p_{c,\pi} \approx 4.65$ GeV/c for pions, and $p_{c,e} \approx 0.2$ GeV/c for electrons. The photon yield is ~ 12 for the typical path length of ~ 1.2 m traversed in the RICH gas volume by the almost straight moving electrons whose momenta are in the range between $p_{c,e}$ and $p_{c,\pi}$, while the typical Čerenkov ring diameter corresponds to ~ 8 cm.

II.4.5 Electromagnetic Calorimeter

The PHENIX Electromagnetic calorimeter (EMCal) [88] is the outer most detector of the central arms (very top of Fig. II.1, p. 40). Its main objective is to provide energy and spatial position measurements for electromagnetic showers, allowing the EMCal to play an important role in electron identification. Due to a deliberately light construction ($\sim$18X$_0$ of radiation length) hadrons more energetic than 200 MeV do not deposit the totality of their energy in the EMCal. A comparison of the energy measurement E from this detector with the momentum measurement p from tracking can thus be used as a tool to enhance hadron rejection. This aspect will be discussed in more detail in Sec. IV.3.

The EMCal covers the full geometrical acceptance of the PHENIX central arm detector, $|\eta| < 0.35$ and $34° < |\phi| < 124°$ with respect to the vertical axis, in each arm. It starts from a radial position of 5.10 m. The EMCal is arranged in eight sectors (each with $\Delta\phi$=22.5°), of which there are four in each arm referred to as E(0-3) and W(0-3) for east and west respectively going from top to down. The sectors are arranged in a non projective geometry. Two different technologies are used to characterize electromagnetic showers. The two lower sectors of the east arm, E0 and E1, called Lead Glass (PbGl) are Čerenkov based sampling detectors whereas the rest E2, E3 and the four west arm sectors referred to as Lead Scintillator (PbSc) are sampling calorimeters based on scintillation (recall Fig. II.1, p. 40).

Lead Glass calorimeters

The PHENIX PbGl system is a Čerenkov emission based calorimeter that was recovered from the CERN experiment WA98 [89]. The basic building blocks are a 51% lead oxide doped glass

rods with the dimension of 4x4x40 cm^3 fitted at one end with FEU-84 photomultiplier for light readout. These modules are wrapped with an aluminium mylar foil, and glued together in groups of 24 modules (4x6) using carbon fiber and epoxy resin. This ensemble forms mechanically self supporting structures called *super modules*. Each super module is caped with a gain monitoring system on the front side (the side with no photomultipliers fitted).

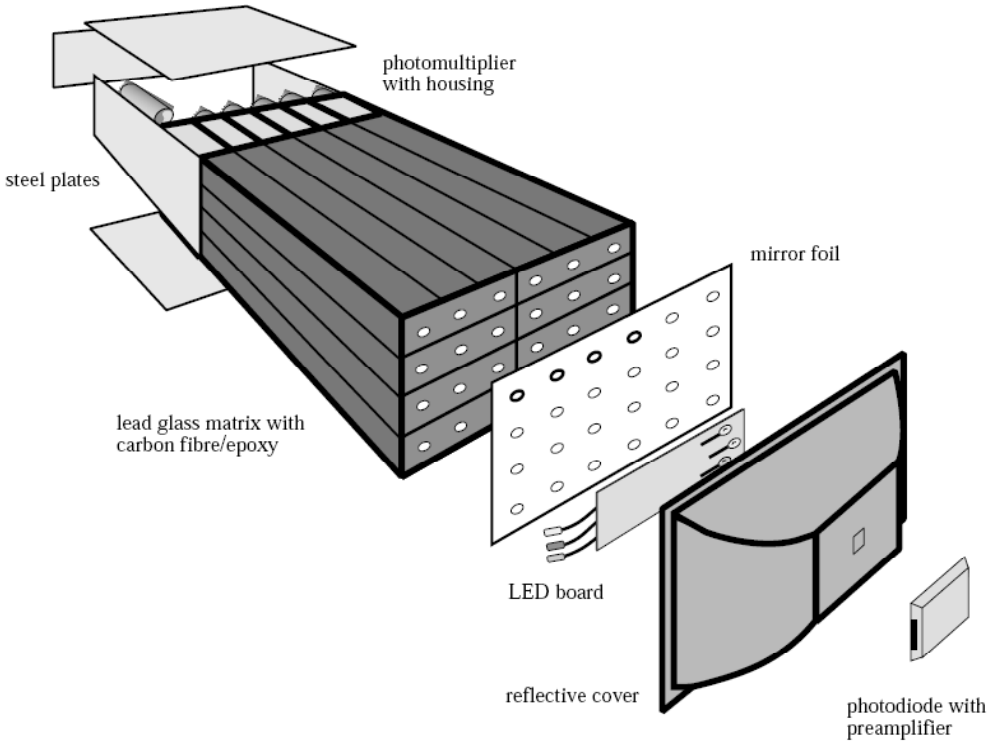

Figure II.14: A detailed view of a lead glass super module.

The gain monitoring system (bottom right on Fig. II.14) consists of a led board with a reflective cover that concentrates the light from the photodiode into the entry holes left at the end of the rods[9]. A photodiode with preamplifiers is fitted at another hole at the top of the reflective cover, and serves as a control detector of the test pulses absolute light yields. At the back end, a 2×3 super module group (144 modules) is read out with a single FEE motherboard.

The measured energy resolution from this detector fits the parametrization

$$\sigma(E)/E = \frac{[5.9 \pm 0.1]\%}{\sqrt{E(GeV)}} \oplus [0.8 \pm 0.1]\% \tag{II.7}$$

whereas position resolution is given by the parametrization

$$\sigma_x(E) = \frac{[8.4 \pm 0.3]\ mm}{\sqrt{E(GeV)}} \oplus [0.2 \pm 0.1]\ mm. \tag{II.8}$$

[9]The calibration LEDs have to be operated at high injection current to get stable enough output. The aluminum foils are used to limit the amount of light that reaches the lead glass rods, to avoid saturating the PMTs.

Lead scintillator calorimeters

The basic unit of this detector, called a module is constructed from four towers (Fig. II.15). A tower is a stack of 66 cells, each made of 1.5 mm lead absorber followed by a 4 mm thick polystyrene[10] based scintillator block.

The cross section of a tower (shown in Fig. II.15) is 5.25x5.25 cm^2, with through holes at a spacing of 8.6 mm. These through holes are penetrated by sampling wavelength shifting optical fibers that also serve mechanically by ganging together the cells in a tower. This scintillator has its emission peak at 420 nm (blue), with a time constant of 3.5 nm and the fibers shift that to a peak emission at 500 nm (green).

The contact surfaces between the towers within a module are plated with aluminium to obtain optical isolation. The light collected by the fibers is read out by 30 mm phototubes attached at the back of the tower.

A 6x6 arrangement of modules is put together by attaching them to a backbone and covering them on the side by a welded stainless steel cage. This structure is called a supermodule, and eighteen (3x6) supermodules make up a sector with the dimension of 2x4 m^2. Four sectors are arranged in a non projective geometry (normal to direction of arrival of particles), to form the West arm calorimeter wall. This gives a total number of 15552 towers.

The 2592 towers per sector that result have each one a photomultiplier tube (FEU115M), that was chosen due to its linear response up to peak output current (100 mA) and a very fast rise time of 5 ns, corresponding to the triggering needs of the EMCal. The signal from this photomultiplier is read out, preamplified, discretized and discriminated by a FEE module similar to the one used for the PbGl.

For gain fluctuation measurement, an Nd-YAG laser beam is split and delivered to each module through a fiber that passes at the center of the module between the four surrounding towers. This fiber is grated in such a way that the light going out of it imitates the depth and profile of scintillation light created by a 1 GeV electromagnetic shower.

After corrections, the energy resolution was measured to be

$$\frac{8.1\%}{\sqrt{E(GeV)}} \oplus 2.1\%. \tag{II.9}$$

The position resolution at incidence angle θ can be parametrized by $\sigma_x(E,\theta) = \sigma_0(E) \oplus \Delta \times sin(\theta)$, where $\Delta \approx L_{rad}$ and the normal incidence position resolution is given by

$$\sigma_0(E) = 1.55mm \oplus \frac{5.7mm}{E(GeV)}, \tag{II.10}$$

The non projective geometry is motivated by the need for avoiding the additional sin(θ) term.

[10]Polystyrene granules are heated molded with small percentage (∼1%) of wavelength shifting colorants POPOP = p-bis[2-(5-Phenyloxazolyl)]-benzene. and p-tetraphenyl).

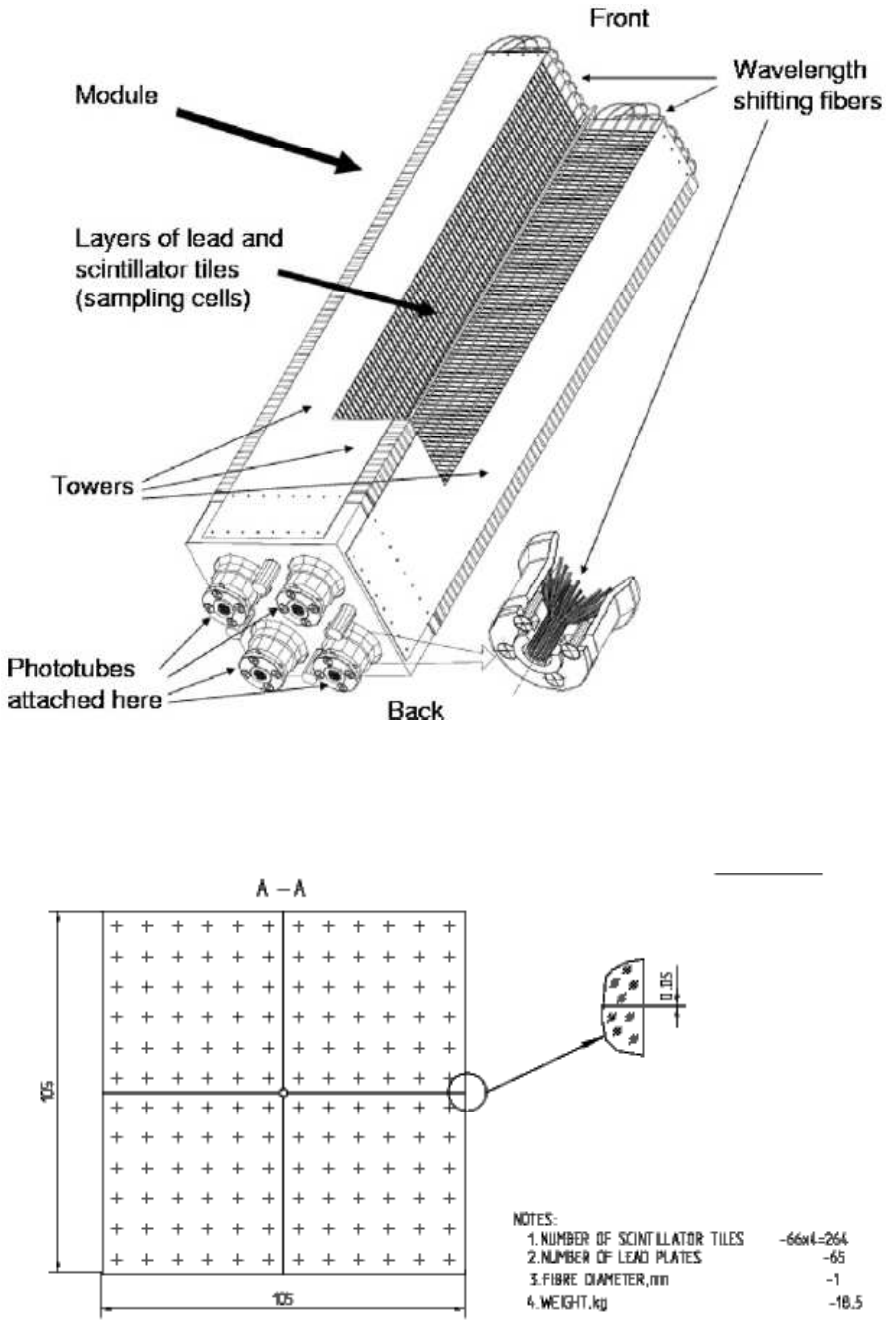

Figure II.15: PbSc calorimeter module (A) Crosscut interior view (B) Cross section view of scintillator layer.

II.4.6 Hadron Blind Detector

The hadron blind detector (HBD) [90] is designed to improve the rejection of Dalitz decays of light hadrons and conversion from the low mass dielectron spectrum, especially in heavy ion collisions. This would allow one to have a good signal to background ratio for the signal from light hadron dielectron decay, which allows to study the effect of a hot QGP medium on the mass and width of light hadrons. The HBD exploits an important distinction between Dalitz/conversion dielectrons and light hadron decay dielectrons. Due to their photonic origin, dielectrons from Dalitz/conversion have a much smaller opening angle than those from light hadron decays. With an appropriate choice of the granularity of the readout, the spatial proximity of small opening angle electrons can be made to translate into a larger signal deposition on a single cluster by Dalitz/conversion pairs than by single electrons. Unfortunately, the abundance of light hadrons (pions and kaons) created in heavy ion collisions can lead to coincidental spatial proximity of two light hadrons or a light hadron with an electron. The task of Dalitz/conversion dielectron rejection will therefore be significantly facilitated if the detector can somehow suppress the signal from the ionization trail of hadrons. That is why the detector has to be 'blind to hadrons'.

The design of the HBD, motivated by the above mentioned objectives, is as follows. The main element of the detector consists of a stack of three GEM (Gas Electron Multiplier) layers (cf. schematic illustration in Fig. II.16, left) separated by 1.5 mm, and enclosing a Čerenkov radiating gas volume. The Čerenkov photons generated by fast electrons in this volume is converted into photoelectrons by a 0.2-0.4 μm layer of CsI coated on the surface of the top most GEM layer. The GEMs are constructed from two thin layers of copper (5 μm) separated by an insulating material layer (50 μm), the ensemble perforated with mesoscopic holes of 60-80 μm diameter separated by 140 μm. This geometry allows to have a huge electrical field inside the holes with a relatively small potential difference between the copper layers, and therefore a comparatively small electric field outside the holes (cf. schematic illustration in Fig. II.16, right). Avalanche creation is therefore stimulated only inside the holes, avoiding spatial dispersion of the signal.

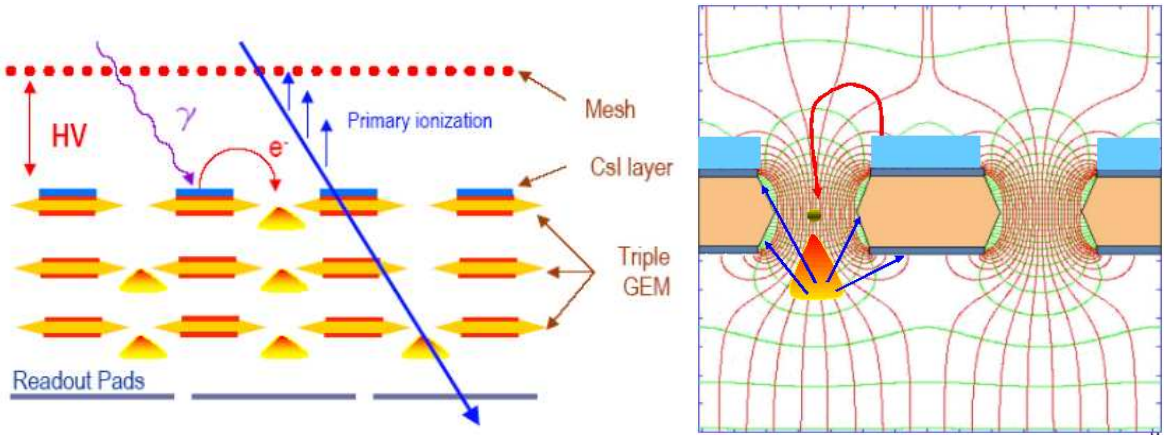

Figure II.16: Left: Working principle the HBD triple GEM stack. Right: Electric field density around a GEM hole.

The two successive layers of GEM collect the electrons from the avalanche in the previous layer and amplify the signal in a similar manner. The signal from the last GEM layer is

collected by hexagonally shaped pads (cf. schematic illustration Fig. II.17, left), etched on a PCB board that carries the readout electronics on the other side, and placed 1.5 mm behind the last layer of GEM. With this configuration alone, electrons from the ionization trail of hadrons inside the Čerenkov radiating gas can mimic the photoelectron signal from the CsI. To stop primary ionization trail electrons from reaching the CsI layer, a wire mesh is placed 1.5 mm above, and biased to create an electric field that pulls electrons away from the GEMs (cf. schematics in Fig. II.16, left). In this configuration, the signal that reaches the pad readout comes exclusively from photoelectrons dislodged from the CsI coating on the front layer of the stack. This high voltage configuration is called reverse biasing, in contrast to forward biasing, where electrons from the ionization trails in the gas volume are allowed to reach the GEM stack, and which by consequence is not 'blind' to hadrons. For the Čerenkov radiating medium, pure CF_4 was chosen for its high pion threshold of ~ 4.8 GeV/c.

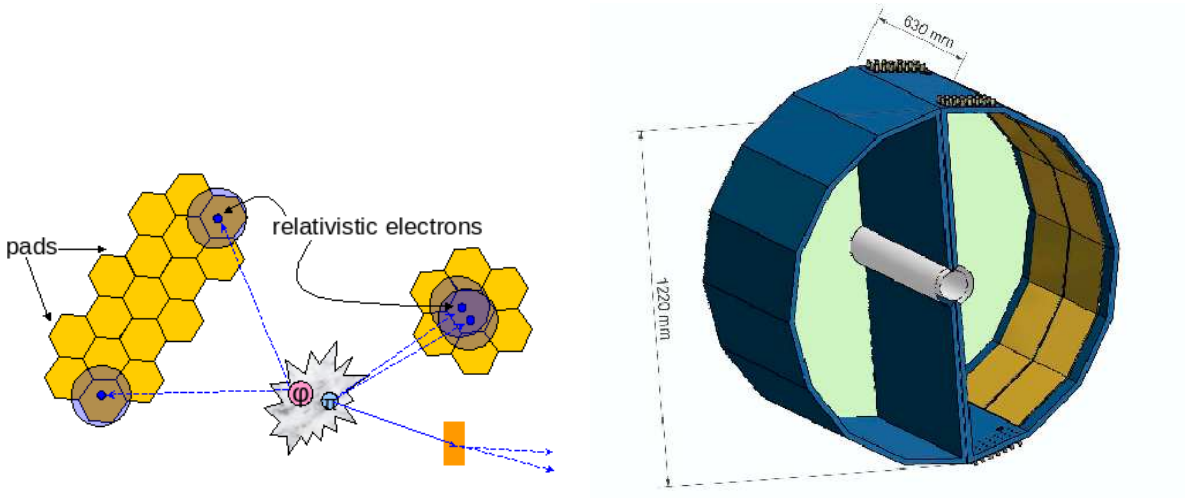

Figure II.17: Left: The hexagonally shaped pad read out. Small opening angle electrons make similar cluster to a single electron but the total photoelectron count is larger for two electrons. Right: The HBD support structure and CF_4 containment vessel.

The GEM stack plus mesh and readout units are prepared in a rectangular format with the dimension of 23×27 cm^2. Twenty four of them are placed on a FR-4 circular frame of radius 60 cm, shown on the right side of Fig. II.17, with a segmentation of two along z and six along ϕ in each arm. The frame also serves as a leak proof vessel for carrying the Čerenkov radiation gas. The vessel is designed to fit into the PHENIX acceptance interior to the DC, and encircling the beam pipe. The azimuthal coverage of the active surface is almost complete (135° per arm) except for the small region (on the top and bottom in Fig. II.17, right) that can not be instrumented for mechanical support and electronic servicing. The rapidity coverage is slightly larger than other PHENIX detectors ($|\eta| < 0.45$).

As discussed above, the HBD has the potential to improve very significantly the signal to background ratio at the low mass end of the dielectron spectrum by rejecting small opening angle dielectrons from Dalitz decays and conversion. It must be noted that conversions that occur beyond the first GEM layer (after the CsI surface) can not be rejected by the HBD, since they do not leave a signal. Besides, for the reverse bias hadron rejection to function, the HBD must lie in a very low magnetic field region, that can be achieved by using the $+-$ configuration for the central arm magnet coils (cf. Sec. II.4.1). However, around the J/ψ

mass window, where the signal to background ratio is not as poor as at the low mass region in the absence of the HBD, the Dalitz/conversion rejection that a fully functional HBD offers is just enough to counterbalance the resolution loss due to smaller magnetic field and multiple scattering.

The HBD was put into the PHENIX acceptance for the first time during the run 7 data taking period, and suffered a number of unexpected difficulties. Part way into the run, the west arm HBD was removed from the acceptance due to high voltage failure, while the east arm HBD was kept in, with the magnetic field still in the +− configuration. It was discovered late into the run that the data from HBD east was not exploitable either, due to an excessive background signal created by photons coming from scintillation inside the CF_4 volume. Consequently the net effect of the HBD on the run 7 $J/\psi \rightarrow e^+e^-$ analysis was to degrade the signal to background ratio through conversion and to lower the resolution due to smaller field integral.

II.4.7 Other central arm subsystems

There are a number of other detectors in the Central Arm acceptance that were not mentioned, because they were not used in the analysis presented in this thesis. For completeness, some of them will be briefly presented here.

- The time of flight detector (TOF) is designed to provide hadron identification through the measurement of the time of flight. Hadrons with different masses are identified by the time they take to propagate from the collision point to the location of the TOF detector at a radius of 5 m which has a dependence on the mass of the particle (cf. Fig. II.18, left). The TOF detector is equipped with planes made up of scintillator rods aligned to cover a honeycomb support. The scintillators are read out with photomultipliers fitted at both ends. The time difference between the TDC read outs in the two PMTs provides the position of the hit along the scintillators axis, whereas the average gives the timing of the hit. The intrinsic resolution of timing is 80 to 100 ps. This allows K/π separation up to a p_T of 2.4 GeV/c and K/p separation up to a p_T of 4 GeV/c. The TOF has a 45° azimuthal coverage in the east arm. An extension in the west arm using resistive plate chambers with a coverage of 2×10° was recently commissioned.

- The time expansion chamber (TEC) is designed to provide position measurements for the tracking in addition to the DC and PC, and to improve the momentum resolution at high p_T. It is located between the RICH and the EMCal at a radial position of 4.1 m<R<4.8 m, with full azimuthal coverage in the east arm. The TEC is a multiwire proportional chamber that localizes tracks by measuring the drift time of ionization electrons. It is also capable of enhancing the p/π separation through the dE/dx measurement. The working principle of the TEC is very similar to the DC (cf. Fig. II.18, right). A grid of anode wires creates a low electric field in a gas volume for the drift of ionization electrons at a controlled low velocity. Cathode wires are installed very close to the sense wires to enhance the electric field just before the drift electrons arrive at the detection point. This enhances the signal thorough avalanche creation. There is only one layer of sense wires.

- The muon piston calorimeter (MPC) is a lead-tungsten homogeneous calorimeter that is located close around the beam pipe at the entrance into the muon arms (hence the

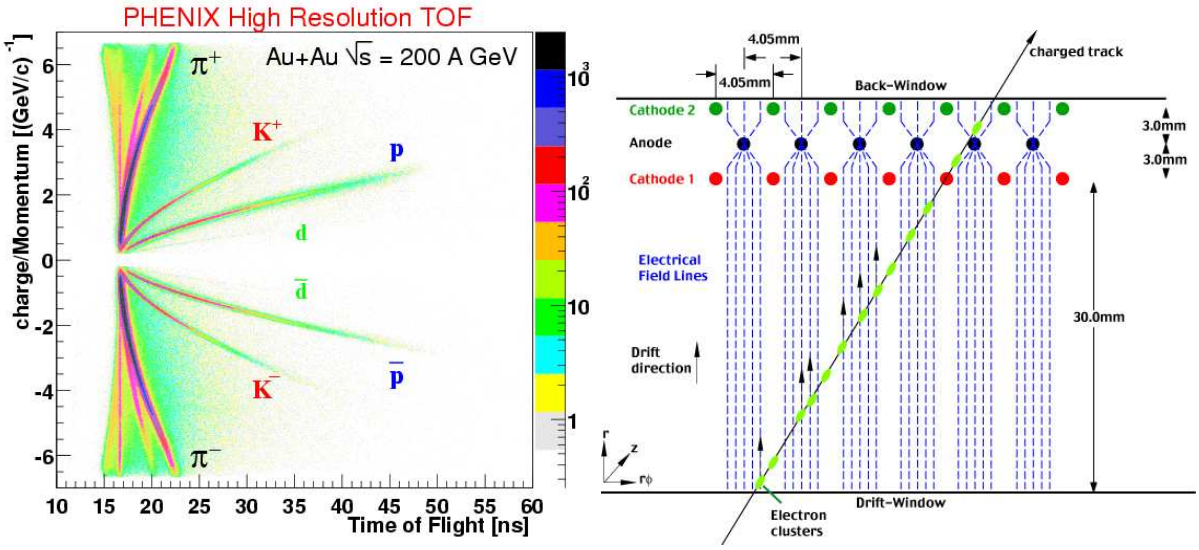

Figure II.18: Left: The correlation between time and momentum for hadrons of different mass. The timing information from the TOF is used together with the momentum measurement from tracking to identify hadrons in this plane. Right: The drift region and amplification regions of the TEC detector. For a single track, its inclination can be inferred from the time difference between the signals produced in the sense wires that are fired by its ionization electrons.

name) (cf. Fig. II.19 left). The rapidity coverage is $3.1<|\eta|<3.9$ in full azimuth, with one MPC in each muon arm. 192 calorimeter crystals in shape of rectangular rods are placed parallel to the beam axis in a circular frame. They are read out at one end with avalanche photodiodes. Avalanche photodiodes are PIN diodes on which a sufficiently high voltage can be applied so that the electric field in the depletion region can enhance avalanche multiplication at the passage of electrons. The mechanism of electromagnetic shower creation is similar to that in the PbGl sector of the EMCal.

- The aerogel detector is a Čerenkov type detector. The basic units are cubes of Aerogel Silica as radiating material fitted with a reflective integration cube serving as coverage on one side. The integration cube collects the light generated in the radiating cube and feeds it to two photomultipliers. 16×10 of these units are assembled on both sides of a mechanical support that is 4 m×1.2 m wide (cf. Fig. II.19, right). The ensemble is placed in the space between the RICH and the EMCal at a radial distance of 4.5 m, with a resulting coverage of 15° in ϕ and $|\eta| < 0.35$. The identification of charged particles proceeds in a similar fashion as in the RICH. But unlike the RICH no ring reconstruction is possible because the radiating medium is very close to the photomultipliers. Instead, the Čerenkov signal created by a single track is collected by the cell through which it passes. The index of refraction of aerogel implies a Čerenkov emission threshold for pions of $\sim$ 1 GeV/c and for protons of $\sim$4 GeV/c. It therefore enhances the p/π identification capability between these two thresholds.

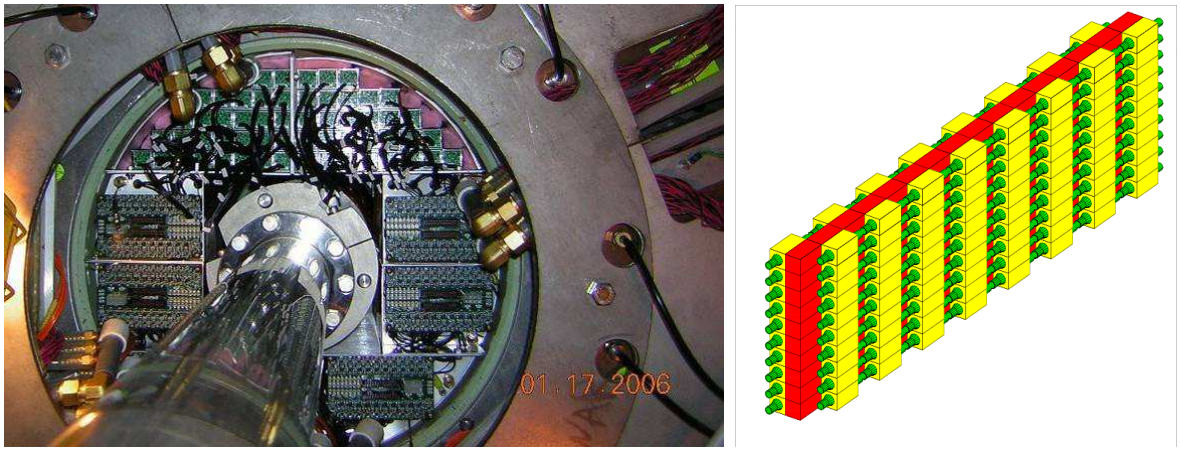

Figure II.19: Left: The MPC calorimeter installed into the 'muon piston' area. Right: The assembled Aerogel. The small yellow boxes represent the integration cubes of the Aerogel counter units, read out by the PMTs depicted as green tubes.

II.5 Tracking algorithm in the central arms

In central Au+Au collisions, up to ≈470 charged particles fall into the PHENIX central arm fiducial volume [11]. The particles have a rather soft distribution that peaks around 250 MeV/c. The presence of a large volume (RICH) between the inner trackers (DC and PC1) and the outer trackers (PC2 and PC3) complicates further the tracking in such an environment. Some of the tracks that traverse the inner detectors leave the fiducial volume without passing through the rear detectors. Besides, the search window in outer detectors on account of multiple scattering becomes large.

Taking into account these constraints, the tracking in the PHENIX central arm is performed in three steps. The first step is the pattern recognition where trajectories are defined from the hits in the tracking detectors (DC and PC1). In a second step the hit positions of the defined tracks are used in association with the knowledge of the magnetic field to determine the momenta of the particles. Finally the tracks are projected and associated with hits in the particle identification detectors. The first two of these three steps will be described briefly below. The third step is briefly described in at the end of this section, and illustrated with the analysis presented in Sec. IV.3.

II.5.1 Track finding

Pattern recognition in the central arm spectrometers of the PHENIX detector is implemented in a global tracking algorithm called a *combinatorial Hough transform*. This algorithm starts with the position of all hits generated in the X1 and X2 layers (cf. Sec. II.4.2) of the DC, which gives no information about the position of the hit along the z axis. At this first step, the track finding is therefore limited to the $x-y$ plane projection. This plane is the bending plane for a perfectly cylindrically symmetric magnetic field, a symmetry that holds true for much of the central arm fiducial volume except near the magnet tips. Next, a straight line is fitted between all possible pairs of hits. The straight line track model within the volume of the DC is a satisfactory one for track finding purposes, taking into account that the magnetic field in this region is small (~ 0.2 T.m for the +− configuration), and that the total depth of

the DC is only 40 cm. The expected deviation in the bend plane within the DC is less than 1°, with practically none in the non bend plane except near the magnet tips.

For N hits in the X1 and X2 layers, this step results in an ensemble of $N \times (N-1)/2$ straight lines which are conveniently parametrized using two variables α and ϕ (Fig. II.20 left). The α parameter is the inclination of the line with respect to the radial unit vector at a reference radius R_{DC} chosen to be at the mid point of the DC. The ϕ parameter is the azimuthal angle of the line's intersection with the circle at R_{DC} with respect to the x axis. These two parameters were chosen over the $ax+b$ parametrization, because the (a, b) space for arbitrary pairs of points is not a bound space whereas the (α,ϕ) space is bound to (-π/2,π/2) for each component. It is also essential that the chosen parameter pair uniquely defines all possible pairs of hits. The value of the parameter pair (α,ϕ) for all the $N \times (N-1)/2$ pairs of hits is then histogrammed as shown in Fig. II.20 on the right.

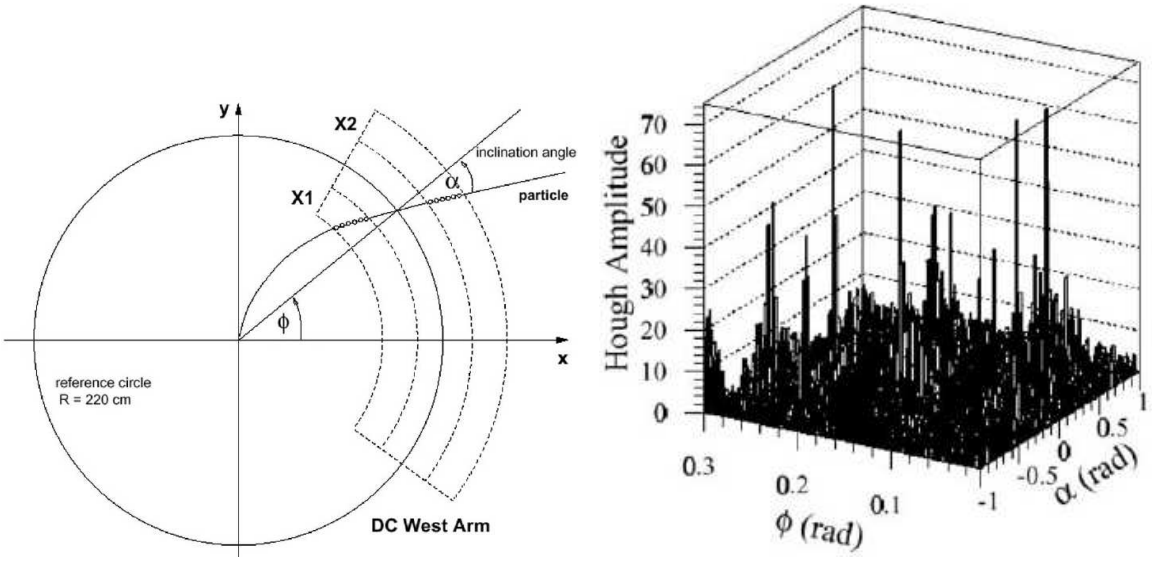

Figure II.20: Hough transform (A) The α and ϕ parameters that fully describe the tracks assumed to be linear inside the drift chamber fiducial volume. (B) Histogram of the α and ϕ values of all possible pairs of points.

Consider an actual track that leaves a large number of aligned hits (up to 24 in the X layers, even though this number can be slightly smaller due to finite wire efficiency of about 90%). All of the pairs formed from the hits belonging to this track (correlated pairs) will fit to the same values (at least very close to) of (α,ϕ). On the other hand, the probability that two arbitrary hits not belonging to the same track (uncorrelated pairs) result in a parameter pair (α,ϕ) close to that of a hit pair belonging to any true track is small. This implies that correlated pairs will result in localized peaks in the (α,ϕ) histogram. The problem of finding tracks from the DC hits is therefore reduced to finding localized peaks on the (α,ϕ) histogram created from all possible pairs in an event. This is the essence of the combinatorial Hough transform.

A peak finding algorithm is therefore executed on the resulting histogram. The basic idea of this algorithm is to scan the whole area of the (α,ϕ) histogram by summing the contents of neighbouring tile of bins (say of size $S \times S$, where S is picked from $S = 1, 3, 5, ...$), and

comparing the result to some threshold value. If the sum for any tile exceeds the threshold, the parameter pair (α,ϕ) of the central bin of the tile is added to the list of found tracks (a track being completely defined by its (α,ϕ) value). The performance of this method of localizing tracks critically depends on the binning size, threshold cut value and the size of the bin tile over which the content sum is computed for comparison with the threshold. To illustrate this, if the bin size is too fine compared to the actual resolution of hit position and/or the content summing tile size (S) is too small, then the (α,ϕ) pairs of the same track will not be localized by the peak finding algorithm as they would be dispersed around over a large number of bins. These quantities are therefore optimized to maximize the efficiency of track finding.

Once all the tracks have been identified, the next step is a background removal procedure which is applied to remove points that are too far away from a linear fit to the group of points to which they belong. This is done iteratively by weighting and deweighting points according to their distance from the result of the previous fit. Finally hits that were found by the algorithm to belong to more than one independent tracks (hit sharing) are attributed to the closest track, and removed from the list of hits belonging to the other tracks. At the end of this procedure, one ends up with a list of solutions in the $x-y$ plane, whose z position has to be looked for in the PC1 cluster list.

The association of DC tracks in the (r,ϕ) plane to PC clusters starts by searching for an unambiguous z position among the PC1 clusters for the tracks reconstructed in the (r,ϕ) plane by the DC. The algorithm then tries to localize z position by using the hits generated by the stereo wire planes (UV plane) in the DC. If a unique solution was found in the PC, the stereo wire results are used just for verification. Otherwise, the stereo wire solution (the best one in case of multiple solutions) is used to choose between the multiple PC1 solutions.

A track quality parameter that encodes the success/failure of this procedure is then defined and can be used at analysis to restrict to the most robust pattern recognition solutions. The quality parameter is a binary coded integer with 6 bits. The least significant two bits are used to encode the usage of the X2 and X1 layers of the DC in decreasing order of significance, with three possible solutions: 01 for only X1 used, 10 for only X2 used, 11 for both X1 and X2 used).

The two most significant bits (6 and 5) give the uniqueness and availability of PC1 solution(s) in decreasing order of significance.

$$\begin{aligned} 00 &= \textit{not found} \\ 01 &= \textit{found but not unique} \\ 11 &= \textit{found and unique} \end{aligned} \tag{II.11}$$

The two next most significant bits (4 and 3) are used to encode the uniqueness and availability of solution(s) in the stereo wires in exactly the same convention as in Eq. II.11. In case of multiple PC1 solution, the uniqueness in the UV layers means that the solution found in the DC was able to resolve ambiguities between the PC1 solutions.

The possible values of the quality parameter and their meanings are given in Tab. II.1. It is to be noted that if no PC1 solution is found, then the track quality will only have the X bits coded, thus the quality value will be < 4. These are the worst quality tracks. The best quality tracks are those where both X1 and X2 are used, and the unique solution found in the PC was confirmed by a unique solution found in the DC (quality=63).

PC1	DC UV layers	possible solutions
found and unique (11)	not found(00)	49,50,51
found and unique (11)	found and matches PC (11)	61,62,63
found and ambiguous (01)	not found(00)	17,18,19
found and ambiguous (01)	found but does not solve PC ambiguity(01)	21,22,23
found and ambiguous (01)	found and solves PC1 ambiguity(11)	29,30,31

Table II.1: Definition of track quality parameter.

II.5.2 Momentum reconstruction

Once the tracks have been found and their associated hits in the tracking layers identified, the next step is to reconstruct the particle momenta. The magnetic field (cf. Sec. II.4.1) is too complicated to allow using analytic parametrizations for momentum determination. Low momentum particles and large track multiplicity as well as energy loss effects and multiple scatterings limit the use of numerical momentum reconstruction due to extreme complexity and high computing resource consumption. A grid interpolation technique is therefore adapted as an alternate solution.

The basic idea of this method [91, 92] is to identify *initial track parameters* that uniquely determine where a trajectory hits the various tracking planes, and make a discrete look up table (LUT) between the initial track parameters and hit positions in the tracker for points lying at the nodes of a four dimensional grid.

The association grid is constructed by swimming test particles within the detector in a full simulation that takes into account multiple scattering, energy loss and the magnetic field. The PHENIX momentum reconstruction algorithm uses an association grid between the initial track parameters (p_t, θ, z_v,ϕ_v) and the geometrical parameters (α, β, z_{pad},Φ) defined for each pattern recognition solution. The actual meaning of these parameters is illustrated in Fig. II.21. A projection of the grid in the α vs. β plane is shown in Fig. II.22.

Once these grids have been made, the geometrical parameters (α, β, z_{pad},Φ) is calculated for each pattern recognition solution, allowing to localize the grid volume element to which the particular solution belongs to. The (α, β, z_{pad},Φ) grid volume element is then translated to a (p_t, θ, z_v, ϕ_v) grid volume element using the look up table.

II.5.3 Track association

In a final step, the tracks found by the pattern recognition algorithm are projected onto the particle identification detector subsystems and associated with the nearest hits within a cut off distance dependent on the resolution of the subsystem. For association with the RICH and EMCal, the information of the PC layers just before their entrance is used to have a better estimation of the position where the projected track should hit. The distances between the track projections and the particle hit positions are calculated for each particle identification detector and used later as quality parameters in analysis cuts.

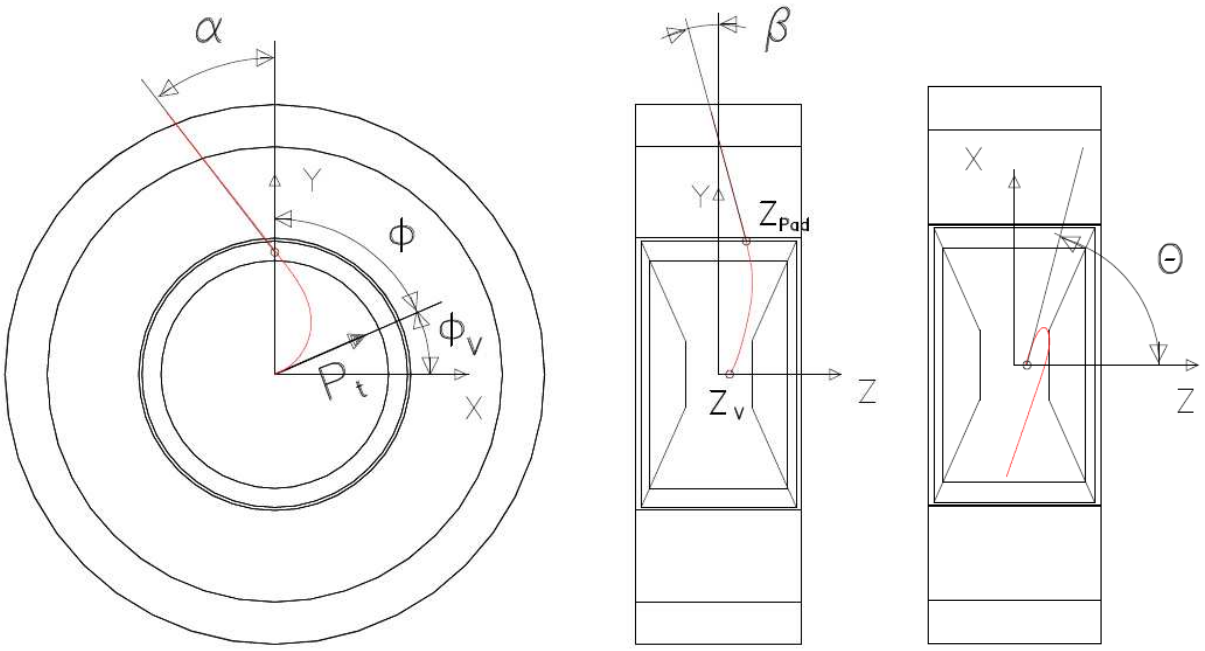

Figure II.21: Geometrical parameters of the pattern recognition solutions. The left most figure is the beam view point of the detector. The two figures on the right are sideways views.

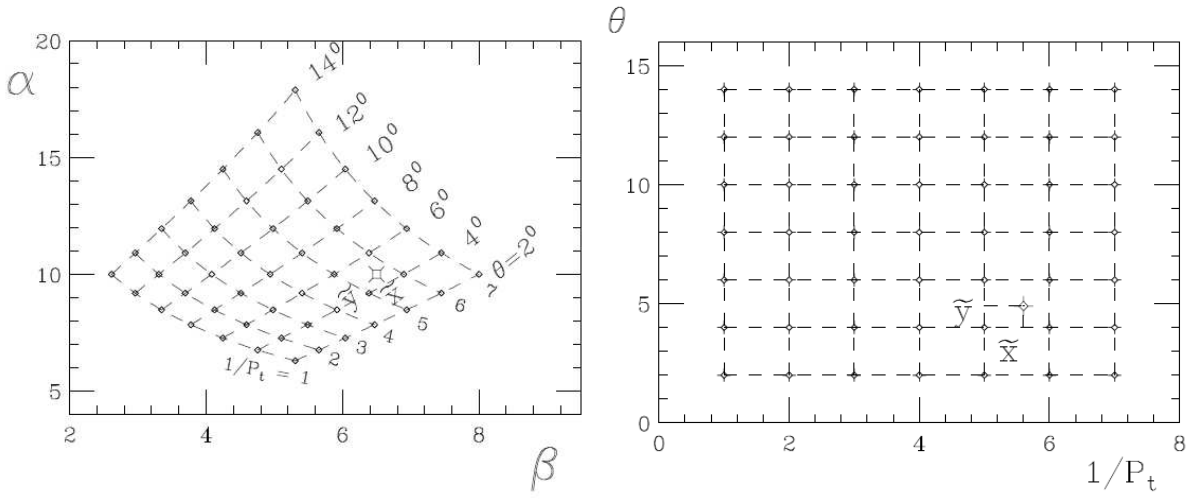

Figure II.22: Momentum interpolation grid.

Chapter III

Data Taking and Quality Assurance

III.1 Introduction

The results shown in this thesis involve two Au+Au and one p+p data sets. The p+p data set was not analysed in the course of the thesis, and final cross sections and p_T and rapidity dependencies that were calculated independently and published in reference [52] are used to normalize the Au+Au yields. In this chapter the data taking conditions that prevailed for the two Au+Au data sets used as well as the quality assurance procedure that was employed will be explained.

The first of the two Au+Au data sets on which I worked was collected in the course of the fourth RHIC data taking season during the winter of 2003-2004, and will be referred to as *run 4*. The detector configuration of this period is shown in Fig. III.1 on the left. The second one was taken during the seventh data taking season of RHIC during the winter of 2006-2007, and will be referred to as *run 7*. The detector configuration for this period in the central arm, is shown on the right side of Fig. III.1. The analysis presented in this thesis is based on the run 7 data set [93], but part of the techniques were first exercised on the run 4 data, as a crosscheck of the mainstream analysis published in reference [75].

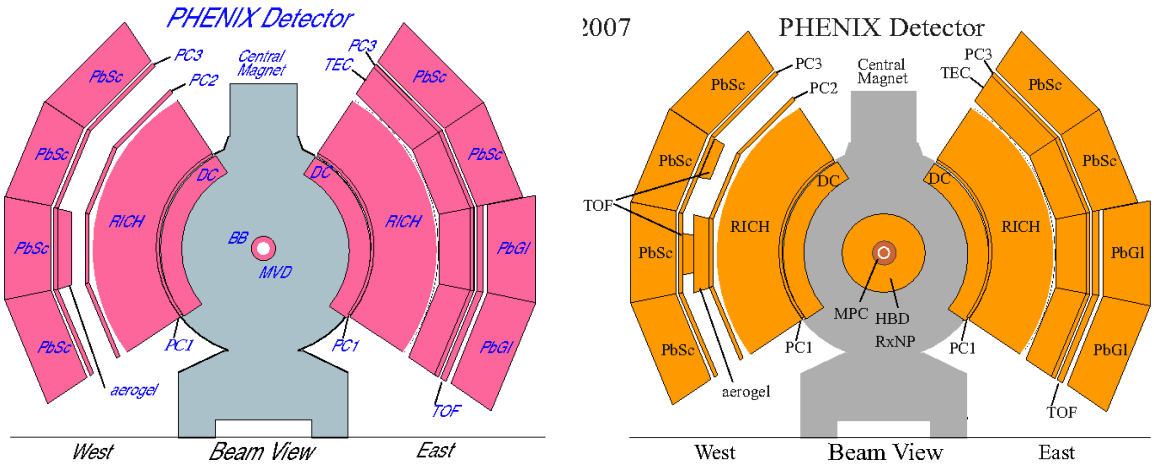

Figure III.1: Run 4 (left) and run 7 (right) detector configuration in the central arm.

III.2 Data Taking

The DAQ (Data AcQuisition) system is responsible for collecting the data packets from the various subsystems synchronously, assembling them into full events, and logging them to hard disk. The data flow in the PHENIX DAQ is schematically shown in Fig. III.2. Below is a list of its main components.

- Subsystem Front End Modules (FEM) are responsible for collecting digital signal (bits) from individual detectors. The FEMs have a capacity to buffer up to 40 events while waiting for event acceptance/rejection decision.
- Global level 1 (GL1) is responsible for processing event acceptance/rejection conditions based on reduced bits collected directly from relevant subsystems. If an event is accepted, the GL1 sends a signal to the FEM to pass the data to the next component.
- Data collection modules (DCM) perform zero suppression[1] and completeness checks on data bits and arrange them into subsystem-wise packets following a standard format.
- The Event Builder (EvB) is composed of one Sub Event Buffer (SEB) per detector subsystem, which is used as a buffer and interface of the DCM modules, and a switch that concatenates the subsystem packets into full events. The full events are then sent to the Assembly and Trigger Processors (ATP) that provide an environment to possibly process additional event acceptance/rejection conditions on-line. Since full events transit through the ATPs, more information is available than inside the GL1 allowing more sophisticated algorithms for event selection.
- The Buffer Box (BB) server is responsible for concatenating and recording full events to hard disk.

The duration between the start logging and end logging commands issued to the DAQ is called a run[2]. Runs are sequentially numbered by the order in which the start logging command was passed. The run number that is given this way identifies uniquely a given set of events. The events within a run are also assigned sequential event numbers following the order at which the event occurred. The duration of a run is typically of one hour, unless an error forces the shift crew to stop the DAQ earlier.

The number of events (τ_{evt}) that can logged to disk in a fixed amount of time is limited by the bandwidth of DAQ elements. The data writing rate is less than the speed of the slowest element. Within PHENIX, the limiting element are the FEMs. The FEMs can process events at a maximum rate of $\lesssim 8$ kHz. The next limit comes from event logging by the buffer box server, with maximum available bandwidth of $\lesssim 700$ MBytes/s.

It sometimes happens that the available effective bandwidth is not sufficient to throttle all the events to disk. While this has so far not been true for Au+Au collisions ($\tau_{evt} \lesssim 5$ kHz), it is the case for p+p collisions and d+Au collisions where much higher event rates are achieved (peak rates are ~ 250 kHz for p+p and ~ 85 kHz for d+Au). For this reason it is essential

[1] Zero suppression refers to the suppression of channels where the pedestal subtracted measured signal is lower than a preset threshold value. It aims at reducing the data volume.

[2] This is distinct from the data taking seasons which are also called runs. The implied meaning of the word run is usually clear from the context.

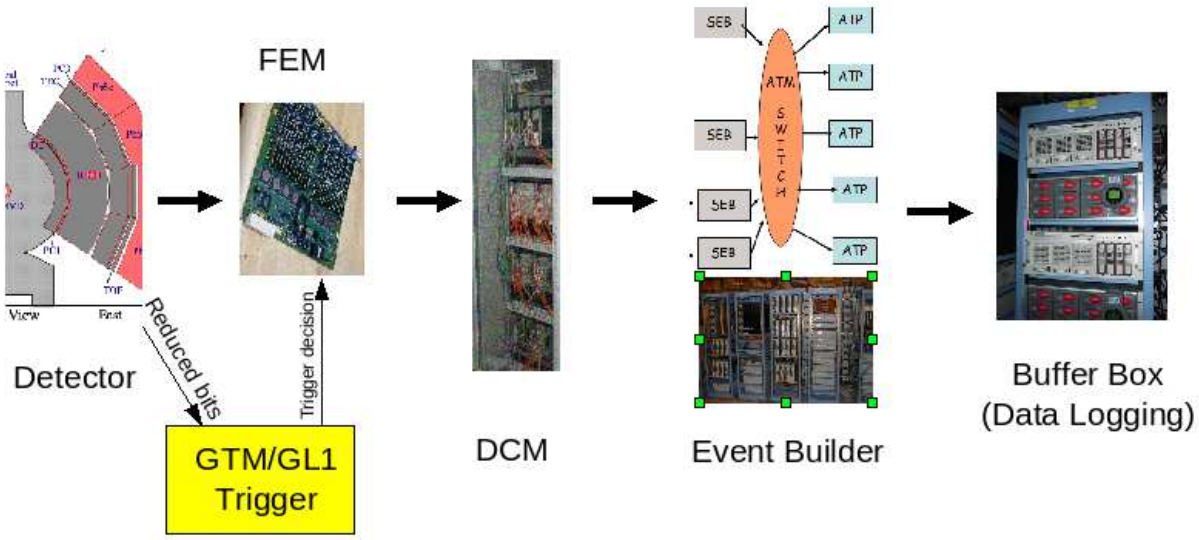

Figure III.2: Schematized data flow in the PHENIX DAQ system. The pictures show the actual DAQ component.

to select for logging only those events in which an interesting physics signal has occurred. The process of selection is called triggering, and the hardware and/or software architecture used for selection is called a trigger. The trigger conditions are processed either by the GL1 architecture or by the ATPs.

The most general (least selective) trigger is one that would allow all detected inelastic collisions to be written to disk. Such a trigger is called a *minimum bias (MB)* trigger, because no additional condition is applied to select events. Inelastic collisions deposit fast charged particles at forward rapidity. They can therefore be detected by charged particle detector with quick response and decay times paced at this rapidity. In PHENIX, the task of signaling an inelastic collision is done by a combination of signals from the BBC and ZDC. The specifics for Au+Au collisions will be discussed in Sec. III.2.1 and Sec. III.2.2 below.

If the MB trigger requires too much trigger bandwidth, the inelastic collision condition is augmented by some other condition that will restrict the event selection further. This is usually done by requiring that at least one energetic particle is detected in one of the spectrometers. This is called Level 1 trigger (lvl-1). Most p+p and d+Au data are taken using a combination of lvl-1 triggers. A part of the total bandwidth is used in parallel to store a randomly chosen set of events among the minimum bias inelastic collisions. The process of randomly choosing a fraction of events that satisfy a specific trigger condition is called *prescaling*. To achieve an event reduction of the size of $1/N_{pscl}$, the most convenient solution is logging events that satisfy the conditions of the trigger intended for prescaling once every N_{pscl} times they occur. The value N_{pscl}[3] is called the prescaling factor.

A prescaled MB sample is always written in parallel with the lvl-1 triggered sample to enable cross checks and allow trigger efficiency estimation. In reality, a combination of lvl-1 triggers and the minimum bias trigger is used with prescale factors optimized for each trigger

[3]The convention within PHENIX is slightly different. After an accepted event, a new event is taken after waiting N'_{pscl} other events that satisfy the trigger condition. The event reduction is therefore $1/(N'_{pscl}+1)$.

by a compromise between getting an event rate from the combined triggers which is below the DAQ bandwidth, and getting enough statistics from every trigger to perform the physics analyses that they are intended for. A typical lvl-1 trigger mix used for a p+p run is shown on the screen shot of Fig. III.3. The prescale factors (column "Scale Down") use the PHENIX convention. For instance, a prescale of 0/1 means all/half of the triggered events are kept. Only those triggers that are relevant for the central arm and that were not prescaled out[4] are shown. The live trigger rate is the actual number of events satisfying the event that could be processed. This number is smaller than the raw trigger rate because of the dead time to process the trigger conditions. In other words, an event that occurs while the previous event is being processed by the ATPs is lost even if it satisfies the trigger conditions. The live time, which is the ratio between the live rate and the raw rate is given in the last column. It was of the order of 80% for this typical p+p run. Note that the $BBCLL1(> 0\ tubes)$ is the minimum bias trigger used.

Name	Bit Mask	Scale Down	State	Raw Trigger Count	Raw Trigger Rate	Live Trigger Count	Live Trigger Rate	Scaled Trigger Count	Scaled Trigger Rate	Livetime
Clock	0x00000002	9999999	Enabled	-956205965	-313304.71	450242070	147523.61	2192	0.72	-0.47
BBCLL1(>0 tubes)	0x00000004	60	Enabled	209615217	68681.26	158450917	51917.08	2597556	851.10	0.76
BBCLL1(noVertexCut)	0x00000008	1600	Enabled	511320911	167536.34	385401948	126278.49	240725	78.87	0.75
ZDCLL1wide	0x00000010	14	Enabled	12341265	4043.66	9571360	3136.09	638090	209.07	0.78
ZDCLL1narrow	0x00000020	900	Enabled	5043954	1652.67	3910880	1281.42	4340	1.42	0.78
BBCLL1&(ZDCN|ZDCS)	0x00000040	45	Enabled	30755366	10077.12	23849206	7814.29	518461	169.88	0.78
ERTLL1_4x4a&BBCLL1	0x00000200	0	Enabled	376278	123.29	289743	94.94	289743	94.94	0.77
ERTLL1_4x4c	0x00000400	8000	Enabled	302239093	99029.85	256837489	84153.83	32100	10.52	0.85
ERTLL1_4x4b&BBCLL1	0x00000800	0	Enabled	107342	35.17	80847	26.49	80847	26.49	0.75
ERTLL1_4x4c&BBCLL1	0x00001000	0	Enabled	3972316	1301.55	3202813	1049.41	3202813	1049.41	0.81
ERTLL1_E&BBCLL1	0x00002000	0	Enabled	816451	267.51	639372	209.49	639372	209.49	0.78
ZDCN||ZDCS	0x00800000	615	Enabled	178596293	58517.79	138374956	45339.11	224634	73.60	0.77
ZDCNS	0x01000000	14	Enabled	8110057	2657.29	6133907	2009.80	408927	133.99	0.76
ERTLL1_4x4b	0x08000000	0	Enabled	256888	84.17	153830	50.40	153830	50.40	0.60

Figure III.3: Part of the trigger mix for p+p data taking.

Even in the case in which there is sufficient bandwidth to record all events to disk, it is sometimes useful to execute a trigger and record events meeting a trigger condition designed for a specific physics signal in parallel to the minimum bias events but to a separate file. This procedure, which is not a necessity in contrast to triggering, is called *filtering*. Filtered data, which by design is smaller in size than the minimum bias sample and takes less time to process, can be analyzed quickly. It is also used to perform on-line sanity checks during data taking, which would otherwise be impossible until the full minimum bias sample is processed. A downside is the possibility that the filtering condition might create a bias on the background and/or signal spectra. In this case, the bias has to be accounted for during analysis.

Filtering usually requires a sophisticated algorithm for the selection of events, usually called a level 2 trigger (lvl-2 for short). The execution of lvl-2 triggers is usually much slower than lvl-1 triggers, and therefore requires more computing power. Lvl-2 triggers can be executed either inside the trigger processors (ATP) of the data acquisition system, or once the data has been written to permanent storage. A relevant example is a dilepton trigger, where in addition to the MB trigger two energetic particles that form some predefined

[4]Prescaling out means fixing the prescale factor of the trigger much larger than the typical number of events in a run. No event satisfying only this trigger would then be written down.

minimum invariant mass can be required. Such a filter would select the signal from dilepton decay of mesons with masses higher than the mass cut applied. The case of the J/ψ lvl-2 trigger will be illustrated in Sec. III.2.2.

III.2.1 Run 4, Au+Au at $\sqrt{s_{NN}} = 200$ GeV

III.2.1.1 Detector and magnetic field configuration

Starting from the interaction point outwards, the central arm detector composition for run 4 was (cf. Fig. III.1 left)[5]. The detector subsystems directly relevant for the analysis of J/ψ were written in bold. The azimuthal coverage is given next to the detector name

- **Drift chambers (DC)** , 2×90°, (cf. Sec. II.4.2)
- **Pad chamber, layer (PC1)** , 2×90°, (cf. Sec. II.4.3)
- **Ring imaging Čerenkov (RICH)** , 2×90°, (cf. Sec. II.4.4)
- **Pad chambers layer 2 (PC2)**, 1×90°, west arm, (cf. Sec. II.4.3)
- **Pad chambers layer 3 (PC3)**, 2×90°, (cf. Sec. II.4.3)
- Aerogel, 1×22.5°, west arm, (cf. Sec. II.4.7)
- Time of flight (TOF), 1×90°, east arm, (cf. Sec. II.4.7)
- Time expansion chamber (TEC), 1×90°, east arm, (cf. Sec. II.4.7)
- **Electromagnetic calorimeters (EMCal)** (cf. Sec. II.4.5),
  - Lead Scintillator (PbSc), 1×45° west arm and 2×90° east arm
  - Lead Glass (PbGl), 1×45° east arm

The pseudorapidity coverage for all detector subsystems listed above is $|\eta| < 0.35$, except for the Aerogel where the coverage was only $0 < \eta < 0.35$. The global detectors used for this run were the beam beam counter (BBC) and zero degree calorimeter (ZDC). The ++ and −− magnetic field configurations, where the two central arm coils are polarized in the same direction, were employed. There were also a few runs taken with a zero field configuration used, among other things, for localization of the event vertex in the transverse plane.

III.2.1.2 Triggers and on-line filtering

The triggers that were enabled during run 4 are shown in the screen capture from the DAQ control software shown in Fig. III.4, together with the corresponding prescale factors. The maximum delivered event rate for this run was ∼ 3.5 kHz, so no lvl-1 trigger was necessary. The minimum bias trigger definition used in analysis is

$$BBCLL1\ (>1\ tube)\ \ \&\&\ \ (ZDCLL1wide\ \ ||\ \ ZDCNS) \tag{III.1}$$

[5]The barrel part of the Multiplicity Vertex Detector (MVD), figuring in the schematics, was removed. Only the end caps were left in the forward rapidity region.

where the $BBCLL1$ (> 1 *tube*) requires at least one BBC tube hit on each side (North and South), $ZDCLL1wide$ and $ZDCNS$ require the sum of the energies measured by the north and south ZCDs to pass an energy threshold together with a cut of 40 cm on the z-vertex measured by the BBC. The reason the ZDC trigger conditions are added is that the interactions of the beam halo with the ambient atmosphere (also known as beam–gaz interactions) are much more likely to create hits in the BBC than in the ZDC. Putting a ZDC condition allows to reject the contamination from these background events.

Name	Bit Mask	Scale Down	State	Raw Trigger Count	Raw Trigger Rate	Live Trigger Count	Live Trigger Rate	Scaled Trigger Count	Scaled Trigger Rate	Livetime
Clock	0x00000002	943400	Enabled	3279355641	554038.80	3694447920	624167.58	49443	8.35	1.13
BBCLL1	0x00000004	0	Enabled	4767108	805.39	3954445	668.09	3954445	668.09	0.83
ZDCNS	0x00000008	200	Enabled	13831157	2336.74	11737731	1983.06	58397	9.87	0.85
ZDCLL1wide	0x00000010	200	Enabled	16401280	2770.95	12419510	2098.24	61789	10.44	0.76
ZDCLL1narrow	0x00000020	100	Enabled	8796448	1486.14	7239751	1223.14	71681	12.11	0.82
UltraPeripheral	0x00000040	0	Enabled	64467	10.89	32535	5.50	32535	5.50	0.50

Figure III.4: Lvl-1 and MB trigger mix and prescale factors used for run 4.

III.2.1.3 Integrated luminosity

In ion-ion collisions, as in p+p collisions, the total number of recorded events N_{evt} and the integrated luminosity $\mathcal{L}_{int}$ are related through

$$N_{evt} = \epsilon_{trig} \times \mathcal{L}_{int}^{A+A} \times \sigma_{A+A} \tag{III.2}$$

where ϵ_{trig} is the efficiency of the trigger used to record the data, and σ_{A+A} is the total inelastic cross section of A+A type collision. For Au+Au collisions, $\sigma_{Au+Au} = 6.85 \pm 0.54$ b. The efficiency of the MB trigger as defined by Eq. III.1 is approximately 93% of the total inelastic gold gold cross section. During run 4 an integrated luminosity of 1370 μb^{-1} was delivered[6] out of which 240 μb^{-1} (equivalent to 1.5×10^9 MB events) could be recorded. After quality assurance selections, the analysed data sample in the central arm contained about 10^9 MB events.

III.2.2 Run 7, Au+Au at $\sqrt{s_{NN}} = 200$ GeV

III.2.2.1 Detector and magnetic field configuration

For run 7, the new detectors listed below were added in the central arm:

- Triple GEM Hadron blind detector (HBD), 2×135°, $|\eta| < 0.45$, placed between the interaction region and the drift chambers, (cf. Sec. II.4.6)
- **Reaction plane detector (RxNP)**, 2π, $1<\eta<2.8$, (cf. Sec. II.3.4)
- Time of flight detector (TOF), 2×10°, $|\eta| < 0.35$, west arm (cf. Sec. II.4.7)
- Muon piston calorimeter (MPC), 2π, $3<\eta<4$, (cf. Sec. II.4.7)

[6]Only about half of the total delivered luminosity falls within ±30 cm of $z = 0$, used as a cut in the minimum bias trigger.

After a few weeks of running, the HBD in the west arm encountered serious high voltage failures. It was thus removed from the acceptance. Much of the data taking was done with only one HBD in the east arm. Overall, the HBD in the east arm was also unable to produce usable data for this analysis, but this was realized only very late in the run. Consequently it stayed in the acceptance until the end of the run.

As discussed in Sec. II.4.6, the HBD requires a low magnetic field to have a good rejection of hadrons. To achieve this the central arm magnets were operated with opposite polarities, leading to a field strength at the position of the HBD of the order of 1 kG, well within the operation specification of the HBD. In the first half of the run the central arm magnets were operated in the fully reversed +− polarity configuration whereas the remaining part the reverse −+ configuration was used. Zero field runs were also taken after each detector carriage moves.

III.2.2.2 Triggers and on-line filtering

The run 7 MB trigger condition was essentially unchanged from what was used during run 4 (Eq. III.1). Fig. III.5 shows a snapshot of a table with the triggers that were not completely prescaled out. A lvl-2 filtering was based on four selection algorithms (cf.Sec. III.3.1) was executed. The algorithm and performance of the lvl-2 triggers will be discussed in Sec. III.3.1.

Name	Bit Mask	Scale Down	State	Raw Trigger Count	Raw Trigger Rate	Live Trigger Count	Live Trigger Rate	Scaled Trigger Count	Scaled Trigger Rate	Livetime
Clock	0x00000001	9999999	Enabled	-2050745385	-598408.34	584037586	170422.41	3065	0.89	-0.28
BBCLL1(>1 tubes)	0x00000004	0	Enabled	9440755	2754.82	8815316	2572.31	8815316	2572.31	0.93
BBCLL1(noVertexCut)	0x00000008	200	Enabled	21896149	6389.31	20378896	5946.57	101388	29.59	0.93
ZDCLL1wide	0x00000010	400	Enabled	37937382	11070.14	32324717	9432.37	80610	23.52	0.85
ZDCLL1narrow	0x00000020	1000	Enabled	17005225	4962.13	14130249	4123.21	14117	4.12	0.83
Ultraperiph	0x00100000	0	Enabled	64045	18.69	59317	17.31	59317	17.31	0.93
BBCLL1(>0 tubes)	0x04000000	119	Enabled	17798388	5193.58	16374409	4778.06	136454	39.82	0.92
ZDCNS	0x08000000	400	Enabled	0	0.00	0	0.00	0	0.00	0.00

Figure III.5: Lvl-1 and MB trigger mix and prescale factors used during run 7.

III.2.2.3 Integrated luminosity

During run 7 an integrated luminosity of 3260 μb^{-1} was delivered[7], out of which 813 μb^{-1} (equivalent to 5.12×10^9 MB events) could be recorded. After quality assurance selections for the $J/\psi \to e^+e^-$ analysis (and removal of runs taken with the HBD installed in both arms), there were 3.62×10^9 MB events remaining in the data sample. Compared to run 4 there is a significant improvement of the data recording efficiency mostly due to improved data acquisition software.

III.3 Data reduction

During a run the *raw data* recorded directly from the detector consists of channel by channel hit information from subsystems. For PHENIX, the raw data is written out into files referred to in

[7]Only about half of the total delivered luminosity falls within ±30 cm of $z = 0$, used as a cut in the minimum bias trigger.

our jargon PHENIX Raw Data File (PRDF). At analysis level, one is only interested in the four momenta of detected tracks and identification parameters, and not the detailed response of the detectors. *Reconstruction* refers to the process of reducing raw data to an analyzable data (n-tuple of pattern recognition solutions with their momenta and identification parameters). The output files that contain the analyzable n-tuples are called Data Summary Tapes (DST). Reconstruction involves running the pattern recognition algorithms, followed by momentum reconstruction and track-hit associations to outer identification detectors on the raw data (cf. Sec. II.5 for the details of these algorithms). The inputs (outputs) to reconstruction are the PRDF (DST) files. Reconstruction requires a huge data processing and storage capacity, due to the large number of events that are usually recorded (as a reminder $\sim$ 5.1 billion events were recorded during run 7). Handling the reconstruction (independently of writing the tracking algorithm) in itself requires dedicated effort because of the technical challenges it involves. Part of the work preparing this thesis was dedicated to the reconstruction of the level 2 filtered sample from the run 7 data taking season. In this section, the details of this reconstruction work will be given after a brief description of the level 2 filtering that was implemented during run 7.

III.3.1 Level 2 filtering

During the run 7 data taking period, fast high level triggers were used to filter data on-line. As discussed in the introduction of this chapter, the main objective of these filters is to obtain analyzable data sample that is enriched with events in which a particular signal was produced on a faster time scale than unfiltered MB data. If the filter is well designed, a significant gain can be achieved in resources required for raw data processing. In general, the quality of a trigger is determined by its efficiency and rejection power which are defined below.

Trigger efficiency and rejection

The efficiency of a trigger measures what fraction of the recorded events that actually produced the required signal were identified by the trigger as having done so. In the simple case where at most one signal is expected per event (which holds for rare probes like the J/ψ) this efficiency can be expressed by the simple formula

$$\epsilon_{trig} = \frac{N_{sig}^{ok}}{N_{sig}} \tag{III.3}$$

where N_{sig}^{ok} is the number of events in the filtered sample that produced the signal, whereas N_{sig} is the number of events that produced the signal in all collisions (filtered or non filtered). A low trigger efficiency implies that the power of the trigger algorithm to identify events that produced a signal is not optimal. In other words, the triggers capacity to get filtered sample enriched with the required signal is poor. This will be reflected by an increase of the statistical error on the signal, as well as by a systematical error on the trigger efficiency itself. To calculate the efficiency of the trigger, one can start with a minimum bias sample and count the number of signal events in the whole sample (N_{sig}^{MB}) and the number of signal events that also fire the trigger ($N_{sig}^{trig+MB}$). The ratio between these two numbers gives the trigger efficiency:

$$\epsilon_{trig} = \frac{N_{sig}^{trig+MB}}{N_{sig}^{MB}} \tag{III.4}$$

This procedure does not make sense if all the minimum bias data is necessary to estimate the trigger efficiency, because then, there would be no need to use the filtered data sample. The fraction of minimum bias events required is constrained by the expected error on the trigger efficiency[8].

Another important measure of the quality of a trigger is the rejection, which measures the inverse of the fraction of all events that actually met the trigger conditions.

$$R_{trig} = \frac{N_{evt}^{tot}}{N_{evt}^{ok}} \tag{III.5}$$

where N_{evt}^{tot} is the total number of events and N_{evt}^{ok} is the number of events that meet the trigger conditions. The rejection factor R_{trig} measures the reduction in number of events that the trigger achieves. Higher rejection factor implies smaller filtered data sample, and lower computing resources (bandwidth, storage, processing) which constitute the main objective of lvl-2 filtering.

The two quantities ϵ_{trig} and R_{trig} are both correlated to the tightness of trigger conditions, but in opposite directions. A higher rejection factor can be achieved by putting a more stringent trigger condition, but too stringent could result in loosing too many signal events and lower the efficiency. Inversely a high efficiency can be achieved easily by taking looser trigger conditions. But looser trigger conditions would immediately lead to worse rejection factor. Trigger conditions should therefore be optimized to achieve a compromise between rejection and efficiency.

Algorithm

Three lvl2 filtering algorithms were employed during run 7.

- **Central arm dielectron filter:** Combines a MB trigger with two identified electrons in the central arm and minimum invariant mass cut from fast momentum estimation greater than 2.45 GeV/c^2.
- **Muon arm dimuon filter:** combines a MB trigger with two identified energetic muons with a minimum mass cut
- **Central arm high p_T photon filter:** combines a MB trigger with a high p_T photon trigger in the central arms, consisting of an electromagnetic shower in the EMCal to which no associated RICH signal is found.

The physics signal that is relevant for the analysis conducted during this thesis, $J/\psi \rightarrow e^+e^-$, can potentially be enriched by a dielectron filter with a mass cut of 2.45 GeV/c^2, since the invariant mass of a J/ψ is above this cut. An attempt was therefore made to quickly extract the above mentioned signal on the dielectron filtered data sample. Before showing the results, the trigger algorithm is described schematically below.

[8]For the special case where the background is low, a fraction of $1/N$ of the whole minimum bias sample allows to measure a trigger efficiency of $1/N$ with an uncertainty equal to the statistical error on the signal.

1. **Look for track candidates:** This process starts from the list of RICH rings. A look up table is used to delimit regions in the EMCal where the electron that produced the RICH ring might hit. A *track candidate* list is then constructed by pairing up cluster positions recorded in the PC1 ($\overrightarrow{x}_{PC1}$) with the positions of EMCal towers ($\overrightarrow{x}_{EMC}$) with total energy E > 0.5 GeV in the above delimited regions.

2. **First rough estimate of momentum:** Each *track candidate* is then projected towards the BBC vertex and $\overrightarrow{x}_{BBC}$ = (0,0,z_{BBC}) of the event. This allows to estimate the three momentum ($\overrightarrow{p}$) from the bend angle between the lines determined by BBC-PC1 position pair ($\overrightarrow{x}_{BBC}$, $\overrightarrow{x}_{PC1}$) and the PC1-EMCal position pair ($\overrightarrow{x}_{PC1}$, $\overrightarrow{x}_{EMC}$). *Track candidates* that do not point to the BBC z vertex are rejected.

3. **Electron identification:** The remaining *track candidates* are projected towards the RICH PMT plane to look back for a RICH ring nearby. If a RICH ring is found, the *track candidate* becomes *electron candidate*.

4. **Refine momentum estimation:** Each *electron candidate* is projected to the PC3, and if no PC3 hit is found, the candidate is rejected. Otherwise, the momentum is recalculated using the bend angle between the line determined by the PC1 - PC3 cluster and the line determined by the BBC z vertex - PC1 cluster, since the PC3 position measurement is more precise than the EMCal one.

5. **Further electron identification:** The remaining *electron candidates* are tested for EMCal energy to momentum matching. If the E/p ratio is less than 0.5, then the *electron candidate* is rejected. In the same way, if the number of photo electrons in the associated RICH ring is less than or equal to three, the *electron candidate* is rejected.

6. **Pairing and invariant mass:** The remaining candidates are paired up, and the invariant mass of each pair is calculated from the momentum and opening angle between the candidate pair to find a pair with an invariant mass greater than 2.45 GeV/c^2.

If at the end of this process, no pair is found with an invariant mass greater than the preset mass cut (2.45 GeV/c^2), then the event fails the filtering test. If a pair that satisfies the mass cut is found, the event is accepted and the trigger algorithm exits the pairing loop.

The reason that a simplified momentum calculation algorithm is used instead of the more reliable full reconstruction algorithms is because there is not enough time between events to do the full processing. The trigger decision for each event has to be issued faster than the average temporal separation of events, failing which, the ensuing pile up of events will clog the data routes and eventually lead to event loss. To give an estimate, the peak data rate for the run 7 data taking period was 5 kHz, leaving only $\sim$ 0.2 ms between events to do the filtering decision. Compared to this, the typical time scale to process an event using full reconstruction algorithm is of the order of 2 to 3 seconds. Full reconstruction is therefore impractical for this purpose since it would require up to 2 s/0.2 ms $\sim$ 10 thousand parallel processing units to avoid pile up. The improved algorithm discussed above runs at a speed of $\sim$ 10 ms per event, enabling use of filtering with a more reasonable count ($\sim$ 50) of processing units.

III.3.2 Dielectron fast processing

A substantial fraction of time during this thesis was devoted to the design and implementation of a software solution to handle the reconstruction of the level 2 filtered data sample. The initial goal of this step was to do a complete analysis leading to the extraction of J/ψ v_2 and potentially R_{AA} at mid rapidity in the J/$\psi \rightarrow e^+e^-$ channel. Due to the reduction of the data volume by level 2 filtering, the hope was that the reconstruction of the filtered data sample would take a considerably shorter time, giving the opportunity to finalize the analysis by the time gained in this manner. Unfortunately, for reasons that will be described later in this section, it was not possible to do so in the dielectron channel.

The reconstruction work was not limited to only the dielectron filter, but was carried out on data taken with the three (including the dielectron) level 2 trigger algorithms described in Sec. III.3.1. Even though the dielectron filtered data sample did not make it to the final results presented in this thesis, it was used as a sample on which to train the analysis software, and also to optimize the electron identification cuts. The reconstructed level 2 dimuon filtered data sample however was used to extract the J/ψ v_2 and R_{AA} and ended up in another PhD thesis [94].

Although the level 2 filtered data sample was only partially relevant to the J/$\psi \rightarrow e^+e^-$ analysis presented in this thesis, the objectives, challenges and solutions adapted for the reconstruction work that contributed in a way to the delay in getting the final results will be briefly explained here. The data sample was taken at RHIC BNL, and the reconstruction work was done at the "Centre de Calcul de l'IN2P3, Lyon, France" or CCF for short in the PHENIX jargon. It therefore required transferring the files from RHIC to CCF. The flow chart in Fig. III.6 shows the overall path that the data had to follow. More details on the different steps in this flow chart will be described below. The central objective of the reconstruction work is to keep track of the history of all the file segments, making sure that each file segment is reconstructed successfully, and write the output n-tuples from each input file segment to hard disk in an organized fashion. The main challenge is the huge number of input file segments (∼40 thousand) to keep track of. The solution adapted and implemented was to design a relational database into which each action taken on a segment and its outputs are logged. The use of this database, what information was written into it and how the information was used will be described in the relevant paragraphs below.

Filtering

As described in Sec. III.2, the ATPs are an ideal place to execute level 2 filtering algorithms, because for each event, the information from all the detector sub systems is available all together for the first time. The execution of the level 2 triggers however can slow the overall speed of the logging of events if it takes a long time. During data taking, especially at the beginning of run 7, the level 2 filtering algorithms were being tested. It was not clear if they were contributing to slow down of the DAQ system below its designated full speed. Until the issue was resolved, it was therefore decided not to execute the level 2 filtering inside the ATPs. During the run, there were also periods where the level 2 filtering was not executed at run time. For such runs, it was therefore necessary to run the filtering code on the full MB data sample that has been written on to disk. This kind of filtering is called *offline filtering*, in distinction from *ATP filtering*. Approximately half of the reconstructed data was filtered offline and the remaining half in the ATPs.

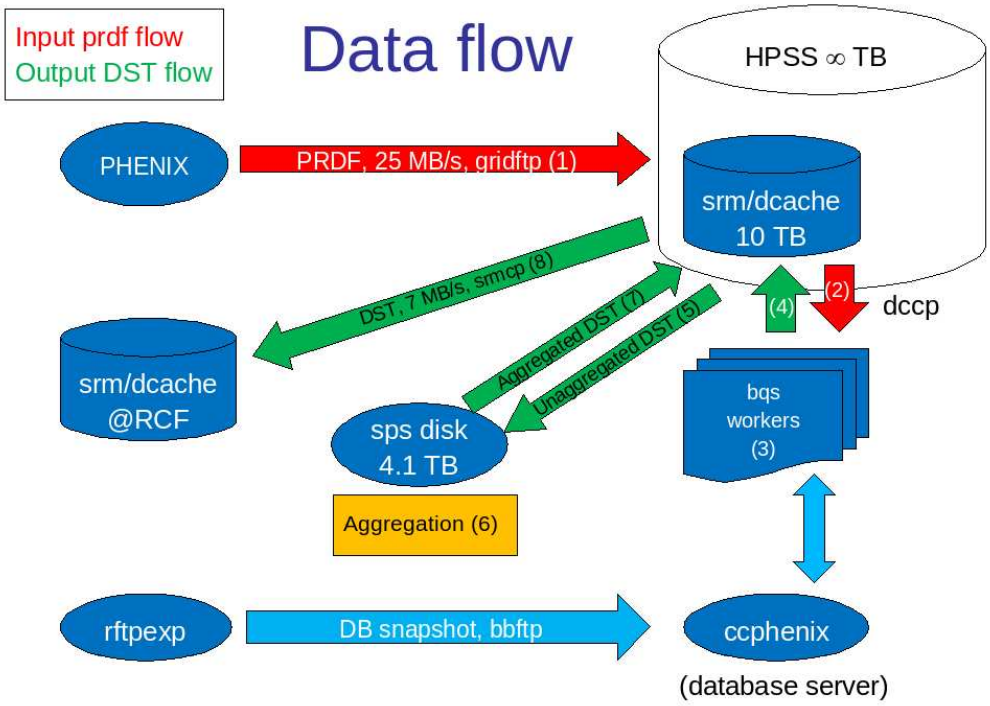

Figure III.6: Reconstruction data flow. The acronyms are described in the text.

Rejection

During run 7, the filtered data using all the level 2 triggers was written to the same output stream. This choice was made because it is more practical for data transfer. In addition, if the events from each filter were written separately, the overlapping events (events that pass multiple level 2 triggers) would be written multiple times, although the extra space due to overlaps is very small compared to the total size of the data sample. As a result, no individual rejection factor could be estimated directly from the collected data for the separate filters. The combined filters had an average rejection factor of ∼16, corresponding to an input file size reduction of 1/0.12. Independent tests were done before the start of data taking on a tiny fraction of the collected data, and the rejection factor and file size reduction estimations from these studies are shown in Tab. III.1. This is a satisfactory rejection factor, taking into account the bandwidth of the data transfer from BNL to CCF.

Trigger Name	Trigger rejection factor	File size reduction
L2AuAuDiElectronTrigger	67.1	1/0.033
L2MuidDimuonNorthTrigger	51.5	1/0.04
L2MuidDimuonSouthTrigger	72.4	1/0.028
L2EmcHighPtTileTrigger	49.1	1/0.036

Table III.1: The rejection factors for the three triggers executed during run 7. The dimuon filter is split into two algorithms that trigger on dimuons in the north arm and dimuons in the south arm.

Transfer

The transfer of input PRDFs (step 1 in Fig. III.6) was done by using the GRID FTP infrastructure, set up in anticipation of using the RHIC Computing Facility (RCF) for the reconstruction of the data from ATLAS LHC. This data route was not yet being used at the time of run 7 for its originally intended purpose. The main interest of this data route is the higher transfer rates achievable compared to traditional disk to disk transfer data routes (bbftp for example).

In Fig. III.7, the evolution of the daily transfer speed (in MBytes/s) is plotted as the function of date from the start of transfer. Daily transfer speeds as high as 17.4 MBytes/s were achieved. However the overall average transfer speed was only 2 MBytes/s. This very low efficiency was mainly due to the fact that there were some considerably long periods during which the GRID FTP infrastructure was in maintenance, and transfer couldn't be done. Besides, the continuous functioning of the transfer, a prerequisite for high efficiency, requires constant attention to restart the process whenever there are failures[9]. Unfortunately this couldn't be done due to the lack of manpower. The total transfer took 8 months and a half, although much of the data has already been transferred by the 6 months mark. If the GRID FTP down days could be avoided throughout the whole period, the speed of 3.9 MBytes/s could have been attained, allowing to do the whole transfer in $\sim$ 2 times less time.

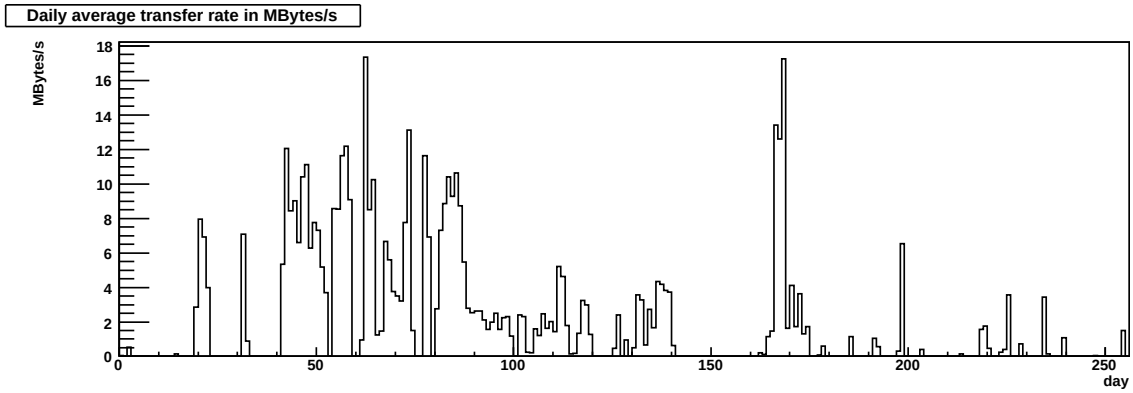

Figure III.7: Daily average transfer rate in MBytes/s over the whole transfer period.

The input raw data ($\sim$ 70 TBytes) could not be stored in the available Semi Permanent disk Space (sps) that was available ($\sim$ 4 TBytes). It was therefore stored into a dCache architecture made of 10 TBytes of hard disks and serving as a buffer to the permanent storage (HPSS). These storage spaces are depicted on the top right corner of Fig. III.6. After the transfer of each input PRDF file is done, a database table of input files is updated with information on the size of the file and on whether it comes from offline or ATP filtering.

Reconstruction

The original copies of the reconstruction code and the database containing calibration constants calculated at the moment of data taking reside at RHIC. It was thus necessary to

[9]Failures of transfer were very frequent, as the technology that was used (SRM) was a new and in its testing phase of development.

replicate them at CCF in order to proceed with the reconstruction of raw data. The replication of the reconstruction code and environment was done by copying the binaries and libraries of the compiled code each time that there was a code version change (overall there were four version changes during the whole reconstruction period). The calibration constants database however required a more frequent replication. Ideally this replication should be done daily, since the database is updated at RHIC at that frequency. But since the reconstruction had some delay, the calibration constants database needed to be replicated only when there were transferred files whose calibration constants were not available in the replicated database existing already at CCF.

The job submission scripts had therefore to check in advance whether to submit a job to the batch system (bqs workers in Fig. III.6). If there were new files without calibration, then another set of scripts that were designed to replicate the database without interfering with the jobs that are already in machine are executed. These scripts copy the database snapshots from RHIC through bbftp (bottom arrow in Fig. III.6), and recreate the database structure on the database server (ccphenix) at CCF. If a raw data file segment is ready to be submitted, then the jobs copy the input raw data files from dCache directly to the workers (step 2), where the outputs are also written. At the end of the job (step 3), the outputs are copied back to the dCache server (step 4 in Fig. III.6). The set of scripts that submit a reconstruction job for each input raw data file to the workers interact with the reconstruction database table to get information on the file segment status, telling if it has been successfully reconstructed already or not.

The most tedious part of the reconstruction work is to keep track of the reconstruction jobs that have failed and to make sure that they are are resubmitted to the workers, on the next cycle of submissions. There are various of reasons for failure. The most common ones are:

- Memory leaks,
- Loss of connection to the database,
- Loss of connection to dCache server for input/output transfer.

In order to facilitate the identification of failed jobs, a database table that holds the following information about the jobs is created:

- time when the job was submitted to workers,
- the duration of the reconstruction job,
- the amount of memory size it consumed.

A combination of these informations usually helps to localize pathological jobs that usually take untypical amounts of resources (time and memory) with respect to successful jobs.

When a job is completed successfully, the output is first written directly to the dCache system (step 4). The full path of the files is then logged to another database table with columns for input file name, output file name and sizes. This is another source of information that allows the identification of failed jobs.

Another important aspect of the reconstruction work is to manage the resources that are required for each job. The two types of filtered files (ATP and offline) have very different file

sizes. The ATP files are written until the limit of ∼5 GBytes[10] is attained. The offline filtered files however are extracted from unfiltered ones, which also have a size of ∼ 5 GBytes. This results in a file size of ∼ 500 MBytes for the offline filtered data files. The resources to be required for these (hard disk and computing time) have to reflect this difference.

Output file sizes and aggregation, transfer back to RCF

Some output files from reconstruction are of a very small size. It is not recommended to store such small files to permanent tape storage (HPSS), since the dominant resource consumer in this type of storage while retrieving files is the sequential search of those files rather than the actual copying. To avoid overburdening HPSS, it is necessary to concatenate a number of these small output files to create a bigger one suitable for tape storage. The concatenation is referred to as *aggregation*. The aggregation is done by copying the reconstructed output files from dCache to semi permanent storage (sps) shown in the middle of Fig. III.6 (step 5). Aggregation (step 6) is done run number by run number, after making sure that all the file segments from each run to be aggregated have been successfully reconstructed. At the end of aggregation jobs, the final output files, convenient for permanent storage, are sent back to dCache (step 7 in Fig. III.6), from where they are also sent back to the dCache storage at RHIC (step 8). This constitutes the end of the reconstruction cycle.

Fast analysis of the reconstructed data

The dielectron filtered sample was analyzed from the unaggregated copies that were left on sps disks. While data was still being taken, the invariant mass spectrum from MB equivalent 1665.63 M events (264.42 μb^{-1}) worth of data that emerged is shown in Fig. III.8. This analysis revealed that unfortunately the dielectron level 2 trigger efficiency was relatively low. The estimated trigger efficiency from this plot (assuming the number J/ψ per event rate of 10^{-6} found in the run 4 analysis) is ∼50%. This estimation is strongly dependant on the assumption of 10^{-6} J/ψ per event, which is only partly justified since there are many analysis differences (background level and subtraction method, efficiency correction...) that might have changed from the run 4 reference.

The full MB data production that was being undertaken at the same time having already processed 50% of the data volume, it was no longer useful to continue working on the level 2 filtered data sample in terms of statistics. No attempts to have a more precise efficiency estimation were undertaken. Moreover, this work has prompted an investigation of the trigger algorithm which revealed that the low filtering efficiency was real and due to readout electronics problems encountered in some sectors of the PC3 during run 7. The PC3 was excluded from the algorithm in subsequent runs. Only PC1-EMCal pairs are now being used to estimate the momentum, pending the full resolution of defective PC3 sectors. Although the analysis presented hereafter was preformed using the MB data reconstruction, the lvl-2 data sample was used for the optimization of the electron identification cuts. The procedure and arguments of the optimization will be the subject of a section in Sec. IV.4.

[10]The file size reduction factor is not the same as the rejection factor because central events tend to fire the triggers more often than peripheral events, resulting in a bias that results on an average event size increase in filtered events compared to minimum bias events.

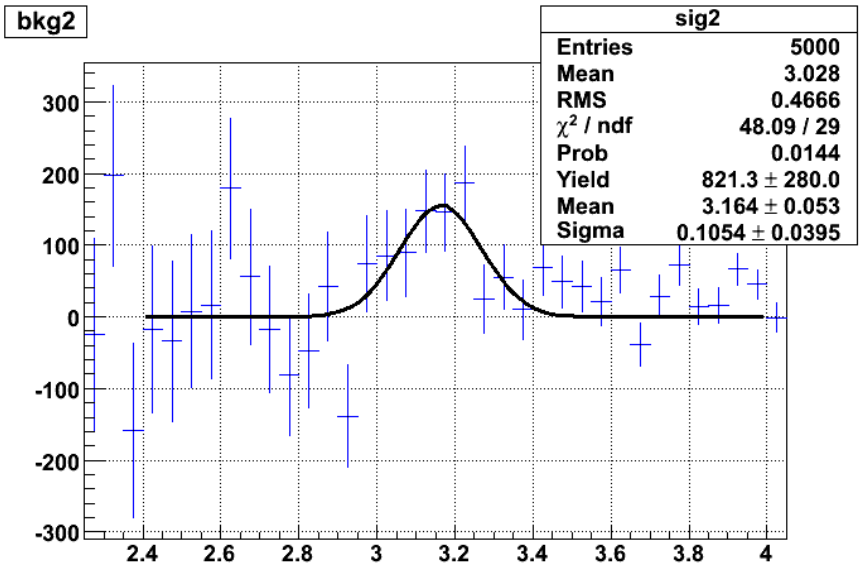

Figure III.8: Background subtracted dielectron invariant mass distribution from 22.9 B lvl-2 filtered events reconstructed at CCF, corresponding to 1.6 B equivalent MB events.

III.3.3 Other level 2 filters

In this section, the plots extracted on-line from the other level 2 filters that were reconstructed at CCF will be shown, with a brief summary of what the physics target of the filters was, and what the reconstructed data eventually served for. The actual analysis of the data to extract the plots shown below was done by the respective analyzers, while the reconstruction was carried out by myself in parallel to the dielectron sample.

Dimuon lvl-2 trigger

This trigger selects events in which at least two energetic muons ($E > 1.5$ GeV/c) with a minimum invariant mass of 2.0 GeV/c^2 were detected. Its physics interest is focused on the $J/\psi \rightarrow \mu^+\mu^-$ decay process. The plot in Fig. III.9 shows the invariant mass spectrum of dimuons that was plotted by dimuon analysers from the sample during data taking. The full reconstruction of the dimuon sample was eventually used to extract the J/ψ v_2 and R_{AA}, reported in [94].

High p_T photon lvl-2 trigger

This trigger selects events with at least one 4×4 EMCal tower tile that registers a total energy of 3.5 $>$ GeV. The main physics target of this trigger is the electromagnetic decay of low mass neutral mesons, especially the π^0 and the η. For the η, it was the first time that a peak could be seen on-line at Au+Au data taking in PHENIX. Similarly to the dielectron filtered

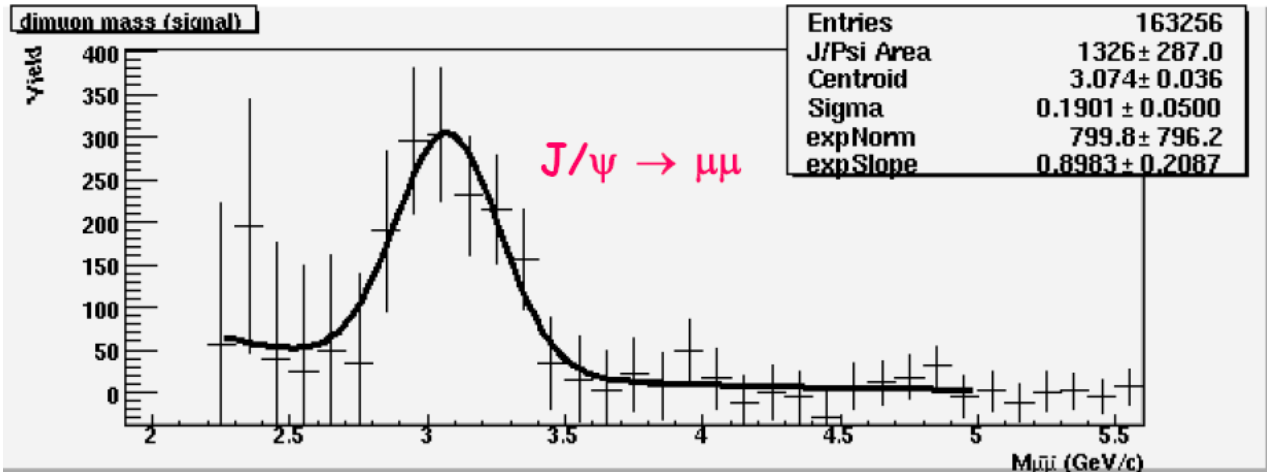

Figure III.9: The dimuon spectrum around the J/ψ mass window from the lvl-2 dimuon trigger filtered data sample.

sample, this data set was finally dropped when the full minimum bias data reconstruction was completed.

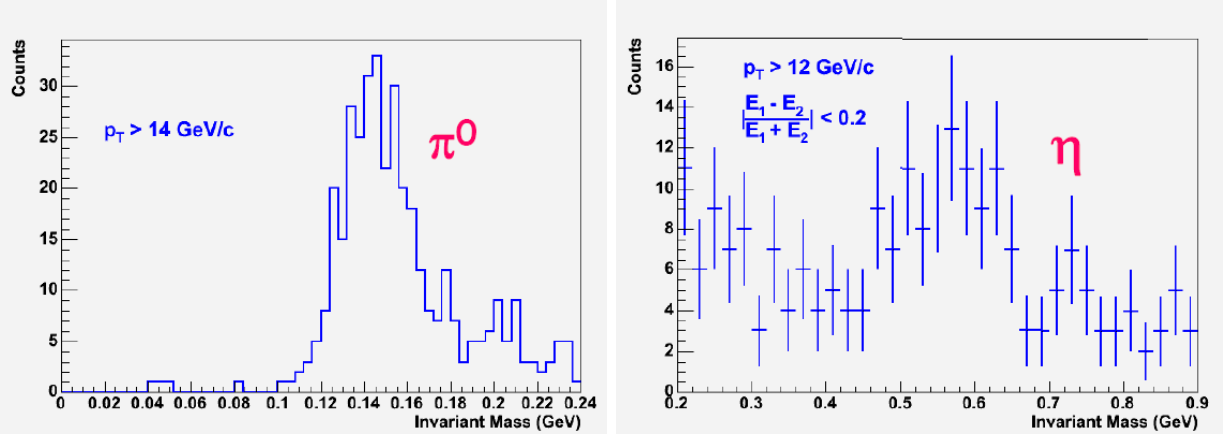

Figure III.10: The diphoton spectra from the lvl-2 high p_T trigger filtered data sample, extracted at run time in the mass window of the π^0 (left) and η (right).

III.4 Good run selection

During data taking, the actual conditions met for a given run can adversely affect the quality of data. For example, if a subsystem has a high voltage trip off, then particles going through the affected part of the apparatus will not be detected, altering the reconstruction efficiency in a non trivial way that is difficult to correct. It is the shift crew's duty in such cases to stop the run, recover the tripped high voltage and restart a new run. The run that was stopped is then tagged to be useless with the reason for which that was so. This constitutes the most basic good run selection, and runs tagged for failure by the shift crew are automatically excluded from reconstruction.

Beyond massive high voltage trips, and problems that are detectable by the on-line monitoring system, there can also be other causes that affect the efficiency of a subsystem, in a way that is not easy to detect at run time. A typical example is a change in atmospheric pressure, which affects the efficiency of gas detectors. Such runs are usually reconstructed. It is the analyzer's task to select those runs that are unfit for use by independent means. This procedure is called Quality Assurance (QA).

I was not personally involved in the QA of either the run 7 or the run 4 Au+Au samples, and it was carried out by collaborators. However, for completeness, the basic idea and procedure will be described here. QA is done by looking at the run by run variation of conveniently chosen measured parameters. Bad runs are then identified by comparing these quantities for each run to what is 'typical' for all the runs. The average over all runs is compared to the average in each run, and a run that deviates from the global tendency by some number of sigmas is excluded from analysis.

An example of such a parameter is the ratio of the number of identified electrons in the east arm to the number in the west arm ($N_{el}^{east}/N_{el}^{west}$). Since the cumulative production of electrons from many collisions has no reason to be anisotropic in azimuth, this ratio in principle should be close to one if the radiation length of the material in the acceptance before the electron identification detectors is the same in the two arms. A deviation from one indicates that either the material budget is not the same in the two arms, or there is an efficiency difference between the east and the west arm. The variation of this parameter as a function of run number for the run 7 data taking period is shown in Fig. III.11. In this figure, the removal of the HBD in the west arm is clearly seen by a jump of the ratio $N_{el}^{east}/N_{el}^{west}$ from unity to a value close to 2.25, a few runs before run number 231470. This ratio is the fractional increase in conversion electron production due to the HBD material.

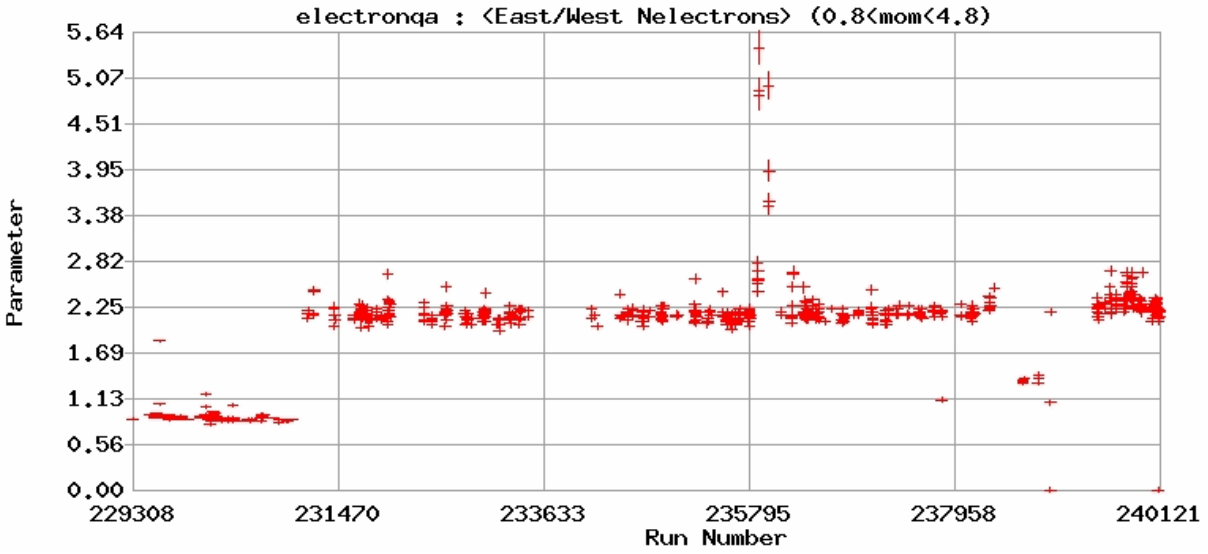

Figure III.11: The evolution of the ratio of the number of identified electrons in the east arm to the number in the west arm as a function of run number for the run 7 data set.

These two run groups (taken before and after HBD west removal) constitutes a clear classification that emerges from this QA plot. The value of the ratio is relatively stable in each of the two groups, except at two regions in the second period. The first one, visible as a

peak to the right of run number 235795, is due to the change in the magnetic field to the ++ configuration that was done for a few runs for purpose of testing. The second one is a dip approximately half the way between run number 237958 and run number 240121. In this run period, a converter of radiation length similar to that of the HBD ($\sim 2.4\%$) was introduced in the east arm. Converter runs are useful for the calculation of open charm yield through non photonic electron yields as outlined in Sec. I.2.2.3.

In addition to HBD west in/out, another classification will be made between runs before and after the magnetic field polarization reversal from +− to −+. This variation has no consequence on the ratio $N_{el}^{east}/N_{el}^{west}$, and is not visible in Fig. III.11. Reference will be made in the coming chapters to the following three run groups.

1. **Group 1 (G1):** Runs with both HBD east and west in and taken with the +− magnetic field configuration

2. **Group 2 (G2):** Runs with only HBD east in and taken with the +− magnetic field configuration

3. **Group 3 (G3):** Runs with only HBD east in and taken with the −+ magnetic field configuration

The QA plot in Fig. III.11 also shows a statistically significant deviation for some runs with respect to the general tendency of other runs in the same group. In the QA process, such runs are removed for safety. The condition for removal is that for a run, the QA parameter, here $N_{el}^{east}/N_{el}^{west}$ plus/minus its errors, is outside of the ± 4 standard deviation band formed by averaging $N_{el}^{east}/N_{el}^{west}$ values over all runs in the group where it belongs. Another variable considered in the QA for run 7 is the number of light meson Dalitz decay electrons in each EMCal sector.

After the QA, the number of accepted runs and events for each group stated above is given in Tab. III.2, with the corresponding luminosity.

Run group	Number of runs	Number of events	Luminosity(μb^{-1})
G1	106	675509699	106.1
G2	1798	1300899165	204.1
G3	2780	1646304805	205.9

Table III.2: Number of runs, events and the corresponding recorded luminosity for the three run groups.

Chapter IV

Analysis

In this chapter, the analysis steps taken to extract the J/$\psi \rightarrow e^+e^-$ nuclear modification factor R_{AA} and elliptic flow v_2 from the run 7 Au+Au data set will be described. Some of the steps were trained and used as a cross check of the main analysis at the time of the run 4 data set publication [75]. The analysis can be schematically divided into *signal counting* and *efficiency corrections*. This chapter starts by stating all ingredient necessary for the calculation of the R_{AA} (Sec. IV.1). This is followed by a description of the procedures of producing simulated data used to calculate the efficiency corrections (Sec. IV.2). The parameters used in identification of electrons from the hadronic background composed mainly of pions and kaons will be the subjects of Sec. IV.3. The raw electron identification parameters are corrected to absorb their momentum and EMCal sector by sector variations (Sec. IV.3.2.2). After corrections, all distributions in simulation must reflect those in real data for the simulation to be reliable for acceptance and efficiency calculations. Such comparisons are shown when relevant. In the efficiency correction calculations, two types of efficiencies which will be assumed to be decoupled are considered. The first one of these is acceptance times reconstruction and electron identification efficiency, which exhibits a p_T dependence that arises from the acceptance effects (Sec. IV.5). The second one is the occupancy dependent efficiency correction (Sec. IV.5.3). In the next section, the J/ψ signal counting using the invariant mass distribution of electron pairs, and the subtraction of various background sources (Sec. IV.6) will be detailed. Before concluding, a summary of the systematic error sources from all the steps will be given (Sec. IV.7).

IV.1 Invariant yield calculation

The J/ψ nuclear modification factor at a given rapidity (y), p_T and within a given centrality class (cent) bin is expressed as

$$R_{AA}(y, p_T, cent) = \frac{Y_{AA}(y, p_T, cent)}{< N_{coll}(cent) > Y_{pp}(y, p_T)} \tag{IV.1}$$

where $Y_{pp}(y, p_T)$ and $Y_{AA}(y, p_T, cent)$ are the J/ψ invariant yields in A+A collisions within the centrality class *cent* and p+p collisions respectively as a function of transverse momentum p_T and rapidity y. $< N_{coll}(cent) >$ is the average number of collisions corresponding to the centrality class *cent*.

The J/ψ invariant yield in A+A type collisions is given by

$$Y_{AA}(y, p_T, cent) = \frac{B_{ll}}{2\pi p_T}\frac{d^2N_{AA}(y, p_T, cent)}{dydp_T} = \frac{B_{ll}}{2\pi p_T}\frac{N_{AA}(y, p_T, cent)}{\Delta y \Delta p_T} \times \frac{1}{N_{evt}} \times \frac{1}{\epsilon(p_T) \times \epsilon(cent)}. \quad \text{(IV.2)}$$

The right hand side of this expression is composed of

- B_{ll}: The branching ratio of the dileptonic decay of the J/ψ equal to 5.94 ± 0.06 for J/$\psi \to e^+e^-$ and 5.93 ± 0.06 for J/$\psi \to \mu^+\mu^-$ [39].
- $\frac{N_{AA}(y,p_T,cent)}{\Delta y \Delta p_T}$: The signal count in the centrality selection *cent* within transverse momentum and rapidity bins Δy and Δp_T centred at y and p_T (Sec. IV.6).
- N_{evt}: The number of minimum bias events in the centrality selection from which the signal counting has been done.
- $\epsilon(p_T)$: The acceptance $\times$ electron identification efficiency correction dependent on p_T, calculated from simulation by the expression:

$$\epsilon(p_T) = \frac{dN_{sig\_rec}/dp_{T,rec}}{dN_{sig\_gen}/dp_{T,gen}}. \quad \text{(IV.3)}$$

  The denominator is the number of generated signal particles in a given $p_{T,gen}$ window, where $p_{T,gen}$ is the transverse momentum of the *generated* J/ψ. The numerator is the number of signal that it was possible to reconstruct in a $p_{T,rec}$ window of the same range as above, but using the *reconstructed* transverse momentum. Using the two different p_Ts takes into account the migration of J/ψs into a different p_T bin at reconstruction due to finite momentum resolution. The same electron identification cuts as those used in signal counting are employed. The calculation of $\epsilon(p_T)$ is explained in Sec. IV.5.2.
- $\epsilon(cent)$: The calculation of $\epsilon(cent)$ is done by embedding simulated J/ψ hits into real data hits and running the reconstruction algorithms. The ratio of the number of J/ψs retrieved to the number of J/ψ initially embedded gives the occupancy dependent efficiency loss correction. This procedure is detailed in Sec. IV.5.3.
- $\frac{1}{2\pi p_T}$: This factor arises from the relativistically invariant differential volume element that should be used to derive the cross section

$$Y_{AA}(\overrightarrow{p}) = dN/d\Omega = E\frac{dN}{d^3\overrightarrow{p}} \quad \text{(IV.4)}$$

  where $\overrightarrow{p}$ is the three momentum and E is the energy[1]. One can then express the volume element $d^3\overrightarrow{p}/E$, in terms of the (y, p_T, ϕ) coordinate by using the transformation from three three momentum vector (p_x, p_y, p_y)

$$(p_x, p_y, p_z) = (p_T\sin(\phi), p_T\cos(\phi), \sqrt{p_T^2 + m^2}\sinh(y)) \quad \text{(IV.5)}$$

[1]The invariance of $\frac{E}{d^3\overrightarrow{p}}$ arises from the fact that E and the momentum component along the boost axis transform identically whereas the other momentum coordinates remain as they are.

and its Jacobian

$$\mathcal{J} = det \begin{pmatrix} 0 & \sin(\phi) & p_T\cos(\phi) \\ 0 & \cos(\phi) & -p_T\sin(\phi) \\ -\sqrt{p_T^2+m^2}\cosh(y) & \frac{\sinh(y)}{\sqrt{p_T^2+m^2}} & 0 \end{pmatrix} = p_T\sqrt{p_T^2+m^2}\cosh(y) \tag{IV.6}$$

The expression of the volume element in Eq. IV.4 then becomes:

$$d\Omega = \frac{dp_x dp_y dp_z}{E} = \mathcal{J}\times\frac{dp_T dy d\phi}{E} \tag{IV.7}$$

$$= \frac{p_T\sqrt{p_T^2+m^2}\cosh(y)}{E} dp_T dy d\phi = p_T dp_T dy d\phi = \Omega' \tag{IV.8}$$

where in the last step the equality $E = \sqrt{p_T^2+m^2}\cosh(y)$ is used [2]. Since there is no dependence in ϕ this differential volume element can be integrated over ϕ to construct a ϕ independent volume element that is also relativistically invariant

$$d\Omega'' = \int_{\phi=0}^{2\pi} d\Omega' = 2\pi p_T dp_T dy \tag{IV.9}$$

which is the volume element used in Eq. IV.2.

The invariant yield in p+p collisions $Y_{pp}(y,p_T)$ is calculated as

$$Y_{pp}(y,p_T) = \frac{B_{ll}}{2\pi p_T}\frac{d^2N_{p+p}(y,p_T)}{dydp_T} = \frac{B_{ll}}{2\pi p_T}\frac{N_{p+p}(y,p_T)}{\Delta y\Delta p_T}\times\frac{1}{N_{evt}}\times\frac{1}{\epsilon(p_T)} \tag{IV.10}$$

where the terms N_{evt}, $\frac{N_{p+p}(y,p_T)}{\Delta y\Delta p_T}$, $\frac{1}{2\pi p_T}$ and $\epsilon(p_T)$ are analogous to their A+A counterparts except for the centrality dependence.

The invariant yield is related to the invariant cross section $\frac{d\sigma_{pp}^{J/\psi}}{dy}$ through a multiplicative factor equal to the total p+p inelastic cross section $\sigma_{pp}^{inel} = 42$ mb:

$$B_{ll}\frac{d\sigma_{pp}^{J/\psi}}{dy} = \sigma_{pp}^{inel}\times Y_{pp}(y,p_T). \tag{IV.11}$$

The p+p invariant yield as a function of p_T was not calculated in this thesis. Instead, values published by PHENIX [52] are used. For completeness, the invariant yield in p+p collisions is given in Tab. IV.1 and plotted in Fig. IV.1. For R_{AA} calculation as a function of centrality only the p_T integrated invariant yield is required. Its value is

$$B_{ll}\frac{d\sigma_{pp}^{J/\psi}}{dy} = 44.3\pm1.4(stat)\pm5.1(syst.\ corr.)\pm4.5(syst.\ uncorr.)\ \text{nb}, \tag{IV.12}$$

where the systematical uncertainties are split into a correlated systematical part and a global normalization part, the later resulting from the uncertainty on the efficiency of the BBC trigger. The uncorrelated systematical errors are added in quadrature to the statistical errors.

[2] This results from inverting the rapidity definition $y = \frac{1}{2}\ln(\frac{E+p_z}{E-p_z})$.

p_T(GeV/c)	$\frac{1}{2\pi p_T} \times \frac{d\sigma_{pp}^{J/\psi}{}^2}{dp_T dy}$ (nb)	stat.	syst. uncorr.	global
0.125	4.26	$^{+0.78}_{-0.78}$	± 0.49	± 0.43
0.375	4.42	$^{+0.43}_{-0.43}$	± 0.50	± 0.45
0.625	3.29	$^{+0.34}_{-0.34}$	± 0.38	± 0.33
0.875	3.04	$^{+0.26}_{-0.26}$	± 0.35	± 0.31
1.125	2.55	$^{+0.22}_{-0.22}$	± 0.29	± 0.26
1.375	1.99	$^{+0.19}_{-0.19}$	± 0.23	± 0.20
1.625	1.52	$^{+0.15}_{-0.15}$	± 0.17	± 0.15
1.875	1.29	$^{+0.14}_{-0.14}$	± 0.15	± 0.13
2.125	1.18	$^{+0.13}_{-0.13}$	± 0.13	± 0.12
2.375	0.618	$^{+0.103}_{-0.103}$	± 0.070	± 0.062
2.625	0.557	$^{+0.091}_{-0.091}$	± 0.064	± 0.056
2.875	0.443	$^{+0.079}_{-0.079}$	± 0.050	± 0.045
3.125	0.194	$^{+0.061}_{-0.061}$	± 0.022	± 0.020
3.375	0.257	$^{+0.059}_{-0.059}$	± 0.029	± 0.026
3.625	0.145	$^{+0.045}_{-0.045}$	± 0.017	± 0.015
3.875	0.136	$^{+0.047}_{-0.047}$	± 0.015	± 0.014
4.5	0.0356	$^{+0.0111335}_{-0.0111}$	± 0.0041	± 0.0036
5.5	0.0000	$^{+0.0041884}_{-0.0000}$	± 0.0000	± 0.0000
6.5	0.00445	$^{+0.00273}_{-0.00273}$	± 0.00051	± 0.00045
7.5	0.000377	$^{+0.000998}_{-0.00037}$	± 0.000043	± 0.000038
8.5	0.00105	$^{+0.00074}_{-0.00074}$	± 0.00012	± 0.00011

Table IV.1: The invariant cross section of J/ψ production in p+p collisions at $\sqrt{s} = 200$ GeV, as a function of p_T at mid rapidity ($|y|$<0.35). The error columns are for the statistical $\oplus$ point to point uncorrelated systematical uncertainties, point to point correlated systematical uncertainties and global uncertainty respectively.

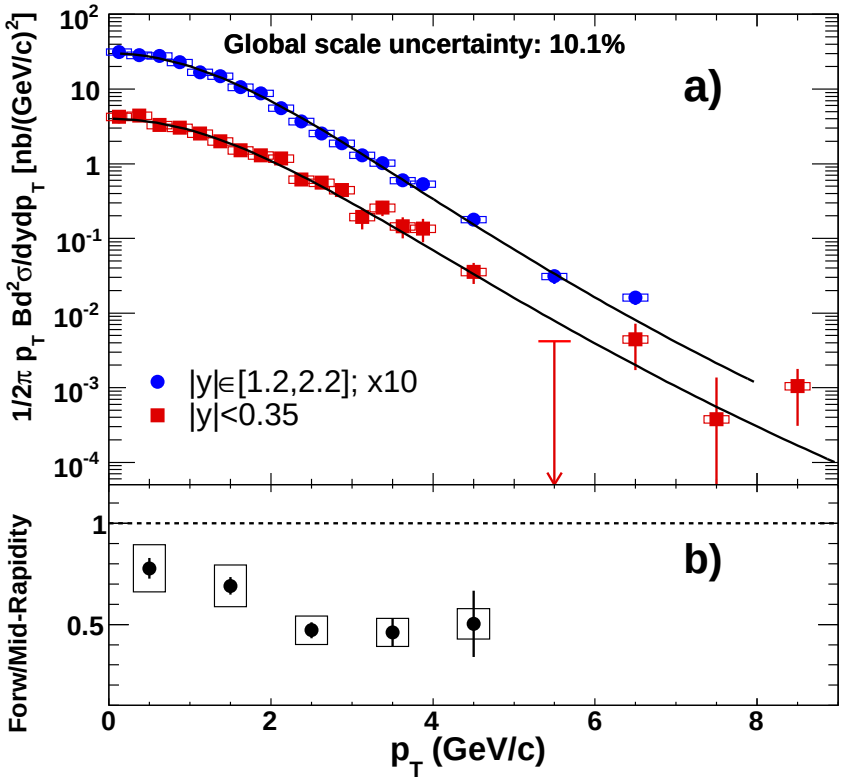

Figure IV.1: Top panel: The invariant cross section of J/ψ production in p+p collisions at $\sqrt{s}$ = 200 GeV, as a function of p_T at mid rapidity (red points) and at forward rapidity (blue points). The black lines are phenomenological fit to the data points with the function $(A \times (1 + (p_T/B)^2)^{-6})$. Bottom panel: The forward rapidity to mid rapidity cross section ratios.

IV.2 Simulation

The simulation used to calculate the p_T dependent efficiency is done in three steps that will be described briefly here. First, the J/ψ signal has to be generated with a choice of vertex, transverse momentum and rapidity distributions that reflects as closely as possible the real distributions. The generated J/ψs are then forced to decay into an electron positron pair. The four momenta and vertices of the decay electrons are then fed into a GEANT 3 [95] based full simulation of the PHENIX detector. The last step is to simulate the detector and reconstruct the tracks. Finally the reconstructed tracks are analyzed using the same framework as real data.

IV.2.1 Event generation

For the acceptance $\times$ efficiency to make any sense, the distribution of the creation points of the generated J/ψs, $\overrightarrow{x}_{vtx} = (x_{vtx}, y_{vtx}, z_{vtx})$, as well as the distributions of transverse momentum, p_T and rapidity, y should be as close as possible to the real distributions. In the transverse plane, the J/ψs are assumed to be created at (x_{vtx}, y_{vtx})=(0,0)[3]. The real distribution of longitudinal vertex position z_{vtx} can be readily inferred from the measured distributions of the vertex positions, since with the exception of those from B meson decays (a few % at most), all J/ψs are created through hard processes at the collision vertex. Fig. IV.2 shows the longitudinal collision vertex distribution of events within a $\pm$30 cm window for a typical Au+Au run. The distribution reflects the form of the ion bunches along the beam axis. A Gaussian fit to the distribution gives a width of 23.9 cm.

The p_T and y distributions are more difficult to know in advance. Fortunately, the acceptance $\times$ efficiency result varies little with the input distributions. As an example, a previous study has shown that the effect of changing the input y distributions within reasonable limits affects the overall efficiency by $\sim$ 0.7% [96]. This value is added to the list of point to point correlated systematical errors. The input y and p_T distributions used here are originally fixed by using the PYTHIA event generator [97] (v. 6.205). The algorithm used to select J/ψ events from PYTHIA can be schematically described as

```
loop (Generate a p+p event at 200 GeV/c)
    if ( event contains a J/ψ )
        Record generated y, p_T and z_vtx of J/ψ for normalization
        Increment number of generated event counter (ngen)
        Force the J/ψ to decay into an electron positron pair)
            if ( Polar angle θ of electrons falls within 69.° < θ <111.°)
                    Write four momenta of decay particles
                    Generate and write z_vtx for the event
                    Increment number of accepted event counter (nacc)
            endif
        endif
    endif
```

[3]The position along the transverse plane of the creation point of J/ψs influences the momentum resolution and the center of the reconstructed J/ψ mass peak. Its influence is however small (of the order of a few MeVs), and can be bypassed by taking a signal counting window of size three times the reconstructed width of J/ψ ($\pm 3\sigma_{J/\psi\ rec.}$), which is much larger than a few MeVs.

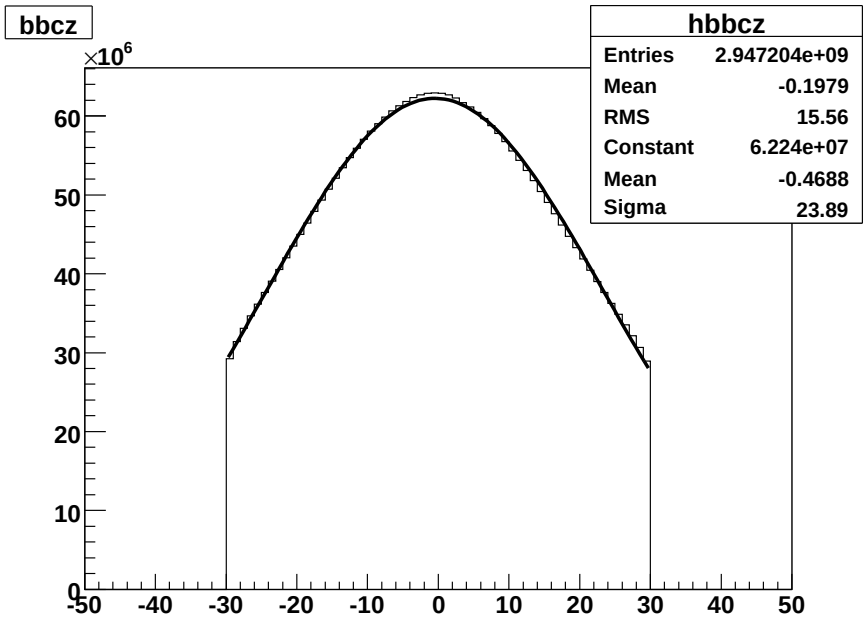

Figure IV.2: Longitudinal vertex distribution of collision points measured by the BBC, with a cut at ±30 cm. The distribution is fitted in its range with a Gaussian function whose width is 23.9 cm.

endloop

The actual PHENIX central arm acceptance in polar angle is $70.4° < \theta < 109.6°$. The condition of acceptance for decay electrons and positrons is deliberately made slightly wider than the actual acceptance to accommodate for edge effects and bending in the magnetic field. The left most plot in Fig. IV.3 shows the z_{vtx} distribution of generated J/ψ in red and accepted J/ψs in blue on a log scale. The middle and right most plots in the same figure provide a comparison of the p_T and y distributions of the generated (red) and accepted (blue) J/ψs. A rough estimate of the central arm acceptance is provided by the ratio of the integral between the generated and accepted distributions. For a vertex cut of $|z_{vtx}| < 30$ cm and rapidity cut of $|y| < 0.35$, this ratio is of the order of 20%. Note that this number alone is not of much use, because it doesn't account for the efficiency of detection and reconstruction, which will be the objective of the next steps.

IV.2.2 Particle propagation

The electron - positron pair per event of the selected events is written in the OSCAR (Open Standard Codes And Routines) [98] format, where for each event the header contains the number of particles in the event, and the body part contains particle identification number, four momenta, mass and vertex positions of the decay products. This is fed to PISA (PHENIX Integrated Simulation Application), the standard PHENIX simulation package based on GEANT 3 [95].

PISA implements the detailed geometry and material composition of the detector as well as the relevant magnetic field. The particles that are fed to PISA are propagated under the

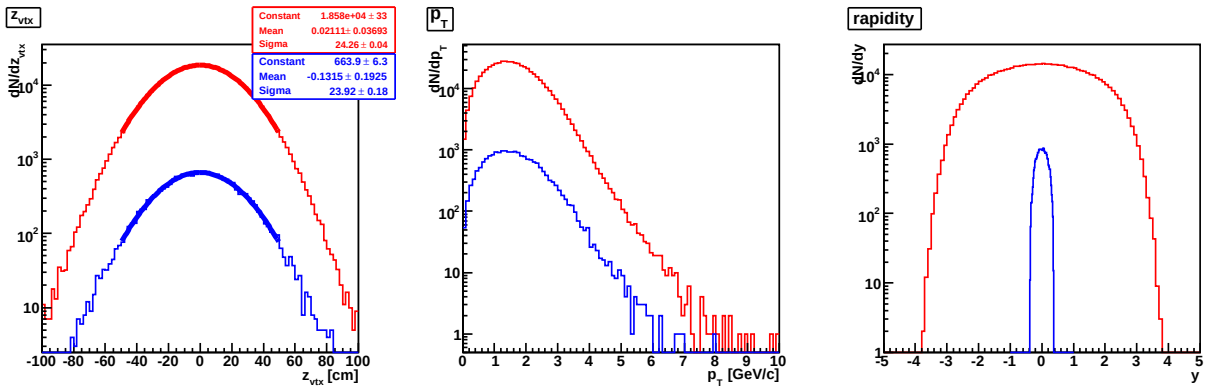

Figure IV.3: The z vertex position in cm (left panel), p_T in GeV/c (middle panel) and rapidity (right panel) distributions of generated (red) and accepted (blue) J/ψ.

influence of the magnetic field. Whenever a surface is encountered, the particle is subjected to multiple scattering and energy loss that reflect the material content of the surface. At the end of the propagation process, an n-tuple is written which contains at each line full spatial information of each interaction point of the particles with the detector surfaces, and the incoming and outgoing four momenta as well as the energy loss suffered by the particle.

IV.2.3 Response simulation and reconstruction

The next step uses the interaction positions and associated energy loss information written out by PISA to simulate the actual response of the active detector surfaces to the energy deposit by each interaction. Gain and noise are implemented at this step as close as possible to real life detector. The response by each detector is transferred to an emulator of the acquisition electronics, that writes down the simulated detector response in a similar format to that used for real data. This format is called the 'hit DST' format. For a simulation of only the J/ψ decay products into the central arms (not full events), none of the decay products reach the BBC, and therefore it is not possible to simulate the BBC response. For this reason, the z_{vtx} is manually transferred from the event generator to the global event information containers.

Beyond this stage, the same algorithm as the one used for real data reconstruction is implemented. For convenience the detector response simulation and reconstruction are performed in a single step. The fully reconstructed tracks from reconstruction are written out in a ROOT [99] tree, and stored in a file that also contains the hit DST data containers from the response simulation step. As an example, the DCH hit container has the information of all 'events' in the DCH, namely, the geography (arm, sector, wire and plane) and timing (time, width of hit) of every signal detected by the wires. The reconstructed tracks are written out in the same type of container as that of real data tracks that contain tracking and outer detector association solutions. The ROOT tree structure that stores central arm track information is called PHCentralTrack. It contains, for each pattern recognition solution (track), the following information

- **Tracking solutions:** Momentum, polar and azimuthal angles at vertex, polar and azimuthal angles at tracker radius, z position at tracker radius, track quality ...

- **Outer detector association:** Solutions to attempts of associating tracks to outer identification detectors. This includes the measurements in outer detectors that serve as electron identification parameters, and the distance between the track projection and the cluster in the outer detector to which the track was associated

IV.3 Electron Identification

PHENIX has a very powerful electron identification (EId) capability, attained by the combined use of the RICH and EMCal. After pattern recognition, the solutions are projected outwards in an attempt to associate them with clusters in the EMCal and rings in the RICH[4]. If the projection succeeds, in other words, if the track projection falls next to a cluster in the EMCal or a ring in the RICH within a window whose size is fixed. The properties of the cluster/ring to which track was associated are added to the list of parameters of the track and used for EId. The identification parameters that involve RICH and EMCal detectors will be discussed separately below.

IV.3.1 RICH based EId

The simplest and most straightforward EId is provided by the RICH. As it was discussed in Sec. II.4.4, the mass dependence of the momentum threshold of Čerenkov emission results in a momentum range where only electrons and no hadron can emit Čerenkov radiation. In the RICH volume, when CF_4 is used as radiation material, this range is 0.2 GeV/c to 4.8 GeV/c. In this dynamical range, the successful association of a track to Čerenkov ring formed in the RICH PMT is therefore a strong indication that the track is formed by an electron. One can then use ring parameters and track - ring association parameters for electron identification. Below is a list of these parameters.

1. **Number of fired PMTs (n_0).** This number is counted within a given range of radii from the ring center. There are a number of radius ranges used, depending on the particle to be identified. The typical ring radius for an electron at the PMT surface is $\sim 5.9 \pm 2.5$ cm. The most relevant parameter for electron identification is therefore n_0, the number of fired PMTs within a range of 3.4 cm to 8.4 cm from ring center.

2. **Number of photoelectrons (npe_0).** can be estimated from the sum of the ADC counts of fired PMTs within the nominal ring radius range for electrons (3.4 cm to 8.4 cm).

3. **Quality of a circular fit to the ring (χ^2).** After the ring finding algorithm successfully identifies a ring in the PMT plane, a circular fit is attempted on the positions of the centers of fired PMTs. The χ^2 of this fit can be used as an EId parameter. It is normalized by the npe0 variable to account for the purely statistical effect of better fit quality attained for rings where larger number of photons are collected.

4. **Distance between track projection and center of ring (disp).** This measure is used as an estimate of how well the track is associated with the RICH ring.

The distributions of these parameters for simulated electrons are shown in Fig. IV.4.

[4]Association is also done to other outer detectors (TOF, TEC, Aerogel), but these are not used here.

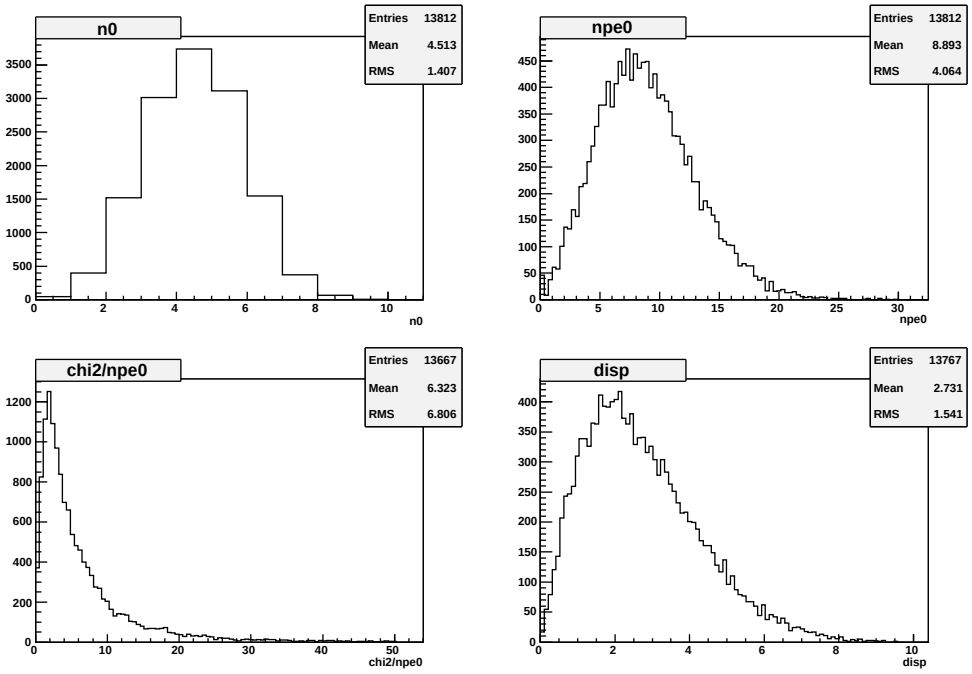

Figure IV.4: Distributions of RICH based EId parameters, n_0 (upper left), npe_0 (upper right), χ^2/npe_0 (lower left) and disp (lower right).

IV.3.2 EMCal based EId

The EMCal collects the energy deposited by showers of a charged particle passing through it. Electrons, positrons and photons form electromagnetic showers. The two dominating processes in electromagnetic showers are bremsstrahlung radiation and photon conversion. The parent first radiates photons if it is an electron/positron and converts into an electron positron pair if it is a photon. This cascade-like process continues until the created photons are lower in energy than $2\times M_e$ (where $M_e = 511$ keV/c^2 is the mass of an electron), and the electron–positron pair is produced almost with no kinetic energy. At this point, the remaining energy of electrons is dissipated through ionisation and that of photons through Compton scattering. This shower creation mechanism is typical of electromagnetic showers. If the radiation length[5] of the material inside which the shower is created is large, the rate of radiation and conversion becomes frequent enough so that even energetic electrons are completely stopped, leaving their kinetic energy in the form of photons that are detected by the calorimeter.

There is an important distinction between electromagnetic and hadronic showers that is exploited to identify electrons. Hadronic showers are formed by the repeated inelastic scattering of energetic hadrons on atomic nuclei. The secondaries of such processes are decay products of the excited nuclei, mostly pions and nucleons. There is also production of some π^0s which will lead to an electromagnetic component through almost exclusive decay of π^0s into a photon pair. Unless the inelastic cross section is made high by a deliberate choice of materials (ex. Tungsten), there is a good chance that hadrons do not leave much energy. This

[5] Radiation length X_0 is a scaling variable for the probability of occurrence of bremsstrahlung or pair conversion. It is given in g/cm^2, and the energy loss rate of an electron is given by $-dE/dx = E/X_0$.

is particularly true of the materials which are chosen for the construction of the EMCal in PHENIX. Consequently, electrons and photons are stopped inside the EMCal, leaving almost all their energy, and pions and kaons generally deposit only a small fraction of their kinetic energy.

It is thus very reasonable to identify electrons by comparing the energy E measured in the EMCal cluster with the momentum p reconstructed in the tracking for the associated candidate. For electrons the E/p ratio should be $\sim$ 1 while for hadrons, smaller values prevail. The distribution of E/p in a simulation of electrons and in real data where a typical RICH based EId cut of $n_0 \geq 2$, $\chi^2/npe_0 \leq 20$ and $disp \leq 5$ cut is applied[6] is shown in Fig. IV.5.

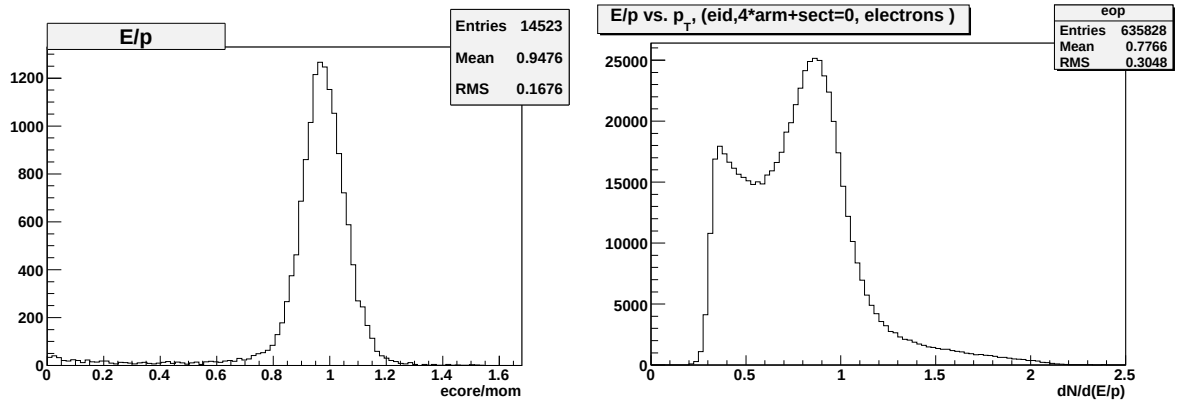

Figure IV.5: E/p distribution in simulation (left) and real data with RICH based EId cut for $E/p > 0.3$ (right).

A notable difference can be seen between the two distributions. While for simulation of electrons, a clear peak emerges at $E/p \simeq 1$, the peak in real data lies above a decreasing background that is much more pronounced than in the distribution of simulated electrons. This background is due to the non perfect rejection power of RICH based EId cuts and accidental association of hadrons (mostly pions) to RICH rings created by electrons. Such an occurrence is possible because hadrons are far more copiously produced than electrons especially in A+A type collisions, from which the plot on the right side of Fig. IV.5 is extracted. The following section discusses about how to statistically subtract out (at least partially) the background contribution from mis associated hadrons.

IV.3.2.1 Swapped track subtraction

Swapped track subtraction consists in running the ring association algorithm on all tracks after reflecting them around the $z = 0$ plane while leaving the RICH rings where they are (or equivalently reflecting the RICH rings around $z = 0$ while leaving the tracks where they are). Each track has therefore a fictitious set of identification parameters (called swapped EId parameters, sn_0 equivalent to n_0, $snpe_0$ equivalent to npe_0, etc) that are produced by associating it to RICH rings on the wrong side of the detector. The basic idea behind this procedure is that the distribution of tracks that were successfully associated with a RICH ring on the wrong side is a robust statistical estimation of the distribution of accidentally associated true hadrons tracks, and can be subtracted out from the electron/positron distribution ensuing

[6]There is a global cut $E/p \geq 0.3$ applied on the data.

from regular EId parameter cuts. This is true because hadrons are produced in much larger numbers than electrons, in such a way that the number of true electron tracks that are associated to RICH rings in the swapped configuration is much smaller than the number of true pion tracks associated to RICH rings in the swapped configuration.

Practically, for any single electron/positron distribution extracted from a given sample of tracks with a given set of regular RICH based cuts (say $n_0 \geq n_0^{min}$, $\chi^2/npe_0 < (\chi^2/npe_0)_{max}$ and $disp < disp_{max}$), the contribution of accidentally associated hadrons can be subtracted out by an estimation based on the distribution ensuing from the same sample of tracks with the application of an identical set of cuts on the swapped identification parameters ($sn_0 \geq n_0^{min}$, $s\chi^2/snpe_0 < (\chi^2/npe_0)_{max}$ and $sdisp < disp_{max}$). As an illustration, Fig. IV.6, shows a distribution E/p of electron tracks selected with the set of RICH cuts $n_0 \geq 2$, $\chi^2/npe_0 < 20$ and $disp < 5$ in black, and the estimation of the contribution of accidentally associated hadrons with the same cuts on the swapped EId parameters on the same set of initial tracks $sn_0 \geq 2$, $s\chi^2/snpe_0 < 20$ and $sdisp < 5$ in red. The bottom blue histogram is what remains after subtracting the middle red from the upper black histogram. The background contribution is considerably reduced, although not completely. The remaining distribution is at least due to high momentum pions that actually produced a RICH hit. The resultant E/p distribution can be described fairly well by a Gaussian (for the electron peak) plus exponential (for the residual background) as shown by the fit function in red. The Gaussian peak has a width of $\sigma_{E/p} \sim 0.15$. One can use a cut on the E/p value of a track at a given number of $\sigma_{E/p}$s from the center of the Gaussian peak. But as it will be seen in Sec. IV.3.2.2, the E/p distribution peak has a momentum and EMCal sector dependence that must be corrected to attain maximum identification efficiency using this cut.

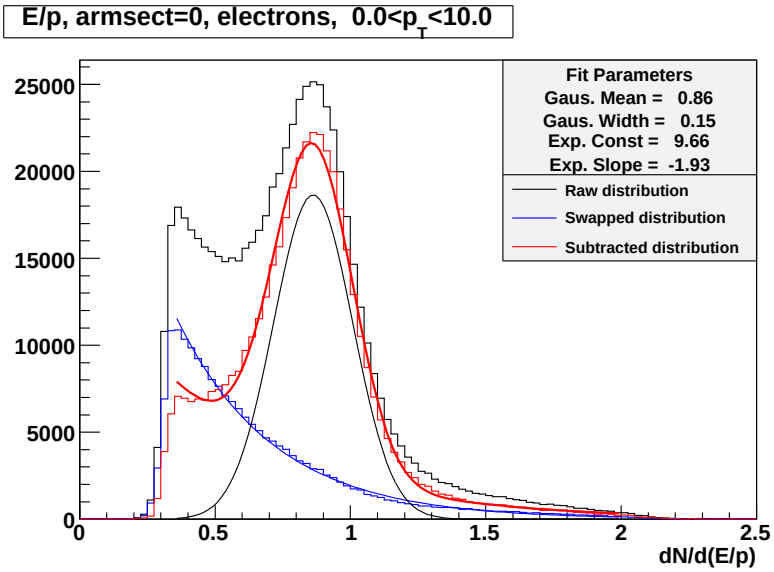

Figure IV.6: E/p distribution of normal tracks (upper black histogram) and swapped tracks (middle red histogram). The lower blue histogram is what remains after subtracting the swapped track E/p distribution to that of the normal tracks. The exponential tail composed of accidentally associated hadrons is suppressed.

In addition to the E/p distribution, it is also possible to use the distance between the EMCal shower center of gravity (CG) and the track projection to the EMCal surface as an

identification parameter. This parameter is an estimate of the quality of the matching between the track and its associated shower in the EMCal. Projections of tracks from true electrons are in general closer to the shower CG than mis-associated hadrons. An upper cut on this parameter can thus provide further pion rejection. Two matching parameters are employed, one in the azimuthal direction, called *emcdphi* (radians) and another in the longitudinal direction called *emcdz* (cm). The distributions of these matching parameters in pure electron simulation[7] are shown in Fig. IV.7.

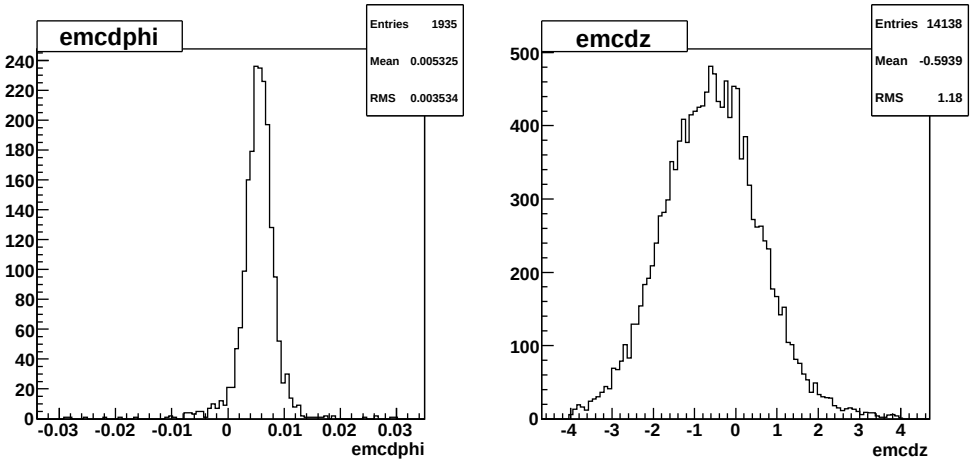

Figure IV.7: The raw EMCal matching parameters emcdphi and emcdz in single electron simulations.

IV.3.2.2 Recalibration of E/p

The EMCal matching parameters are sensitive to the alignment of the EMCal sectors. Similarly the E/p ratio can be sensitive to the quality of calibrations that may be different from sector to sector. In addition, both matching and E/p distributions depend on the momentum resolution that varies with the electron momentum. The momentum dependence of E/p resolution can be expressed as a function of parameters of the EMCal energy resolution which can be described by $\sigma_E/E = const1 + a1/\sqrt{E}$ and those of the momentum resolution which can be expressed as $\sigma_p = const0 + a0 \times p$:

$$\sigma(E/p) = \sqrt{const + \frac{a1}{p} + (a0 \times p)^2}. \tag{IV.13}$$

EId cut parameters with non uniform mean and standard deviation are inconvenient to use during analysis, because one will have to implement momentum, sector and charge dependent cuts. To avoid this complication, a *sigmalization* of the distributions is performed. Sigmalization refers to reducing the distributions at all momenta and in all sectors to a Gaussian distribution centered at 0 and with unit width. The sigmalization corrections, which are applied on a track by track basis at analysis level, are called *recalibration* in contrast

[7]These distributions are only approximately Gaussian. Before use, they should be normalized to have a Gaussian distribution centered at zero and with one standard deviation using a procedure that will be described in the next section.

to the calibration corrections of the detector applied during reconstruction. Recalibration is required mainly to maximize the efficiency of identification cuts, which would otherwise be compromised due to unavoidable imperfections in the initial calibrations and uncertainties in the exact geometry of the detector (misalignments). The sigmalization (extraction of correction factors to be applied to recalibrate the EId parameters) is done in three steps[8] that are described below, using E/p as an illustration.

1. The first step consists in parametrizing the dependencies of the width and peak values of the distribution of cut parameters. A physically motivated parametrization is used if one exists, like in the case of the momentum dependence of the E/p width (Eq. IV.13). If no such physical parametrisation exists (an example is the peak position of the E/p distribution) a polynomial function of 2^{nd} or 3^{rd} degree is used.

   The E/p plots for various momentum bins from a portion of the run 7 Au+Au data are shown in Fig. IV.8 for the E0[9] sector (PbGl) and in Fig. IV.9 for the W0 sector (PbSc). The top black histogram is the raw E/p distribution with RICH cuts ($n_0 \geq 2$, $\chi^2/npe_0 \leq 20$ and $disp < 5$ cm), the middle blue histogram is the distribution with the same cuts on swapped RICH cuts ($sn_0 \geq 2$, $s\chi^2/snpe_0 \leq 20$ and $sdisp < 5$ cm), whereas the bottom red histogram is the subtracted distribution.

   The swapped subtracted distribution is fitted with a Gaussian + exponential fit,

$$\exp(A + B \times x) + C \times \exp((x - M)/\sigma)^2. \tag{IV.14}$$

   The exponential is used to represent the residual background, so that the Gaussian mean M and width σ are the true electron E/p mean and width.

2. M and σ are then plotted as a function of momentum, and fitted with the chosen parametrization. The plots in Fig. IV.10 show M and σ collected from the plots in Fig. IV.8 and Fig. IV.9. The parametrization used for σ is the formula in Eq. IV.13 whereas the peak M is fitted with a 3^{rd} degree polynomial of the inverse of the momentum

$$M(s,q) = p_0(s,q) + p_1(s,q) \times \frac{1}{p} + p_2(s,q) \times \frac{1}{p^2} + p_3(s,q) \times \frac{1}{p^3} \tag{IV.15}$$

   where p is the momentum, s the sector number and q is the charge of the particle. The parameters describing the weighting functions are stored in the form of an histogram.

3. The last step is to calculate a sigmalized identification parameter called *dep* from the sector (s), charge (q), energy (E) and momentum (p) for each particle through

$$dep(p,E,s,q) = \frac{E/p - M(p,s,q)}{\sigma(p,s,q)} \tag{IV.16}$$

[8] Sigmalization is also performed on simulation, in order to have an efficiency loss in simulation that is as close as possible to the signal loss in real data due to the cuts in sigmalized EId parameters.

[9] The naming convention of the EMCal sectors is defined in Sec. II.4.5, p. 56.

The distribution of *dep* for electrons is by construction a Gaussian of width one and centered at zero, irrespective of the momentum, sector or charge. A cut on the *dep* variable $dep > dep_{min}$ will thus exclude tracks with E/p deviating by dep_{min} standard deviations on the lower side from the mean value.

At low momentum, ($p < 1.2$ GeV/c) one can see a peak in the swapped distribution (cf. Fig. IV.8, second raw, and Fig. IV.9, starting from middle of first raw to middle of second raw). The peak position shifts with the momentum in the range of $E/p \sim 0.3$ to 0.7. This peak is formed by pions that are detected at their minimum ionizing particle (MIP) energy. In a given momentum bin at p_{bin}, the probability of false association to a RICH ring created by an electron in the same event is therefore enhanced at a value of E/p such that, $E_{mip}/p_{bin} \sim (E/p)_{peak}$. The values $(E/p)_{peak}$ where the MIP peak is found versus the mean value of the bin, p_{bin}, are plotted in Fig. IV.11. The MIP value can be extracted by fitting the $1/p_{bin}$ dependence of the value of E/p where the peak is formed. MIP energies of 290 MeV and 396 MeV are extracted for the PbSc sectors and PbGl sectors, which are known to have different MIP energies due to different material composition.

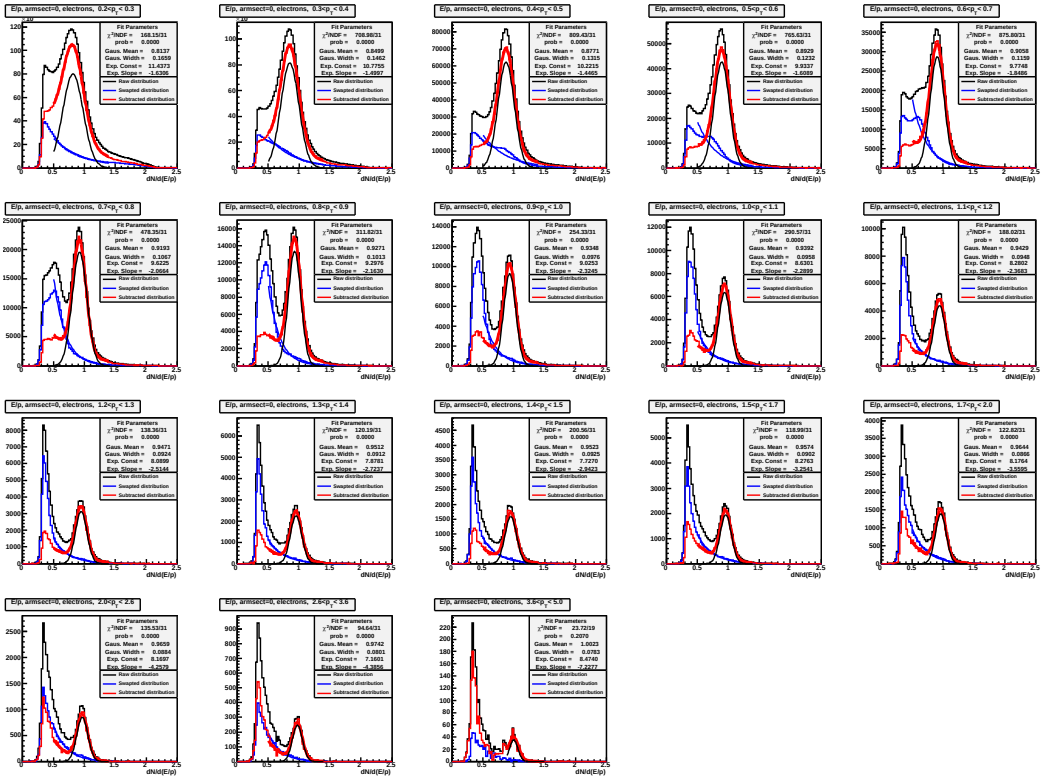

Figure IV.8: E/p distribution as a function of momentum for electrons in the E0 sector (PbGl).

IV.3.2.3 Recalibration of other EMCal based EId parameters

A similar procedure can be used with the *emcdz* and *emcdphi* variables. For these, further dependencies have to be taken care of. In the case of *emcdphi*, the raw distribution shows a

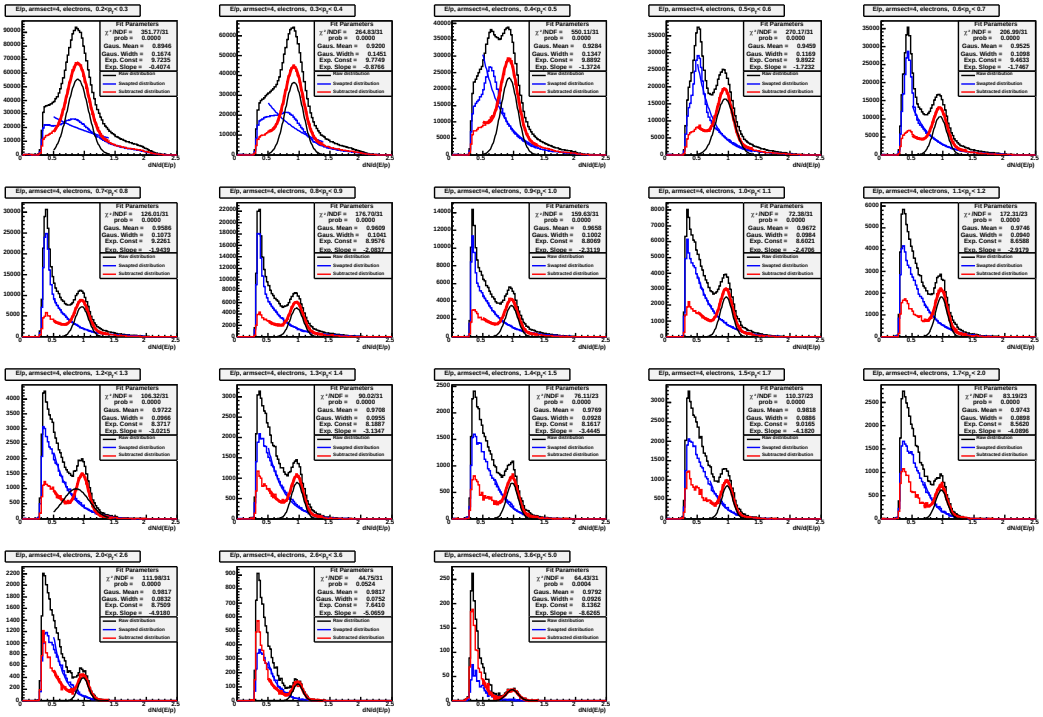

Figure IV.9: E/p distribution as a function of momentum for electrons in the W0 sector (PbSc).

dependence on the *zed* variable (longitudinal position of track at the PC1 radius). Similarly the *emcdz* distribution depends on the θ_0 variable (reconstructed polar angle of the track with respect to the z axis at primary vertex). The recalibration of *emcdphi* and *emcdz* leads to sigmalized variables *emcsdphi* and *emcsdz*, which are more appropriate to cut on because they have a uniform mean and standard deviation.

IV.4 EId parameter tuning

In this section the procedure used to decide on a cut set for this analysis is briefly described. The objective of the procedure was to see if a new set of cuts other than the ones used in a previous J/ψ analysis (on the run 4 data) is necessary. The idea is to have as good a background rejection as possible, this question being particularly important for the run 7 data because of additional background from the HBD.

Ideally this work should be done on simulated di-electrons from J/ψ embedded in realistic background from central data. For reasons that will be explained in Sec. IV.5.3 the embedding framework used for this analysis can reproduce neither the form of the background from real data nor (and especially) the signal to background ratio, so this approach is not applicable, at least until the embedding simulation is made to reproduce correctly the background in data. Therefore, the only other option left, namely directly optimizing the signal and background from a somewhat restricted sample of the total analyzed statistics was adopted. Of course, when doing this, one has to be careful not to bias the signal. The optimization was consequently restricted to a fraction of the whole data analyzed by taking part of the

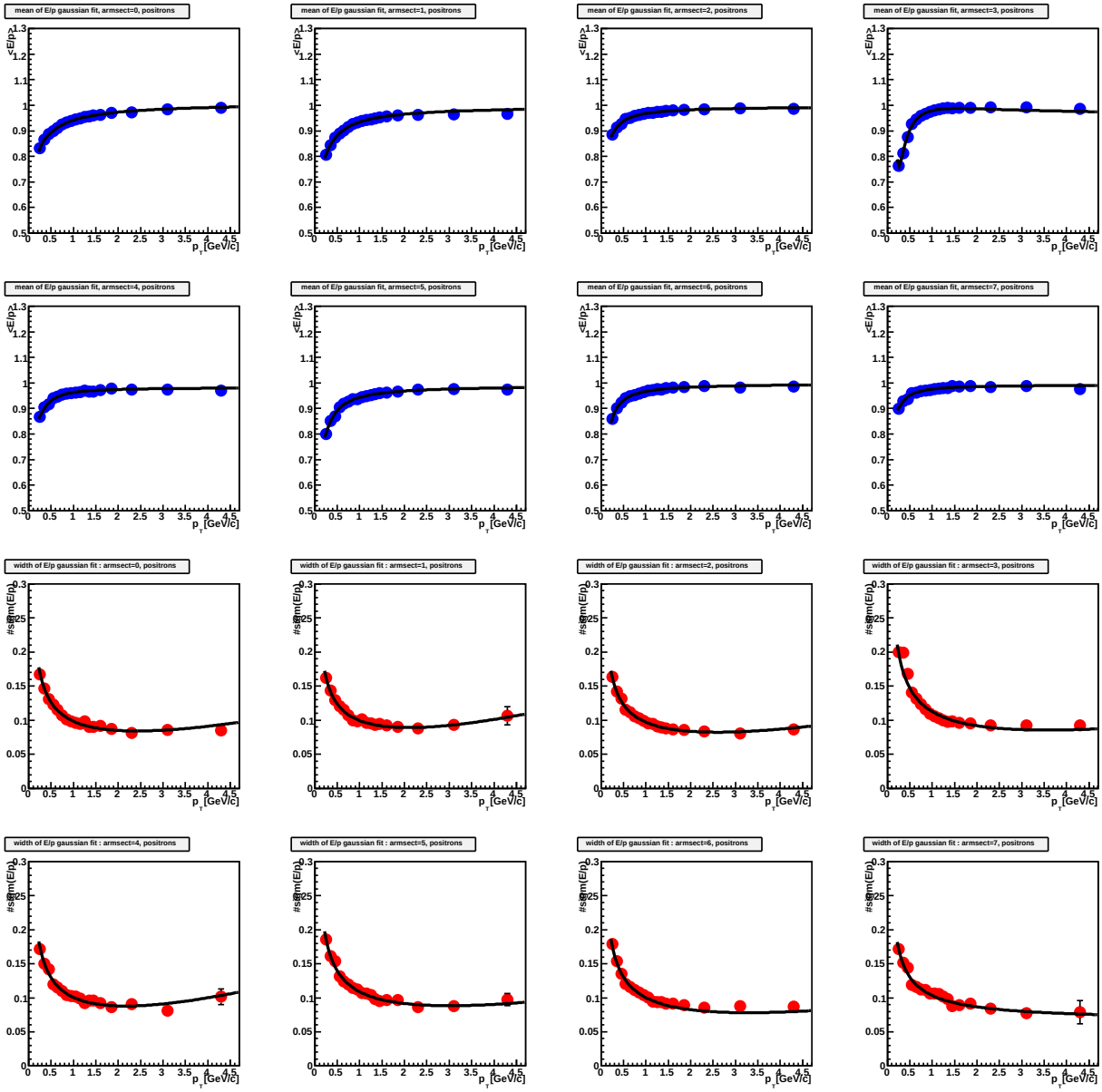

Figure IV.10: The variation of E/p mean value (top in blue) and width (bottom in red) for positrons as a function of momentum for all the eight EMCal sectors.

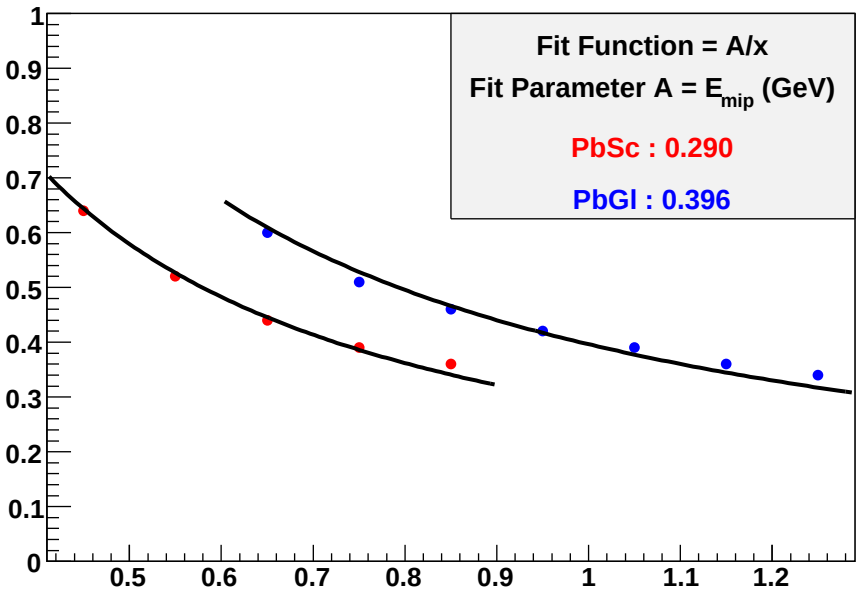

Figure IV.11: E/p MIP peak maxima as a function of the momentum selection for two EMCal sectors (PbSc in red (lower) and PbGl in blue (upper)).

level 2 filtered data sample, and a same event like sign combinatorial background subtraction technique, slightly less sophisticated than the mixed event method (cf. Sec. IV.6) used for the final signal counting.

The total statistics used for this study represents about 24M level 2 filtered events roughly equivalent to 2B MB events, by using the nominal value for the rejection factor of about 130 for the run period, and a rough conservative estimate of 60% for the J/ψ efficiency. The total J/ψ count in the tuning sample was about 1550 (about half of the whole MB sample analyzed).

To minimize the risk of biasing the signal the cuts were not fine-tuned. To be on the safe side, we took as a basic criteria to only elect cuts which entail a *minimal* loss of signal while maximizing a figure of merit, that we chose to be the significance: $s/\sqrt{s+b}$ with the signal s and background b evaluated from signal counting in a mass window of $\{2.9\ \mathrm{GeV}/c^2, 3.4\ \mathrm{GeV}/c^2\}$. Cut sets were rejected if the resulting subtracted spectrum outside the mass window gives a pathological background estimation (too high or too low), even if the figure of merit they resulted in is favorable.

Here is a list of the cut parameters that were finally adopted:

- RICH cuts: $n_0 \geq 2$, $disp \leq 5.0$, $\chi^2/npe_0 \leq 20.0$
- EMCAL cuts: $dep \geq -2.0$, $emcsdz \leq 3.0$, $emcsdphi \leq 3.0$
- other cuts: $quality > 10$[10], $p > 0.2$ GeV/c

[10]The variable *quality*, explained in Sec. II.5, p. 64, describes the robustness of the association of the track in the DC (cf. Sec. II.4.2, p. 51) with the clusters in the PC1 (cf. Sec II.4.3, 53)), as well as the number of hits in the DC that were used to reconstruct the track.

This approach is admittedly not an ideal approach. But it should be noted that the difference between the best (significance $\sim$ 13) and worst (significance $\sim$ 10) figures of merit is not large. In addition, whichever set of cuts is adopted, in the end, its inefficiency will be corrected for. Therefore the only major concern here was to make sure that the precise choice does not suppress unnecessarily the signal. This is insured by the figure of merit of this set of cuts ($\sim$ 12.4) which is close to the higher end of the range that was obtained by all the cut sets that were attempted.

IV.5 Efficiency corrections

The spatial distribution of electron tracks in simulation needs to be similar to that from real data, before using the simulation procedure to calculate the acceptance correction. Any deviation should be estimated and propagated to a systematic uncertainty on the efficiency calculation. But before doing comparisons, the dead areas in real data have to be accounted for in simulation, and the momenta of the simulated electrons have to be weighted to reflect the distribution observed in real data. The steps to do the comparisons as well as the result are given in this section, together with an estimation of the associated systematical error on the efficiency calculation.

IV.5.1 Fiducial cut method

The spatial distribution of electron tracks is sensitive to inefficiencies in the detector, because the track density is lower in less efficient regions. This can be corrected by introducing in the simulation the inefficiencies that were present during data taking. In this thesis, a different approach is used. It consists in removing inefficient/dead detector regions through fiducial cuts, that will be applied at the analysis level identically to real data and to a perfect detector simulation. This solution introduces an acceptance loss because the fiducial cuts must be made slightly wider than the actual inefficient region to avoid edge effects. But the acceptance loss is marginal and the method has a much smaller resource and time consumption and a faster turn around time than fully simulated inefficiencies.

The inefficient zones are localized by looking at the electron track multiplicity in the various subsystems (DC+PC, RICH, EMC) through scatter plots in two dimensions. The basic idea is to find areas where the track multiplicity is lower than the typical value in the detector. This can be done either by visual inspection or through an algorithm that compares bin by bin the number of entries to the average over the whole detector surface. For the inefficient/dead zone localization to make sense, variables which are local to the detector should be used. For each of the distributions, the EId cuts listed below are applied for electron selection, followed by swapped subtraction.

- RICH cuts: $n_0 \geq 3$, $\chi^2/npe_0 \leq 20.0$, $disp \leq 5.0$ cm
- EMCal cuts: $dep \geq -2.0$, $emcsdz \leq 3.0$, $emcsdphi \leq 3.0$
- miscellaneous cuts: 1.0 GeV/c$\leq p_T \leq$ 4.5 GeV/c, $p \geq 0.15$ GeV/c, $E \geq 0.15$ GeV

Conversion electrons have a much softer distribution than electrons from the collision point. They can not be reproduced by simulation, since only electrons and no photons are

injected in the simulation. Conversion electrons thus need to be rejected in real data in some way if acceptance matching is to be achieved between data and simulation. Although it is not an ideal solution, a $p_T \geq 1.0$ GeV/c cut is a good compromise between loss of statistics and conversion rejection. The upper cut on p_T is applied to have maximum rejection with the RICH cuts.

The following two dimensional distributions are considered. The scatter plots shown as examples are from a typical run taken in group 2 as defined in chapter 3 (HBD.W out, with the inner and outer coils of the magnets polarized oppositely ($+-$ / $-+$ configurations, cf. Sec. II.4.1, p. 49)).

1. ϕ_{dc} vs zed_{pc} : The azimuthal measurement ϕ from the DC vs. the longitudinal measurement zed from the PC. Fig. IV.12 shows this distribution for the reference run in the east arm for positrons (left) and electrons (right). Low efficiency zones, identified by visual inspection on this plot, and surrounded with red lines are excluded by fiducial cuts applied independently for electrons and positrons.

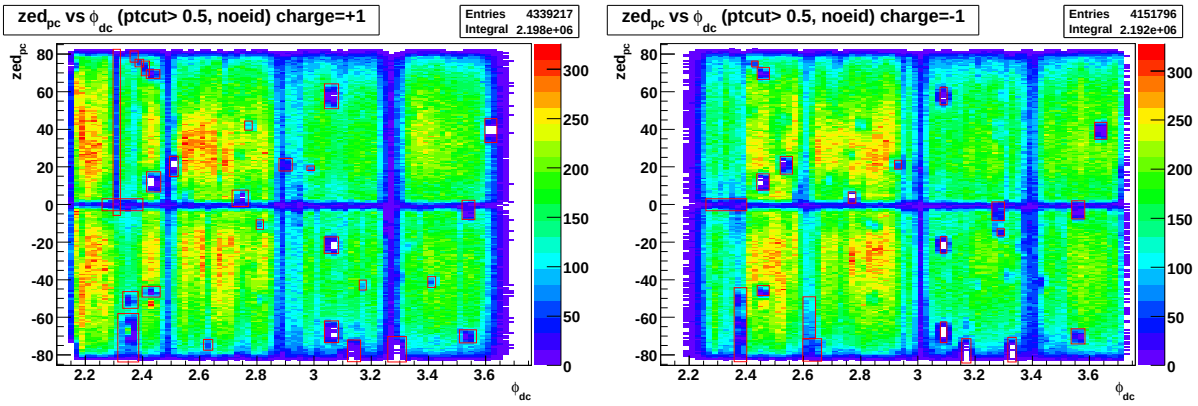

Figure IV.12: ϕ_{dc} (rad) vs zed_{pc} (cm) distribution for reference run.

2. $ysect_{emc}$ vs $zsect_{emc}$: These are the positions of the center of gravity of electromagnetic showers in the EMCal, in tower coordinates. The tower coordinates are defined for each sector by starting at $(ysect, zsect) = (0, 0)$ for the tower at the lower left corner of the sector, and incremented from left to right for $zsect$ and from bottom to top for $ysect$, looking at the arm from the collision point. Fig. IV.13 on the top left shows the scatter plot of tracks in the $ysect_{emc}$ vs $zsect_{emc}$ space in the first PbSc sector of the east arm for the reference run applying the EId cuts mentioned above. The plot on the top right shows the tower by tower ratio $R_{el/tr}$ of electron to unidentified track multiplicities. Towers with unusually low efficiency will result in a value of $R_{el/tr}$ that deviates significantly from the sectors tendency. The plot on the lower left corner shows the distribution of $R_{el/tr}$ over all towers of this sector. This ratio peaks at around 0.7. Towers with a value of $R_{el/tr} < 0.56$ (shown in the bottom right figure) are excluded by fiducial cuts. The exact position of the cut on the $R_{el/tr}$ is determined individually for each tower at $\sim$ 2 standard deviations from the peak.

3. ϕ_{RICH} vs zed_{RICH} : These are the positions the RICH ring centers as calculated from circular fits to the fired PMTs. Fig. IV.14 shows this distribution for the reference run.

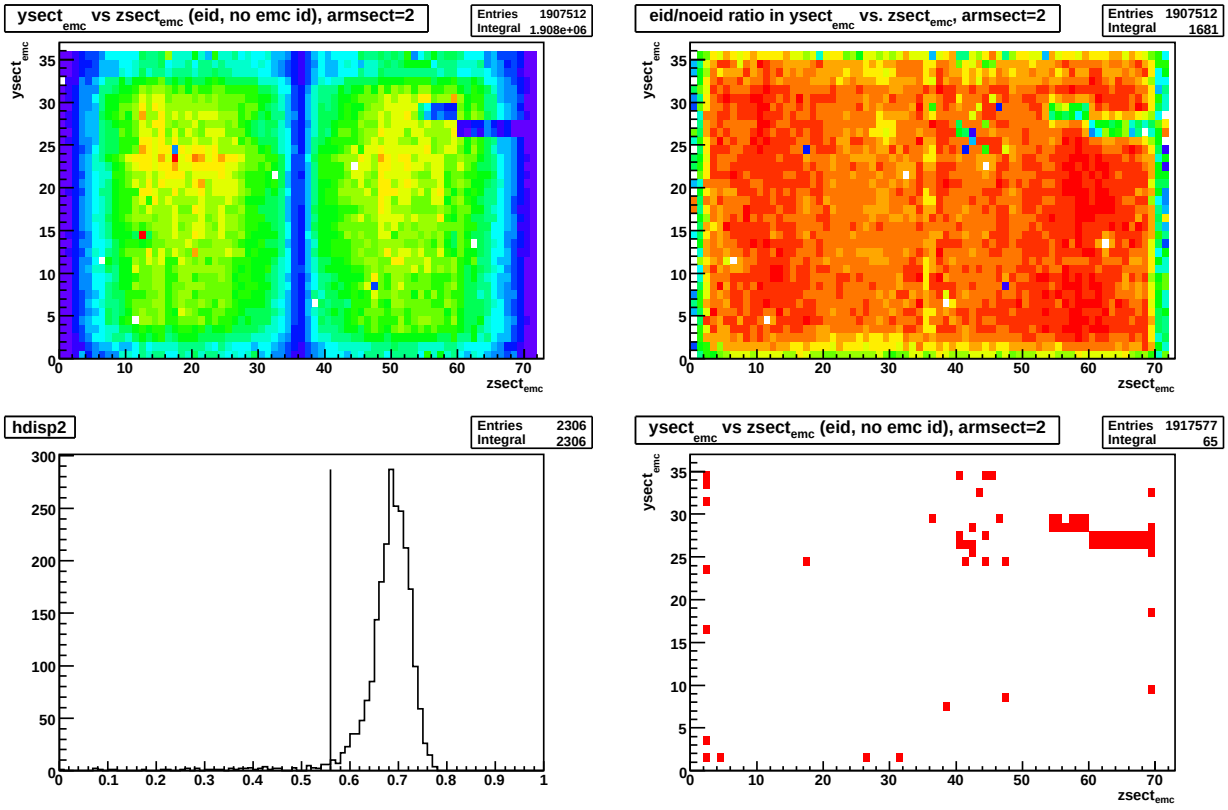

Figure IV.13: Top left: Identified electron multiplicity vs. tower id ($ysect_{emc}$,$ysect_{emc}$) in sector 2 (PbSc) of the east arm. Top right: The ratio $R_{el/tr}$ of identified electron to total track multiplicities vs. tower id. Bottom left: The distribution of $R_{el/tr}$ over all towers in the sector. Bottom right: The towers excluded by fiducial cuts based on a cut on the value of $R_{el/tr}$ in the tower.

In this space, the inefficient zones are decided by visual inspection, and are delimited in Fig. IV.14 by red lines. The delimited zones are excluded by fiducial cuts.

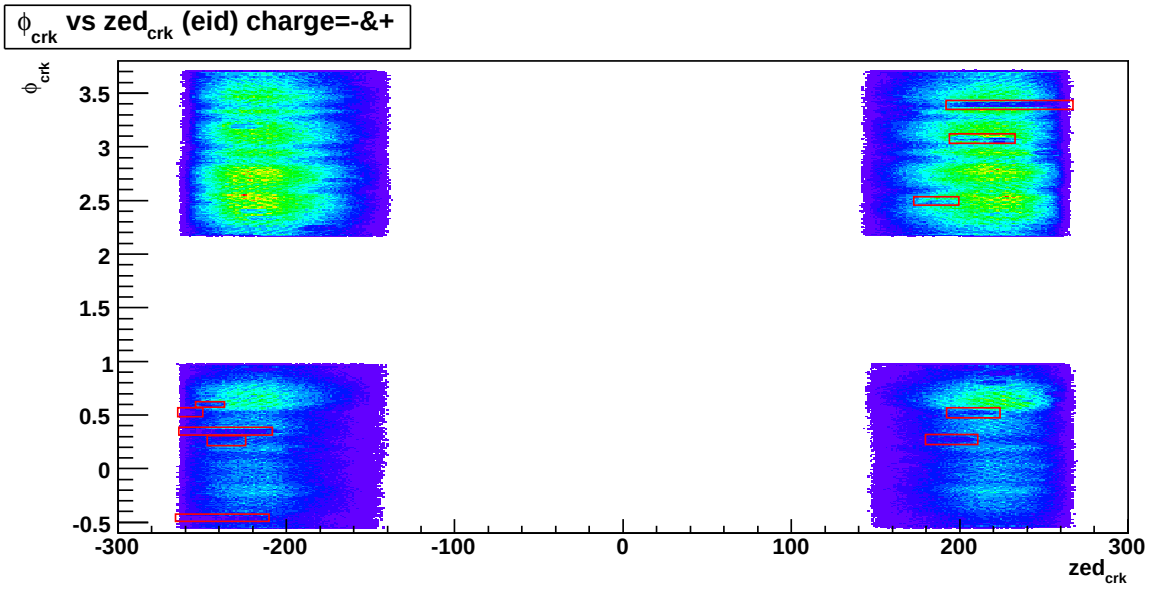

Figure IV.14: ϕ_{RICH} vs zed_{RICH} distribution for the reference run.

4. $1/\tan(\theta)$ vs zed_{BBC} : θ is the reconstructed polar angle of the track at the vertex position. For a given BBC z vertex position, $1/\tan(\theta)$ fixes the z position at which the track intersects the tracker layer.

   This space is well adapted to see the non instrumented space between the north and south sides of the drift chamber, which in simulation is actually sensitive. Unless this region is removed in simulation through fiducial cuts, then it is impossible to reproduce the data *zed* distribution.

   Assuming straight tracks in the $r-z$ (non bend) plane, tracks that hit at this spacing ($zed_{tracker}$=0) satisfy the relation $\tan(\theta) = D/zed_{BBC}$ where D is the radius of the tracker layer. This manifests itself in the ($1/\tan(\theta)$,zed_{BBC}) distribution from real data as a diagonal band (cf. Fig. IV.15, right) for the real data distribution from the reference run.

   The assumption of zero bending in the non bend plane is not quite right, and results in the curved edge of this band. Tracks produced far from $z = 0$ show more dispersion with respect to the $\tan(\theta) = D/zed_{BBC}$ relation than those produced at $z = 0$, because they travel a longer distance, and the effect of their curvature is larger than that of the tracks near $z = 0$ that travel a shorter distance before arriving at the tracker radius. This is why the fully unpopulated band (white band) looks wider at $z = 0$ than at $|z| = 30$ cm, whereas the partly populated zone forming the edge between the unpopulated and fully populated region (purple zone) gets wider at $|z| \to 30$ cm. To reproduce this effect, and reject the purple band, the fiducial cut applied uses a second order polynomial function shown by the black line in the figure. This cut throws out tracks produced away from $z = 0$ and headed towards the non instrumented joint between the north and south sides of the DC. Additional low efficiency regions that are visible with inclinations slightly

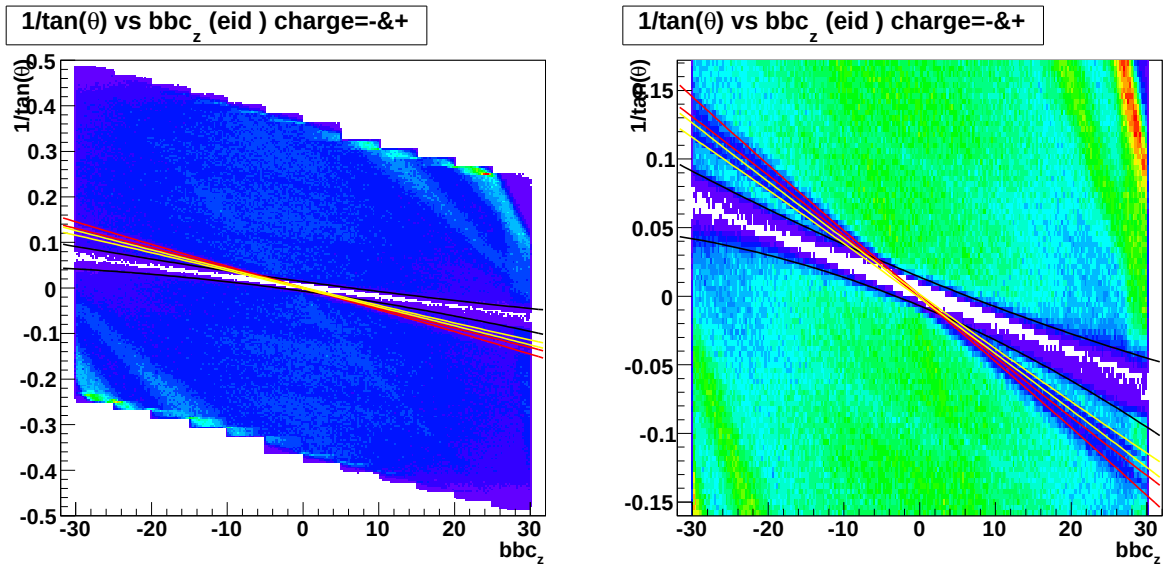

Figure IV.15: $1/\tan(\theta)$ vs zed_{BBC} distribution for the reference run.

larger than the main band are also cut out using quadratic function to represent the edge. Finally, tracks with $|1/\tan(\theta)| \geq 0.38$ are removed because the simulation does not reproduce correctly this zone.

Once the fiducial cuts have been fixed, one has to compare the spatial distribution of tracks. The choice is made here to use the ϕ_{dc} and the zed_{pc} distributions. Fig. IV.16 shows the *raw* ϕ_{dc} distributions in data and simulation after the application of the fiducial cuts, but before p_T weighting. The two distributions disagree by a considerable amount.

The matching has to be checked separately for electrons and positrons due to the momentum dependence of the acceptance with charge. In addition, the difference in momentum distribution between data and simulation has to be accounted for, since electrons with different momenta do not necessarily have the same acceptance distribution. This is done by weighting the p_T distribution of electrons in simulation to make it identical to the distribution in real data. The p_T weighting has to be done separately for the east and west arm because the conversion electrons in the east arm due to the presence of the HBD.E can not be reproduced by the simulation which does not include photons. The steps for the assimilation of the p_T distributions in data and simulation is as follows.

- Produce the p_T distribution of electrons and positrons for each arm a and side s of the DC in real data and simulation, with the fiducial cuts defined above plugged in.
- Extract the ratio of the distributions in data and simulation $f(p_T)$ as a function of p_T for each arm and side combination for electrons and positrons.

$$f_{a,s}(p_T) = \frac{dN^{data}_{a,s}/dp_T}{dN^{sim}_{a,s}/dp_T} \tag{IV.17}$$

- Redo the ϕ and zed distributions for simulation while applying track by track the p_T weighting function extracted in the previous step.

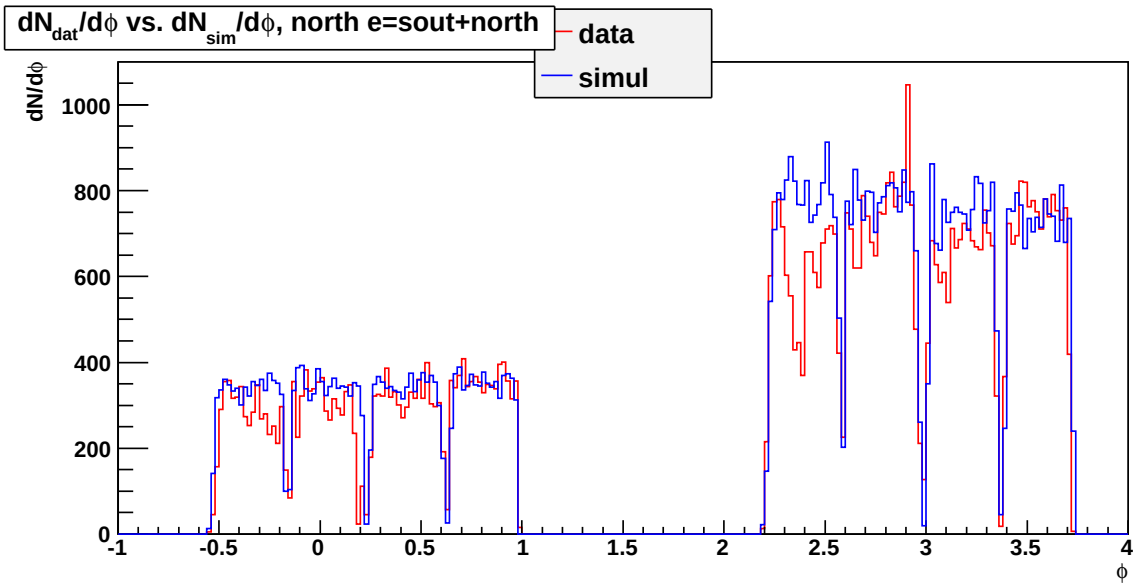

Figure IV.16: ϕ_{dc} distribution of positrons in data (red histogram) and simulation (blue histogram) before the application of fiducial cuts.

After these steps, the comparison for ϕ_{dc} and zed_{pc} between data and simulation are shown in Fig. IV.17 and Fig. IV.18.

The matching between data and simulation improves after the weighting procedure, but still not perfect. The mismatch needs therefore to be accounted for as a systematical uncertainty. The estimation of this systematical uncertainty is done as follows. In each side and arm, the area covered by the difference between the two distributions is normalized by their average integral:

$$err_{syst} = \frac{\sum_{bins} |dN_{sim} - dN_{dat}|}{\sum_{bins} (dN_{sim} + dN_{dat})/2} \tag{IV.18}$$

This ratio depends on the binning of the histograms; if the binning is fine, the statistics contained in each bin is small, and the fluctuations large. For very fine binning, the value of the systematical uncertainty diverges, dominantly due to statistical fluctuation. At the other extreme, if the distributions are not binned, the value of the systematical uncertainty, estimated as in Eq. IV.18, is by construction equal to unity within the numerical precision. To isolate the systematical effects, the binning size is varied and the error is calculated for each binning size. The variation of the systematical error with the bin size is shown in Fig. IV.19 for each of the arms and sides. The systematical error for each comparison is chosen to be the result of Eq. IV.18 around a region on the binning axis where it varies little. This value can be extracted by fitting a constant function in this region.

Finally the propagation of these errors to the effect on J/ψ is estimated as follows. Due to the fact that electrons and positrons from J/ψ decays at the p_T range accessible within the PHENIX acceptance dominantly go separately to the east and the west arm, it is reasonable to propagate the error on the electrons ($\delta_\phi e_w, \delta_\phi e_e$) and positrons ($\delta_\phi p_w, \delta_\phi p_e$) in the east and west arm using the relation

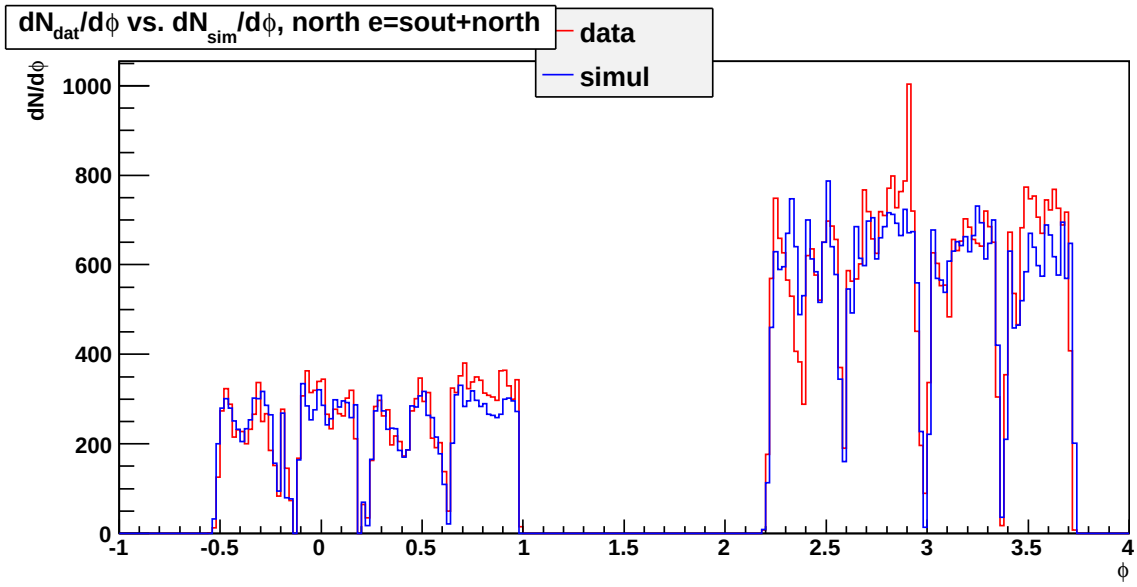

Figure IV.17: ϕ_{dc} comparison between data (red histogram) and simulation (blue histogram) after application of fiducial cuts and p_T weighting.

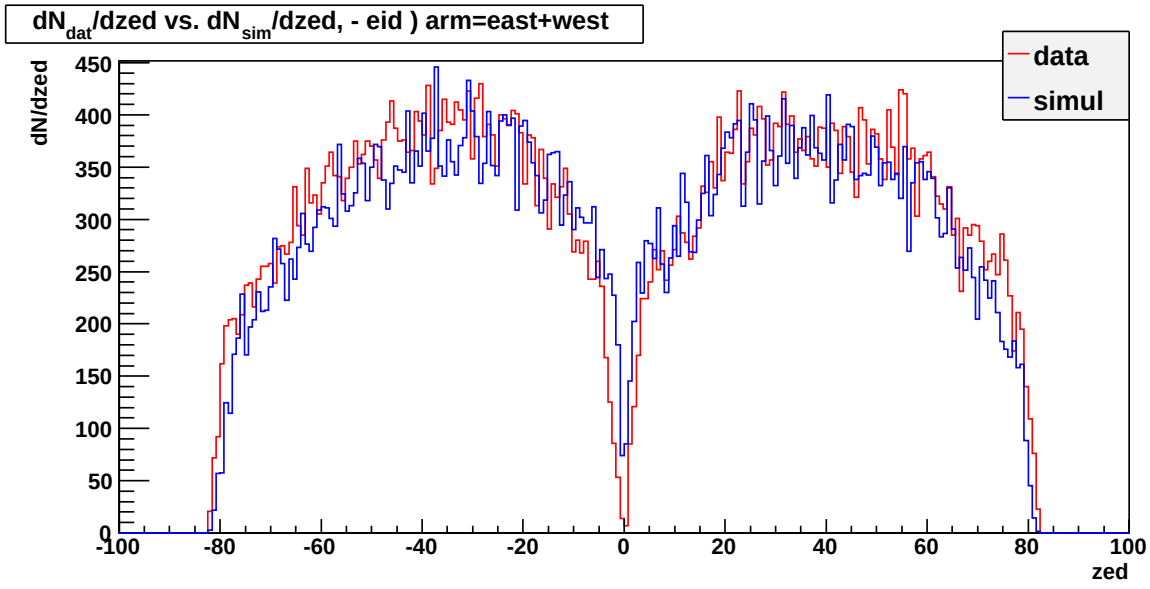

Figure IV.18: zed_{pc} comparison between data (red histogram) and simulation (blue histogram) after application of fiducial cuts and p_T weighting.

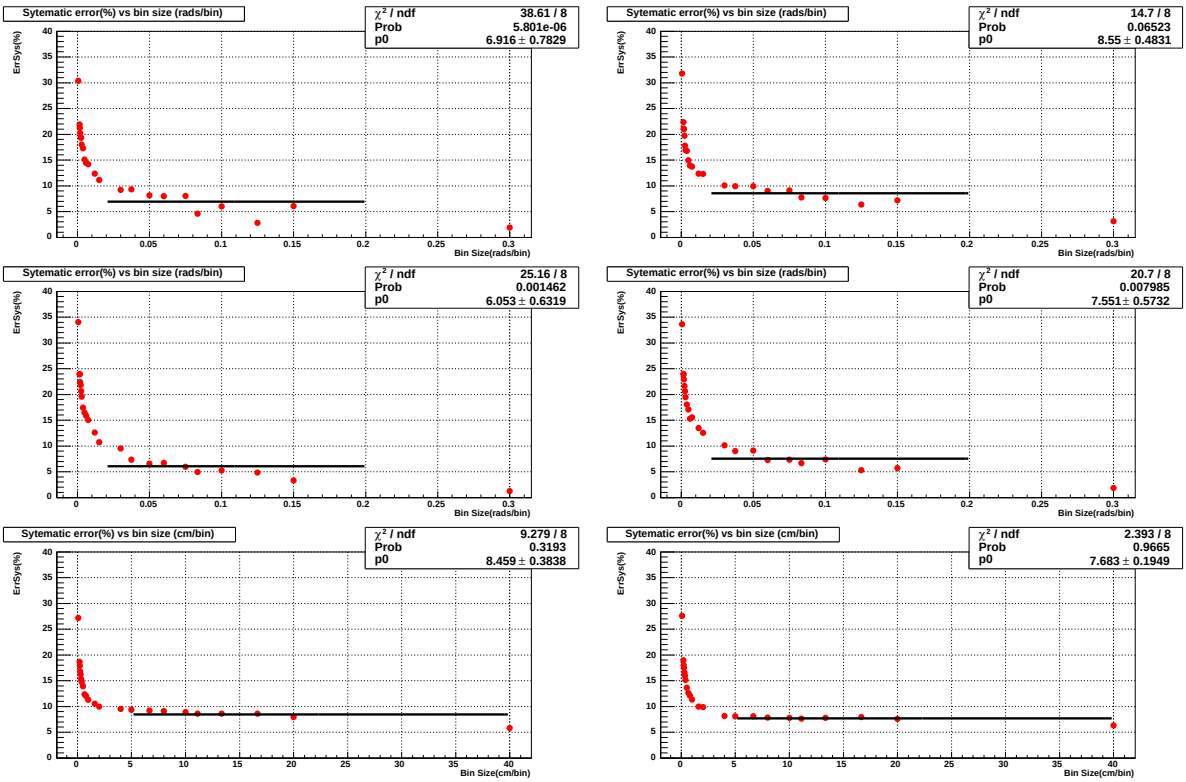

Figure IV.19: The variation of the systematical error calculated by Eq. IV.18. Top two plots are for positrons in ϕ (east on left and west on right). The second row is for electrons in ϕ (east on left and west on right). Third row of plots is for positrons (left) and electrons (right) in *zed*.

$$\delta_\phi(J/\psi) = \frac{(\delta_\phi e_w \oplus \delta_\phi p_e) + (\delta_\phi e_e \oplus \delta_\phi p_w)}{2} = 10.4\% \quad \text{(IV.19)}$$

For the *zed* comparison, the above observation does not hold (the z side on which the electron and positron hit are not correlated). The propagation of the error for electrons ($\delta_{zed}e$) and positrons ($\delta_{zed}p$)) is done using

$$\delta_{zed}(J/\psi) = \delta_{zed}e \oplus \delta_{zed}p = 11.5\% \quad \text{(IV.20)}$$

The more conservative choice of 11.5%, found with the comparison in the *zed* direction, is taken for the systematics of data - simulation acceptance matching.

IV.5.2 Electron ID efficiency × acceptance correction

After the application of the above specified fiducial cuts, the acceptance × efficiency versus p_T for a given set of cuts[11], denoted by $A\varepsilon(p_T)$ integrated over the full rapidity acceptance of PHENIX ($|y| < 0.35$) in a window delimited by $p_{T,min} < p_T < p_{T,min}$ is calculated as

$$A\varepsilon(p_T) = \frac{N_{J/\psi,rec}|p_{T,min} < p_{T,rec} < p_{T,min}, |y_{rec}| < 0.35, |z_{vtx,rec}| < 30}{N_{J/\psi,gen}|p_{T,min} < p_{T,gen} < p_{T,min}, |y_{gen}| < 0.35, |z_{vtx,gen}| < 30} \quad \text{(IV.21)}$$

where in the numerator, the number of reconstructed J/ψ is counted in a p_T window delimited using the reconstructed p_T and in the denominator, the number of generated J/ψ is counted in the same p_T window, but delimited here using the p_T at generation. The resulting $A\varepsilon(p_T)$ is shown in Fig. IV.20 (red markers), where the $A\varepsilon$ calculated without applying any fiducial cuts is also shown (black markers) for comparison. For the p_T integrated results (R_{AA} vs. centrality for example), each centrality bin is corrected by the p_T integrated efficiency correction. The p_T integrated efficiency correction, calculated by removing the p_T cuts both in the numerator and denominator of Eq. IV.21, is equal to $A\varepsilon = (1.535 \pm 0.003)\%$. The fiducial cuts reduce the efficiency by a factor of $\sim$ 42%, whereas in data, the signal loss is $\sim$ 19%. The real data signal loss is, as expected, smaller than the efficiency loss, because the fiducial cuts essentially remove parts of the detector that have low/no efficiency for electrons, with a slightly wider area.

IV.5.3 Multiplicity dependent efficiency correction

The pattern recognition and reconstruction efficiency depend on the multiplicity of the events. It is therefore important to pin down the efficiency loss or gain due to multiplicity. This is done through an *embedding* simulation. In this section the details of the procedure are exposed. The basic idea is to merge hits from simulated signal and from real data events at the detector level, and run the reconstruction on the combined hits. Schematically, the fraction of the number of simulated tracks that were retrieved to the number of tracks that were injected to produce the simulated hits gives the efficiency in high multiplicity environment. A number of details have to be carefully considered.

[11] As a reminder, the nominal electron identification cuts are used in this plots: $quality \geq 10$, $dep \geq -2$, $n_0 \geq 2$, $\chi^2/npe_0 \leq 20$, $disp \leq 5$, $emcdphi \leq 3\sigma$ and $emcdz \leq 3\sigma$ (cf. Sec. IV.4).

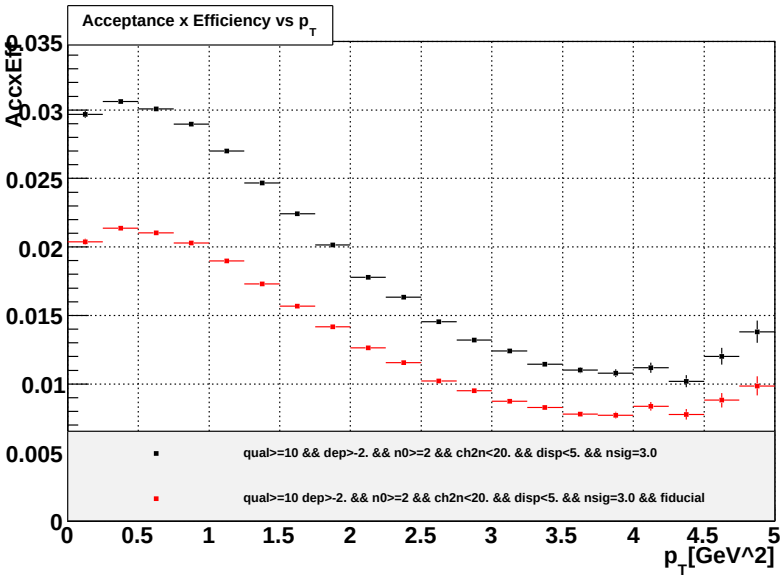

Figure IV.20: The J/ψ acceptance $\times$ efficiency correction as a function of p_T, with (red) and without (black) fiducial cuts.

$p_{T\,(\mathrm{GeV/c})}$	$N_{gen,0}$	N^{*}_{gen}	$N^{\dagger}_{rec,EId}$	$N_{rec,EId+Fid}$	$A\varepsilon^{\dagger\dagger}_{EId}$	$A\varepsilon_{EId+Fid.}$
0.0– 0.5	11640000	1581470	47133±217	32755±181	0.02980±0.00014	0.02071±0.00011
0.5– 1.0	31897400	4321020	124684±353	87343±295	0.02886±0.00008	0.02021±0.00007
1.0– 1.5	42469900	5754760	145531±381	102163±319	0.02529±0.00007	0.01775±0.00006
1.5– 2.0	39492500	5398060	113063±336	79313±281	0.02095±0.00006	0.01469±0.00005
2.0– 2.5	27284800	3790400	63806±252	45264±212	0.01683±0.00007	0.01194±0.00006
2.5– 3.0	14473900	2058390	28273±168	20081±141	0.01374±0.00008	0.00976±0.00007
3.0– 3.5	6176860	903224	10681±103	7592± 87	0.01183±0.00011	0.00841±0.00010
3.5– 4.0	2293670	347729	3723± 61	2649± 51	0.01071±0.00017	0.00762±0.00015
4.0– 4.5	822478	131410	1398± 37	1054± 32	0.01064±0.00028	0.00802±0.00025
4.5– 5.0	308389	52039	644± 25	471± 21	0.01238±0.00048	0.00905±0.00042
No p_T cut	1.77×10^{8}	2.44×10^{7}	529120± 728	371821±610	0.02170±0.00003	0.01525±0.00002

$^{*}N_{gen} = N_{J/\psi,gen}(|z_{bbc}| < 30.0, |y_{gen}| < 0.35, p_{T,min} < p_{T,rec} < p_{T,max})$
$^{\dagger}N_{rec} = N_{J/\psi,rec}(|z_{bbc}| < 30.0, |y_{rec}| < 0.35, p_{T,min} < p_{T,rec} < p_{T,max})$
$^{\dagger\dagger}A\varepsilon(EId + Fid.) = N_{rec}/N_{gen}$

Table IV.2: Efficiency vs. p_T. The columns are: (1) p_T range (2) $N_{gen,0}$, total number of generated J/ψ, within generated $p_{T,gen}$ in the range of column 1 (3) N_{gen} number of generated J/ψ with a cut on z_{bbc} of the event, and generated rapidity y_{gen} and $p_{T,gen}$ of the J/ψ (4) N_{rec}, number of reconstructed J/ψ with reconstructed $p_{T,rec}$ in the range of column 1, and EId cuts (cf. Sec. IV.4) (5) same as in column 4 with fiducial cuts added (6) $A\varepsilon_{EId}$ Acceptance times efficiency calculated by taking the ratio of column 4 to column 3 (7) $A\varepsilon_{EId+Fid.}$ ratio of column 5 to column 3.

IV.5.3.1 Hit data production

The first step in doing embedding simulations is to produce the detector level hits from simulation and from real data. In the reconstruction algorithm of both real data and simulated data, there is an intermediate step where the electronic addresses and their signals (encoded in the raw PRDF for real data, and produced in the response simulation step for simulated data) are translated to hit positions in a common coordinate. The hit position information is available at this step in subsystem specific container objects. These containers are usually not written on disk because of their relatively large size, and also because they are not necessary for doing analysis. The standard simulation and reconstruction software are modified to stream these objects to a file to produce the corresponding hit data files.

As an illustration, the DCH hit container object holds the following hit information: The hit TDC timing distribution for data and simulation from $\sim$ 100 events is shown in Fig. II.10. Although the timing distributions are similar, due to framework differences, the detector geometry used in simulation is not the same as the geometry that prevailed at data taking. This is because simulation reconstruction is done with a common geometry that is encoded in the PISA package and not easily changeable.

IV.5.3.2 Merging simulated and real data hits

Merging simulated and real data is done by creating a new empty hit container object and copying successively the simulated and real data hits into the new container event by event. Simulation events are produced with the exact same z vertex sequence as the data events into which they are to be embedded. This insures that the simulated tracks emanate from exactly the same position on the beam axis as the tracks that produced the real data hits. The copying is straightforward whenever the hits from data and simulation do not overlap.

Overlaps should however be handled with some care. In some subsystems where hits don't have temporal extent, an overlap is simply defined as a hit in the same read out channel. This kind of simplistic approach doesn't work when the hit has a temporal extent. In this case, a more appropriate definition is employed, where data and simulation hits overlap when the duration between the central value of the hit times is smaller than the sum of the temporal widths of the hits.

Overlap handling is also different depending on the nature of the hits. In the RICH, whenever there is an overlap, a new hit is created in the merged hit container pointing to the common PMT and whose signal (ADC sum) is the sum of the signal in the simulated hit and the real data hit. The earlier time between data and simulation is taken at the time of the new hit. For the case of the DCH, if there is an overlap on the same wire, then a new hit is created in the merged container, whose central value is the earlier of the two (data or simulation) times, and the width is taken to be

$$max(t_{MC} + w_{MC}, t_{RD} + w_{RD}) - min(t_{MC}, t_{RD}) \tag{IV.22}$$

where t_{MC} (t_{RD}) is the time of the signal peak and w_{MC} (w_{RD}) is the width of the signal for simulation (real data) hits.

IV.5.3.3 Reconstructing the merged hits

At this point the merged hit containers are fed into the same pattern recognition and association algorithm as the ones used in the data and simulation production. The pattern recognition algorithm critically depends on the detector geometry parameters which it uses to spatially distribute the subsystem hit information in a common 3D reference frame. Since the simulation and real data geometries are slightly different[12], the simulation tracks would be lost if one were to use the real data geometry and inversely, the real data tracks will be lost if the simulation geometry is used. Since it is absolutely crucial to reconstruct the simulated tracks, the choice is made to adopt the simulation geometry for the reconstruction of merged hits. Even if the real data tracks are not reconstructed with this choice, the occupancy dependence of the reconstruction efficiency can be studied by attempting to reconstruct simulated tracks in the high hit multiplicity environment provided by the presence of hits from real data tracks.

After reconstructing the merged hits, for each real-simulated data event pair, a new *embedded event* is created. The header of the embedded event contains the event characterisation information copied from the real data event, such as the z vertex information (which by construction is the same for real data and simulation), and most importantly the centrality of the underlying real event. In addition to the header, the events consist of a list of the tracks reconstructed from the merged hits. The containers used to store track and event information of embedded events at this stage are identical to those used for storing real data and simulated events. The embedded events can therefore be analyzed using the same utilities as those used for data and simulation.

The majority of the tracks from embedded events are false pattern recognition solutions from real data hits. As stated previously, real tracks are not retrieved correctly from the merged hit containers because of the mismatch between the simulation geometry (the one used by the reconstruction algorithm) and the real data geometry. The quality distribution of tracks from the embedded DSTs is shown on the left of Fig. IV.21. The fraction of tracks with good PC-DC matching (quality > 4) mostly coming from simulated hits is about 1% of the total track multiplicity.

The right side of Fig. IV.21 shows the track multiplicity vs. centrality for the embedded events. The average track multiplicity per centrality class decreases monotonously, in a similar fashion as for real data, demonstrating that the centrality propagation from the real events to the merged events was done properly.

IV.5.3.4 Evaluation of the efficiency

Once the embedded events have been produced, and checked for number of tracks - centrality correlation (cf. Fig. IV.21, right), the next step is to calculate what fraction of the tracks from simulation are actually reconstructed after they are embedded into hits from real data. The embedding efficiency as a function of centrality for single tracks can be calculated as

[12] Simulation hits are generated with the geometry defined in the GEANT based PISA package (cf. Sec. IV.2). If one wishes to modify the simulation geometry to match exactly the real data geometry, the real data geometry has to be encoded into the PISA package for each detector and for each run into which simulation hits are to be embedded. This is a very tedious task and was not tried.

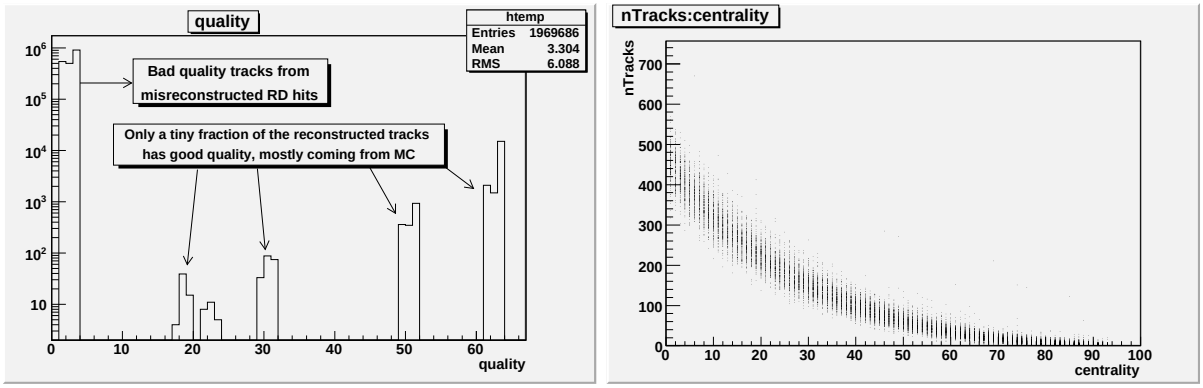

Figure IV.21: Left: Quality distribution of tracks reconstructed from the merged hit containers. Right: Track multiplicity vs. centrality of the embedded events.

$$\epsilon_{emb.}(cent) = \frac{N_{tr}^{emb.}}{N_{all\ tr}^{sim.}}, \tag{IV.23}$$

where $N_{tr}^{emb.}$ is the number of tracks in the embedded events for which the main hit contributors[13] are simulated hits, and $N_{all\ tr}^{sim.}$ is the number of simulated tracks that were embedded into the real data events, both the numerator and denominator counted within a centrality class *cent*. This method of calculating the efficiency has two drawbacks for J/ψ embedding efficiency calculation. First, the implementation of the 'main contributor' condition is not straightforward because it would require a complex algorithm for tagging the hits of each track as coming from real data or from simulation. Second, computing the efficiency for the reconstruction of dielectron tracks from J/ψ decay from the single electron efficiency in Eq. IV.23 requires making an assumption on how the single efficiency loss affects dielectron efficiency.

In order to avoid these two inconveniences, the approach used here is to embed simulated di-electrons from J/ψ decays and to reconstruct the J/ψ mass peak from both the non-embedded (pure simulation) and the embedded events. The fraction of J/ψs that can be retrieved in the embedded events among the simulated J/ψs that were embedded into real data gives directly the efficiency loss of J/ψ detection due to the high occupancy of real data. Mathematically the efficiency is calculated as

$$\epsilon_{J/\psi}^{emb}(cent) = \frac{N_{J/\psi}^{EMB}/N_{evt}^{EMB}}{N_{J/\psi}^{MC}/N_{evt}^{MC}}. \tag{IV.24}$$

where $N_{J/\psi}^{EMB}/N_{evt}^{EMB}$ is the number of reconstructed J/ψs per embedded event within the centrality class *cent*, and $N_{J/\psi}^{MC}/N_{evt}^{MC}$ is the number of reconstructed J/ψs per simulated events. The idea behind this normalization is that if there were no efficiency loss due to higher occupancy, then all the MC J/ψs that fell into the acceptance should be found after running reconstruction on merged node, and by construction $\epsilon_{J/\psi}^{emb}$ as defined in Eq. IV.24 is automatically equal to one when the effect of occupancy on the reconstruction is negligible (for example in a peripheral event selection). The observation that a J/ψ signal can only be formed

[13]This condition can be implemented by a lower cut on the ratio of the number of hits that the track is composed of coming from simulation to the total number of hits that the track is composed of.

by electrons from simulation[14] is implicit in this argument, and insures that what enters in the numerator of Eq. IV.24 comes from tracks with simulation hits as main contributors.

Fig. IV.22 shows the invariant mass distribution of di-electrons from J/ψ decay in embedded events compared to the distribution from the totality simulated events both normalized by the number of simulated events, as a function of centrality selection in bins of 10%. The same set of electron identification cuts[15] as used in real data are employed both in the numerator and the denominator. A decreasing fraction of the input J/ψ is reconstructed from the embedded events as one goes to the more central collisions. The ratio between the integral of the embedded event invariant mass histograms in the mass window of the J/ψ to that in the simulated events vs. centrality is plotted in Fig. IV.23. The embedding efficiency values in the same centrality binning as the one used for signal counting are shown in Tab. IV.3.

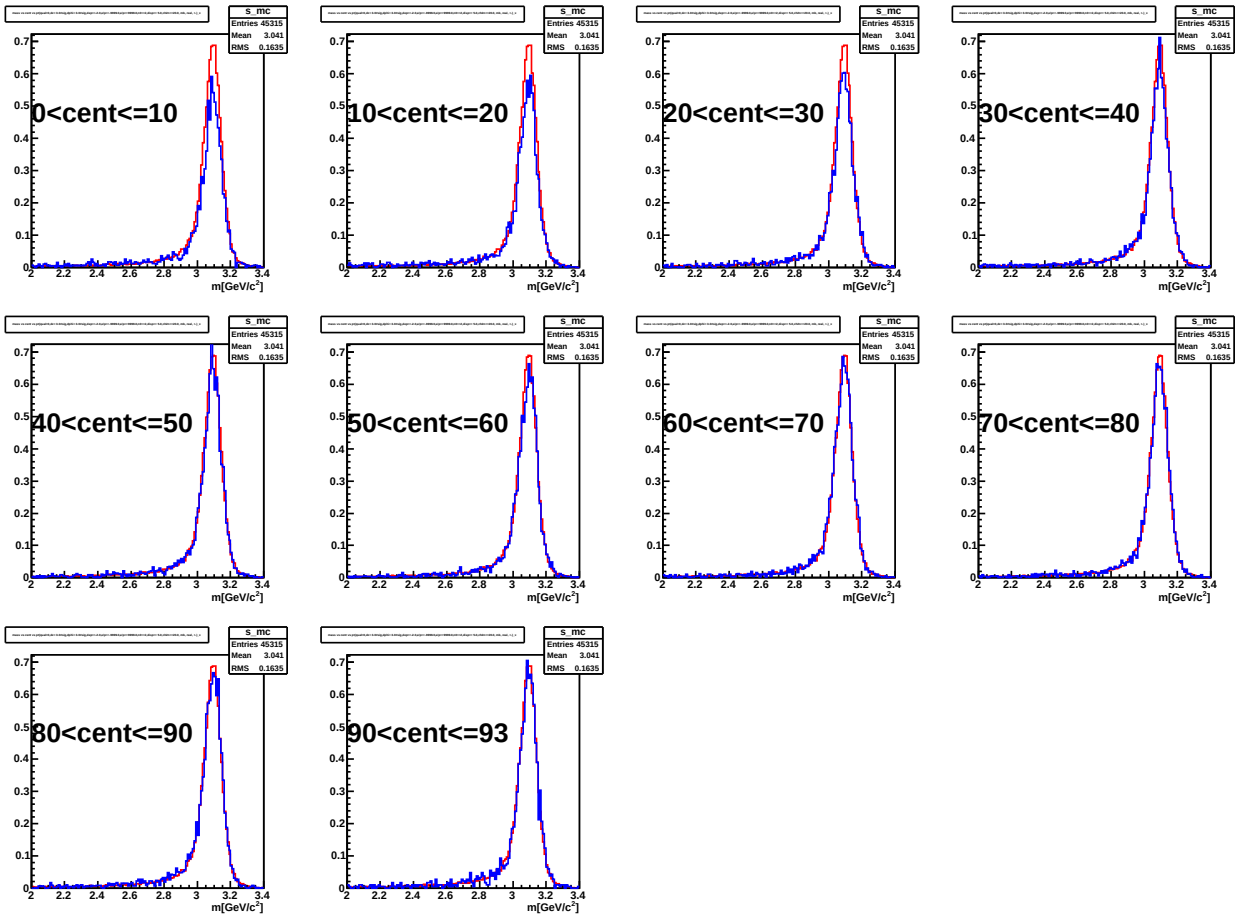

Figure IV.22: Invariant mass distribution of di-electrons from J/ψ decay in simulated events (red) and embedded events (blue) vs. centrality selection.

[14]The typical number of real data events used is of the order of 1×10^6. The number of J/ψs expected from this number of events is $\approx$1. Thus the contribution of track pairs with real data hits as main contributor to the mass peak observed in embedded events is negligible.

[15]As a reminder, the nominal electron identification cuts are used in this plots: $quality \geq 10$, $dep \geq -2$, $n_0 \geq 2$, $\chi^2/npe_0 \leq 20$, $disp \leq 5$, $emcdphi \leq 3\sigma$ and $emcdz \leq 3\sigma$ (cf. Sec. IV.4).

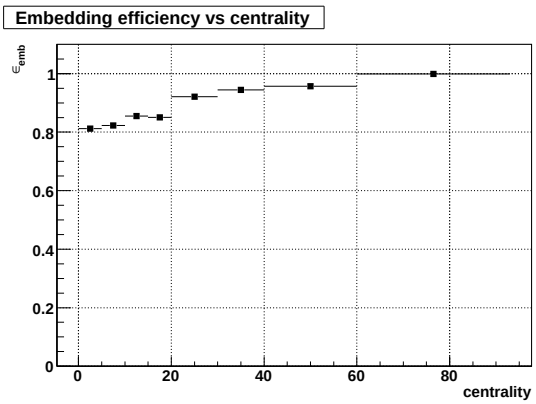

Figure IV.23: Embedding efficiency of di-electrons from J/ψ decay vs. centrality with the same cuts as to be used in signal counting.

centrality	N_{evt}	$N_{J/\psi}$	$N_{J/\psi}/N_{evt}$	ε_{emb}
0% - 5%	12170	1026±32.0	0.0843±0.0025	0.812±0.0245
5% - 10%	26900	2297±47.9	0.0854±0.0017	0.822±0.0168
10% - 15%	22840	2027±45.0	0.0887±0.0019	0.855±0.0185
15% - 20%	22400	1978±44.5	0.0883±0.0019	0.85±0.0187
20% - 30%	44675	4271±65.5	0.0956±0.0014	0.921±0.014
30% - 40%	45725	4484±67.0	0.0981±0.0014	0.944±0.0141
40% - 60%	90935	9031±95.0	0.0993±0.0010	0.956±0.0105
60% - 93%	151240	15693±125.3	0.10376±0.00078	0.9993±0.0088
simulation	421315	43748±209.16	0.10384±0.00047	

Table IV.3: Embedding efficiency.

IV.6 Signal Counting

The J/ψ signal is counted from the invariant mass distribution of electron-positron pairs. The reconstructed invariant mass of electron-positron pairs from resonance decays is equal to the mass of the parent particle within the detector resolution. With enough statistics resonances such as J/ψ therefore show up as peaks over the continuum background in the invariant mass distribution of electron positron pairs. *Signal counting* consists in integrating the peak above the continuum within a reasonably defined mass window. Reproducing and subtracting out the background under the mass peak are consequently essential components of signal counting.

In addition to the J/ψ signal, which is of direct interest here, the inclusive electron-positron pair yield contains contributions from uncorrelated pairs (created from physically independent sources) and correlated pairs (created from physically related sources). An example of uncorrelated electron–positron pair would be an electron coming from a semileptonic kaon decay (K_{e3}) decay and a positron coming from the Dalitz decay of a pion. An electron–positron pair coming from the semileptonic decay of two charmed mesons formed from a $c\bar{c}$ pair created in a hard process would constitute a correlated pair.

In the following sections these two different background sources and how they are subtracted out from the inclusive electron positron pairs will be discussed, followed by the systematics of integration of the signal yield under the J/ψ mass peak.

IV.6.1 Uncorrelated background estimation

The uncorrelated electron positron pair background (also known as *combinatorial* background) is composed of pairs of electrons and positrons that come from uncorrelated physics processes. As such it can be estimated by pairing up electron and positron tracks that are *a priori* uncorrelated. Within an event such a pair population is provided by the *like sign* pairs, because no physical signal produces correlated like sign electron (or positron) pairs, at least near the mass of the J/ψ. The invariant mass spectrum of like sign pairs from the same event therefore provides the most straightforward estimation of the uncorrelated contribution to the inclusive unlike sign pair mass spectrum. This is illustrated by Fig. IV.24, upper panel, where the inclusive electron-positron mass spectrum from minimum bias (no centrality selection) events is shown by the black histogram and the invariant mass spectrum of like sign pairs is plotted in cyan histogram, within the mass window[16] of 2.0 GeV/c^2 to 4.0 GeV/c^2. The like sign spectrum reproduces satisfactorily the continuum, especially above the J/ψ mass peak. Below the J/ψ mass peak, this is less true, which can in part be explained by sources of correlated electron pairs which will be addressed in the next section.

For now, it suffices to note that the like sign background from the same event introduces a relative error of the same order of magnitude as the foreground. For a foreground (unlike sign) count F and a background (like sign) count B, then the statistical error on the subtracted signal $S = F - B$ will be equal to

$$\delta S = \delta F \oplus \delta B = \sqrt{F} \oplus \sqrt{B} = \sqrt{F + B} \tag{IV.25}$$

since the relative statistical errors on F and B are $\sqrt{F}$ and $\sqrt{B}$ respectively.

[16]For computing related practical reasons, and also because it is the mass range of interest for the J/ψ signals, all the distributions to be shown in this section will be restricted to 2.0 GeV/c^2 to 4.0 GeV/c^2.

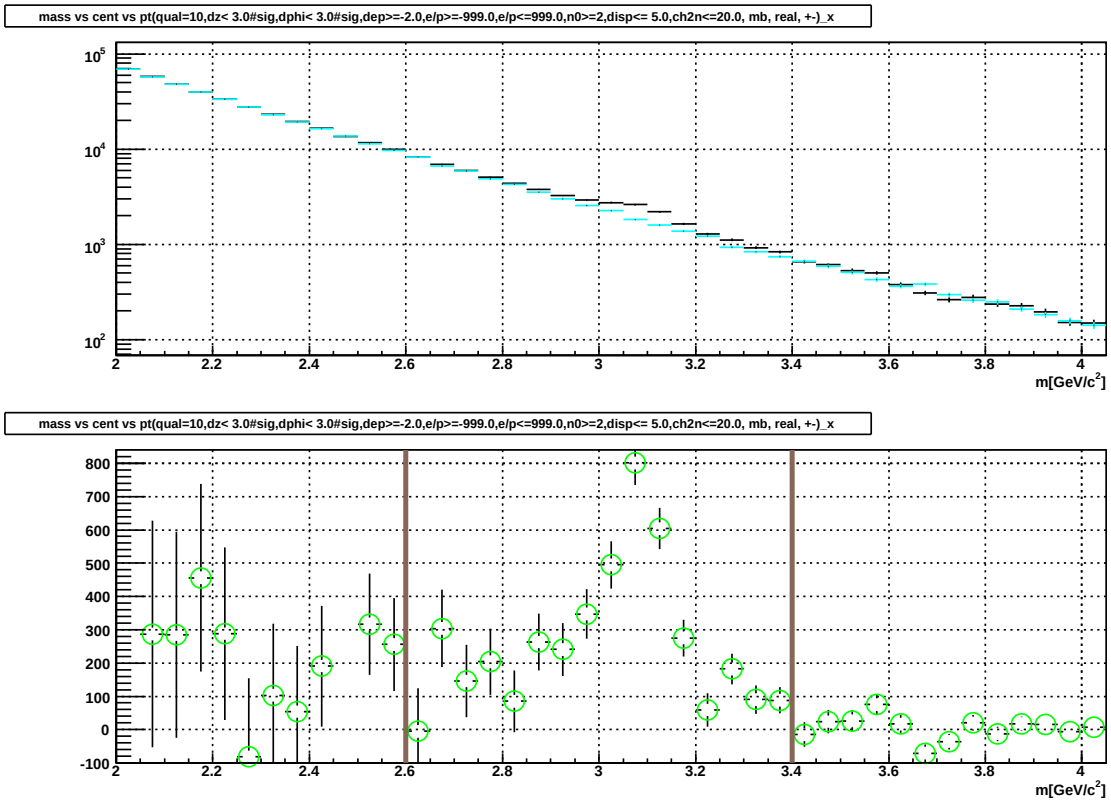

Figure IV.24: The inclusive electron positron pair invariant mass foreground from minimum bias (no centrality selection). The inclusive unlike sign spectrum (black) and the inclusive like sign spectrum (cyan) (top panel). Unlike sign spectrum after subtracting the like sign background (bottom panel).

IV.6.1.1 Mixed event background

The large relative error of the same event like sign estimation of the uncorrelated background has led to look for an optional way to generate a larger population of pairs that reproduce the shape of the uncorrelated continuum. A pair formed from electron/positron tracks that do not come from the same event is obviously physically uncorrelated. A spectrum composed of pairs formed from tracks that come from different events is called a *mixed* event spectrum. In theory, such a spectrum can be made as large as one wishes by raising the number of events on which the mixing is done. Consequently the relative statistical error of such a spectrum can be made as small as wished.

The idea behind mixed event subtraction is to use the mixed event unlike sign pair spectrum as a statistical estimate of the uncorrelated background, largely suppressing the contribution to the error on the subtracted spectrum that comes from the background. This being said, a few precautions have to be taken. Before going to the two main issues to be taken into account (normalization and validation) the algorithm used to generate the same event and mixed event backgrounds is briefly described.

For each event i having $N_{e,i}$ electrons and $N_{p,i}$ positrons, the $n^{+-}_{same,i} = N_{e,i}N_{p,i}$ same event unlike sign pairs are formed by pairing up each one of the $N_{e,i}$ electrons with all the $N_{p,i}$ positrons in the event or vice versa. The $n^{++}_{same,i} = (N_{p,i}-1)N_{p,i}/2$ and $n^{--}_{same,i} = (N_{e,i}-1)N_{e,i}/2$ same event like sign pairs are formed by pairing each $N_{e,i}$ ($N_{p,i}$) electrons (positrons) with the other $N_{e,i}-1$ ($N_{p,i}-1$) positrons (electrons) of the same event. The mixed event pairs are formed by pairing up the electrons/positrons in each events with those from some fixed number of events preceding it. This number, is called the *pool depth*, and will be notated by N_d.

The unlike sign background n^{+-}_{mix} is therefore formed by pairing up each of the $N_{e,i}$ ($N_{p,i}$) electron (positron) in event i with the $\sum_{j=i-N_d}^{i-1} N_{p,j}$ ($\sum_{j=i-N_d}^{i-1} N_{e,j}$) positrons (electrons) in the $i-N_d, ..., i-1$ events prior to event i. Consequently the number of mixed event unlike sign pairs formed for event i is equal to:

$$n^{+-}_{mix} = \sum_{i=0}^{N_{evt}} \Big((N_{e,i} \times \sum_{j=i-N_d}^{i-1} N_{p,j}) + (N_{p,i} \times \sum_{j=i-N_d}^{i-1} N_{e,j}) \Big), \tag{IV.26}$$

whereas in a similar manner, the total number of mixed like sign pairs will be equal to

$$\begin{aligned} n^{--}_{mix} &= \sum_{i=0}^{N_{evt}} \Big(N_{e,i} \times \sum_{j=i-N_d}^{i-1} N_{e,j} \Big) \\ n^{++}_{mix} &= \sum_{i=0}^{N_{evt}} \Big(N_{p,i} \times \sum_{j=i-N_d}^{i-1} N_{p,j} \Big) \end{aligned} \tag{IV.27}$$

A noteworthy point is that due to acceptance and efficiency variation for pairs from events at different longitudinal vertex location (z_{vtx}), centrality (*cent*) or reaction plane (Φ_{RP}), the mixed event pairs formed with the above detailed algorithm might fail to reproduce the actual background. The solution adopted, and used in all the signal plots to be shown in this section, is to mix two events if and only if they are close enough in z_{vtx}, *cent* and Φ_{RP}. This is implemented practically by forming various mixed event pools in bins of z_{vtx}, *cent* and Φ_{RP}, with bin sizes of the order of the resolutions in these measurements. Electrons and

positrons from event i in bin ($z_{vtx,k}$, $cent_l$, $\Phi_{RP,m}$) is consequently mixed only with the N_d previous events belonging to the same pool as itself. A pool depth of 10 was used in this study with bin sizes determined by dividing the (z_{vtx}, $cent$, Φ_{RP}) space into N_Z=30, N_{CENT}=20, N_{RP}=16 equal parts[17].

The resulting gain in the statistics of the combinatorial spectrum is ≈ 18, resulting in a reduction of the statistical error by a factor of $\approx \sqrt{18}$. If the unlike sign foreground count is F, and the mixed event background B_{mix}, with normalization factor $norm$, the error on the subtracted signal $S = (F - (B_{mix}/norm))$ will be

$$\delta S = \delta F \oplus \delta(B_{mix}/norm) \approx \sqrt{F} \oplus \frac{\sqrt{B_{mix}}}{norm} = \sqrt{F + \frac{B_{mix}}{norm^2}}, \tag{IV.28}$$

where, similar to the like sign subtraction error calculation, the statistical errors on F and $B_{mix}/norm$ are taken to be $\sqrt{F}$ and $\sqrt{B_{mix}}/norm$ respectively. Comparing Eq. IV.25 and Eq. IV.28, and assuming the approximate equality between B_{same} and $B_{mix}/norm$, one notices that the improvement on the statistical error of the signal by using the mixed event subtraction is

$$\delta S_{mix}/\delta S_{same} \approx \frac{\sqrt{F + B_{mix}/norm^2}}{\sqrt{F + B_{same}}} \approx \frac{\sqrt{F + (B_{same}/norm)}}{\sqrt{F + B_{same}}}. \tag{IV.29}$$

The gain in relative statistical error on the signal therefore improves as $norm$ increases, in other words as the depth of the pool increases. For an infinitely deep pool, ($norm >> 1$), the error on the signal when using the mixed event technique approaches to $\sqrt{F}$, equivalent to a gain of $\sqrt{2}$ if $F \approx B_{same}$, namely if the signal is small with respect to the background.

It should also be noted that the mixing scheme works if the total number of events in one execution of this algorithm is much larger than the pool depth times the number of pool bins (in our case, $N_d \times N_Z \times N_{CENT} \times N_{RP} \sim 96 \times 10^3$), in such a way that only the first small fraction of events are not mixed with the full depth of events, until the pools are fully occupied. This condition is fulfilled in our case where the typical number of events in one job are of the order of $\sim$ $1{\times}10^6$. When a pool is completely filled, the first event that was pushed in the pool is ejected to leave the place to a new event. The factor of $\approx 18\times$ gain in statistics is not equal to the full $\approx 2{\times}N_d = 20$ theoretically expected[18] partly because of the finite number of events that need ($\sim$ 10% from the numbers cited above) to be processed on the average before all the pools are completely filled.

IV.6.1.2 Normalization of the mixed event background

Once the same and mixed event, like and unlike sign pair mass spectra, named

$$n^{+-}_{same}(m),\ n^{--}_{same}(m),\ n^{++}_{same}(m),\ n^{+-}_{mix}(m),\ n^{--}_{mix}(m),\ n^{++}_{mix}(m) \tag{IV.30}$$

[17] Taking into account the ranges of variation for $z_{vtx} \in \{-30\text{ cm}, 30\text{ cm}\}$, $cent \in \{0, 100\}$ and $\Phi_{RP} \in \{-\pi\text{ rad}, \pi\text{ rad}\}$, the bin sizes are therefore $\Delta z_{vtx} = 2$ cm, $\Delta cent = 5\%$ and $\Delta\Phi_{RP} = \pi/8$.

[18] This factor of $\approx 2{\times}N_d$ gain in statistics by mixing N_d events can be understood in the over simplified case where all events have the same large number of electrons and positrons. It can be obtained by dividing the expression for n^{++}_{mix} from Eq. IV.27 by $n^{++}_{same} = \sum_i (1 - N_{e,i})N_{e,i}/2$ after replacing $N_{e,i}$ by N_e, the same for all events. $n^{++}_{mix}/n^{++}_{same} = \frac{N_{evt}N_d N_e^2}{N_{evt}N_e(N_e-1)/2} \approx 2N_d$.

are formed, one has to normalize the mixed event background to the level of the actual combinatorial background. There is some arbitrariness in this choice, since the actual combinatorial background is not known in advance. However various normalization schemes can be motivated based on physical arguments. Here the chosen normalization can be expressed as

$$norm = \frac{1}{2} \times \left(\frac{n^{++}_{mix}}{n^{++}_{same}} + \frac{n^{--}_{mix}}{n^{--}_{same}}\right) \tag{IV.31}$$

where $n^{++/--}_{mix/same}$ are integrated values of the spectra notated in Eq. IV.30 over as wide a mass range as possible (2 to 4 GeV/c^2 here). The rational behind this choice is that the same event like sign yield is the best estimate available of the level of combinatorial background. Since the same number of events are involved in the mixing, the normalization factor that scales down the overall mixed event like sign yield to be equal to the same event like sign yield should in principle also scale down the mixed event unlike sign distribution to the same event unlike sign combinatorial background.

IV.6.1.3 Validation of the mixed event background

The *a posteriori* validation of the mixing consists in making sure that the form of the same event uncorrelated background is reproduced correctly by the normalized mixed event spectrum. The method of validation adapted here involves the comparison of the same event like sign spectrum
($n^{like}_{same} = n^{--}_{same}(m, p_T) + n^{++}_{same}(m, p_T)$) to the normalized like sign mixed event spectrum
($norm \times n^{like}_{mix} = norm \times (n^{--}_{mix}(m, p_T) + n^{++}_{mix}(m, p_T))$). The comparison is done by plotting the differential

$$\frac{n^{like}_{same} - norm \times n^{like}_{mix}}{n^{like}_{same}}, \tag{IV.32}$$

as a function of mass and p_T. A statistical check of the 'flatness' (versus mass and p_T) of this differential is performed by fitting a first degree polynomial, leaving the slope a free parameter, as shown in the two plots of Fig. IV.25 as a function of mass and p_T. If the slope is compatible to zero within the errors, then the event mixing has reproduced satisfactorily the shape of uncorrelated background. The extracted slopes ($p1$) are more or less compatible, within the statistical errors, with zero. The maximum of the two slopes (4×10^{-3}/GeV/c^2 for the mass dependence) is used to vary the global normalization *norm* up and down once to study the robustness of the signal counting with respect to such variations. The results found are added to the systematical error estimation as explained in Sec. IV.6.3. It should however be noted that the normalization is not a very critical issue, because if it is underestimated, the residual combinatorial background is accounted for with an exponential function, together with the background contribution from correlated sources, as it will be discussed in the next section.

IV.6.2 Correlated background estimation

If the uncorrelated background is subtracted out correctly, the remaining continuum can only be attributed to correlated sources. Correlated background is sometimes also called physical background. The most important contributor of correlated unlike sign pairs at the mass range relevant for J/ψ signal counting is open charm (two D mesons from the same parent $c\bar{c}$ decaying

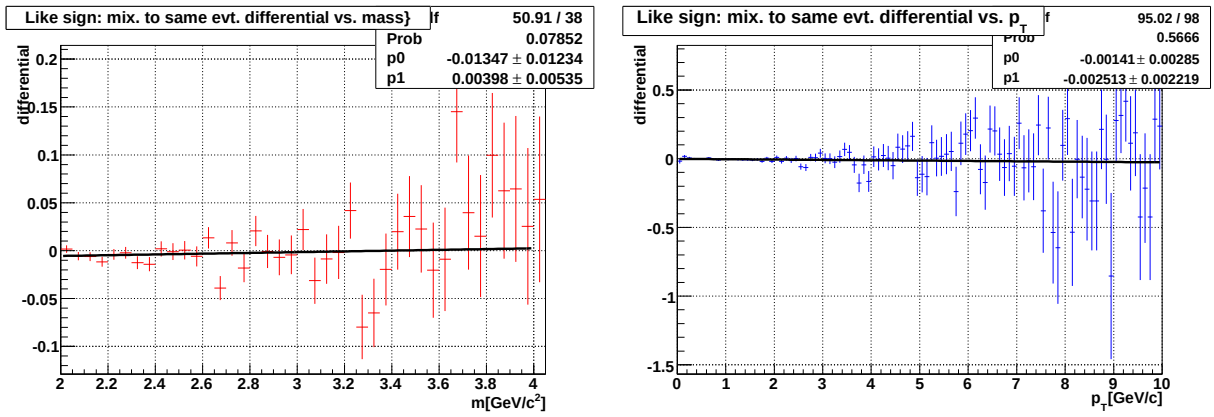

Figure IV.25: The differential between the mixed event and same event like sign spectra as a function of mass (left) and p_T (right).

semileptonically in to $K_0 e^- \bar{\nu}_e$ and $\bar{K}_0 e^+ \nu_e$ respectively). The Drell-Yan process(conversion of photons from quark - antiquark annihilation), and double semileptonic decay of correlated B meson pairs are also believed to contribute to the physical background [100].

As shown in the previous section, there is some uncertainty on the normalization of the mixed event subtraction. The statistics available does not allow to pin down the normalization with sufficient precision to claim that the continuum after subtraction comes exclusively from correlated sources. In the approach adopted here, no attempt is done to calculate the open charm cross section from the continuum background. Instead, the residual combinatorial plus physics background are accounted for collectively by an exponential fit to the unlike sign spectrum outside of the J/ψ mass window, as depicted in Fig. IV.26.

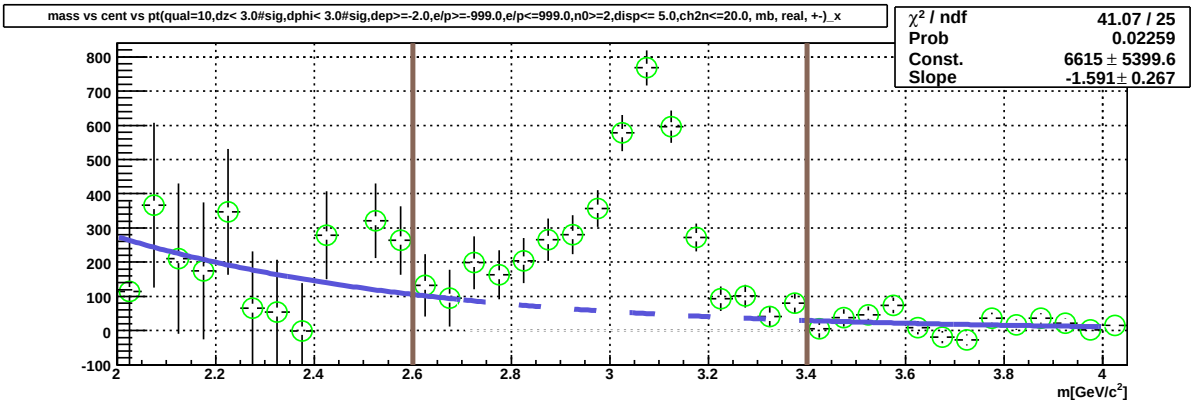

Figure IV.26: Residual and physical backgrounds fitted by an exponential outside of the J/ψ mass window for the minimum bias data sample (without centrality selection).

The signal counting is done for each centrality class bin by integrating the pedestal (purple fit in Fig. IV.26) subtracted bin contents in a mass window from 2.6 GeV/c^2 to 3.4 GeV/c^2 shown by the vertical brown bars, where the pedestal is defined by the exponential fit shown in Fig. IV.26. The effect of varying the exclusion range is to move up and down the resulting exponential fit.

Four different ranges were used for the exclusion of the data points from the exponen-

tial fit, and the resulting signal counts are included in the calculation of the systematical errors (cf. Sec. IV.6.3). The next section details what other variations of the signal counting technique were employed for the calculation of the systematical error on the signal counting.

IV.6.3 Systematics of signal counting

The idea behind the systematical error evaluation is to vary the hypothesis that were inherent in the central signal counting method, and take the dispersion of the resulting signal counts as a systematical error. The motivation is to test the robustness of the simple signal counting method explained in the previous section. Direct integration of the histogram after subtraction of the exponential fit to the residual background will be taken as the central value of the signal counting, because it involves the least number of assumptions. Most of the other methods explained in this section proceed by fitting a function to the signal, whose form needs to be assumed in addition to that of the background. The procedure is repeated for each centrality bin.

The minimum bias invariant mass spectrum in Fig. IV.26 shows a prominent low mass tail in the region $\sim$ 2.8 GeV/c^2 to $\sim$ 3.0 GeV/c^2 in addition to the residual background. This low mass tail is known to be caused by radiative energy loss by the electrons and positrons, as well as by a population of low resolution tacks[19] [52]. Here a double Gaussian fit suffices to describe correctly the minimum bias and peripheral (60% to 93% centrality class) spectra as shown in Fig. IV.27, where the function

$$C \times \exp(-S \times m) + N_{J/\psi}\left(\frac{R}{\sigma_1\sqrt{2\pi}}\exp-\left(\frac{m-\bar{m}_1}{\sqrt{2}\sigma_1}\right)^2 + \frac{1-R}{\sigma_2\sqrt{2\pi}}\exp-\left(\frac{m-\bar{m}_2}{\sqrt{2}\sigma_2}\right)^2\right), \quad \text{(IV.33)}$$

a sum of an exponential term ($C \times \exp(S \times m)$) and two Gaussians with mass centers $\bar{m}_1$ and $\bar{m}_2$, widths σ_1 and σ_2 and integrals related through the proportionality constant R, is fitted with no constraints to the data points. In more centrality bins, a free fit does not converge due to the unfavourable signal to background ratio. Instead, in these centrality bins, the parameters ($\bar{m}_1$,$\bar{m}_2$,σ_1,σ_2,R) extracted from the minimum bias and peripheral free fits, and listed in Tab. IV.4 together with the values from embedding simulations, are assumed, and the resulting signal counts (sum of the integrals of the two Gaussian) is included in the systematical error calculation. These two sets of constraints represent in some sense two extremes, peripheral events where the signal to background is most favourable, and minimum bias where this is not so much the case. Ideally, one would like to extract these parameters for the most central case, but the statistics in this bin does not allow to do the exercise.

For the systematics only the 60-93% and MB values are used. The 40-60% and the embedding results are here just for comparison. The 40-60% fit results are very close to the 60-93%. They are about one standard deviation from the MB fit results. Embedding (from all centralities) does not reproduce the ratio between the main peak and the tail Gaussian seen in MB. This is due to the fact that the double Gaussian approximation fails in cases where there is high statistics and the background is negligible with respect to the signal as is the case for embedding simulations. However, note that the main mass peak widths between MB and embedding are compatible.

[19] The bad quality tracks have worse resolution than the good quality ones.

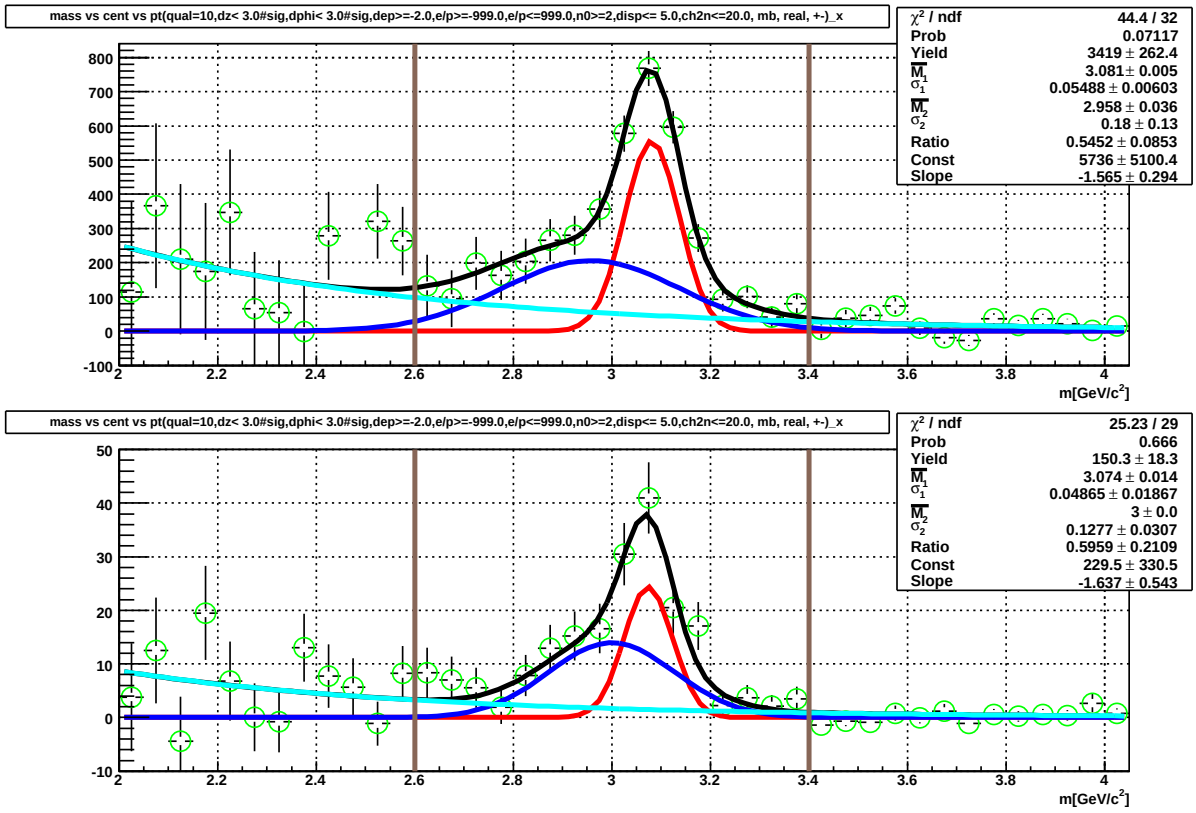

Figure IV.27: The double Gaussian fit to the minimum bias (top) and peripheral (bottom) centrality bins using the double Gaussian plus exponential function assumption with no fixed parameters.

set	$\bar{m}_1$	σ_1	$\bar{m}_2$	σ_2	R
MB	3.081 ± 0.005	0.055 ± 0.006	2.958 ± 0.038	0.18 ± 0.136	0.543 ±0.087
40%-60%	3.073 ± 0.009	0.048 ± 0.008	3.034 ± 0.033	0.159 ± 0.036	0.636 ± 0.112
60%-93%	3.074 ± 0.014	0.049 ± 0.025	3.001 ± 0.042	0.127 ± 0.03	0.596 ± 0.213
embedding	3.089 ± 0.0004	0.058 ± 0.0004	2.82 ± 0.009	0.256 ± 0.006	0.158 ± 0.003

Table IV.4: Values of the parameters ($\bar{m}_1$,$\bar{m}_2$,σ_1,σ_2,R) extracted from free fits to minimum bias, 40%-60%, 60%-93% selections in real data and embedding simulations.

In each centrality bin, the signal was extracted with the following assumptions and constraints

- Signal counting after subtracting the residual background estimated by an exponential whose parameters are *fixed* at values obtained from a free exponential fit that excludes the mass range $m \in$\{2.7-3.4\} GeV/c^2
  - methods 0, 1 and 2 : vary the mixed event normalization by 0, $+4\times10^{-3}$ and -4×10^{-3} respectively.
- Exponential + 2 Gaussians with parameters (m_1,m_2,σ_1,σ_2,R) fixed from MB and the parameters of the exponential *set* to values obtained from a free exponential fit that excludes the mass range $m \in$\{2.7-3.4\} GeV/c^2.
  - methods 3, 4 and 5 : vary the mixed event normalization by 0, $+4\times10^{-3}$ and -4×10^{-3} respectively.
- Exponential + 2 Gaussians, with parameters (m_1,m_2,σ_1,σ_2,R) fixed from 40-60% centrality, and the parameters of the exponential *set* to values obtained from a free exponential fit that excludes the mass range $m \in$\{2.7-3.4\} GeV/c^2.
  - methods 6, 7 and 8 : vary the normalization by 0, $+4\times10^{-3}$ and -4×10^{-3} respectively.
- Vary the exclusion range for fitting the free exponential to
  - $m \in$\{2.6-3.4\} GeV/c^2, \{2.8-3.4\} GeV/c^2, \{2.9-3.4\} GeV/c^2, method 9,10,11 (variants of method 0)

The results of fitting with methods 1 through 11 are summarized in Fig. IV.28 as a function of centrality. The central count (method 0) together with the relative systematical error estimated by the difference in yield between the methods giving the maximum/minimum yields and yield from method 0, are listed in Tab. IV.5 as a function of centrality selection. The actual error is calculated by the maximum difference divided by $\sqrt{12}$, assuming that the signal counts using the different methods are distributed uniformly[20] to reflect complete uncertainty. In the same table, the mean and relative root mean square (RMS/mean) values are also shown for comparison. The statistical error from method 0 is also shown.

The systematic uncertainties on the signal counting $\frac{Max-Meth0}{\sqrt{12}\times Meth0}$ and $\frac{Meth0-Min}{\sqrt{12}\times Meth0}$ are asymmetric with the exception of a few points because the signal counting (without fitting) in general tends to give higher results than the fitting method. It should also be noted that the general tendency for the evolution of the systematical error as the centrality decreases (going to peripheral collisions) is monotonically decreasing (again, there are a couple of points where this is violated). This reflects the fact that the systematical error on the signal counting is higher where the signal to background ratio is unfavourable. These errors are accounted for as uncorrelated systematical errors.

[20] The RMS of a uniform distribution between points a and b is $(a-b)/\sqrt{12}$.

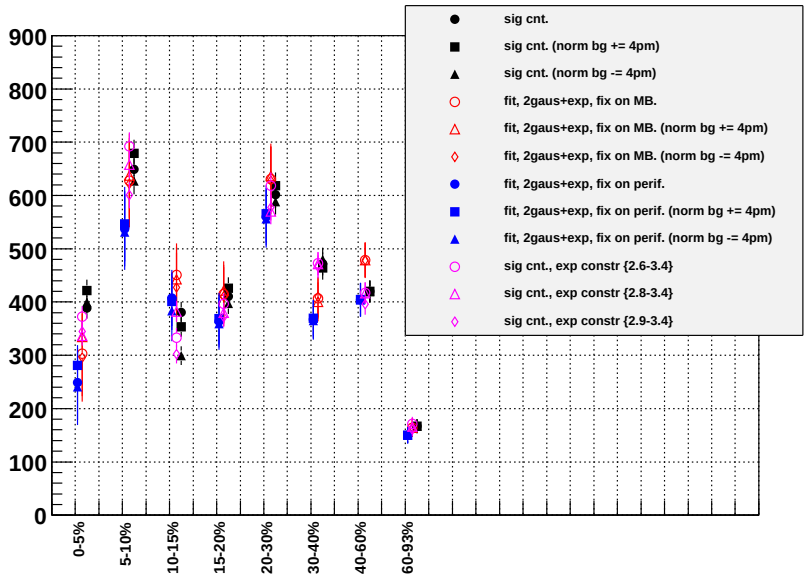

Figure IV.28: Summary plot for the signal counting systematics using 12 methods.

centrality	0-5%	5-10%	10-15%	15-20%	20-30%	30-40%	40-60%	60-93%
Method 0	388.9	649.4	380.6	410.3	601.4	471.8	419.7	167.0
Stat. Er.								
$\frac{Max-Min}{\sqrt{12}\times Meth0}$	12.6%	8.3%	14.2%	5.8%	4.2%	7.6%	5.2%	3.1%
$\frac{Max-Meth0}{\sqrt{12}\times Meth0}$	1.4%	2.8%	5.3%	2.0%	1.9%	1.0%	4.1%	0.1%
$\frac{Meth0-Min}{\sqrt{12}\times Meth0}$	11.2%	5.4%	8.9%	3.8%	2.3%	6.6%	1.1%	3.0%
Mean	316.5	610.0	385.9	397.6	599.7	413.0	434.1	160.4
RMS/Mean	18.4%	9.3%	14.4%	6.9%	5.4%	10.9%	7.3%	4.7%

Table IV.5: Summary table for the signal counting and systematics.

IV.7 Summary of systematical errors

The following table summarizes the systematical errors that come from various sources. The systematical errors have been classified into two types. The type A systematical errors are the point to point (centrality selection wise) uncorrelated systematical errors where a modification in the source of the systematical error in question affects the yield in each bin independently. The type B systematical errors are correlated in the sense that varying the source of such systematical errors affects the yields in all bins coherently (although not necessarily in the same direction). In plotting the results, the type A (uncorrelated) systematical errors are added up to the statistical errors in quadrature, whereas the type B (correlated) systematical errors are represented separately by brackets (or boxes). In addition to the systematical errors listed above, there is a global normalization error that comes from the combined statistical plus uncorrelated systematical error on the p+p invariant yield of $\sim$ 10%. This error will not be plotted, but will be indicated in writing.

Systematic error source	value	type
Signal counting, up (Sec. IV.6.3)	1.4%,2.8%,5.3%,2.0%,1.9%,1.0%,4.1%,0.1%	A
Signal counting, down (Sec. IV.6.3)	11.2%,5.4%,8.9%,3.8%,2.3%,6.6%,1.1%,3.0%	B
Data-MC mismatch (EId pars) (Sec. IV.3)	4%	B
Data-MC mismatch (Acceptance comparison) (Sec. IV.5.1)	11.5%	B
Unknown rapidity distribution of J/ψ simulation (Sec. IV.2.1)	0.7%	B

Table IV.6: Summary of systematical errors on signal counts. The references to the sections where each systematics is discussed is given in the parentheses of the first column.

Chapter V

J/ψ Suppression

In this chapter, the final results of the analysis presented in chapter 4 are shown and discussed. The nuclear modification factor, R_{AA}, as a function of centrality is an observable that encodes the interaction of the prehadronic $c\bar{c}$ and/or formed J/ψ on its path out of the collision region. As already discussed in chapter 1, this includes breakup by hadronic matter from fragments of colliding nuclei in addition to any eventual melting in the hot QGP created if the temperature achieved in the collision is high enough to stimulate a phase transition. The J/ψ R_{AA} is also affected by the possible recombination of uncorrelated $c\bar{c}$ pairs within a deconfined medium.

V.1 Centrality dependence of J/ψ R_{AA}

In the previous chapter, the methods for the calculation of all the ingredients necessary to calculate the nuclear modification factor using Eq. I.13 were described, and the results from these calculations were tabulated. The resulting R_{AA} as a function of centrality (represented by $< N_{part} >$) from these numbers is shown in Fig. V.1. The left most point is from 60-93% peripheral events, and the event selection becomes more and more central going to the right.

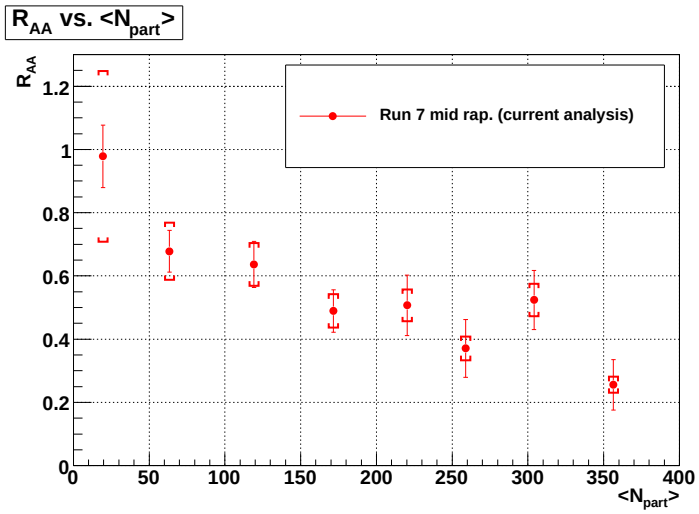

Figure V.1: R_{AA} vs. $< N_{part} >$ from run 7 Au+Au collisions, from an integrated luminosity of 2.9B events. There is an additional global uncertainty of 12% coming from the p+p normalization.

The uncorrelated systematical errors (of type A in Tab. IV.6, p.132) are added in quadrature to the statistical errors and plotted as error bars. The correlated systematical errors (of type B in Tab. IV.6) are shown as brackets. In addition, there is a global 12% uncertainty that comes from the error on the p+p J/ψ invariant yield that is used for the normalization of the Au+Au yield. The average number of collisions $< N_{coll} >$ (used to normalize the R_{AA}) and the average number of participants $< N_{part} >$ are calculated for the event selections used for the signal counting based on a Glauber approach (cf. Sec. I.2.1.1, p.6 and Sec. II.3.3, p.45). The values of these quantities as well as their errors (accounted for as correlated systematical errors) are listed in Tab. V.1.

centrality	0-5%	5-10%	10-15%	15-20%	20-30%	30-40%	40-60%	60-93%
$< N_{part} >$	351.4	299.0	253.9	215.3	166.6	114.2	58.4	14.5
$\sigma < N_{part} >$	2.9	3.8	4.3	5.3	4.7	5.4	3.8	2.5
$< N_{coll} >$	1065.4	845.4	672.5	532.7	373.8	219.8	90.6	14.5
$\sigma < N_{coll} >$	105	82	67	52	40	23	12	4

Table V.1: Values of $< N_{coll} >$ and $< N_{part} >$ calculated for the signal counting centrality selections based on a Glauber model approach.

The first thing to notice is the most peripheral R_{AA} is compatible to unity within the statistical error bars and large systematical uncertainty (∼28%, essentially due to the $< N_{coll} >$ computation). J/ψ produced in peripheral collisions are not dramatically affected on travelling out of the collision region. The most central R_{AA} (largest n_{coll}), shows a suppression by a factor of more than three.

In the following sections, the result is compared to and combined with a similar measurement on the run 4 data set, and compared to the forward rapidity measurement, as well as to a projection of the cold nuclear matter effects measured in d+Au collisions, and to a model prediction incorporating regeneration.

V.2 Comparison to a previous measurement

The same measurement of R_{AA} in Au+Au collisions at 200 GeV was performed on the run 4 data set. The published result from the run 4 analysis [75] is compared in Fig. V.2 (left) to the result found from the analysis of the run 7 data. The new results (in red) are slightly displaced on the horizontal axis to render the plot more readable, though the real abscissa of these points is the same as that of the run 4 data point (in green) nearest to them.

The two results are compatible within statistical errors for most of the centrality bins. The centrality bin $< N_{part} >= 14.5$ ($< N_{part} >= 299$) deviates by more than one (less than two) standard deviation from the run 4 analysis, if the statistical error only are considered (for the first point, most of the systematic uncertainty is coming from N_{coll} which is common to both measurements). The probability that an isolated measurement with a Gaussian error deviates by more than one standard deviation in either way due to purely statistical fluctuation is 31.7%. The probability that there are *exactly* two measurements out of eight that deviate farther than one standard deviation is given by the binomial distribution $f_{bin}(r; N, p) = \frac{N!}{r!(N-r)!} p^r (1-p)^{N-r}$ where $r = 2$, $N = 8$ and $p = 31.7\%$. The numerical value for this probability is 28.6%. The probability that there are *at least* two measurements that differ

by more than one sigma, $\sum_{i=2}^{8} f_{bin}(i; 8, 31.7\%)$, is 77.7%, more appropriate to estimate the "statistical" nature of these deviations. This proves that the deviations are expected, and it is concluded that the two sets of measurements are in reasonable agreement, enough to warranty combining them to have reduced error bars.

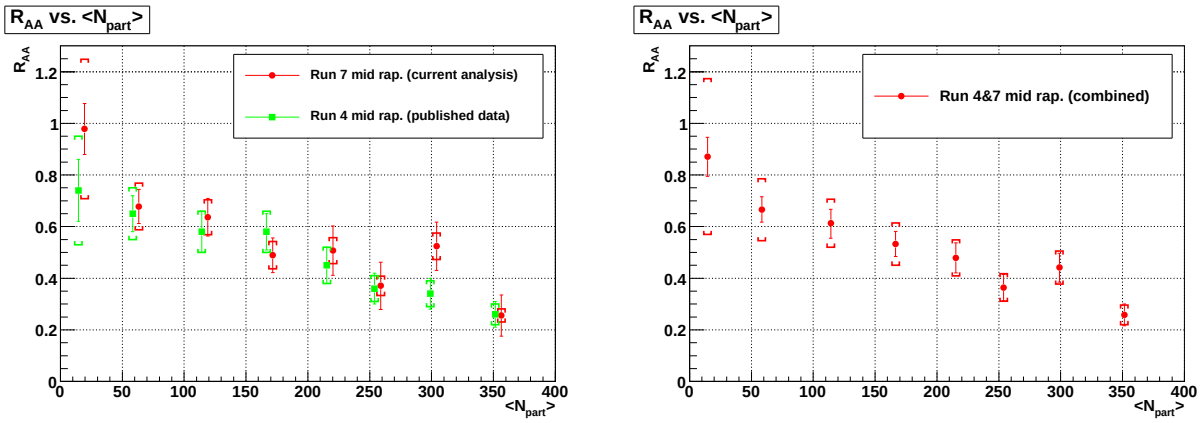

Figure V.2: Left: Comparison of R_{AA} from run 7 (red) to R_{AA} from run 4 (green). Right: The combined R_{AA} from run 4 and run 7. The procedure for combining is described in the text. In both plots, there is an additional global uncertainty of 12% coming from the p+p normalization, and common to the two data sets.

To combine the two results, the Particle Data Group prescription (chapter 32 in [39]) is implemented. For n measurements m_i with *independent* relative error δ_i and *common* errors δ_{com}, the average can be calculated using

$$\bar{m} = \frac{\sum_i^n \left(\frac{m_i}{(\delta_i)^2}\right)}{\sum_i^n \frac{1}{\delta_i^2}}, \tag{V.1}$$

where the common error does not intervene, since it confers the same weight to all the measurements. The error on the average is given by using

$$\delta_{\bar{m}} = \frac{1}{\left(\sum_i^n \frac{1}{\delta_i^2}\right)^{1/2}} \oplus \delta_{com}. \tag{V.2}$$

All the errors for the run 7 and run 4 R_{AA} are independent, except for the error on the average number of collisions and the systematical uncertainty related to the choice of a rapidity distribution for the simulation. The statistical plus uncorrelated systematical uncertainties

$$\delta_{stat} + \delta_{stat}^{com} = \delta R_{AA}(stat)/R_{AA} + \delta R_{AA}(stat, common)/R_{AA} \tag{V.3}$$

on the one hand and the correlated systematical errors

$$\delta_{sys} + \delta_{syst}^{com} = \delta R_{AA}(syst)/R_{AA} + \delta R_{AA}(syst, common)/R_{AA} \tag{V.4}$$

on the other hand are handled separately. For the two (run 4 and run 7) R_{AA} measurements:

$$\begin{aligned} &R_{AA}^4 \pm R_{AA}^4(\delta_{stat}^4 \oplus \delta_{stat}^{com}) \pm R_{AA}^4(\delta_{syst}^4 \oplus \delta_{syst}^{com}) \\ &R_{AA}^7 \pm R_{AA}^7(\delta_{stat}^7 \oplus \delta_{stat}^{com}) \pm R_{AA}^7(\delta_{syst}^7 \oplus \delta_{syst}^{com}) \end{aligned} \tag{V.5}$$

the error weighted average according to Eq. V.1 is

$$R_{AA} = \frac{\left(\frac{R^4_{AA}}{(\delta^4_{stat}\oplus\delta^4_{syst})^2} + \frac{R^7_{AA}}{(\delta^7_{stat}\oplus\delta^7_{syst})^2}\right)}{\left(\frac{1}{(\delta^4_{stat}\oplus\delta^4_{syst})^2} + \frac{1}{(\delta^7_{stat}\oplus\delta^7_{syst})^2}\right)}. \tag{V.6}$$

The correlated systematical errors of the two runs are essentially independent except for the systematics from the rapidity dependence of the efficiency (δ_y =0.7%, cf. Tab. IV.6), the error on $< N_{coll} >$ (relatively large for peripheral events, δ_{ncoll}, cf. Tab. V.1 for values.) and can be combined based on Eq. V.2 as

$$\delta_{syst} = \left(\frac{1}{(\delta^4_{syst} \ominus (\delta_y \oplus \delta_{ncoll}))^2} + \frac{1}{(\delta^7_{syst} \ominus (\delta_y \oplus \delta_{ncoll}))^2}\right)^{-1/2} \oplus \delta_y \oplus \delta_{ncoll}. \tag{V.7}$$

The statistical plus uncorrelated systematical errors are combined similarly. In this case there is no common error between run 4 and run 7. As a result, the relative statistical error on the combined R_{AA} can be expressed as

$$\delta_{stat} = \left(\frac{1}{(\delta^4_{stat})^2} + \frac{1}{(\delta^7_{stat})^2}\right)^{-1/2}. \tag{V.8}$$

The combined R_{AA} and its errors calculated using Eq. V.6, Eq. V.7 and Eq. V.8 is plotted on the right side of Fig. V.2.

V.3 Comparison to forward rapidity measurement

The run 7 Au+Au data set was also analyzed for the J/ψ nuclear modification factor in the dimuon decay channel at forward rapidity (1.2< |y| <2.2), but not combined to run 4. The preliminary result from this analysis is shown in Fig. V.3 on the left together with the result from the combination of run 4 and run 7 results current mid rapidity.

The rapidity dependence of the measured R_{AA} reflects a narrowing of the J/ψ rapidity distribution in going from p+p collisions to Au+Au collisions. This ordering has an inverse tendency from what is expected according to models that incorporate a suppression that increases with local density. Higher local density is expected at the mid rapidity region, since the distribution of produced particles peaks at mid rapidity. Before going to comparisons to models of the forward and mid rapidity R_{AA}s, the next section will compare the cold nuclear matter absorption expectation to the measured R_{AA}s to try to answer the question whether there is statistically significant suppression beyond cold nuclear matter effects in either the forward or mid rapidity measured suppression.

V.4 Comparison to cold nuclear matter effect projections

Despite the larger error bars, the result from the less model dependent R_{dAu} data points extrapolation method, explained in Sec. I.3.3 is used as a cold nuclear matter effects benchmark.

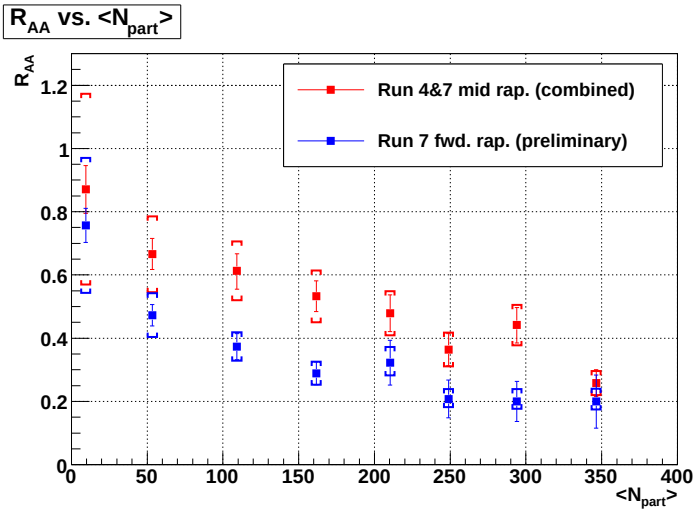

Figure V.3: Comparison of R_{AA} from combined run 7 and run 4 Au+Au analysis at mid rapidity (red) and run 7 analysis at forward rapidity (blue).

Recall that this method uses a physically motivated symmetrization of the R_{dAu} measurement (Eq. I.25) in conjunction with the Glauber model, and a plausible assumption that the cold nuclear matter effects on a J/ψ depend only on the local impact parameter of the collision that produced the J/ψ. In Fig. V.4 on the left the data points from this analysis combined with the run 4 analysis (red) are plotted together with the cold nuclear matter extrapolation at the corresponding average $< N_{part} >$ values. The same figure on the right side shows the ratio of measured R_{AA} to the R_{AA} extrapolated form R_{dA} (denoted R_{AA}^{CNM}). The ratio R_{AA}/R_{AA}^{CNM} can be seen as the survival probability of the J/ψ in the medium left behind in heavy ion collisions *after* the effects of cold nuclear matter. If this ratio is equal to one, then it means that there is no *anomalous* suppression.

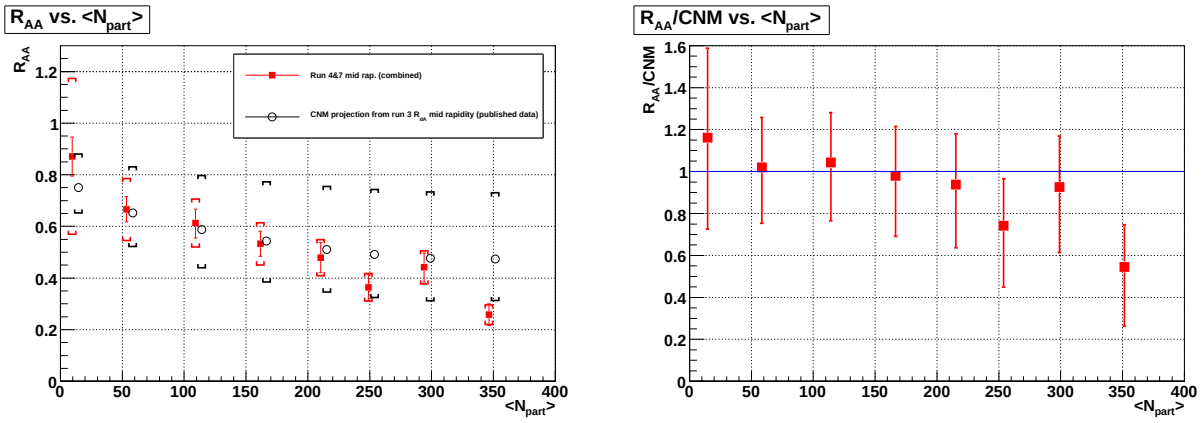

Figure V.4: Left: R_{AA} compared to cold nuclear matter projection. Right: The ratio of R_{AA} to the nuclear matter effect projection (survival probability).

The value of R_{AA}/R_{AA}^{CNM} (survival probability) is compatible to unity for most of the bins except for the most peripheral one ($< N_{part} >$=350) and falls below one (by more than two standard deviations) for more central event selection. A systematical trend of decreasing

survival probability is observed with increasing centrality, again with the exception of the point at $< N_{part} >$=300. However, most of the uncertainty comes from the d+Au extrapolation (black circles and brackets in Fig. V.4) and an improved error from the d+Au extrapolation (and the R_{AA} measurement) is direly needed.

V.5 Comparison to model predictions

In this section, the R_{AA} measurements are compared to a phenomenological calculation [73] that modelizes the charm-medium interaction within the framework of the Hadron-String Dynamics(HSD) transport approach [101]. HSD allows mapping the evolution of the local energy density achieved in heavy ion collisions as a function of time from the ion crossing. The reliability of this model is tested by comparing the J/ψ production in p+p and d+Au collisions, the analysis of which allows also to extract J/ψ-baryon interaction to estimate the effect of cold nuclear matter absorption in Au+Au collisions. Another important input parameter, the number of c and $\bar{c}$ quarks available per nucleon-nucleon collision is estimated by fitting a phenomenological function to the world charmonium cross sections. Once these ingredients are fixed, the authors modelize different kinds of possible interactions of the prehadronic $c\bar{c}$ state or the formed quarkonia (J/ψ, χ_c, ψ') with the collided matter. The distinction between the prehadronic state and formed quarkonium is done based on the estimation of formation time according to $\tau_f \approx 1/m_T \approx 0.05$ fm/c at $m_T \sim 4$ GeV/c.

1. Cold nuclear matter (baryonic) absorption. The break up of prehadronic $c\bar{c}$ resonance by baryonic matter B (fragments of initial nucleons). A global cross section ($\sigma_{c\bar{c}B}$=4.18 mb) independent of the energy is chosen. At early stages when such reactions take place, the $c\bar{c}$ has not had enough time to form, therefore, no distinction is made between the different resonances. The break up of formed quarkonia resonance by baryonic matter, encoded again by empiric estimates ($\sigma_{J/\psi B}$=4.18 mb, $\sigma_{\chi_c B}$=4.18 mb, $\sigma_{\psi' B}$=7.6 mb).

2. Anomalous suppression by *hadronic* co-mover absorption. This refers to the dissociation by interaction with other types of mesons co-moving with the formed charmonium. The breakup process $c\bar{c} + m \rightarrow D + \bar{D}$ is accompanied by a balanced reverse interaction $D + \bar{D} \rightarrow c\bar{c} + m$ in each channel (a channel being defined by the D meson type and co-moving mesons type involved in the reaction). The cross sections used for the hadronic co-mover absorption are chosen to reproduce correctly the SPS J/ψ suppression measurements.

3. Anomalous suppression by *prehadronic* co-mover absorption. In this scenario, the scattering of a $c\bar{c}$ state on an unformed co-moving hadron is allowed as long as the local temperature is higher than the co-moving hadrons dissociation temperature. The net effect of allowing this mechanism is to enhance both the breakup and reverse creation processes discussed in 2, by letting them take place much earlier in the reaction with partons as opposed to hadrons.

4. Threshold melting. This is the sequential dissociation of charmonia beyond their temperature inferred from lattice QCD, and it is modelized using the temperature at the location $c\bar{c}$ pair, that is, a formed charmonium state is fully dissociated to a c and $\bar{c}$ quark whenever the temperature at its location exceeds its lattice inferred dissociation

temperature. In this scenario, no mechanism is implemented for the recombination of c and $\bar{c}$ quarks.

In both scenarios 2 and 3, the baryonic absorption of scenario 1 is implemented as a common baseline. The resulting J/ψ R_{AA} in Au+Au collision at top RHIC energy are shown at forward and mid rapidities in Fig. V.5. On the left is the hadronic co-mover scenario (that reproduced the SPS measurements) at forward rapidity (in blue) and mid rapidity (in red) together with the data points from the combined run 4 plus run 7 analysis. The predictions are shown as open crosses whereas the data points are shown as full squares. The hadronic absorption scenario clearly fails to reproduce the rapidity dependence of the RHIC data. In the prehadronic co-mover absorption approach, for which the results are shown on the right hand side plot in the same figure by open stars (same color code for the rapidity), the qualitative agreement is significantly improved.

It is important to note that this post-diction is only one among a variety of other models (a non exhaustive example is cf. references [102, 103, 104, 105, 106, 107, 108, 109]), most of them reproducing the rapidity tendency of the observed R_{AA} as a function of rapidity whenever the recombination mechanism is included in the calculations.

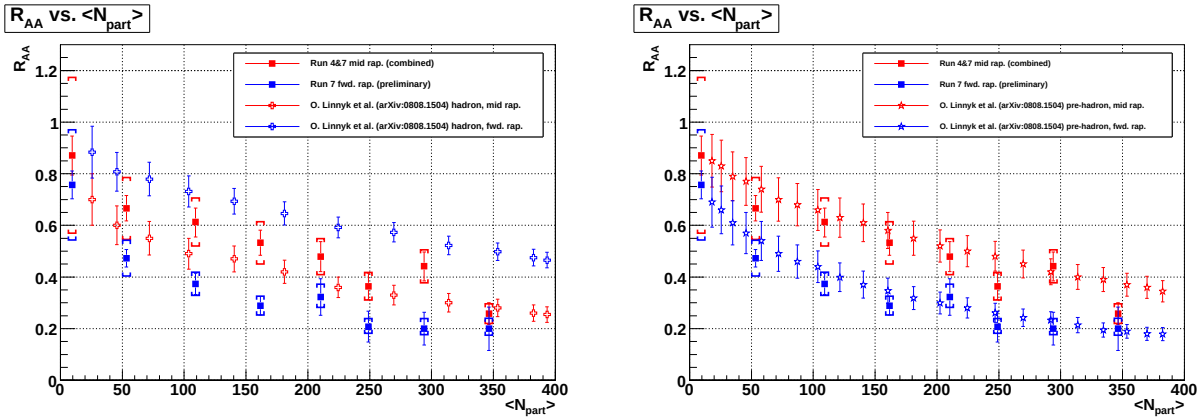

Figure V.5: J/ψ R_{AA} from the combined run 4 - run 7 at mid rapidity and run 7 at forward rapidity compared to the predictions of reference [73] in the hadronic co-mover absorption approach (left) and in the prehadronic co-mover absorption approach (right).

Chapter VI

J/ψ Elliptic Flow

In chapter 5, the nuclear modification factor R_{AA} of J/ψ measured at mid rapidity was compared to the forward rapidity results. It was noted that, contrary to what is expected from a higher density at mid rapidity, the suppression is stronger at forward rapidity. A number of explanations were put forth. One of them relies on the possibility that a fraction of the J/ψ yield measured in A+A type collisions comes from recombination of c and $\bar{c}$ quarks that were not created in the same hard process. If this mechanism of production is indeed at play, it can compensate for a stronger suppression of J/ψ at mid rapidity, and even reverse the tendency of the suppression ratio. The 'regeneration' of J/ψ grows with the number of $c\bar{c}$ pairs created in the A+A collision. The recombination probability is indeed an increasing function of the spatial density of c and $\bar{c}$ quarks. Quite little is known however on the exact condition of proximity in momentum and position space that any particular c and $\bar{c}$ pair should satisfy in order to be able to recombine into a J/ψ. This uncertainty, coupled with the large experimental uncertainty ($\sim$25%) on the conserved number of $c\bar{c}$ pairs created initially in the collision, renders the theoretical predictions of the R_{AA} resulting from recombination not very quantitative.

This is where the recent intense interest in the elliptic flow of J/ψ intervenes. It is an established fact that despite their heavy mass, charm and maybe bottom quarks must thermalize sufficiently early and develop a strong elliptic flow in order to explain the large non-photonic electron elliptic flow measured in Au+Au collisions at mid rapidity [33]. It is natural that a J/ψ created through a regeneration process inherits the flow of the thermalized c and $\bar{c}$ quarks from which it is created. In contrast, prompt J/ψ (from hard processes) are *created* isotropically, since hard processes do not have information about the geometry of the collision. However, the path length dependence of energy loss by the formed J/ψ as it goes out of the collided medium can induce some anisotropy that reflects the geometry of the collision. But such an effect is predicted not to be strong due to the small interaction cross section of a J/ψ with medium. The magnitude of the flow of prompt J/ψ is predicted by some models [107] to be quite small compared to the flow from regenerated J/ψ, based on the measured flow of non-photonic electrons. Therefore, the elliptic flow of J/ψ may be a rather clean (model independent) experimental test of regeneration. The measurement of elliptic flow is however statistics intensive. In the following section an attempt to extract the p_T dependence of the J/ψ elliptic flow from the run 7 Au+Au data is detailed, and the result is discussed.

VI.1 Extraction of the elliptic flow parameter v_2

The elliptic flow parameter v_2 of J/ψ for collisions at a given impact parameter is extracted from the Fourier expansion of the azimuthal distribution of the emission angle of J/ψ

$$\frac{dN_{J/\psi}}{d(\phi_{J/\psi}-\Phi_{RP})}(b) = A\left(1+2v_2^i(b)\cos\left(2(\phi_{J/\psi}-\Phi_{RP})\right)+\cdots\right). \tag{VI.1}$$

The necessary ingredients to calculate the elliptic flow are the event by event reaction plane angle (Φ_{RP}) and the azimuthal emission angle of the reconstructed J/ψ ($\phi_{J/\psi}$) from which the cumulative distribution of $\frac{dN}{d(\phi_{J/\psi}-\Phi_{RP})}$ can be constructed. For the sake of simplicity, the indexes J/ψ and RP are dropped hereafter. The lower case ϕ will refer to the J/ψ azimuthal angle and the upper case Φ will refer to the reaction plane of the event.

VI.1.1 Reaction plane resolution

The reaction plane angle Φ is estimated from the angular distribution of a subsets of particles within an event. As such, it is susceptible to statistical fluctuations. In fact the resolution of the reaction plane is inversely proportional to the square root of the number of particles that were used for its determination [110].

Irrespective of the method used to extract the raw or measured J/ψ v_2, denoted hereafter as v_2^{mes}, the finite detector resolution for the measurement of the collision reaction plane introduces a net bias. Before going into specifics of the extraction methods, this section describes briefly how the effect of finite resolution the measured elliptic flow v_2^{mes} can be corrected for. The resolution correction is independent of the extraction method. It depends however on the centrality of the collision. The reaction plane resolution is best for mid central collisions, where the shape of the overlap region has a strong asymmetry and the number of produced particles is still high. The resolution decreases with both increasing and decreasing centrality. For more central collisions the initial spatial anisotropy is not high enough for significant elliptic flow to develop. For more peripheral collisions, the multiplicity of produced particles is too low to determine the reaction plane with good accuracy.

To facilitate the understanding of the resolution correction derivation, it is convenient to express v_2 in terms of the Fourier coefficients of Eq. VI.1 as follows. If the distribution $\frac{dN}{d(\phi-\Phi)}$ can be described by the function $f(x)$, where $x=\phi-\Phi$, then the second coefficient v_2 of the Fourier series of $f(x)$ is given by

$$v_2 = \frac{1}{2\pi}\int_{-\pi}^{\pi} f(x)\cos(2x)dx. \tag{VI.2}$$

This relation can be discretized by considering N J/ψ forming angles relative to the reaction plane of their underlying events $\phi^i-\Phi^i$ that are distributed according to $f(x)$. The relation Eq. VI.2 can then be expressed as

$$v_2 = \frac{1}{N}\sum_{i=0}^{N}\cos(2(\phi^i-\Phi^i)) =< \cos(2(\phi-\Phi)) > \tag{VI.3}$$

This equation as well as Eq. VI.1 assume that the true reaction plane angles Φ^i are known. In reality the true value of Φ^i can not be experimentally determined with infinite resolution.

Instead a subset of the tracks in the full event are used to determine the event reaction plane. Such a subset called a *subevent*. The only condition that the subevent has to satisfy is that it should be measured at a different pseudorapidity range than the signal to insure that there is no correlation of the signal particle azimuthal angle with the reaction plane determination. In other words, that the signal particle (or the jet that it belongs to) does not bias the reaction plane angle determination. If the reaction plane angle determined by the subevent is denoted Φ^{mes}, then the measured v_2 can be expressed as

$$v_2^{mes} =< \cos(2(\phi - \Phi^{mes})) > \tag{VI.4}$$

This relation can be expressed as

$$\begin{aligned} v_2^{mes} &= < \cos(2(\phi - \Phi_A^{mes})) > \\ &= < \cos(2(\phi - \Phi_A^{true} + \Phi^{true} - \Phi_A^{mes})) > \\ &= < \cos(2(\phi - \Phi^{true})) >< \cos(2(\Phi^{true} - \Phi_A^{mes})) > \\ &= v_2^{true}\sigma_{RP} \end{aligned} \tag{VI.5}$$

where the trigonometric relation $\cos(a+b) = \cos(a)\cos(b) - \sin(a)\sin(b)$ is used in the third equality, together with the fact that the average of the odd sin function is zero. In addition, the values $\phi - \Phi^{true}$ and $2\Phi^{true} - \Phi^{mes}$ are assumed to be distributed independently[1] to allow the decomposition in the third equality.

There are a number of ways to estimate σ_{RP} proposed in the literature. The simplest approximation is given by the event-wise average

$$\sigma_{RP} =< \cos(2(\Phi_A^{mes} - \Phi_B^{mes})) > \tag{VI.6}$$

where Φ_A^{mes} and Φ_B^{mes} are the reaction planes determined by two equivalent sub events (for example, using two identical reaction plane detectors at forward and backward rapidities at approximately the same distance from the event collision point). This is motivated by the fact that the distribution of $\Phi_A^{mes} - \Phi_B^{mes}$ should not be far from the distribution of $\Phi^{true} - \Phi^{mes}$. A more sophisticated method, suggested in [111, 110], is adopted for this analysis. The implementation was not carried out by me, and the resolution obtained by other analyzers is used here. The method proceeds by fitting an exactly derived analytic expression of the distribution of $\Phi_A^{mes} - \Phi_B^{mes}$, whose only parameter is the reaction plane resolution in addition to the global normalization.

Within PHENIX, the two independent measurements of Φ can be done using the reaction plane detectors in the north and south arms (cf. Sec. II.3.4), in other words, $\Phi_A = \Phi_N$ and $\Phi_B = \Phi_S$. The two reaction plane detectors are used in conjunction to determine the event reaction plane $\Phi^{mes} = \Phi_{NS}$. The resultant resolution of the reaction plane determined using Eq. VI.6 as a function of centrality is shown in Fig. VI.1 on the left together with the resolutions of the BBC (cf. Sec. II.3 and the MPC (cf. Sec. II.4.7 detectors.

Ideally, the measured v_2 at each centrality should be corrected with the resolution at the corresponding centrality. For J/ψ it is practically impossible to measure the v_2 with fine centrality selections due to lack of statistics. The approach used is therefore to average the resolution over a wide centrality selection over which the measurement is done. The choice is

[1] An important property of independently distributed random variables X and Y is that for any continuous functions f and g, $< f(X)g(Y) >=< f(X) >< g(Y) >$.

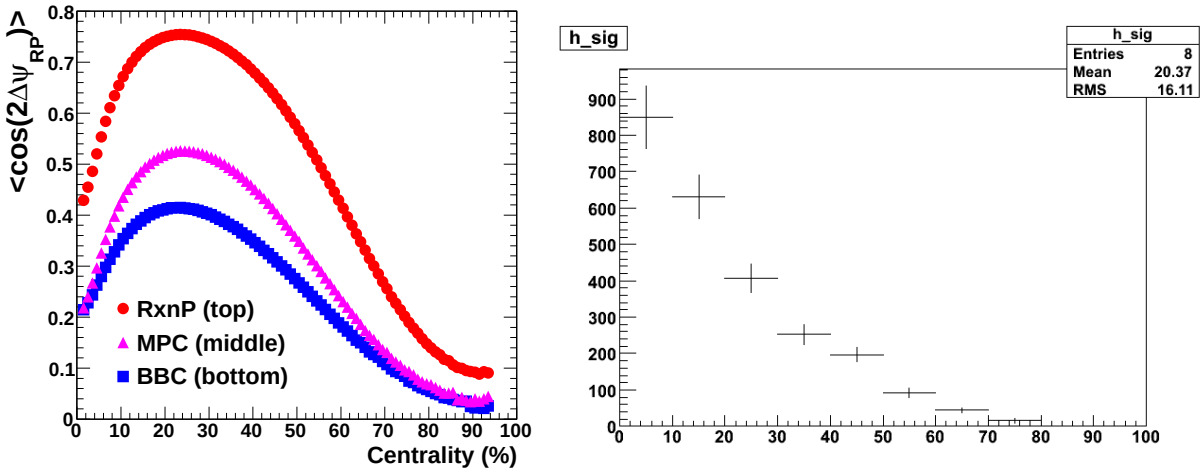

Figure VI.1: Left: The dependence of the reaction plane resolution on centrality. Right: The J/ψ yield as a function of centrality (cf. Sec. IV.6).

made here to use the centrality selection 20-60%. This is the mid centrality region where the compromise between J/ψ statistics and resolution is the best.

A J/ψ yield (cf. Fig. VI.1, right) weighted average of the reaction plane resolutions within 10% bins of centrality over the 20-60% selection is used as a global resolution correction. The raw yield in a given centrality bin is therefore corrected by the embedding efficiency[2] before being used in the weight, according to

$$\sigma_{RP} = \frac{\sum_i \frac{N_{J/\psi}(cent_i)}{\varepsilon_{emb}(cent_i)} \sigma_{RP}(cent_i)}{\sum_i \frac{N_{J/\psi}(cent_i)}{\varepsilon_{emb}(cent_i)}}, \tag{VI.7}$$

where the index i represents the centrality selections. This weighted average, evaluated on the bins 20-30%, 30-40%, 40-50% and 50-60% results in a value of σ_{RP}=66.4%±2.6% [112].

VI.1.2 Methods of extracting raw v_2

All the methods adopted here for the extraction of the J/ψ v_2 make use of Eq. VI.1, that involves the determination of the signal counts in bins of $\phi-\Phi$. To this end, the same technique as the one used in the extraction of R_{AA} is implemented. The basic idea is to subtract out the combinatorial background in the inclusive unlike sign dielectron foreground using an event mixing technique and to account for the residual background by an exponential function fitted on the subtracted unlike sign mass spectrum outside the mass range of the J/ψ. The systematics in the case of R_{AA} was extracted by using fits and varying underlying assumptions (cf. Sec. IV.6.3). Here, in addition to varying the signal extraction method, analogous to the R_{AA}, three different methods are used to extract v_2 and thus estimate systematics as the width of the dispersion of the results.

[2]Other efficiencies, for example the reconstruction efficiency, are not relevant, since they are independent of the reaction plane angle.

VI.1.2.1 Fitting method

In this method the signal is extracted in five bins of $\phi - \Phi$ ($[-\pi/2,\ -3\pi/10]$, $[-3\pi/10,\ -\pi/10]$, $[-\pi/10,\ \pi/10]$, $[\pi/10,\ 3\pi/10]$ and $[3\pi/10,\ \pi/2]$) and four bins of p_T ([0, 1], [1, 2], [2, 3] and [3, 5] in GeV/c). The J/ψ yield as a function of $\phi - \Phi$ and p_T, counted with the simplest method[3] in the range 2.9-3.3 GeV/c^2 are plotted with the errors in Fig. VI.2.

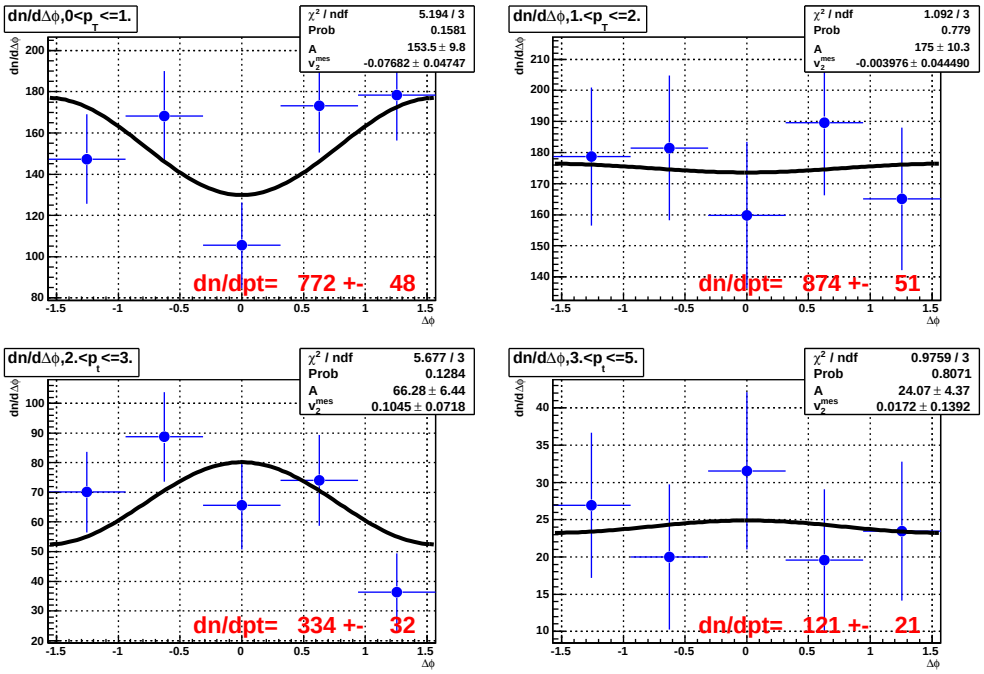

Figure VI.2: Differential yield as a function of $\Delta\phi = \phi - \Phi$ in four bins of p_T (given in the text), with smallest p_T range on the upper left panel and highest p_T range on the bottom right.

For each p_T bin, the resulting $\phi - \Phi$ dependence of the signal count is fitted with Eq. VI.1 in the range from $-\pi/2$ to $\pi/2$. The two fit parameters (global normalization A and raw v_2^{mes}) are not constrained. The χ^2 fit is done by using the integral of the function over the p_T bin and not its value at the center. The fitting error on the v_2^{mes} is propagated to the corrected v_2. The v_2 values corrected for the resolution effect using Eq. VI.5 for the above stated four p_T bins are shown in Fig. VI.3.

VI.1.2.2 Ratio method

The fitting method is challenged by lack of statistics especially for the higher p_T bins. Instead of fitting the function in Eq. VI.1 on less than five points, an option is to do the signal counting in just two $\phi - \Phi$ bins: one in the *in plane* direction (N_{in}) and another in the *out of plane* direction (N_{out}). By integrating Eq. VI.1 over the definitions of the in plane and out of plane directions, one can relate v_2 to the signal counts N_{in} and N_{out}. The range of possible values for $\phi - \Phi$ is $[-\pi/2, \pi/2]$. If one defines the in plane direction as the range $[-a, a]$ and

[3]Subtracting the combinatorial background by mixed event technique and estimating the residual background by an exponential fit outside the J/ψ mass range.

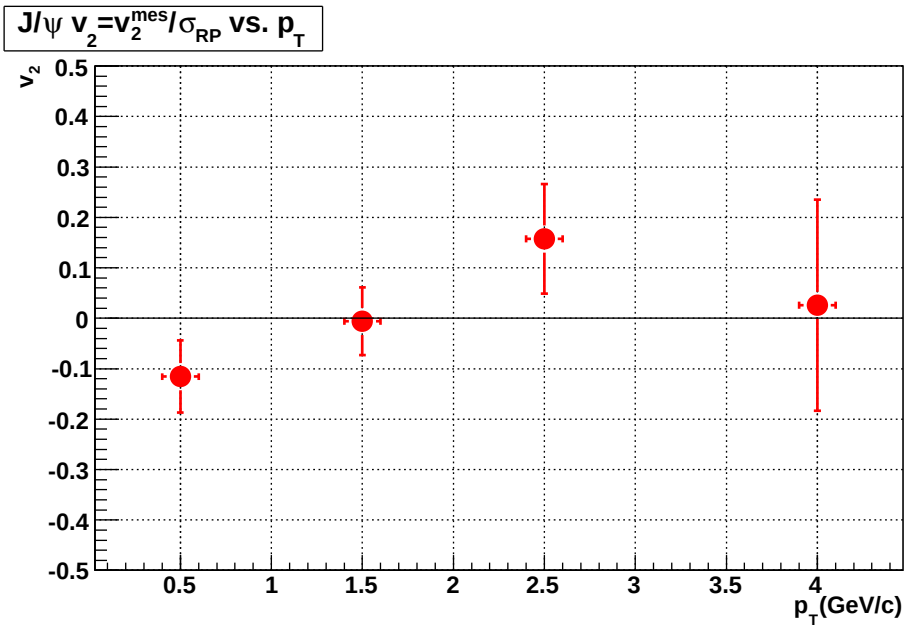

Figure VI.3: Resolution corrected v_2 as a function of p_T, from the fitting method.

the out of plane direction as the range $[-\pi/2, -a] \bigcup [a, \pi/2]$, the integration of the function $f(x) = A(1 + 2v_2 \cos(2x))$ over these two regions gives:

$$\begin{aligned} N_{in} &= \int_{-a}^{a} dx A(1 + 2v_2\cos(2x)) = A(x + v_2\sin(2x))|_{-a}^{a} \\ &= 2A(a + v_2\sin(2a)) \qquad \text{(VI.8)} \\ N_{out} &= \int_{-\pi/2}^{-a} + \int_{a}^{\pi/2} dx A(1 + 2v_2\cos(2x)) \\ &= A(x + v_2\sin(2x))|_{-\pi/2}^{-a} + |_{a}^{\pi/2} = 2A(\pi/2 - a - v_2\sin(2a)) \qquad \text{(VI.9)} \end{aligned}$$

Summing Eq. VI.8 and Eq. VI.9 gives $A = (N_{out} + N_{in})/2$, which inserted back into Eq. VI.8 leads to the relation between N_{in}, N_{out} and v_2:

$$\begin{aligned} N_{in} &= \frac{2(N_{in} + N_{out})}{\pi}(a + v_2\sin(2a)) \\ \Longrightarrow \qquad v_2 &= \frac{1}{\frac{2}{\pi}\sin(2a)}\left(\frac{(1 - \frac{2a}{\pi})N_{in} - \frac{2a}{\pi}N_{out}}{N_{in} + N_{out}}\right), \qquad \text{(VI.10)} \end{aligned}$$

For the case of $a = \pi/4$, which is the in plane/out of plane convention adopted here, Eq. VI.10 reduces to

$$v_2 = \frac{\pi}{4}\frac{N_{in} - N_{out}}{N_{in} + N_{out}}, \qquad \text{(VI.11)}$$

with the statistical error on v_2 propagated from the errors on N_{in} and N_{out} (δ_{in} and δ_{out} respectively, and assumed to be independent) given by

$$\delta_{v_2} = \frac{\pi}{4}\left(\left(\frac{\partial v_2}{\partial N_{in}}\right)^2\delta_{in}^2 + \left(\frac{\partial v_2}{\partial N_{out}}\right)^2\delta_{out}^2\right)^{1/2} = \frac{\pi}{2(N_{in} + N_{out})^2}\sqrt{N_{out}^2\delta_{in}^2 + N_{in}^2\delta_{out}^2}. \qquad \text{(VI.12)}$$

The J/ψ v_2 and its error calculated using Eq. VI.11 and Eq. VI.12 in the same p_T bins as in the fitting method is shown on the left of Fig. VI.4. The signal counting for this plot is done with the same basic method as in the case of the fitting method.

VI.1.2.3 Folded fitting method

An alternative way to reduce the number of bins in which the signal counting has to be done is to "fold" the $\phi - \Phi$ axis around 0 and doing the fitting on the range restricted between 0 and $\pi/2$ with less number of bins than in the simple fitting method. This is authorized by the symmetry of Eq. VI.1. The folded ϕ range ($[0,\ \pi/2]$) is divided into three bins ($[0,\ \pi/6]$, $[\pi/6,\ \pi/3]$ and $[\pi/3,\ \pi/2]$), with the same p_T bins as in the fitting method. The resulting signal counts (extracted using the same basic method as for the fitting and ratio methods) are shown in Fig. VI.5 together with the fits of the function from Eq. VI.4. The parameters are identical to those explained in the fitting method. The resulting v_2 corrected for resolution and with the fitting errors appropriately propagated is shown in the right part of Fig. VI.5.

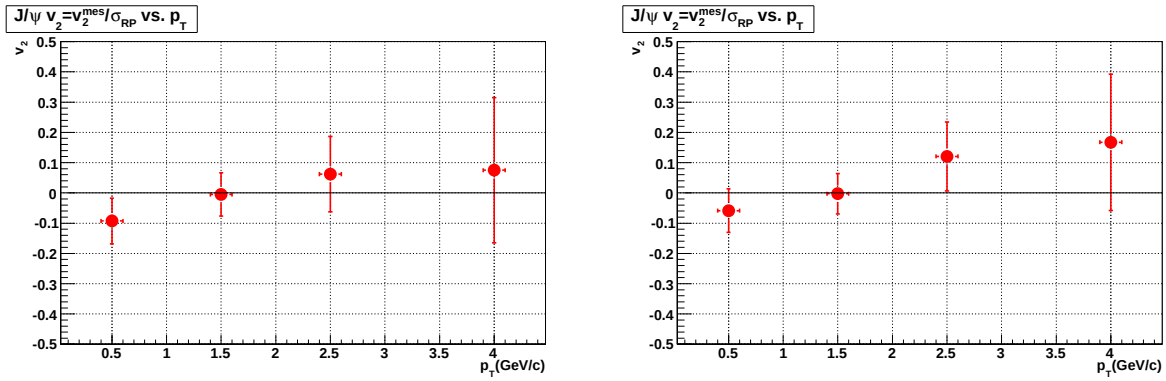

Figure VI.4: Resolution corrected v_2 from the ratio method (left) and folded fitting method (right).

VI.2 Systematics

The systematics on v_2 are estimated in a similar manner as the systematics on the signal counting of the J/ψ R_{AA} measurement. Fig. VI.6 on the top left shows the v_2 extracted using the fitting method when extracting the J/ψ signal with the 12 methods that are listed on the top right panel and described in Sec. IV.6, p. 122. Similarly the figures on the bottom show the dispersion plots of v_2 vs. p_T using the other two methods: ratio method (left) and folded fitting method (right).

The systematical error is set to be equal to $1/\sqrt{12}$ times the maximum difference between the resulting v_2 when the signal counting and the raw v_2 extraction methods are varied. As in the case of the systematical error for signal counting in the calculation of R_{AA}, this choice assumes that the systematical error is distributed uniformly. If so, the RMS of the distribution is related to the maximum difference Δ_{max} through $RMS = \Delta_{max}/\sqrt{12}$. In contrast to the case of R_{AA}, the central value here is chosen to be the average of all the methods (3×12 variations). This choice is justified because the largest variation on the resultant v_2 comes

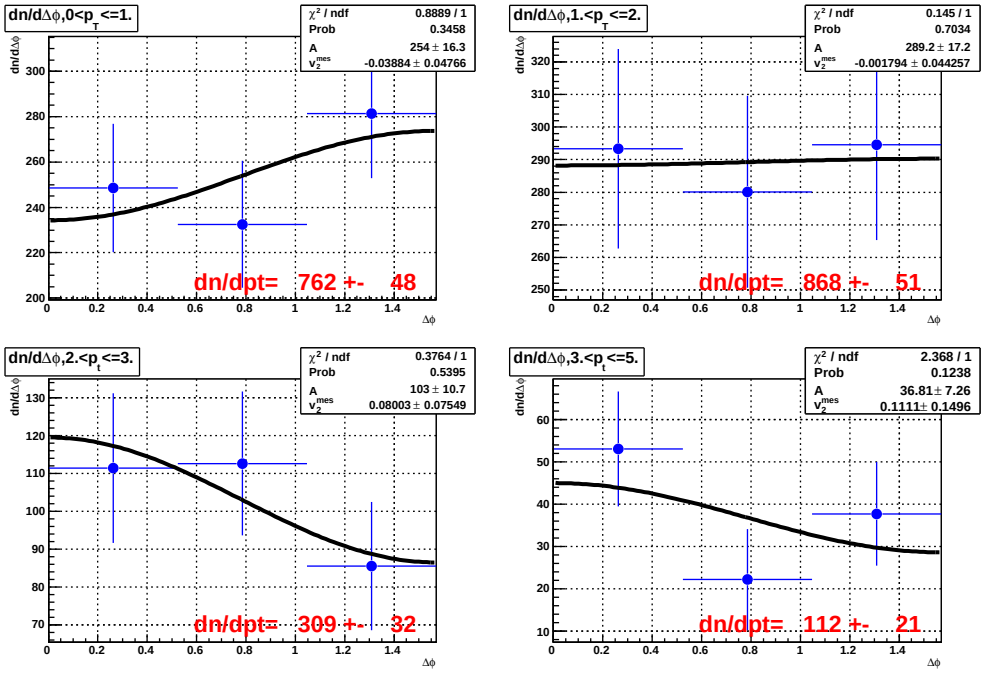

Figure VI.5: Differential yield as a function of $\Delta\phi = \phi - \Phi$ in four bins of p_T (given in the text), with smallest p_T range on the upper left panel and highest p_T range on the bottom right.

from the change in the method of the raw v_2 extraction, and unlike the case of signal counting systematics, there is no *a priori* reason to favor any of the raw v_2 extraction methods above the others.

In Fig. VI.7, the systematical errors estimated this way are represented as boxes whereas the average statistical errors are shown as error bars. Together with this final result for the v_2 are also shown curves from a few model prediction of the p_T dependence of J/ψ v_2. The values of v_2 are tabulated in Tab. VI.1.

p_T(GeV/c)	Fitting (%)	Ratio (%)	Folded fitting (%)	Overall average (%)
0−1	−7.54±7.46±2.96	−7.20±7.71±2.17	−1.23±7.42±2.77	−5.33±7.53±4.56
1−2	−0.22±6.95±1.13	0.66±7.40±1.56	0.01±6.88±1.74	0.15±7.07±2.23
2−3	18.73±11.09±2.42	13.36±12.43±5.13	17.04±11.53±3.94	16.38±11.69±5.56
3−5	5.15±27.87±4.23	9.96±27.52±3.31	15.48±25.97±1.22	10.20±27.12±5.70
1−5	0.35±4.70±1.35	1.13±5.09±1.24	0.55±4.76±1.59	0.68±4.85±1.61

Table VI.1: The resolution corrected v_2 (in %), with associated statistical and systematical errors for the three methods and the final average value.

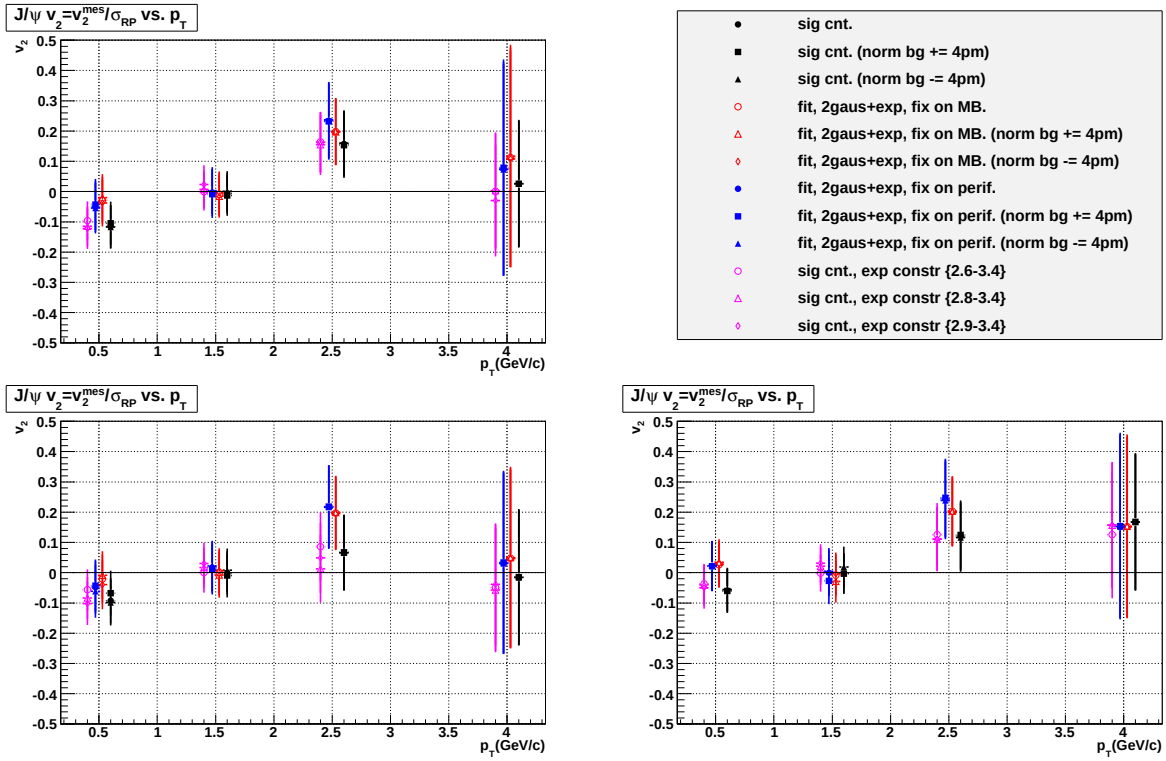

Figure VI.6: Resolution corrected v_2 employing various signal extraction methods and fitting methods (top left), ratio method (bottom left) and folded fitting method (bottom right). A legend of the signal extraction methods is displayed on the top right panel.

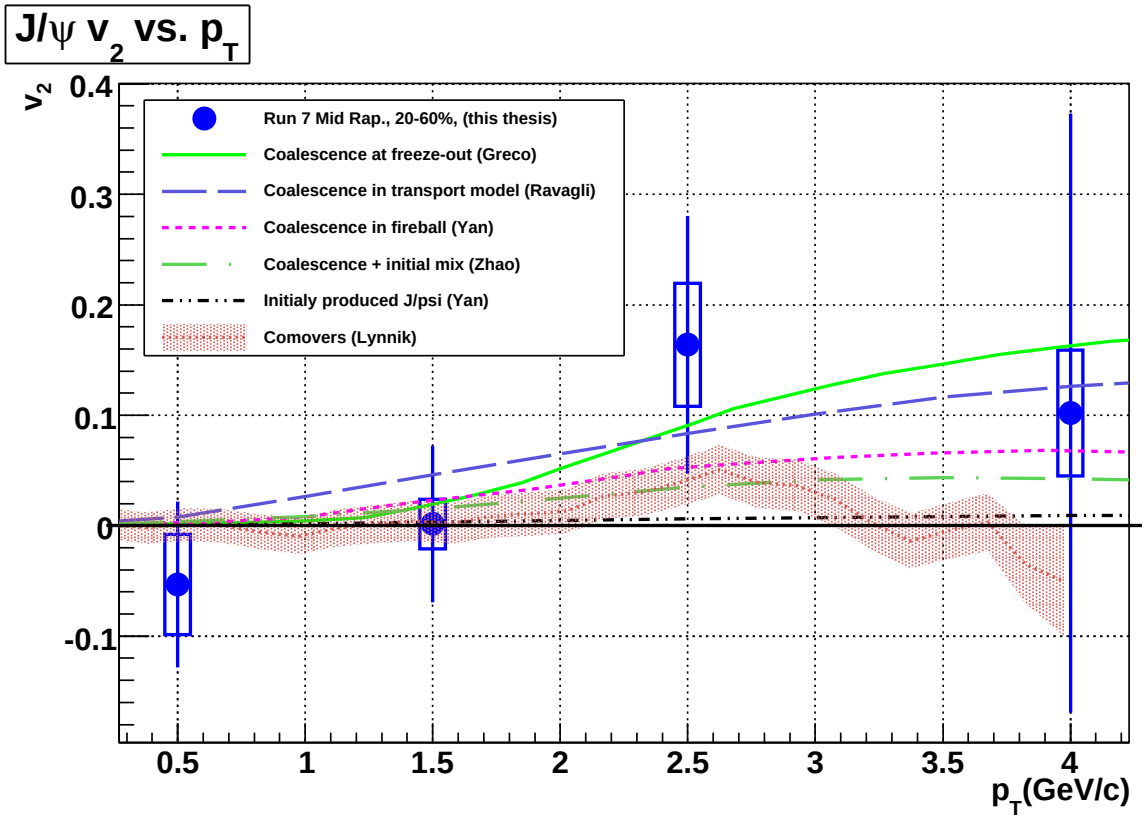

Figure VI.7: Final v_2 with statistical errors (bars) and correlated systematical errors (boxes) together with curves from model predictions.

VI.3 Discussion

In this section, the following three points will be addressed.

- Compatibility with a preliminary result [112] on half of the statistics employed here,
- Comparison with model predictions.

The run 7 Au+Au data set was analysed for J/ψ v_2 shortly after data taking with approximately half of the statistics used here. Fig. VI.8 on the left shows the preliminary result from this previous analysis (in red square markers) together with the results presented here (blue circular markers). The preliminary analysis could only be done up to a p_T of 2.5 GeV/c due to unreasonably large uncertainties for the $p_T = 4$ GeV/c point. As expected, the two results are quite compatible within the statistical error bars alone, since both are obtained using data from the same group of runs. However the data point at $p_T = 1.5$ GeV/c, which has the highest J/ψ statistics among all the p_T bins, shows a slightly negative v_2 (central value) in the preliminary result and a very close to zero result for the new analysis presented here. Since there was speculation about this unexpected negative value, it was compelling to verify whether or not the difference at p_T=1.5 GeV/c is due to simple statistical fluctuation. The exact same half of the data that was used for the preliminary result as well as its complement were analyzed using the method presented in this chapter. Fig. VI.8 on the right compares the preliminary result (red full squares) with results found employing the method detailed in this chapter on the two halves of the statistics: on the preliminary set (blue empty circles) and on its complement (green empty squares). Within this bin, it is clear that using the same sample as the preliminary analysis, a very similar negative v_2 is obtained. The v_2 obtained using the complimentary set is 3.2 standard deviations away. Although the probability of this occurring due to statistical fluctuation alone is very small[4], the fact that the result from the half on which the preliminary analysis was performed gives very similar results to the preliminary analysis increases somewhat the confidence that the difference can still be due to statistical fluctuation than analysis error.

Fig. VI.9 shows the v_2 obtained in this work at mid rapidity (Tab. VI.1) with the v_2 obtained at forward rapidity, together with some model predictions.

In [113], Greco, Ko and Rapp compute some properties of charmed mesons (D and J/ψ) coming from quark coalescence at freeze-out. The full line in Fig. VI.9 is what they get for J/ψ elliptic flow, namely a v_2 slowly raising with p_T, up to 17 % at 5 GeV/c. In a more recent paper [114], Ravagli and Rapp refine the coalescence picture by formulating hadron production in terms of transport equation. They obtain 14 % at 5 GeV/c (as reported as a dash-dotted curve on Fig. VI.9). In [104], Yan, Zhuang and Xu have a slightly different approach, considering that since J/ψ are very tightly bound, they can be (re)produced earlier and throughout in the QGP history and thus inherit less elliptic flow. The dashed line in Fig. VI.9 shows their prediction for an impact parameter of 7.8 fm (corresponding to 28% centrality in our Glauber code) with the following scenarios:

- Initial production only (no coalescence): The small v_2 of initially produced J/ψ comes from the *leakage effect*, namely J/ψ forming outside of the fire ball, which is more likely

[4]For one measurement, the probability of a 3 standard deviation difference is $\approx 2.7\times10^{-}3$, but the probability that one out four measurements is off by three standard deviations is given approximately by the binomial law $\approx$ $f_{binom}(1;4,0.0027) = 4 \times 0.0027 \times (0.0027)^3 = 1.07\%$.

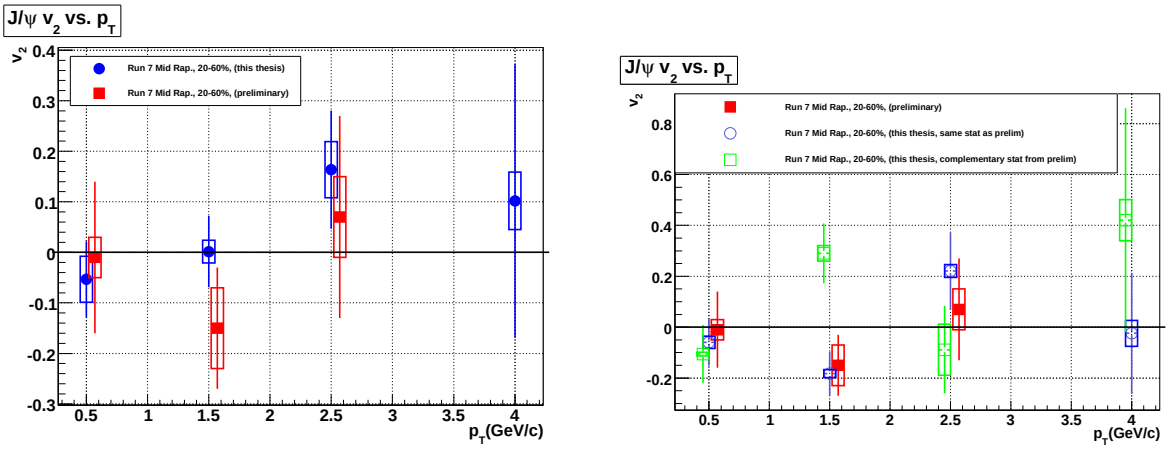

Figure VI.8: Left: Comparison of the result form this thesis (circles) with the preliminary analysis (squares). Right: Result of an analysis restricted to the preliminary data set using methods explained in this chapter (empty circles) compared to the preliminary result (full squares) and complementary data set (empty squares).

to happen on the short axis than on the long axis of the transverse plasma area. The expected flow from pure initial production is shown in Fig. VI.9 as dot dot dashed lines.

- Regeneration of J/ψ: As expected, they reach a higher v_2 in this model, namely 7% at $p_T = 4$ GeV/c. They also quote that they find back the results from the previous authors if they assume that recombination occurs at freeze-out (even though their centrality is not the same).

Zhao and Rapp (see [115]) calculate the J/ψ v_2 within their two components (direct production and regeneration) models that successfully fits the nuclear modification factor described in chapter 5. Their v_2 prediction is reproduced in Fig. VI.9 as a green dash-dotted line. They give a $\sim$ 20 % uncertainty and claim that, within the current uncertainty of their approach, comparing their prediction at 20-40% centrality selection with data from 20-60% centrality selection is not too unreasonable. Finally in [73] Linnyk *et al.* provide a prediction of the J/ψ v_2 based on a co-movers approach that was explained in Sec. V.5, and reproduced in Fig. VI.9 as dash-dotted line with an error band.

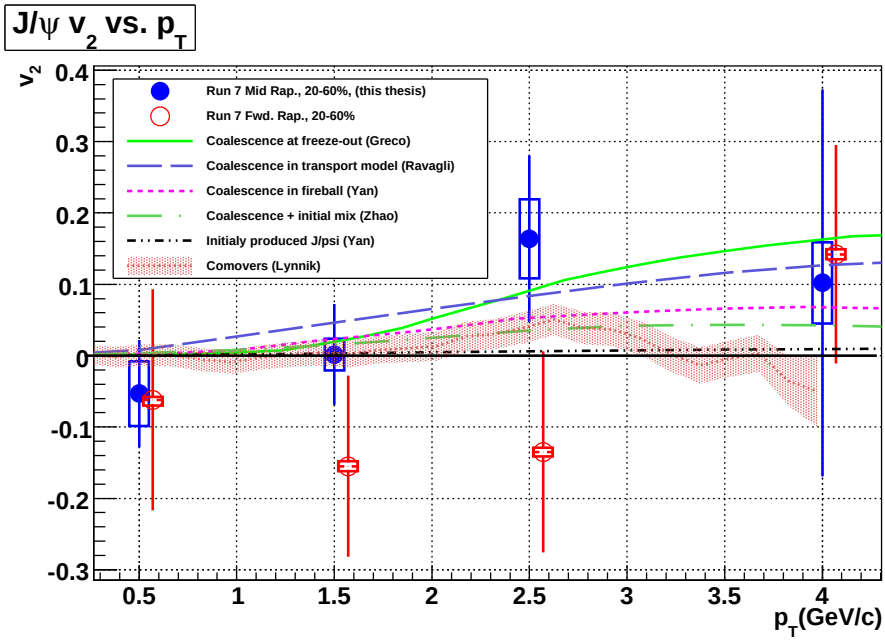

Figure VI.9: Comparison to forward rapidity measurement and model predictions (all are mid rapidity predictions).

Conclusion

In this manuscript, the analysis steps and extraction of J/ψ R_{AA} and elliptic flow v_2 from the run 7 Au+Au data taking period at center of mass energy of $\sqrt{s_{NN}} = 200$ GeV were presented and the results found discussed. The analysis of this data set presented new challenges with respect to the previous analysis of data for the same collision and species at the same energy. The complications arise from a particularly unfavorable signal to background arising from the addition of a detector element in the acceptance that converted photons into electrons, without adding any additional rejection. The magnetic field was also lower than the run 4 value, although the resolution loss due to this change on the main J/ψ peak is marginal.

Despite these differences, the extracted R_{AA} is in good agreement with the previous analysis, adding confidence and robustness to the result. The net statistical error on the new result is very much of the same order of magnitude as the previous one, and therefore did not represent by itself a significant gain on the errors. The final results from the new data sets were however averaged with the old one, and the resulting in a slightly improved statistical uncertainties of R_{AA}.

The new result does reinforce the understanding that the previous data set offered about the effect of the medium created in heavy ion collisions at high energy on the production rate of the J/ψ. Indeed the suppression factor R_{AA} at mid rapidity ($|y| < 0.35$) remains well above the forward rapidity result ($1.2 < |y| < 2.2$), continuing to pose a strong challenge to local energy density dependent suppression models, while corroborating models that incorporate regeneration at some stage. However, this interpretation crucially depends on the largely uncertain cold nuclear matter effects, for which the analysis of the recently taken d+Au data set with a factor of approximately 30$\times$ more statistics than the 2003 data set should bring more stringent constraints.

Another promising prospect to get a better measurement of the J/ψ nuclear modification, and hopefully an improved constraint on the various production/suppression/recombination models is the significant luminosity upgrade of a factor of 10 in the RHIC-II operation era to begin in a few years. Detector upgrades such as the "Silicon VerteX" (SVX) tracker will greatly improve the accuracy of the open charm production measurement through identification by displaced vertices. This will enhance the predictive accuracy of regeneration models that rely on the initially available charm quark abundances to make their projections. There is also a possibility to study final state effects (suppression, regeneration) separately from the initial state effects (shadowing, Cronin effect) by bootstrapping the J/ψ production measurement on the open charm measurement in a similar fashion as the Drell-Yan is used for the SPS measurements. This is currently impossible due to large uncertainty as well as to the inability to separate out charm contribution from bottom contribution in the non photonic single electron production.

There remain a certain number of experimental checks of regeneration. One of these is

the elliptic flow of J/ψ. The idea is that the large elliptic flow observed for electrons from semi-leptonic decays of open heavy flavour, is very likely to come from the elliptic flow of the heavy quarks in the initial stages of the collision. Hence, if J/ψ are regenerated from uncorrelated charm quarks, then they inherit the flow of their parents. Regeneration would thus manifest itself as a strong flow of J/ψ mesons, which in case of direct production, have no apparent reason to develop collectivity due to the low interaction cross section with, and short time of evolution inside the medium.

The results of the measurement of J/ψ v_2 from the PHENIX mid rapidity Au+Au data taken during run 7, and the analysis that led to the results have also been discussed in this thesis. Various methods were used to underpin the robustness of the results, and estimate the associated systematical uncertainty. The measurement of J/ψ v_2 is statistics intensive, and was made possible with the run 7 data taking period essentially due to the addition of a high resolution reaction plane detector. The statistical error however needs substantial improvement before this measurement can be used to really discriminate between models that incorporate regeneration from those that consider only direct J/ψ. This study underlines the feasibility of the measurements and should be seen more as an attempt to provide a ground for future measurements using higher statistics could be done, rather than as a result on which the now long standing question of J/ψ regeneration in the QGP could be answered.

The other experimental checks which can be used to test regeneration are the rapidity and transverse momentum distribution of J/ψ. In comparison to direct J/ψ, regenerated J/ψ should have a narrower rapidity distribution which is observed. Schematically, the reason is that more charm quarks are available for recombination at mid rapidity than at forward rapidity, favoring the creation of more regenerated J/ψ at mid rapidity. Similarly, regenerated J/ψ should have a softer p_T distribution. Although not done during this thesis, these particularities of the spectra of regenerated J/ψ with respect to direct ones can therefore be used to experimentally test regeneration. Finally the measurement of J/ψ suppression (or enhancement) at LHC energies will be a crucial test of regeneration, owing to the rather copious production of charm quarks (up to several hundred $c\bar{c}$ pairs expected in the most central Pb+Pb collisions). Regeneration, if a significant mechanism, will thus manifest as a very large R_{AA}, increasing with centrality of the collision, and possibly attaining values greater than one for the most central collisions.

Bibliography

[1] D. J. Schwarz. The first second of the universe. *Annalen Phys.*, 12:220–270, 2003.

[2] R. Turolla, S. Zane, and J. J. Drake. Bare quark stars or naked neutron stars? The case of RX J1856.5-3754. *Astrophys. J.*, 603:265–282, 2004.

[3] T. D. Lee. Abnormal Nuclear States and Vacuum Excitations. *Rev. Mod. Phys.*, 47:267, 1975.

[4] J. M. Maldacena. The large n limit of superconformal field theories and supergravity. *Adv. Theor. Math. Phys.*, 2:231–252, 1998.

[5] Hong Liu. Heavy ion collisions and AdS/CFT. *J. Phys.*, G34:S361–368, 2007.

[6] F. Karsch and E. Laermann. Thermodynamics and in-medium hadron properties from lattice QCD. *hep-lat/0305025*, 2003.

[7] F. Karsch. Recent lattice results on finite temperature and density QCD, part I. *PoS*, CPOD07:026, 2007.

[8] F. Karsch. Recent lattice results on finite temerature and density QCD, part II. *PoS*, LAT2007:015, 2007.

[9] Z. Fodor and S. D. Katz. Critical point of QCD at finite T and μ, lattice results for physical quark masses. *JHEP*, 04:050, 2004.

[10] K. Adcox et al. Formation of dense partonic matter in relativistic nucleus nucleus collisions at RHIC: Experimental evaluation by the PHENIX collaboration. *Nucl. Phys.*, A757:184–283, 2005.

[11] B. B. Back et al. The phobos perspective on discoveries at rhic. *Nucl. Phys.*, A757:28–101, 2005.

[12] C. Menotti, P. Pedri, and S. Stringari. Expansion of an interacting fermi gas. *Phys. Rev. Lett.*, 89(25):250402, Dec 2002.

[13] M. L. Miller, K. Reygers, S. J. Sanders, and P. Steinberg. Glauber modeling in high energy nuclear collisions. *Ann. Rev. Nucl. Part. Sci.*, 57:205–243, 2007.

[14] P. Shukla. The Glauber model and the heavy ion reaction cross section. *Phys. Rev.*, C67:054607, 2003.

[15] J. D. Bjorken. Highly relativistic nucleus-nucleus collisions: The central rapidity region. *Phys. Rev. D*, 27:140–151, Jan 1983.

[16] P. F. Kolb and U. W. Heinz. Hydrodynamic description of ultrarelativistic heavy-ion collisions. *nucl-th/0305084*, 2003.

[17] M. Csanad, T. Csorgo, and B. Lorstad. Buda-Lund hydro model for ellipsoidally symmetric fireballs and the elliptic flow at RHIC. *Nucl. Phys.*, A742:80–94, 2004.

[18] A. Adare et al. Scaling properties of azimuthal anisotropy in Au +Au and Cu + Cu collisions at $\sqrt{s_{NN}} = 200$ GeV. *Phys. Rev. Lett.*, 98:162301, 2007.

[19] P. Braun-Munzinger, K. Redlich, and J. Stachel. Particle production in heavy ion collisions. *nucl-th/0304013*, 2003.

[20] F. Becattini, L. Maiani, F. Piccinini, A. D. Polosa, and V. Riquer. Correlating strangeness enhancement and J/psi suppression in heavy ion collisions at s(NN)**(1/2) = 17.2-GeV. *Phys. Lett.*, B632:233–237, 2006.

[21] S. S. Adler et al. Measurement of direct photon production in p + p collisions at $\sqrt{s} = 200$ GeV. *Phys. Rev. Lett.*, 98:012002, 2007.

[22] S. S. Adler et al. Centrality dependence of direct photon production in $\sqrt{s_{NN}} = 200$ GeV Au + Au collisions. *Phys. Rev. Lett.*, 94:232301, 2005.

[23] A. Adare et al. Enhanced production of direct photons in Au+Au collisions at $\sqrt{s_{NN}}$ = 200 GeV. *arXiv:0804.4168[nucl-ex]*, 2008.

[24] S. Turbide, R. Rapp, and C. Gale. Hadronic production of thermal photons. *Phys. Rev.*, C69:014903, 2004.

[25] D. G. d'Enterria and D. Peressounko. Probing the QCD equation of state with thermal photons in nucleus nucleus collisions at RHIC. *Eur. Phys. J.*, C46:451–464, 2006.

[26] J. Putschke. First fragmentation function measurements from full jet reconstruction in heavy-ion collisions at $\sqrt{s_{\rm NN}} = 200$ GeV by STAR. *arXiv:0809.1419[nucl-ex]*, 2008.

[27] J. Adams et al. Evidence from d + Au measurements for final-state suppression of high p(T) hadrons in Au + Au collisions at RHIC. *Phys. Rev. Lett.*, 91:072304, 2003.

[28] S. S. Adler et al. Suppressed pi0 production at large transverse momentum in central Au + Au collisions at $\sqrt{s_{NN}} = 200$ GeV. *Phys. Rev. Lett.*, 91:072301, 2003.

[29] S. S. Adler et al. High transverse momentum η meson production in p + p, d + Au and Au + Au collisions at $\sqrt{s_{NN}} = 200$ GeV. *Phys. Rev.*, C75:024909, 2007.

[30] F. Arleo. Hard pion and prompt photon at rhic, from single to double inclusive production. *JHEP*, 09:015, 2006.

[31] K. J. Eskola, V. J. Kolhinen, H. Paukkunen, and C. A. Salgado. A global reanalysis of nuclear parton distribution functions. *JHEP*, 05:002, 2007.

[32] A. Adare et al. Quantitative Constraints on the Opacity of Hot Partonic Matter from Semi-Inclusive Single High Transverse Momentum Pion Suppression in Au+Au collisions at $\sqrt{s_{NN}} = 200$ GeV. *Phys. Rev.*, C77:064907, 2008.

[33] A. Adare et al. Energy Loss and Flow of Heavy Quarks in Au+Au Collisions at $\sqrt{s_{NN}} = 200$ GeV. *Phys. Rev. Lett.*, 98:172301, 2007.

[34] N. Armesto, A. Dainese, C. A. Salgado, and U. A. Wiedemann. Testing the color charge and mass dependence of parton energy loss with heavy-to-light ratios at RHIC and LHC. *Phys. Rev.*, D71:054027, 2005.

[35] G. D. Moore and D. Teaney. How much do heavy quarks thermalize in a heavy ion collision? *Phys. Rev.*, C71:064904, 2005.

[36] H. van Hees, V. Greco, and R. Rapp. Heavy-quark probes of the quark-gluon plasma at RHIC. *Phys. Rev.*, C73:034913, 2006.

[37] P. Kovtun, D. T. Son, and A. O. Starinets. Viscosity in strongly interacting quantum field theories from black hole physics. *Phys. Rev. Lett.*, 94:111601, 2005.

[38] Roy A. Lacey et al. Has the QCD critical point been signaled by observations at RHIC? *Phys. Rev. Lett.*, 98:092301, 2007.

[39] C. Amsler et al. Review of particle physics. *Phys. Lett.*, B667:1, 2008.

[40] T. Matsui and H. Satz. J/ψ suppression by quark gluon plasma formation. *Phys. Lett.*, B178:416, 1986.

[41] A. Mocsy and P. Petreczky. Quarkonia correlators above deconfinement. *Phys. Rev.*, D73:074007, 2006.

[42] M. Asakawa and T. Hatsuda. J/ψ and η/c in the deconfined plasma from lattice QCD. *Phys. Rev. Lett.*, 92:012001, 2004.

[43] A. Pineda and J. Soto. Effective field theory for ultrasoft momenta in NRQCD and NRQED. *Nucl. Phys. Proc. Suppl.*, 64:428–432, 1998.

[44] O. Kaczmarek and F. Zantow. Static quark anti-quark free and internal energy in 2-flavor QCD and bound states in the QGP. *PoS*, LAT2005:192, 2006.

[45] S. Digal, P. Petreczky, and H. Satz. String breaking and quarkonium dissociation at finite temperatures. *Phys. Lett.*, B514:57–62, 2001.

[46] H. Satz. Charm and beauty in a hot environment. *hep-ph/0602245*, 2006.

[47] W. M. Alberico, A. Beraudo, A. De Pace, and A. Molinari. Quarkonia in the deconfined phase: Effective potentials and lattice correlators. *Phys. Rev.*, D75:074009, 2007.

[48] A. Mocsy and P. Petreczky. Color Screening Melts Quarkonium. *Phys. Rev. Lett.*, 99:211602, 2007.

[49] E. G. Ferreiro, F. Fleuret, J. P. Lansberg, and A. Rakotozafindrabe. Cold nuclear matter effects on J/ψ production: intrinsic and extrinsic transverse momentum effects. *arXiv:0809.4684[hep-ph]*, 2008.

[50] J. P. Lansberg. J/ψ, ψ' and Υ production at hadron colliders: A review. *Int. J. Mod. Phys.*, A21:3857–3916, 2006.

[51] F. Abe et al. J/ψ and $\psi(2S)$ production in $p\bar{p}$ collisions at $\sqrt{s} = 1.8$ TeV. *Phys. Rev. Lett.*, 79:572–577, 1997.

[52] A. Adare et al. J/ψ production vs transverse momentum and rapidity in p + p collisions at $\sqrt{s} = 200$ GeV. *Phys. Rev. Lett.*, 98:232002, 2007.

[53] H. Haberzettl and J. P. Lansberg. Possible solution of the J/ψ production puzzle. *Phys. Rev. Lett.*, 100:032006, 2008.

[54] A. A. Affolder et al. Dijet production by double pomeron exchange at the Fermilab Tevatron. *Phys. Rev. Lett.*, 85:4215–4220, 2000.

[55] G. T. Bodwin, E. Braaten, and G. P. Lepage. Rigorous QCD analysis of inclusive annihilation and production of heavy quarkonium. *Phys. Rev.*, D51:1125–1171, 1995.

[56] E. Braaten and S. Fleming. Color octet fragmentation and the ψ' surplus at the Tevatron. *Phys. Rev. Lett.*, 74:3327–3330, 1995.

[57] J. F. Amundson, Oscar J. P. Eboli, E. M. Gregores, and F. Halzen. Colorless States in Perturbative QCD: Charmonium and Rapidity Gaps. *Phys. Lett.*, B372:127–132, 1996.

[58] P. Faccioli, C. Lourenco, J. Seixas, and H. K. Woehri. Study of ψ' and χ_c decays as feed-down sources of J/ψ hadro-production. *JHEP*, 10:004, 2008.

[59] S. X. Oda. J/psi production in Cu+Cu and Au+Au collisions at RHIC- PHENIX. 2008.

[60] M. Arneodo et al. The A dependence of the nuclear structure function ratios. *Nucl. Phys.*, B481:3–22, 1996.

[61] A. Bodek et al. Electron Scattering from Nuclear Targets and Quark Distributions in Nuclei. *Phys. Rev. Lett.*, 50:1431, 1983.

[62] K. J. Eskola, V. J. Kolhinen, and C. A. Salgado. The scale dependent nuclear effects in parton distributions for practical applications. *Eur. Phys. J.*, C9:61–68, 1999.

[63] D. de Florian and R. Sassot. Nuclear parton distributions at next to leading order. *Phys. Rev.*, D69:074028, 2004.

[64] M. Hirai, S. Kumano, and T. H. Nagai. Determination of nuclear parton distribution functions and their uncertainties at next-to-leading order. *Phys. Rev.*, C76:065207, 2007.

[65] K. J. Eskola, H. Paukkunen, and C. A. Salgado. An improved global analysis of nuclear parton distribution functions including RHIC data. *JHEP*, 07:102, 2008.

[66] M. J. Leitch et al. Measurement of J/ψ and ψ' suppression in p+A collisions at 800-GeV/c. *Phys. Rev. Lett.*, 84:3256–3260, 2000.

[67] M. C. Abreu et al. Transverse momentum distributions of J/ψ, ψ', Drell- Yan and continuum dimuons produced in Pb Pb interactions at the SPS. *Phys. Lett.*, B499:85–96, 2001.

[68] M.C. Abreu et al. Anomalous j/ψ suppression in pb - pb interactions at 158 gev/c per nucleon. *Phys. Lett.*, B410:337–343, 1997.

[69] B. Alessandro et al. J/ψ and ψ' production and their normal nuclear absorption in proton nucleus collisions at 400-gev. *Eur. Phys. J.*, C48:260, 2006.

[70] R. Vogt. Baseline cold matter effects on j/ψ production in aa collisions at rhic. *Acta Phys. Hung.*, A25:97–103, 2006.

[71] R. Granier de Cassagnac. A d - Au data-driven prediction of cold nuclear matter effects on J/ψ production in Au - Au collisions at RHIC. *J. Phys.*, G34:S955–958, 2007.

[72] A. Adare et al. Cold Nuclear Matter Effects on J/ψ as Constrained by Deuteron-Gold Measurements at $\sqrt{(}s_{NN}) = 200$ GeV. *Phys. Rev.*, C77:024912, 2008.

[73] O. Linnyk, E. L. Bratkovskaya, and W. Cassing. Open and hidden charm in proton-nucleus and heavy-ion collisions. *arXiv:0808.1504[nucl-th]*, 2008.

[74] A. Capella and D. Sousa. New J/ψ suppression data and the comovers interaction model. *nucl-th/0303055*, 2003.

[75] A. Adare et al. J/ψ production vs centrality, transverse momentum, and rapidity in Au + Au collisions at $\sqrt{s_{NN}} = 200$ GeV. *Phys. Rev. Lett.*, 98:232301, 2007.

[76] Dmitri Kharzeev, Eugene Levin, Marzia Nardi, and Kirill Tuchin. Gluon saturation effects on J/Psi production in heavy ion collisions. *arxiv:0808.2954[hep-ph]*, 2008.

[77] S. S. Adler et al. Centrality dependence of charm production from single electrons measurement in Au + Au collisions at $\sqrt{s_{NN}} = 200$ GeV. *Phys. Rev. Lett.*, 94:082301, 2005.

[78] M. Allen et al. PHENIX inner detectors. *Nucl. Instrum. Meth.*, A499:549–559, 2003.

[79] K. Ikematsu et al. A start-timing detector for the collider experiment PHENIX at RHIC-BNL. *Nucl. Instrum. Meth.*, A411:238–248, 1998.

[80] B. B. Back et al. Pseudorapidity and centrality dependence of the collective flow of charged particles in Au + Au collisions at $\sqrt{s_{NN}} = 130$ GeV. *Phys. Rev. Lett.*, 89:222301, 2002.

[81] C. Adler et al. The RHIC zero degree calorimeters. *Nucl. Instrum. Meth.*, A470:488–499, 2001.

[82] H. Appelshauser et al. Spectator nucleons in Pb + Pb collisions at 158-A-GeV. *Eur. Phys. J.*, A2:383–390, 1998.

[83] Haggerty J. et al. Letter of Intent for PHENIX Reaction Plane Detector. *PHENIX internal*, 2006.

[84] S. H. Aronson et al. PHENIX magnet system. *Nucl. Instrum. Meth.*, A499:480–488, 2003.

[85] V. G. Ryabov. Drift chambers for the PHENIX central tracking system. *Nucl. Instrum. Meth.*, A419:363–369, 1998.

[86] K. Adcox et al. PHENIX central arm tracking detectors. *Nucl. Instrum. Meth.*, A499:489–507, 2003.

[87] M. Aizawa et al. PHENIX central arm particle ID detectors. *Nucl. Instrum. Meth.*, A499:508–520, 2003.

[88] L. Aphecetche et al. PHENIX calorimeter. *Nucl. Instrum. Meth.*, A499:521–536, 2003.

[89] WA98 Collaboration. *CERN Report*, No. SPLC 91-17, 1991.

[90] A. Kozlov et al. Development of a triple GEM UV-photon detector operated in pure CF_4 for the PHENIX experiment. *Nucl. Instrum. Meth.*, A523:345–354, 2004.

[91] J. T. Mitchell et al. Event reconstruction in the PHENIX central arm spectrometers. *Nucl. Instrum. Meth.*, A482:491–512, 2002.

[92] K. Adcox et al. PHENIX detector overview. *Nucl. Instrum. Meth.*, A499:469–479, 2003.

[93] E. T. Atomssa. Detector efficiency evaluation using dead zone removal. *Int. Journ. of Mod. Phys.*, E16, Nos. 7 and 8, 2007.

[94] C. Silvestre. Première mesure de l'asymétrie azimutale de la production du J/ψ dans les collisions Au+Au à 200 GeV par paire de nucléons avec l'expérience PHENIX. *Thèse de l'École Polytechnique.*

[95] GEANT 3.2.1, CERN program library. 1993.

[96] T. Gunji et al. Analysis note of J/$\psi \rightarrow e^+e^-$ in Run 4 Au+Au collisions at $\sqrt{s_{NN}} = 200$ GeV. *PHENIX Internal Analysis Note 589.*

[97] T. Sjostrand, L. Lonnblad, and S. Mrenna. PYTHIA 6.2: Physics and manual. 2001.

[98] http://karman.physics.purdue.edu/oscar/.

[99] http://root.cern.ch/.

[100] A. Adare et al. Dilepton mass spectra in p+p collisions at sqrt(s)= 200 GeV and the contribution from open charm. *arXiv:0802.0050[hep-ex]*, 2008.

[101] W. Cassing and E. L. Bratkovskaya. Hadronic and electromagnetic probes of hot and dense nuclear matter. *Phys. Rept.*, 308:65–233, 1999.

[102] L. Grandchamp and R. Rapp. Two-component approach to J/ψ production in high-energy heavy-ion collisions. *Nucl. Phys.*, A715:545–548, 2003.

[103] R. L. Thews. *Nucl. Phys.*, A783:301–308, 2007.

[104] L. Yan, P. Zhuang, and N. Xu. Competition between J/ψ suppression and regeneration in quark-gluon plasma. *Phys. Rev. Lett.*, 97:232301, 2006.

[105] B. Zhang. J/ψ production from charm coalescence in relativistic heavy ion collisions. *Phys. Lett.*, B647:249–252, 2007.

[106] R. Rapp, D. Cabrera, and H. van Hees. Charm and charmonium in the quark-gluon plasma. *nucl-th/0608033*, 2006.

[107] P. Zhuang, L. Yan, and N. Xu. J/psi continuous regeneration and suppression in quark gluon plasma. *J. Phys.*, G34:S487–S494, 2007.

[108] A. Andronic, P. Braun-Munzinger, K. Redlich, and J. Stachel. Evidence for charmonium generation at the phase boundary in ultra-relativistic nuclear collisions. *Phys. Lett.*, B652:259–261, 2007.

[109] A. Capella et al. Charmonium dissociation and recombination at RHIC and LHC. *arXiv:0712.4331[hep-ph]*, 2007.

[110] A. M. Poskanzer and S. A. Voloshin. Methods for analyzing anisotropic flow in relativistic nuclear collisions. *Phys. Rev.*, C58:1671–1678, 1998.

[111] J. Y. Ollitrault. On the measurement of azimuthal anisotropies in nucleus– nucleus collisions. *nucl-ex/9711003*, 1997.

[112] C. L. Silva, E. T Atomssa, et al. J/$\psi \rightarrow e^+e^-$ Anisotropy Measurement in Run 7 Au+Au for QM08. *PHENIX Internal Analysis Note 666*, 2008.

[113] V. Greco, C. M. Ko, and R. Rapp. Quark coalescence for charmed mesons in ultrarelativistic heavy-ion collisions. *Phys. Lett.*, B595:202–208, 2004.

[114] L. Ravagli and R. Rapp. Quark coalescence based on a transport equation. *Phys. Lett.*, B655:126–131, 2007.

[115] X. Zhao and R. Rapp. Charmonium Production at High p_t at RHIC. *arXiv:0806.1239*, 2008.